



HAL
open science

Experimental study of flow boiling in horizontal minichannels at high saturation temperature

Romain Charnay

► **To cite this version:**

Romain Charnay. Experimental study of flow boiling in horizontal minichannels at high saturation temperature. Thermics [physics.class-ph]. INSA de Lyon, 2014. English. NNT : 2014ISAL0047 . tel-01175805

HAL Id: tel-01175805

<https://theses.hal.science/tel-01175805>

Submitted on 13 Jul 2015

HAL is a multi-disciplinary open access archive for the deposit and dissemination of scientific research documents, whether they are published or not. The documents may come from teaching and research institutions in France or abroad, or from public or private research centers.

L'archive ouverte pluridisciplinaire **HAL**, est destinée au dépôt et à la diffusion de documents scientifiques de niveau recherche, publiés ou non, émanant des établissements d'enseignement et de recherche français ou étrangers, des laboratoires publics ou privés.

Thèse

EXPERIMENTAL STUDY OF FLOW BOILING IN HORIZONTAL MINICHANNELS AT HIGH SATURATION TEMPERATURE

Présentée devant
L'institut national des sciences appliquées de Lyon

Pour obtenir
Le grade de docteur

Formation doctorale: Énergétique
École doctorale: Mécanique, Énergétique, Génie Civil, Acoustique

Par
Romain CHARNAY

Soutenue le 18 février 2014 devant la Commission d'examen

Jury

Remi REVELLIN	Maitre de Conférences HDR (INSA Lyon)	Directeur de thèse
Jocelyn BONJOUR	Professeur (INSA Lyon)	Directeur de thèse
Catherine COLIN	Professeur (IMFT Toulouse)	Rapporteur
Davide DEL COL	Professor (University of Padova)	Rapporteur
John THOME	Professor (EPFL Lausanne)	Examineur
David BRUTIN	Maitre de conférences HDR (IUSTI Marseille)	Examineur
Colin-Yann JACQUIN	Directeur Stratégie Produit, Renault Trucks	Invité

Remerciements

This study has been carried out at the Centre de Thermique de Lyon (CETHIL UMR-5008), National Institute of Applied Sciences (INSA de Lyon), under the direction of Prof. Jocelyn Bonjour and Ass. Prof. Rémi Revellin. This PhD Thesis has been supported financially by the French Environment and Energy Management Agency (ADEME), which are gratefully acknowledged.

I would like to thank Prof. Jocelyn Bonjour and Ass. Prof. Rémi Revellin for their advices and for giving me the opportunity and motivation to undertake this work. They were all the time available for fruitful research discussions and their guidance and encouragement during this period were a beneficial contribution to this study. Finally, I appreciate their total confidence and the responsibility they granted me throughout this period.

I thank Prof. Catherine Colin of IMFT-Toulouse, Prof. Davide Del Col of Padova University, Prof. John Richard Thome of Swiss Federal Institute of Technology in Lausanne, and Ass. Prof. David Brutin of Marseille University for being the examiners of this thesis.

Special thanks to my colleagues of the CETHIL for their cooperation and friendship (Seb, Lucie, Esti, Leon, Ali, Matthieu, Auline, Pierrick...).

I also acknowledge Prof Philippe Haberschill, Eric Mathieu and our technicians Joel, Nicolas, Jean, Antoine and Bernard who have skilfully participated to the construction of the experimental facility.

Last, but not least, many thanks to my family and my lovely Tere for their support and encouragement during this work. Muchas gracias.

Abstract

Because of current environmental issues, some technologies are being developed to reduce the fuel consumption and to reduce the emissions of CO₂. Energy recovery by means of Organic Rankine Cycles or Hirn Cycles is one investigated track to answer these issues. Indeed, these cycles could represent an effective way to recover the waste heat energy of the internal-combustion engines (ICE). At present, some systems based on Organic Rankine Cycle (ORC) are available in industry but advanced studies are needed to allow their application in the road transport industry. A better understanding of the two-phase fluid behaviour is necessary to optimize the design models of the components containing a two-phase refrigerant (evaporator and condenser).

For the Organic Rankine Cycle system, the thermodynamic conditions are fairly different from standards relevant to refrigeration or air-conditioning systems. Indeed, the key characteristic of the ORC system is the evaporation saturation temperature. Exhaust gas temperatures range from 400°C to 900°C so that the refrigerant evaporation occurs at temperatures higher than 100°C. Besides, in the context of research motivated by refrigeration, air-conditioning, or electronic component cooling, almost all the flow boiling heat transfer models or correlations were obtained for saturation temperatures ranging from -20°C to 40°C. The empirical models for boiling in such conditions are limited by the experimental data on which they are based, while analytical and theoretical approaches are needed to achieve advanced knowledge on the thermohydraulic behaviour of two-phase refrigerants.

This PhD thesis aims at studying the flow boiling characteristics of R-245fa in a 3.00 mm inner diameter channel in the thermodynamic conditions typical of the ORC system, i.e. for saturation temperatures ranging from 60°C to 120°C. To achieve this goal, an experimental test facility was specifically designed and built to conduct refrigerant evaporation experiments. This test facility allowed to perform flow regime visualizations, pressure drop and heat transfer measurements in minichannels.

First, an image processing method for two-phase flow pattern characterization was developed. Based on this method and with the help of an adequate analysis of the heat transfer coefficient, the main flow regimes were identified. Their transitions were detected and plotted on flow pattern maps. The influence of saturation temperature on the flow patterns and their transitions was highlighted.

The second objective was to provide new experimental data concerning flow boiling heat transfer in minichannels. Flow boiling heat transfer coefficients at such high temperatures were, so to say, never reported in the open literature so far. The influence of saturation temperature on the heat transfer mechanisms was discussed. In order to evaluate the capability of the current flow boiling prediction methods to predict the heat transfer coefficient at high saturation temperature, the comparison between experimental results and theoretical results predicted with the commonly used correlations and models was made.

Lastly, pressure drop databases were obtained. The influence of the main flow parameters, especially the saturation temperature, was studied and discussed. Experimental values of pressure drops were compared against several methods.

Résumé

La valorisation de l'énergie thermique contenue dans des gaz chauds pour produire de l'électricité est possible grâce à l'utilisation de divers cycles thermodynamiques, parmi lesquels le cycle de Rankine mérite d'être considéré. Cependant, l'industrialisation d'un tel système passe par une connaissance approfondie du comportement thermohydraulique du fluide actif, appelé par abus de langage "fluide frigorigène". Ceci permettra d'améliorer le design des principaux composants du système, spécialement les échangeurs de chaleur (évaporateur et condenseur).

Dans le cas du cycle organique de Rankine, les conditions thermodynamiques du fluide sont éloignées des conditions usuelles rencontrées dans les domaines de la climatisation ou de la réfrigération. En effet, le fluide est mis en oeuvre dans des conditions proches de son point critique, i.e., haute température réduite et haute pression réduite. La température des gaz d'échappement varie entre 400°C et 900°C et l'évaporation se produit à une température de saturation supérieure à 100°C.

En ce qui concerne les caractéristiques des écoulements diphasiques (chute de pression, coefficient de transferts thermiques, régimes d'écoulement), la quasi-totalité des méthodes de prédiction a été développée pour des températures comprises entre -20°C et 40°C correspondant aux domaines de la climatisation ou de la réfrigération. C'est pourquoi la fiabilité de ces modèles reste incertaine dans certaines conditions d'évaporation du cycle de Rankine, car leur utilisation est limitée par la base de données à partir de laquelle ils ont été établis et ils ne peuvent être extrapolés avec précision pour d'autres fluides, géométries ou conditions thermodynamiques.

Cette thèse vise à étudier les caractéristiques thermohydrauliques du R-245fa en ébullition convective dans les conditions thermodynamiques du cycle de Rankine. Dans un premier temps, un banc expérimental a été conçu et construit afin de réaliser des tests en ébullition convective dans un minicanal de 3.00 mm de diamètre. Ce banc expérimental permet de faire des mesures sur les régimes d'écoulement, les coefficients de transfert de chaleur et les pertes de charge par frottement.

Dans un second temps, une méthode de traitement d'image a été développée afin de caractériser différents régimes d'écoulement à partir de données quantitatives. Cette méthode couplée à une analyse des transferts thermiques a permis d'identifier quatre principaux régimes d'écoulement. Les transitions entre les régimes d'écoulement ont été étudiées et différentes cartes d'écoulement tracées. L'influence de la température de saturation sur les régimes d'écoulement et leurs transitions a été soulignée et discutée. Les caractéristiques des bulles ont également été étudiées à l'aide de la méthode de traitement d'image.

Dans un troisième temps, une base de données expérimentale sur les coefficients de transfert de chaleur a été créée pour l'ébullition convective du R-245fa à haute température. L'influence de la température de saturation sur les mécanismes de transfert thermique a été étudiée dans ces conditions originales. Afin de tester la fiabilité des méthodes de prédiction dans ces conditions, les résultats expérimentaux ont été confrontés à différentes méthodes de la littérature.

Finalement, les chutes de pressions ont été mesurées et une analyse paramétrique a été menée. Les mesures expérimentales ont été confrontées aux principales méthodes disponibles dans la littérature.

Nomenclature

Symbols

A	area	m^2
a	thermal diffusivity	m^2/s
B	constant of Chisholm	
C	constant of Lockhart and Martinelli	m
c	specific heat capacity	$J/K \cdot kg$
D	pixel size	pixel
d	tube diameter	m
F	multiplier factor	
f	friction factor	
f	frequency	Hz
G	mass velocity	$kg/m^2 \cdot s$
g	acceleration of gravity	m/s^2
h	specific enthalpy	J/kg
I	intensity	A
J	superficial velocity	m/s
L	pixel length	pixel
l	length	m
M	molar mass	kg/mol
\dot{m}	mass flow rate	kg/s
P	pressure	Pa
p	perimeter	m
\dot{Q}	thermal power	W
\dot{q}	heat flux	W/m^2
q''	volumetric heat flux	W/m^3
R_p	surface roughness	m
r	radius	m
S	suppression factor	
Sc	scale conversion factor	$m/pixel$
s	slip ratio	
T	temperature	$^{\circ}C$
t	time	s
U	voltage	V
u	velocity	m/s
\dot{V}	volumetric flow rate	m^3/s
v	specific volume	m^3/kg
x	vapor quality	
Y	Chisholm parameter	
y	factor of Groeneveld	
z	longitudinal abscisa	m

Greek letters

α	heat transfer coefficient	$W/m^2 \cdot K$
β	contact angle	$^{\circ}$

Δ	difference	
Δ	error	
δ	film thickness	m
ϵ	void fraction	
λ	thermal conductivity	W/m · K
γ	constant of Bankoff	
μ	dynamic viscosity	Pa · s
ν	kinetic viscosity	m ² /s
Φ	two-phase multiplier	
Ψ	enhancement ratio	
ψ	Lee and Lee parameter	
ρ	density	kg/m ³
σ	surface tension	N/m
τ	period	s
θ	constant of Beattie and Whalley	
ζ	Lee and Lee parameter	

Dimensionless numbers

Bd	Bond number
Bo	Boiling number
Co	confinement number
Cv	convective number
Eö	Eötvös number
Fa	Fang number
Fr	Froude number
La	Laplace constant
Nu	Nusselt number
Pr	Prandtl number
Re	Reynolds number
X	Martinelli's parameter
We	Weber number

Sub and super-scripts

A	configuration A
annular	annular
B	configuration B
bottom	bottom position
bubbles	bubbles
c	characteristic
cc	cross-correlation
cap	capillary
cb	convective boiling
crit	critical
D	dimensionless
d	dryout

dry	dried
di	dryout inception
de	dryout completion
dryout	dryout
evap	evaporator
exp	experimental
PF	pressure factor in Gorenflo correlation
F	related to the Fanning equation
Fr	related to Froude number
f	fluid
film	film
frict	frictional
H	homogeneous
h	hydraulic
hor	horizontal
heat	heat transfer
inner	inner
inlet	inlet
L	liquid
l	laminar
LV	boiling
mean	mean
min	minimum
mom	momentum
mist	mist flow
nb	nucleate boiling
O	only
outer	outer
outlet	outlet
PD	post dryout
p	pressure
ph	preheater
profiles	profiles
pre	pre-dryout
pred	predicted
red	reduced
SL	liquid superficial
SUB	subcooled
SV	vapor superficial
sat	saturation
ss	stainless steel
static	static
T	temperature
TP	two-phase
t	turbulent
th	threshold
top	top position
total	total
V	vapor
v	viscous
wall	wall

wet	wetted
x	vapor quality
y	position y
0	initial

Abbreviations

A	annular
ALT	atmosphere life time
AS	annular slug flow
B	bubbly
C	circular
CB	convective boiling
CB	coalescing bubble
D	dryout
G	global warming potential
F	finned
H	horizontal
HFO	hydrofluoroolefin
I	intermittent
IB	isolated bubble
IEA	International Energy Agency
ICE	internal combustion engine
M	mist
M	multiport channel
MAE	mean absolute error
MRE	mean relative error
NB	nucleate boiling
ODP	ozone depletion potential
ORC	organic Rankine cycle
PD	post dryout
R	rectangular
S	slug
S	smooth
SW	stratified wavy

Contents

1	Introduction	1
1.1	Background	1
1.2	Motivation of the study	3
1.3	Objectives of the study	4
1.4	Layout of the thesis	5
2	Fundamental definitions	7
2.1	Two-phase flow	8
2.2	Flow boiling in Tubes	8
2.3	Vapor quality	8
2.4	Cross-sectional void fraction	9
2.5	Velocities	10
2.5.1	Mass velocity	10
2.5.2	Actual velocities	10
2.5.3	Superficial velocities	11
2.6	Non-dimensional numbers	11
2.6.1	Reynolds number	11
2.6.2	Prandtl number	12
2.6.3	Bond number	12
2.6.4	Froude number	12
2.6.5	Weber number	13
2.6.6	Nusselt number	13
2.6.7	Lockart-Martinelli parameter	13
2.7	Chapter conclusions	14
3	State of the art review	15
3.1	Macro-to-microscale transition	16
3.1.1	Geometrical approach	16
3.1.2	Bubble departure diameter approach	17
3.1.3	Confinement number approach	17
3.1.4	Young-Laplace equation approach	19
3.1.5	Comparison of the macro-to-micro transition thresholds	20
3.2	Flow patterns	22
3.2.1	Two-phase flow pattern characterization techniques	22
3.2.2	Experimental studies on flow regimes	26
3.2.3	Flow pattern maps	29
3.2.4	Conclusions	35
3.3	Pressure drop	37
3.3.1	Experimental studies for pressure drop in straight tubes	37
3.3.2	Two-phase pressure drop prediction method	46
3.3.3	Conclusions	60

3.4	Heat transfer coefficient	62
3.4.1	Experimental studies on flow boiling heat transfer	62
3.4.2	Heat transfer studies in mini- and microchannels	67
3.4.3	Two-phase flow boiling heat transfer prediction methods	77
3.4.4	Conclusions	93
3.5	Conclusions on the state-of-the-art review	95
4	Description of the experiments	97
4.1	Description of the experimental test facility	98
4.2	Description of the test section	98
4.3	Measurements and accuracy	101
4.3.1	Tube diameter	102
4.3.2	Tube lengths	103
4.3.3	Temperature	103
4.3.4	Absolute pressure and differential pressure	103
4.3.5	Fluid properties	103
4.3.6	Mass flow and mass velocity	104
4.3.7	Heat flux	105
4.4	Data reduction	106
4.4.1	Vapor quality under configuration B	106
4.4.2	Vapor quality under configuration A	110
4.4.3	Heat transfer coefficient	112
4.4.4	Frictional pressure drop	113
4.5	Validation of the test section for single-phase flows	114
4.5.1	Energy balance	114
4.5.2	Heat transfer test section validation	115
4.5.3	Pressure drop test section validation	115
4.6	Image processing method	119
4.6.1	Description of the technique	119
4.6.2	Experimental validation of the optical method parameters	123
4.7	Experimental procedures	124
4.8	Conclusions	127
5	Flow patterns and bubble dynamics	129
5.1	Flow pattern characterization	130
5.1.1	Visualization	130
5.1.2	Dryout and mist flow regimes characterization	131
5.2	Flow regime transitions	134
5.2.1	Intermittent-to-annular transition	134
5.2.2	Annular-to-dryout transition	138
5.3	Flow pattern maps	141
5.3.1	Comparison with predictive models	145
5.4	Vapor bubble velocity	149
5.5	Conclusions	152
6	Heat transfer	155
6.1	Measurements of the heat transfer coefficient	156
6.1.1	Influence of saturation temperature	156
6.1.2	Influence of mass velocity	159
6.1.3	Influence of heat flux	160
6.1.4	Synthesis	163
6.2	Comparisons of the database to prediction methods	168

6.2.1	Pre-dryout prediction heat transfer methods	168
6.2.2	Dryout and post-dryout methods	191
6.3	Conclusion	193
7	Pressure drops	197
7.1	Frictional pressure drop	198
7.1.1	Pressure drop decomposition	198
7.1.2	Effect of mass velocity	198
7.1.3	Effect of saturation temperature	201
7.2	Comparisons of the database to prediction methods	202
7.2.1	Homogeneous flow model	202
7.2.2	Empirical models based on the separated flow model	206
7.2.3	Phenomenological model	215
7.3	Conclusions	220
8	Conclusions and Perspectives	221
8.1	Synthesis	221
8.2	Perspectives	224

List of Figures

1.1	World CO ₂ emissions by sector in 2009. Source IEA (Railway Handbook 2012).	1
1.2	Energy flow path in internal combustion engine. Source [Yu and Chau (2010)].	2
1.3	Working principle of an ORC cycle with (left) and without (right) recuperator.	3
1.4	Typical temperature-entropy process diagram for the ORC cycle with R-245fa.	3
2.1	Void fraction representation.	10
3.1	Comparison of selected macro-to-microscale transition criteria for R-245fa as a function of saturation temperature (The threshold diameter of [Harirchian and Garimella (2010)] was calculated from Eq. (3.13) with $Re_{LO} = 100$).	21
3.2	Capacitive void fraction signals of R-410A at $T_{sat} = 15^{\circ}C$ obtained by [Canière et al. (2010)]: (a) slug flow, (b) intermittent flow, and (c) annular flow.	23
3.3	Schematic of the laser instrumentation developed by [Revellin et al. (2006)].	24
3.4	Elongated bubble velocity as a function of vapor quality for $T_{sat} = 35^{\circ}C$ with R-134a flowing in a 0.5 mm microchannel (from [Revellin et al. (2008)]).	24
3.5	Frequency of bubbles as a function of vapor quality for various mass velocities and $T_{sat} = 31^{\circ}C$ with R-134a and R-245fa in a 2.32 mm inner diameter tube (from [Arcanjo et al. (2010)]).	25
3.6	Final processed images of different two-phase flow regimes in a 2.0 mm inner diameter channel for air-water provided by [Hanafizadeh et al. (2011)].	25
3.7	Schematic proposed by [Kew and Cornwell (1997)] showing flow regimes results with R-113 in a 1.2 mm × 0.9 mm rectangular channel: IB - isolated bubble, CB - coalescing bubble, and ASF - annular slug flow.	26
3.8	Photographs of air-water flow patterns in a 3.00 inner diameter tube visualized by [Yang and Shieh (2001)]: (a) bubble flow, (b) plug flow, (c) wavy flow, (d) slug flow, (e) annular flow, and (f) dispersed flow.	27
3.9	Elongated bubble for three different channel diameters: (a) 2.0 mm channel, (b) 0.8 mm channel, and (c) 0.5 mm channel. From [Revellin et al. (2006)].	28
3.10	Representation of heat transfer coefficient in the neighborhood of dryout from [Mori et al. (2000)].	29

3.11	Schematic proposed by [Wojtan et al. (2005a)] of (a) dryout zone during evaporation in a horizontal tube and (b) cross sections: A-A onset of dryout in annular flow, B-B dryout, and C-C end of dryout and beginning of mist flow.	30
3.12	Flow pattern map of [Mandhane et al. (1974)] for air-water.	31
3.13	Flow pattern map developed by [Wojtan et al. (2005a)] for R-22 at $T_{\text{sat}} = 5^\circ\text{C}$ in a 13.84 inner tube diameter at $G = 100 \text{ kg/m}^2\cdot\text{s}$ and $\dot{q} = 2.1 \text{ kW/m}^2$	32
3.14	Comparison between [Revellin et al. (2006)] and [Kattan et al. (1998a)] flow pattern maps for R-134a with $d_h = 0.5 \text{ mm}$ and $T_{\text{sat}} = 30^\circ\text{C}$ (A: annular flow; B: bubbly; B/S: bubbly/slug flow; S: slug flow; S/S-A: slug/semi-annular flow; S-A: semi-annular flow).	33
3.15	Diabatic coalescing bubble map of [Revellin and Thome (2007c)] for evaporating flow in circular uniformly heated microchannels for R-134a with $d_f = 0.5 \text{ mm}$ and $T_{\text{sat}} = 30^\circ\text{C}$ (IB: isolated bubble regime, CB: coalescing bubble regime, A: annular regime, and PD: post dry-out regime).	34
3.16	Comparison between the experimental data of [Arcanjo et al. (2010)] and the predictive methods (lines) by [Ong and Thome (2009)] and by [Revellin et al. (2006)] with R-245fa in a 2.32 mm inner diameter channel at (a) $T_{\text{sat}} = 22^\circ\text{C}$ and (b) $T_{\text{sat}} = 41^\circ\text{C}$	35
3.17	Schematic of the 6 primary flow regimes commonly recognized in the literature.	36
3.18	Influence of saturation temperature on elongated bubbles characteristics: (a) elongated bubble velocity as a function of vapor quality for R-134a flowing in a 0.5 mm inner diameter tube at $G = 1000 \text{ kg/m}^2\cdot\text{s}$ from [Revellin et al. (2008)], (b) elongated bubble length as a function of vapor quality for R-134a flowing in a 0.5 mm inner diameter tube at $G = 1000 \text{ kg/m}^2\cdot\text{s}$ from [Revellin et al. (2008)], and (c) elongated bubble frequency as a function of vapor quality from [Arcanjo et al. (2010)].	36
3.19	Number of pressure drop data points (22363 data points in total) for each refrigerant published in 122 articles since 1980 for flow boiling ([Charnay et al. (2011)]).	38
3.20	Schematic of the typical trends of two-phase flow pressure drop observed in macrochannels: influence of the mass velocity and the vapor quality.	38
3.21	R-22 two-phase flow pressure drop measured by [Zhang and Webb (2001)] in a 3.25 mm inner diameter tube.	39
3.22	Schematic of the typical trends of two-phase flow pressure drop observed in macrochannels: influence of the saturation temperature.	39
3.23	Frictional pressure gradients versus vapor quality for different mass velocities. From [Quibén and Thome (2007a)].	40
3.24	Schematic of the typical trends of two-phase flow pressure drop observed in macrochannels: influence of the inner tube diameter.	41
3.25	Schematic of typical trends of the influence of reduced pressure on the two-phase flow pressure drop.	44
3.26	Two-phase frictional pressure drop as a function of the vapor quality for R-134a, $d_h = 0.509 \text{ mm}$ and $T_{\text{sat}} = 30^\circ\text{C}$ and the corresponding flow patterns at the locations (a) and (b): (a) wavy annular and (b) smooth annular flow. From [Revellin and Thome (2007b)].	45

3.27	[Lockhart and Martinelli (1949)] correlation.	51
3.28	Distribution of data points published in 122 articles since 1980 for pressure drop studies with respect to saturation temperature and reduced pressure([Charnay et al. (2011)]).	61
3.29	Comparison among several two-phase pressure drop prediction methods for R-245fa in a 3.00 mm inner tube diameter at 500 kg/m ² ·s for two different saturation temperatures: 40°C and 120°C.	62
3.30	Number of flow boiling heat transfer coefficient data points (28416 data points in total) for each refrigerant published in 130 articles since 1980 for flow boiling ([Charnay et al. (2011)]).	63
3.31	Influence of (a) heat flux and (b) mass velocity on the heat transfer coefficient observed by [Jabardo and Bandarra Filho (2000)].	65
3.32	Schematic of the typical trends of heat transfer coefficient observed with nucleate and convective boiling dominant regions (NB: Nucleate Boiling and CB: Convective Boiling).	67
3.33	Heat transfer coefficient measured by [Lazarek and Black (1982)] as a function of vapor quality for various heat fluxes.	68
3.34	Schematic of flow regimes during nucleate boiling in a horizontal small channel proposed by [Kasza et al. (1997)].	69
3.35	Schematic of the typical trends observed for heat transfer coefficient in the case of nucleate boiling dominance (NB: Nucleate Boiling).	69
3.36	Effect of heat flux and mass flux on heat transfer coefficient observed by [Saitoh et al.(2005)] for two different diameter channels: (a) 3.1 mm and (b) 1.12 mm.	70
3.37	Schematic of the typical trends of heat transfer coefficient when convective boiling is dominant (CB: Convective Boiling).	71
3.38	Influence of saturation temperature on the heat transfer coefficient with R-134a in a 8.0 mm inner diameter channel. From [Del Col (2010)].	74
3.39	Influence of saturation temperature on the heat transfer coefficient. From [Saisorn et al. (2010b)].	75
3.40	Schematic of the typical heat transfer coefficient trends with the influence of saturation temperature.	75
3.41	Annular flow with partial dry-out by [Thome et al. (2004a)].	87
3.42	Three-zone heat transfer model for elongated bubble flow regime in microchannels developed by [Thome et al. (2004a)].	90
3.43	Distribution of data points published (28416 data points) in 130 articles since 1980 for heat transfer studies with respect to saturation temperature and reduced pressure([Charnay et al. (2011)]).	93
3.44	Comparison among several flow boiling heat transfer prediction methods for R-245fa in a 3.00 mm inner tube diameter at 500 kg/m ² ·s and 50 kW/m ² for two different saturation temperatures: 40°C and 120°C.	94
4.1	Schematic of the test facility.	99
4.2	Schematic of the test section.	99
4.3	Image of the heat transfer test section before thermal insulating (i.e. evaporator).	100
4.4	Schematic view of the evaporator (right) and thermocouple locations (left).	101
4.5	Schematic view of the preheater in configuration B.	106

4.6	Variation of R-245fa latent heat of vaporization as a function of the reduced pressure in the extreme case of a pressure drop along the preheater equal to 1.5 bar.	107
4.7	Computational algorithm of the single-phase flow pressure drop and the subcooled length for R-245fa flowing under configuration B. . . .	108
4.8	Schematic view of the evaporator in configurations A.	110
4.9	Energy balance: single-phase validation	116
4.10	Comparison between experimental Nusselt numbers and predicted Nusselt number.	117
4.11	Comparison between experimental friction factors and predicted friction factors.	118
4.12	Comparison between experimental pressure drop measured by the three different sensors and the pressure drop calculated by [Churchill (1977)].	119
4.13	Diagram of the image acquisition system.	120
4.14	Grayscale value used in the image processing.	120
4.15	Profile positions and image information necessary for scale plan calculation.	121
4.16	Example of (a) a grayscale signal and (b) a histogram of its distribution showing the chosen threshold for characterizing a bubbly slug flow: (a) Signal at profile 1 versus time and (b) histogram of 6,000 images segregated into 5 grayscale value steps.	122
4.17	Example of normalized cross-correlation of grayscale value signals from the two profiles.	124
4.18	Method parameters validation for R-245fa with $d_{\text{inner}} = 3.00$ mm and $T_{\text{sat}} = 60$ °C: (a) bubble counts/s at profile 1 versus acquisition time : chosen value of acquisition time parameter, 2 seconds; (b) bubble velocity versus acquisition time : chosen value of acquisition time parameter, 2 seconds; (c) bubble frequency versus distance between two image profiles : chosen distance between two image profiles, 11.5 mm.	125
5.1	Flow pattern photos for R-245fa with $d_{\text{inner}} = 2.96$ mm and $T_{\text{sat}} = 60$ °C : (a) bubbly flow at $x = 0.01$, $G = 500$ kg/m ² ·s and $\dot{q} = 50$ kW/m ² ; (b) bubbly-slug flow at $x = 0.05$, $G = 300$ kg/m ² ·s and $\dot{q} = 50$ kW/m ² ; (c) slug flow at $x = 0.16$, $G = 100$ kg/m ² ·s and $\dot{q} = 30$ kW/m ² ; (d) annular flow at $x = 0.92$, $G = 500$ kg/m ² ·s and $\dot{q} = 50$ kW/m ²	130
5.2	Flow pattern signals with thresholds for R-245fa with $d_{\text{inner}} = 2.96$ mm and $T_{\text{sat}} = 60$ °C.	132
5.3	Influence of the vapor quality on the flow patterns for R-245fa in a 2.96 inner tube diameter at $T_{\text{sat}} = 120$ °C, $\dot{q} = 50$ kW/m ² and $G = 500$ kg/m ² ·s.	132
5.4	Temperatures and heat transfer coefficients as a function of vapor quality at 120°C with flow patterns (I: intermittent; A: annular; D-O: dryout; M: mist flow and V: vapor).	133
5.5	Influence of the mass velocity on the flow patterns for R-245fa in a 2.96 inner tube diameter at $T_{\text{sat}} = 120$ °C, $\dot{q} = 50$ kW/m ² and $x = 0.32$	135
5.6	Influence of the mass velocity on the vapor bubble characteristic for R-245fa, $d_{\text{inner}} = 2.96$ mm, $T_{\text{sat}} = 60$ °C and $\dot{q} = 50$ kW/m ²	136
5.7	Influence of the heat flux on the flow patterns for R-245fa in a 2.96 inner tube diameter at $T_{\text{sat}} = 120$ °C, $G = 500$ kg/m ² ·s and $x = 0.20$	136

5.8	Influence of the heat flux on the vapor bubble characteristic for R-245fa, $d_{\text{inner}} = 2.96$ mm, $T_{\text{sat}} = 80$ °C and $G = 300$ kg/m ² ·s.	137
5.9	Influence of the saturation temperature on the flow patterns for R-245fa in a 2.96 inner tube diameter at $G = 500$ kg/m ² and $\dot{q} = 50$ kW/m ²	138
5.10	Influence of the saturation temperature on the vapor bubble characteristic for R-245fa, $d_{\text{inner}} = 2.96$ mm, $G = 300$ kg/m ² ·s and $\dot{q} = 50$ kW/m ²	139
5.11	Influence of the saturation temperature on the vapor bubble characteristic for R-245fa, $d_{\text{inner}} = 2.96$ mm, $G = 500$ kg/m ² ·s and $\dot{q} = 30$ kW/m ²	139
5.12	Influence of the mass velocity on the dryout.	140
5.13	Influence of the heat flux on the wall temperature and detection of dryout.	140
5.14	Influence of the saturation temperature on the dryout.	141
5.15	Flow pattern maps with transition lines for R-245fa and $\dot{q} = 50$ kW/m ² at four saturation temperatures.	142
5.16	Flow pattern maps with transition lines for R-245fa and $\dot{q} = 50$ kW/m ² at four saturation temperatures.	143
5.17	Influence of the heat flux on the intermittent-to-annular transition.	144
5.18	Influence of the heat flux on the annular-to-dryout and dryout-to-mist flow transition.	144
5.19	Comparison between present intermittent-to-annular transition lines observed for R-245fa at $T_{\text{sat}} = 120$ °C and predicted intermittent-to-annular transition lines.	146
5.20	Comparison between present annular-to-dryout transition lines observed for R-245fa at $T_{\text{sat}} = 120$ °C and predicted annular-to-dryout transition lines proposed by [Sun and Groll (2002)] and [Wojtan et al. (2005a)].	148
5.21	Comparison between present dryout-to-mist transition lines observed for R-245fa at $T_{\text{sat}} = 120$ °C and predicted dryout-to-mist transition lines proposed by [Mori et al. (2000)] and [Wojtan et al. (2005a)].	148
5.22	Effect of the mass velocity on the mean bubble velocity for R-245fa, $d_{\text{inner}} = 2.96$ mm, $\dot{q} = 50$ kW/m ² , and two different saturation temperature and comparison with the predicted void fraction calculated from the homogeneous model.	149
5.23	Effect of saturation temperature on the mean bubble velocity for R-245fa, $d_{\text{inner}} = 2.96$ mm, $\dot{q} = 50$ kW/m ² , and two different mass velocities and comparison with the predicted bubble velocity calculated from the homogeneous model.	150
5.24	Effect of the mass velocity on the void fraction for R-245fa, $d_{\text{inner}} = 2.96$ mm, $\dot{q} = 50$ kW/m ² , and two different saturation temperature and comparison with the predicted void fraction calculated from the homogeneous model.	150
5.25	Comparison of experimental velocity with predictive models.	151
6.1	Influence of the saturation temperature on the heat transfer coefficient for R-245fa at 300 kg/m ² ·s and 700 kg/m ² ·s with a heat flux of 50 kW/m ² (I: intermittent flow and A: annular flow).	158

6.2	Influence of mass velocity on heat transfer coefficient for R-245fa at 60°C, 80°C, 100°C and 120°C with a heat flux of 50 kW/m ² (I: intermittent flow and A: annular flow).	162
6.3	Influence of heat flux on heat transfer coefficient for R-245fa at 60°C, 80°C, 100°C and 120°C with a mass velocity of 500 kg/m ² ·s (I: intermittent and A: annular).	165
6.4	Relation between heat transfer coefficient, flow configuration and heat transfer mechanism (A: Annular, CB: Convective Boiling, D: Dryout, Ev _{droplets} : evaporation of the liquid droplets, Ev _{film} : evaporation of the liquid film, FC _L : liquid forced convection, FC _V : vapor forced convection, I: Intermittent, L: Liquid, M: Mist, NB: Nucleate Boiling and V: Vapor).	167
6.5	Comparison between experimental heat transfer coefficients and those predicted by pool boiling correlations.	170
6.6	Comparison between the experimental trends and those predicted by pool boiling correlations at 60°C and 120°C ((a) T _{sat} = 60°C, q̇ = 50 kW/m ² , and G = 700 kg/m ² ·s and (b) T _{sat} = 120°C, q̇ = 50 kW/m ² , and G = 700 kg/m ² ·s).	171
6.7	Comparison between experimental heat transfer coefficients and those predicted by asymptotic models at 60°C and 120°C.	174
6.8	Comparison between the experimental trends and those predicted by asymptotic models at 60°C and 120°C ((a) T _{sat} = 60°C, q̇ = 50 kW/m ² , and G = 700 kg/m ² ·s and (b) T _{sat} = 120°C, q̇ = 50 kW/m ² , and G = 700 kg/m ² ·s).	175
6.9	Comparison between experimental heat transfer coefficients and those predicted by asymptotic models developed for carbon dioxide with or without other fluids.	178
6.10	Comparison between the experimental trends and those predicted by asymptotic models for carbon dioxide with or without other fluids at 60°C and 120°C((a) T _{sat} = 60°C, q̇ = 50 kW/m ² , and G = 700 kg/m ² ·s and (b) T _{sat} = 120°C, q̇ = 50 kW/m ² , and G = 700 kg/m ² ·s).	179
6.11	Comparison between experimental heat transfer coefficients and those predicted by the correlation of [Shah (1982)] at 60°C and 120°C.	181
6.12	Comparison between the experimental trends and those predicted by the correlation of [Shah (1982)] ((a) T _{sat} = 60°C, q̇ = 50 kW/m ² , and G = 700 kg/m ² ·s and (b) T _{sat} = 120°C, q̇ = 50 kW/m ² , and G = 700 kg/m ² ·s).	182
6.13	Comparison between the experimental heat transfer coefficients and those predicted by Nusselt-type correlations.	184
6.14	Comparison between the experimental trends and those predicted by Nusselt-type correlations at 60°C and 120°C ((a) T _{sat} = 60°C, q̇ = 50 kW/m ² , and G = 700 kg/m ² ·s and (b) T _{sat} = 120°C, q̇ = 50 kW/m ² , and G = 700 kg/m ² ·s).	185
6.15	Comparison between experimental heat transfer coefficients and those predicted by the phenomenological models of [Thome and El Hajal (2004c)] and [Wojtan et al. (2005b)] at 60°C and 120°C.	188
6.16	Comparison between experimental heat transfer coefficients and those predicted by the 3-zone model of [Thome et al. (2004a)].	189
6.17	Comparison between experimental heat transfer coefficients and those predicted by the model of [Cioncolini and Thome (2011)].	189

6.18	Comparison between the experimental trends and those predicted by phenomenological methods ((a) $T_{\text{sat}} = 60^{\circ}\text{C}$, $\dot{q} = 50 \text{ kW/m}^2$, and $G = 700 \text{ kg/m}^2\cdot\text{s}$ and (b) $T_{\text{sat}} = 120^{\circ}\text{C}$, $\dot{q} = 50 \text{ kW/m}^2$, and $G = 700 \text{ kg/m}^2\cdot\text{s}$)	191
6.19	Comparison between experimental heat transfer coefficients and those predicted by post-dryout correlations.	192
6.20	Comparison between the experimental trends and those predicted by post-dryout correlations at 120°C ($T_{\text{sat}} = 120^{\circ}\text{C}$, $\dot{q} = 50 \text{ kW/m}^2$, and $G = 700 \text{ kg/m}^2\cdot\text{s}$).	193
7.1	Total, frictional and momentum pressure drops versus vapor quality at different experimental conditions for R-245fa flowing in a 3.00 mm inner tube diameter.	198
7.2	Relation between frictional pressure drop and flow configuration (A: annular, D: Dryout, and I: Intermittent)	199
7.3	Influence of the mass velocity on the pressure drop for R-245fa in a 3.00 mm inner tube diameter.	200
7.4	Influence of the saturation temperature on the pressure drop for R-245fa in a 3.00 mm inner tube diameter.	201
7.5	Comparison between experimental frictional pressure drop data and those predicted by several correlations based on the homogeneous flow model with different two-phase viscosity definitions.	203
7.6	Comparison between the experimental trends and those predicted by the correlations based on the homogeneous flow model with different two-phase viscosity definitions at 60°C and 120°C ((a) $T_{\text{sat}} = 60^{\circ}\text{C}$ and $G = 500 \text{ kg/m}^2\cdot\text{s}$ and (b) $T_{\text{sat}} = 120^{\circ}\text{C}$ and $G = 500 \text{ kg/m}^2\cdot\text{s}$).	204
7.7	Comparison between experimental frictional pressure drop data and those predicted by correlations based on the separated flow model and the Φ_L^2 , Φ_V^2 method.	209
7.8	Comparison between the experimental trends and those predicted by the Φ_L^2 , Φ_V^2 correlations based on the separated flow model at 60°C and 120°C ((a) $T_{\text{sat}} = 60^{\circ}\text{C}$ and $G = 500 \text{ kg/m}^2\cdot\text{s}$ and (b) $T_{\text{sat}} = 120^{\circ}\text{C}$ and $G = 500 \text{ kg/m}^2\cdot\text{s}$).	210
7.9	Comparison between experimental frictional pressure drop data and those predicted by the Φ_{LO}^2 , Φ_{VO}^2 correlations based on the separated flow model correlations based on the separated flow model.	212
7.10	Comparison between the experimental trends and those predicted by the Φ_{LO}^2 , Φ_{VO}^2 correlations based on the separated flow model at 60°C and 120°C ((a) $T_{\text{sat}} = 60^{\circ}\text{C}$ and $G = 500 \text{ kg/m}^2\cdot\text{s}$ and (b) $T_{\text{sat}} = 120^{\circ}\text{C}$ and $G = 500 \text{ kg/m}^2\cdot\text{s}$).	213
7.11	Comparison between experimental frictional pressure drop data and those predicted by the phenomenological model of [Quibén and Thome (2007b)].	216
7.12	Comparison between experimental frictional pressure drop and those predicted by (a) the microscale model and (b) the macroscale model of [Cioncolini et al. (2009)].	217
7.13	Comparison between the experimental trends and those predicted by the phenomenological models of [Quibén and Thome (2007b)] and [Cioncolini et al. (2009)] for two situations: (a) $T_{\text{sat}} = 60^{\circ}\text{C}$ and $G = 500 \text{ kg/m}^2\cdot\text{s}$ and (b) $T_{\text{sat}} = 120^{\circ}\text{C}$ and $G = 500 \text{ kg/m}^2\cdot\text{s}$	218

List of Tables

3.1	Summary of the threshold diameter expressions and the values of Eötvös number corresponding.	20
3.2	Summary of experimental two-phase flow pressure drop studies in macrochannels (C: circular; F: finned; H: horizontal; M: multiport channel; S: smooth).	43
3.3	Two-phase viscosities proposed by several authors used in the homogeneous flow models.	47
3.4	Summary of experimental two-phase flow pressure drop studies in mini- and microchannels (C: circular; F: finned; H: horizontal; M: multiport; R: rectangular; S: smooth).	49
3.5	Values of C to fit the empirical curves of [Lockhart and Martinelli (1949)].	51
3.6	Empirical constants of [Lee and Lee (2001)].	52
3.7	Values of B for the correlation of [Chisholm (1973)] for smooth tubes.	56
3.8	Summary of experimental flow boiling heat transfer studies in macrochannels.	66
3.9	Summary of experimental flow boiling heat transfer studies in minichannels and microchannels.	72
3.10	Summary of experimental flow boiling heat transfer studies on the influence of saturation temperature.	76
3.11	Experimental conditions used to develop the asymptotic models with $n = 2$ (see Eq. (3.92)) (A: annuli, C: circular, H: horizontal R: rectangular, and V: vertical).	82
3.12	Experimental conditions used to develop the asymptotic models with $n = 3$ (see Eq. (3.92)) (A: annuli, C: circular, H: horizontal R: rectangular, and V: vertical).	84
3.13	Experimental conditions used to develop the Nusselt-type correlations (A: annuli, C: circular, H: horizontal R: rectangular, and V: vertical).	88
3.14	Experimental conditions used to develop the prediction models based on the phenomenological approach (A: annuli, C: circular, H: horizontal R: rectangular, and V: vertical).	92
3.15	Experimental conditions used to develop the prediction correlations and models for post-dryout heat transfer coefficient (A: annuli, C: circular, H: horizontal R: rectangular, and V: vertical).	96
4.1	R-245fa properties (ALT: Atmosphere Life Time - GWP: Global Warming Potential - ODP: Ozone Depletion Potential).	98
4.2	Sensors used for the instrumentation of the experimental setup.	102
4.3	Coefficients for the R-245fa enthalpy calculations.	104
4.4	Uncertainties on heat power and heat flux.	106

4.5	Optical measurement conditions.	119
4.6	Experimental conditions for flow boiling experiments.	126
4.7	Experimental conditions for two-phase flow experiments.	126
5.1	R-245fa properties at 60°C and 120°C	137
5.2	Comparison between the experimental results and the predicted results.	152
6.1	R-245fa properties at 60°C and 120°C.	156
6.2	Summary of the statistical analysis of the comparisons between experimental heat transfer coefficients and those predicted by pool boiling correlations (MAE: Mean Absolute Error, MRE: Mean Relative Error and $\pm 30\%$: percentage of data predicted within 30% error bar).	172
6.3	Summary of the statistical analysis of the comparisons between experimental heat transfer coefficients and those predicted by asymptotic models (MAE: Mean Absolute Error, MRE: Mean Relative Error and $\pm 30\%$: percentage of data predicted within 30% error bar).	176
6.4	Summary of the statistical analysis of the comparisons between experimental heat transfer coefficients and those predicted by asymptotic models developed for carbon dioxide with or without other fluids (MAE: Mean Absolute Error, MRE: Mean Relative Error and $\pm 30\%$: percentage of data predicted within 30% error bar).	180
6.5	Summary of the statistical analysis of the comparisons between experimental heat transfer coefficients and those predicted by the correlation of [Shah (1982)] (MAE: Mean Absolute Error, MRE: Mean Relative Error and $\pm 30\%$: percentage of data predicted within 30% error bar).	183
6.6	Summary of the statistical analysis of the comparisons between experimental heat transfer coefficients and those predicted by Nusselt-type correlations (MAE: Mean Absolute Error, MRE: Mean Relative Error and $\pm 30\%$: percentage of data predicted within 30% error bar).	186
6.7	Summary of the statistical analysis of the comparisons between experimental heat transfer coefficients and those predicted by models based on the phenomenological approach (MAE: Mean Absolute Error, MRE: Mean Relative Error and $\pm 30\%$: percentage of data predicted within 30% error bar).	190
6.8	Summary of the statistical analysis of the comparisons between experimental heat transfer coefficients and those predicted by post-dryout correlations (MAE: Mean Absolute Error, MRE: Mean Relative Error and $\pm 30\%$: percentage of data predicted within 30% error bar).	195
7.1	Summary of the statistical analysis of the comparisons between experimental frictional pressure drops and those predicted by the correlations based on the homogeneous flow model with different two-phase viscosity definitions (MAE: Mean Absolute Error, MRE: Mean Relative Error and $\pm 30\%$: percentage of data predicted within 30% error bar).	205

7.2	Summary of the statistical analysis of the comparisons between experimental frictional pressure drops and those predicted by the Φ_L^2 , Φ_V^2 correlations based on the separated flow model (MAE: Mean Absolute Error, MRE: Mean Relative Error and $\pm 30\%$: percentage of data predicted within 30% error bar).	207
7.3	Summary of the statistical analysis of the comparisons between experimental frictional pressure drops and those predicted the Φ_{LO}^2 , Φ_{VO}^2 correlations based on the separated flow model (MAE: Mean Absolute Error, MRE: Mean Relative Error and $\pm 30\%$: percentage of data predicted within 30% error bar).	214
7.4	Summary of the statistical analysis of the comparisons between experimental frictional pressure drops and those predicted by the phenomenological models (MAE: Mean Absolute Error, MRE: Mean Relative Error and $\pm 30\%$: percentage of data predicted within 30% error bar).	219

Chapter 1

Introduction

1.1 Background

Despite technological improvements, transport CO₂ total emissions have constantly increased since 1990 and all transport modes have increased their greenhouse gas emissions due to the fuel combustion (IEA, 2011). The transport sector in 2009 was responsible for about 31% of total CO₂ emissions from fuel combustion. In this sector, the road was the main responsible with 71% of total CO₂ emissions as shown in Fig. 1.1. Moreover transport CO₂ total emissions carried out about 28% of growth from 1990 to 2009 and about 5% from 2000 to 2009: all transport modes - except railways - have increased their total emissions. In order to limit the climate change due to the increase of greenhouse effect, the CO₂ emissions associated with the consumption of fossil fuel need to be minimized.

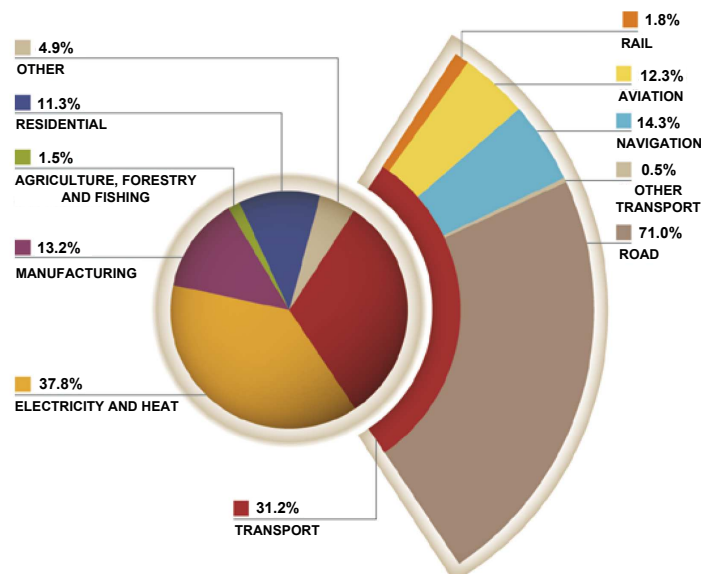


Figure 1.1: World CO₂ emissions by sector in 2009. Source IEA (Railway Handbook 2012).

With the huge increase in oil price and growing the awareness on the environmental concerns, energy saving measures have been taken with an accelerated pace to minimize the CO₂ emissions. Previous studies have shown that the efficiency

during the fuel combustion is about 25% in a internal combustion engine. The produced energy is converted into the vehicle motion and its loads. The remainder is engine waste heat that is dissipated by the engine exhaust system, coolant system, and convection as well as radiation from engine block (see Fig. 1.2). Nearly 40% of heat energy is wasted with the engine exhaust gas. If this part of waste heat could be harnessed, energy efficiency would be enhanced, and thus vehicles all over the world could save lots of energy. Furthermore, CO₂ emissions would be decreased which is recognized as an important factor in anthropogenic climate change.

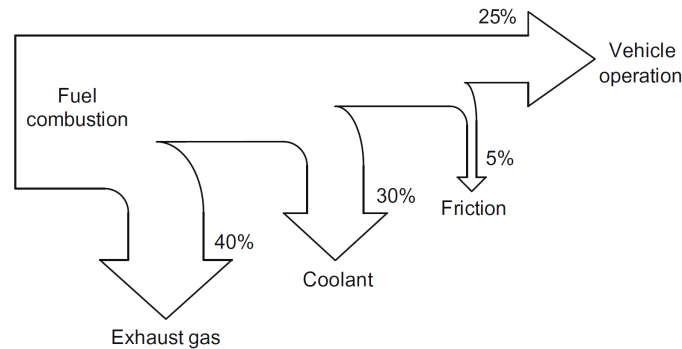


Figure 1.2: Energy flow path in internal combustion engine. Source [Yu and Chau (2010)].

Energy recovery by means of Organic Rankine Cycles is one of the investigated tracks to recover this energy from exhaust gas. The ORC system is a vapor power cycle that works using the same principles as the steam Rankine cycle, except that a fluid with a lower boiling point and higher molecular mass is used. This enables the operation of the cycle at a much lower temperatures than a steam Rankine cycle. Thus, using the energy from the heat sources of the low temperature waste, the ORC can produce electricity and thus represents an effective way to recover the waste heat energy of internal combustion engines (ICE).

The Rankine cycle is composed of four main components: evaporator, turbine, condenser and pump. As represented on Fig. 1.3, an organic working fluid¹ is evaporated to run through a turbine to generate electricity. Figure 1.4 displays the typical temperature-entropy process diagram for the ORC cycle with R-245fa. Depending on the working fluid, a recuperator might be advantageous. ORC systems offer a wide range of parameters for optimization. Among these parameters, the selection of working fluid is the most obvious.

At present, some systems based on Organic Rankine Cycles (ORC) are available in industry but advanced studies are needed to allow their application in the road transport industry. A better understanding of the two-phase fluid behaviour is necessary to optimize the design models of the components containing a two-phase fluid (evaporator and condenser). As reported by [Srinivasan et al. (2010)], the evaporator is the key heat exchanger in Organic Rankine Cycle system. Indeed, the key characteristic of the ORC is the evaporation saturation temperature. Exhaust gases temperature ranges from 400°C to 900°C and the refrigerant evap-

¹Because of the nature of the fluid choose in the present work, and as this is also a common practice with ORC using synthetic fluids, the working fluid will often be referred to as "refrigerant".

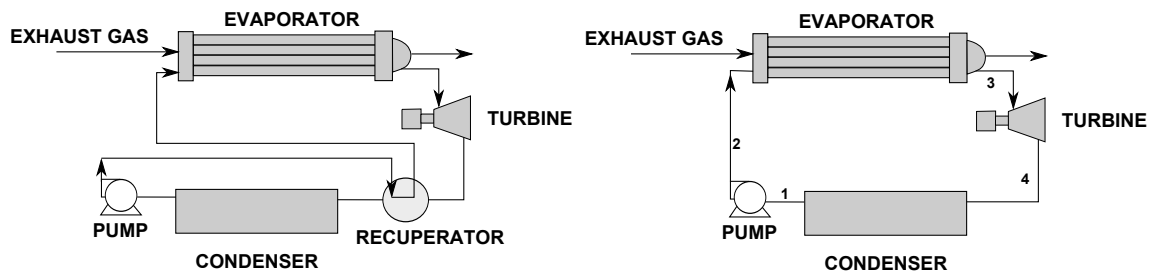


Figure 1.3: Working principle of an ORC cycle with (left) and without (right) recuperator.

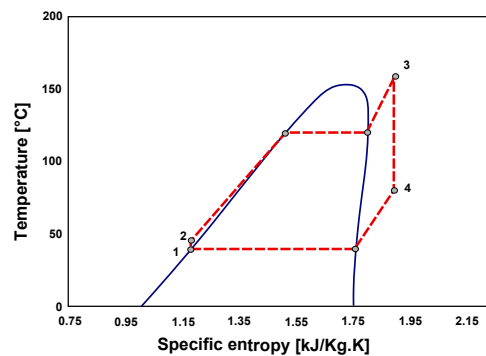


Figure 1.4: Typical temperature-entropy process diagram for the ORC cycle with R-245fa.

oration occurs at temperatures higher than 100°C . These temperatures are much higher than standards relevant to refrigeration or air conditioning systems.

1.2 Motivation of the study

The ORC system efficiency optimization is linked to a better sizing and design of the each component, especially heat exchangers. For the design of phase-change heat exchangers, pressure drops, heat transfer coefficients and flow patterns are the required data.

Heat transfer coefficients and pressure drops are related to the local two-phase flow structure of the fluid. Besides recent heat transfer models for predicting boiling are based on the local flow pattern and therefore require reliable two-phase flow pattern maps to identify what type of flow pattern exists at the local flow conditions.

Moreover, the prediction models or correlations cannot be extrapolated with accuracy for different fluids because of the change of properties (mostly viscosity, density and surface tension), different geometries or different thermodynamic conditions (pressure, temperature) from those for which they were initially developed. The empirical models for boiling in such conditions are limited by the experimental data on which they are based, whereas analytical and theoretical approaches are needed to gain improved knowledge on the thermohydraulic behaviour two-phase refrigerant. Furthermore, miniaturization has recently become the key word in these emerging technologies, both for reducing the weight of the system and the fluid charge. The transition from conventional to compact heat exchangers is

however not completely ready yet.

Since the paper published by [Cooper (1984)], it is usually recognized that different fluids, at similar reduced pressure, may present similar behaviors. As a matter of fact, invoking the principle of corresponding states, one could expect that, at a first order, two fluids would have the same thermohydraulic characteristics when at the same reduced pressure and reduced temperature. However, a literature analysis shows that there is a gap in knowledge of the flow boiling for synthetic refrigerants at high saturation temperature (60-120 °C) and moderate reduced pressure (0.2-0.5) while data were reported for the same range of reduced pressure but for lower saturation temperatures. Indeed, most of publications available in the literature are focused on the saturation temperatures ranging from -20°C to 40°C corresponding to the following applications:

- -20 °C to 0 °C: commercial refrigeration and operation of heat pump in winter
- 0 °C to 10 °C: static air conditioning
- 10 °C to 20 °C: heat pump in summer and middle-season
- 20 °C to 40 °C: cooling of electronic components

Hence, the reliability of the correlations or predictive models used for the ORC evaporator sizing is not ensured ($T_{\text{sat}} > 120$ °C). Indeed, when the saturation temperature increases toward the critical point (i.e. when the reduced temperature increases), the density and the viscosity of vapor phase increase while the viscosity and the density of liquid phase decrease. These both trends tend to reduce the vapor phase velocity and to increase the liquid phase velocity. In other words, the slip ratio tends to 1. An increase in reduced temperature also leads to a decrease in surface tension and thus, the Bond Number decreases (gravity forces become predominant). All these properties widely influence the liquid-vapor interactions, and thus the flow patterns.

Thus, it is very risky to extrapolate two-phase flow boiling models to high saturation temperatures. Providing accurate and reliable heat transfer and pressure drop models is hence the first step to optimize the design of the Organic Rankine Cycles. An accurate prediction of heat transfer and pressure drop coefficients can reduce costs by avoiding both undersizing and oversizing of evaporators. Moreover, the optimal design of the evaporator permits to reduce the weight of these embedded systems on cars or trucks.

1.3 Objectives of the study

The present thesis aims at providing experimental results on flow boiling at a high saturation temperature in a minichannel. To reach this general goal, we defined several objectives that are summed up in the following.

The first objective was to develop a test facility in order to perform refrigerant evaporation experiments in the conditions of ORC systems. The test facility was to be built in such a way that flow visualizations, flow boiling heat transfer coefficient measurements, and two-phase pressure drop measurements could be done on the same system.

The second objective was to develop an image processing method to characterize the two-phase flow regimes from quantitative details such as bubble frequency and bubble size.

The third objective of this experimental investigation was to investigate the influence of the main flow parameters and the saturation conditions on the flow patterns, the bubble characteristics, the heat transfer mechanisms and the pressure drop.

The fourth objective was to develop heat transfer coefficient and pressure drop databases for a wide range of experimental conditions.

The fifth objective was to assess the well-known flow boiling heat transfer coefficients and two-phase pressure drop prediction methods in the conditions of the ORC systems.

1.4 Layout of the thesis

The thesis is divided into eight chapters. It is organized as follows:

- *Chapter 1* provides a background to the study, by motivating the study and stating the research objectives.

- In *Chapter 2*, the definition of main parameters and basic equations used in two-phase flow are presented as well as the main dimensionless numbers.

- *Chapter 3* gives an overview of the state-of-the-art review related to the existing studies on flow visualization, flow pattern map, pressure drop, and heat transfer during flow boiling of refrigerants. The most quoted flow pattern maps, two-phase pressure drop predictive methods and flow boiling heat transfer predictive methods are presented and classified. The objective is to illustrate typical trends observed in the literature on the influence of the main flow parameters and thermodynamic conditions.

- *Chapter 4* describes the experimental test facility as well as the test sections used for visualization and heat transfer and pressure drop measurements. Additionally, an image processing method to characterize the two-phase flow regimes is presented. The experimental methodology and data reduction procedure are also described.

- In *Chapter 5*, a description of the two-phase flow patterns observed for R-245fa in a minichannel at high saturation temperature is presented. The effect of the heat flux, the mass velocity and the saturation temperature is introduced and discussed. New diabatic flow pattern maps are presented and the experimental transition lines are compared against predictions available in the literature. Additionally, bubble characteristics results are presented.

- *Chapter 6* presents experimental data concerning flow boiling heat transfer in minichannel at high saturation temperatures. The database is composed of 5964 data points covering four flow patterns. This chapter aims at highlighting the influence of the saturation temperature on the heat transfer mechanisms. The experimental results are compared to the commonly used correlations or models. The effect of the saturation temperature and the kind of flow pattern on the capability

of these methods to predict the flow boiling heat transfer coefficient is investigated.

- *Chapter 7* provides experimental results on two-phase frictional pressure drop. The present database is composed of 249 data points. A parametric analysis is presented. The experimental data set is compared against 21 well-known two-phase frictional pressure drop prediction methods.

- *Chapter 8* presents the general conclusions of this study and the perspectives.

Chapter 2

Fundamental definitions

This chapter presents the fundamentals two-phase fluid mechanics and provides information on the primary parameters used throughout this work and derives some simple relationships between them for the case of one-dimensional flow.

To distinguish between vapor and liquid the subscripts "L" for liquid and "V" for vapor will be used. Basic equations for two-phase flows are also introduced at the end of the chapter.

2.1 Two-phase flow

A phase, from Classical thermodynamics view, is a macroscopic state of matter which is homogeneous in chemical composition and physical structure; e.g. a gas, a liquid or solid of a pure component. Two-phase flow is the simplest case of multiphase flow in which two phases are present for a pure component.

In internal flow boiling processes, the vapor and liquid are in simultaneous motion inside the pipe. The resulting two-phase flow is generally more complicated physically than single-flow. In addition to the usual inertia, viscous, and pressure forces present in single-phase flow, two-phase flows are also affected by interfacial tension forces, the flow regime, the thermodynamic and transport properties of both the vapor and the liquid, the wetting characteristics of the surface-liquid pair, and other parameters.

Two-phase flow is encountered extensively in the air-conditioning, heating, and refrigeration industries. A combination of liquid and vapor refrigerant exists in coolers (e.g. direct-expansion coolers), plate evaporators and condensers (e.g. brazed plates), and tube-in-tube evaporators and condensers, as well as in air-cooled evaporators and condensers.

2.2 Flow boiling in Tubes

Boiling occurs when a liquid is in contact with a surface maintained at a temperature T_s sufficiently above the saturation temperature T_{sat} of the liquid. Boiling is classified as *pool boiling* or *flow boiling*, depending on the presence of bulk fluid motion. Boiling is called pool boiling in the absence of bulk fluid flow and flow boiling (or forced convection boiling) in the presence of it. Pool boiling involves a pool of seemingly motionless liquid, with vapor bubbles rising to the top as a result of buoyancy effects. In flow boiling, the fluid is forced to move by an external source such as a pump as it undergoes a phase-change process. The boiling in this case exhibits the combined effects of convection and pool boiling.

In *Internal flow boiling*, which is the case of study of the present investigation, both the liquid and the vapor are forced to flow together inside a duct.

2.3 Vapor quality

The vapor quality x is defined as the vapor mass flow rate \dot{m}_V ($\text{kg}\cdot\text{s}^{-1}$) divided by the total mass flow rate $\dot{m}_V + \dot{m}_L$:

$$x = \frac{\dot{m}_V}{\dot{m}_V + \dot{m}_L} \quad (2.1)$$

To determine the quality when phase change does not take place in the tube, one can measure the mass flow rate of each phase, as the quality is constant all along the entire tube. In case there is a phase change in the tube, e.g. if the tube is heated and boiling takes place, then the quality increases along the tube. Since there is often no thermal equilibrium between the phases, it is difficult to calculate the quality merely by knowing the inlet quality and the heat flux from the wall.

[Revellin et al. (2012)] defined the vapor quality variation as the sum of the vapor quality variations due to the heat transfer with the surroundings (dx_{heat}), the temperature variation (dx_T), the friction at the channel walls (dx_{frict}), and the capillary work (dx_{cap}):

$$dx = dx_{\text{heat}} + dx_T + dx_{\text{frict}} + dx_{\text{cap}} \quad (2.2)$$

If the phases are at equilibrium ($P_V = P_L = P_{\text{sat}}$ and $T_V = T_L = T_{\text{sat}}$) and if we neglect the temperature variation, the friction at the channel walls, and the capillary work, Eq. (2.2) reduces to:

$$dx = \frac{\delta \dot{Q}}{\dot{m} \cdot h_{\text{LV}}} \quad (2.3)$$

where \dot{Q} is the heat supplied to the fluid and \dot{m} is the total mass flow rate of the two-phase flow.

Integrating over a length dz and assuming constant properties, we can calculate the variation of the vapor quality along this length. Firstly, we need to distinguish two distinct configurations:

- the fluid enters as subcooled liquid: in that case the vapor quality variation is calculated as:

$$\Delta x = \frac{h_{\text{inlet}} + \frac{\dot{q} \cdot \pi \cdot d_h \cdot \Delta z}{\dot{m}} - h_{\text{sat}}}{h_{\text{LV}}} \quad (2.4)$$

where h_{inlet} is the specific enthalpy of the liquid, h_{sat} is the specific enthalpy of the saturated liquid, h_{LV} is the latent heat of vaporization, and \dot{q} is the heat flux.

- the fluid enters as saturated two-phase flow: in that case the vapor quality variation is calculated as:

$$\Delta x = \frac{\dot{q} \cdot \pi \cdot d_h \cdot \Delta z}{\dot{m} \cdot h_{\text{LV}}} \quad (2.5)$$

2.4 Cross-sectional void fraction

In two-phase flow, cross-sectional void fraction is one of the most important parameters to be determined. It defines the cross-sectional area occupied by each phase (Fig. 2.1). As it determines mean velocities of the liquid and the vapor, it represents a fundamental parameter in the calculation of pressure drop, flow pattern transitions and heat transfer coefficients.

The void fraction is defined as:

$$\epsilon = \frac{A_V}{A_V + A_L} \quad (2.6)$$

where A_V is the sum of areas occupied by the vapor and A_L is the sum of areas occupied by the liquid. The total cross-sectional area of the tube is denoted A .

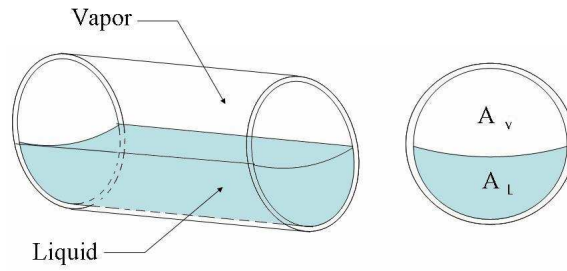


Figure 2.1: Void fraction representation.

2.5 Velocities

There are a number of velocities which can be defined in a two-phase flow. In general, the two phases will not have the same velocity, and there will be a relative velocity between them, as discussed below.

2.5.1 Mass velocity

The **mass velocity**, also known as mass flux, is defined by the mass flow rate divided by the total cross-sectional area:

$$G = \frac{\dot{m}}{A} \quad (2.7)$$

The principal unit of the mass velocity is $[\text{kg} \cdot \text{m}^{-2} \cdot \text{s}^{-1}]$. Considering the continuity law, the mass velocity is also the expression of the mean flow velocity multiplied by the mean density.

2.5.2 Actual velocities

The **actual velocities** (or true mean velocities) of the phases u_V and u_L , are the mean velocities at which the phases actually travel. The cross-sectional velocities are determined by the volumetric flow rates \dot{V}_V and \dot{V}_L ($\text{m}^3 \cdot \text{s}^{-1}$) and divided by the cross-sectional areas which are actually occupied by the phases as:

$$u_V = \frac{\dot{V}_V}{A_V} = \frac{\dot{V}_V}{\epsilon \cdot A} \quad (2.8)$$

$$u_L = \frac{\dot{V}_L}{A_L} = \frac{\dot{V}_L}{(1 - \epsilon) \cdot A} \quad (2.9)$$

From the continuity law, it is possible to define both liquid and vapor actual velocities:

$$u_V = \frac{x}{\epsilon} \cdot \frac{\dot{m}}{\rho_V \cdot A} = \frac{G}{\rho_V} \cdot \frac{x}{\epsilon} \quad (2.10)$$

$$u_L = \frac{(1 - x)}{(1 - \epsilon)} \cdot \frac{\dot{m}}{\rho_L \cdot A} = \frac{G}{\rho_L} \cdot \frac{(1 - x)}{(1 - \epsilon)} \quad (2.11)$$

2.5.3 Superficial velocities

The **superficial velocities** (also called volumetric flux densities) J_V and J_L are the velocities of the phases as if they were each flowing alone in the tube, occupying the total cross-sectional area. They are defined as:

$$J_V = \frac{\dot{V}_V}{A} = \epsilon \cdot u_V \quad (2.12)$$

$$J_L = \frac{\dot{V}_L}{A} = (1 - \epsilon) \cdot u_L \quad (2.13)$$

and the **total superficial velocity** is the sum of the vapor and liquid superficial velocities:

$$J = J_V + J_L \quad (2.14)$$

2.6 Non-dimensional numbers

The main non-dimensional numbers used in the present study are defined below. Different definitions of main non-dimensional numbers, particularly for the Reynolds and Froude number, can be found in the literature. In order to be consistent in this work, the corresponding definitions used in this work are introduced.

2.6.1 Reynolds number

The Reynolds number represents the ratio of the inertial forces to the viscous forces. For the particular case of forced convection inside a tube, the liquid Reynolds number for a single-phase flow in a tube can be expressed in the following form:

$$\text{Re} = \frac{\rho \cdot u \cdot d_h}{\mu} \quad (2.15)$$

where d_h is the hydraulic diameter defined as the ratio of the cross-sectional A to the wetted perimeter p_L and is calculated as follows:

$$d_h = \frac{4 \cdot A}{p_L} \quad (2.16)$$

In the particular case of circular tubes, $d_h = d$.

Considering one-dimensional flow and using the definition of the actual velocity from Eq. (2.9), the liquid Reynolds number in a two-phase flow can be expressed as:

$$\text{Re}_L = \frac{G \cdot d_h}{\mu_L} \cdot \frac{(1 - x)}{(1 - \epsilon)} \quad (2.17)$$

where d_h for the liquid phase is expressed in the following form:

$$d_h = \frac{4 \cdot A_L}{p_L} = \frac{4 \cdot (1 - \epsilon) \cdot A}{p_L} \quad (2.18)$$

The same approach will be used for the vapor Reynolds number which is defined as:

$$\text{Re}_V = \frac{G \cdot d_h}{\mu_V} \cdot \frac{x}{\epsilon} \quad (2.19)$$

where d_h for the vapor phase is expressed as:

$$d_h = \frac{4 \cdot A_V}{p_L} = \frac{4 \cdot A \cdot \epsilon}{p_L} \quad (2.20)$$

Due to the difficulty in calculating p_L , p_V and ϵ , other definitions of the Reynolds number may be found in the literature. As the void fraction is difficult to determine, the following expressions are also used for circular tubes:

$$\text{Re}_L = \frac{G \cdot (1 - x) \cdot d_h}{\mu_L} \quad (2.21)$$

$$\text{Re}_V = \frac{G \cdot x \cdot d_h}{\mu_V} \quad (2.22)$$

Another type of Reynolds number may be calculated when considering each phase flowing alone in the complete cross-section of the tube at its own velocity:

$$\text{Re}_{LO} = \frac{G \cdot d_h}{\mu_L} \quad (2.23)$$

$$\text{Re}_{VO} = \frac{G \cdot d_h}{\mu_V} \quad (2.24)$$

It represents the liquid (or the vapor) phase only flowing alone in the complete cross-section of the tube at the total mass velocity.

2.6.2 Prandtl number

The Prandtl number is the ratio of the molecular diffusivity of momentum (μ/ρ) to the molecular diffusivity of heat ($\lambda/\rho \cdot c_p$). It is a function only of the fluid properties and can thus be expressed for the vapor phase Pr_V and for the liquid phase Pr_L :

$$\text{Pr}_L = \frac{\mu_L \cdot c_{p,L}}{\lambda_L} \quad (2.25)$$

$$\text{Pr}_V = \frac{\mu_V \cdot c_{p,V}}{\lambda_V} \quad (2.26)$$

2.6.3 Bond number

The Bond number is related to the ratio of the gravitational forces to the surface tension forces. The characteristic length that will be used in the present work is the hydraulic diameter. It is defined as:

$$\text{Bd} = \frac{g \cdot (\rho_L - \rho_V) \cdot d_h^2}{\sigma} \quad (2.27)$$

2.6.4 Froude number

The Froude number represents the ratio of the inertia forces to the gravitational forces. The general expression is:

$$\text{Fr} = \frac{G^2}{g \cdot d_h \cdot \rho^2} \quad (2.28)$$

The liquid Froude number for the liquid phase in a tube can be expressed as:

$$\text{Fr}_L = \frac{G^2}{g \cdot d_h \cdot \rho_L^2} \quad (2.29)$$

and for the vapor Froude number as:

$$\text{Fr}_V = \frac{G^2}{g \cdot d_h \cdot \rho_V^2} \quad (2.30)$$

2.6.5 Weber number

The Weber number expresses a ratio of inertia to surface tension forces. The characteristic length is the tube diameter. It is expressed for the liquid phase as:

$$\text{We}_L = \frac{\rho_L \cdot u_L^2 \cdot d_h}{\sigma} \quad (2.31)$$

2.6.6 Nusselt number

The Nusselt number is based on a ratio of convection to conduction heat transfer, with α the convective heat transfer coefficient and λ the thermal conductivity of the fluid. The characteristic length used here is the hydraulic diameter. The Nusselt number is expressed as:

$$\text{Nu} = \frac{\alpha \cdot d_h}{\lambda} \quad (2.32)$$

where d_h is the tube diameter calculated by Eq. (2.18) or Eq. (2.20) according to the phases considered.

2.6.7 Lockart-Martinelli parameter

The Lockart-Martinelli parameter [Lockhart and Martinelli (1949)] is defined as the ratio between the theoretical pressure gradients which would occur if each phase would flow alone in the pipe with the original flow rate of each phase. The Martinelli parameter X_{tt}^2 is calculated as:

$$X_{tt}^2 = \frac{\left(\frac{dP_{\text{frict}}}{dz} \right)_{\text{LO}}}{\left(\frac{dP_{\text{frict}}}{dz} \right)_{\text{VO}}} \quad (2.33)$$

X_{tt}^2 is void fraction independent and is a measure of the degree to which the two-phase mixture is close to being a liquid, i.e. $X_{tt}^2 \gg 1$, or to being a vapor, i.e. $X_{tt}^2 \ll 1$. Modeling the pressure drop of each phase with its superficial velocity and friction factors in the classical form:

$$f_L = C_L \cdot \text{Re}_L^{-n} \quad (2.34)$$

$$f_V = C_V \cdot \text{Re}_V^{-m} \quad (2.35)$$

and assuming the same friction model for both phases (both turbulent or both laminar) which means that $m = n$ and $C_L = C_V$, Eq. (2.33) reduces to:

$$X_{tt} = \left(\frac{1-x}{x} \right)^{-n+2/2} \cdot \left(\frac{\mu_L}{\mu_V} \right)^{n/2} \cdot \left(\frac{\rho_V}{\rho_L} \right)^{1/2} \quad (2.36)$$

[Lockhart and Martinelli (1949)] and then [Taitel and Dukler (1976)] used $n = m = 0.2$ and $C_L = C_V = 0.046$ for a smooth pipe. In this work, the same expression as [Lockhart and Martinelli (1949)] and [Taitel and Dukler (1976)] will be used:

$$X_{tt} = \left(\frac{1-x}{x} \right)^{0.9} \cdot \left(\frac{\rho_V}{\rho_L} \right)^{0.5} \cdot \left(\frac{\mu_L}{\mu_V} \right)^{0.1} \quad (2.37)$$

The subscript tt means that both phases are turbulent. Modes of calculation of the Lockhart-Martinelli parameter for one of both fluids flowing in laminar regime (X_{tl} , X_{lt} , X_{ll}) were presented in the literature but they will not be required in the next chapters.

2.7 Chapter conclusions

Fundamental parameters and basic principles of two-phase flow used throughout this work have been presented. Relevant information on the primary variables and some simple relationships between them are derived for the case of one-dimensional flow.

Chapter 3

State of the art review

This chapter presents a state-of-the-art review of in-tube flow boiling. The first part will highlight the various descriptions of macro-to-micro transition existing in the literature in order to relate the configuration used in the present investigation to these descriptions. Next, a literature review on flow pattern studies in macrochannels, minichannels, and microchannels will be presented to illustrate the geometric characteristics of flow patterns inside tubes. The most quoted flow pattern maps available in the literature and their ranges of applicability will be recalled.

Then a literature review on two-phase pressure drop studies will be presented in order to illustrate the main trends and to identify the mechanisms which govern the two-phase pressure drop in adiabatic configuration. Several two-phase flow prediction methods will be reported and the differences between them will be studied.

Finally, a survey of two-phase flow heat transfer coefficient investigations will be presented. The goal is to illustrate the typical heat transfer trends and the influence of several flow parameters. In addition, several prediction methods will be described.

This state-of-the-art focuses mainly on the influence of saturation temperature. The objective is to identify the limit saturation temperature beyond which no data point is available for two-phase flow of refrigerants.

3.1 Macro-to-microscale transition

The literature dealing with heat transfer and flow characteristics in small channels is replete with terms to describe channel size (e.g. micro-, meso-, compact, ultra-compact, etc.). There is no unique hydraulic diameter separating microchannels from the conventional scale and a precise terminology for describing heat exchanger sizes does not exist. Several macro-to-microscale transition criteria for two-phase flows and heat transfer are available in the literature. They are based on several approaches as described below.

3.1.1 Geometrical approach

[Shah (1986)] defined a compact heat exchanger as an exchanger with a surface area density ratio greater than $700 \text{ m}^2/\text{m}^3$, corresponding to a hydraulic diameter lower than 6 mm, a value that was therefore retained as the transition diameter. [Mehendale et al. (2000)] classified heat exchanger types according to the hydraulic diameter, d_h :

- Conventional heat exchanger: $d_h > 6 \text{ mm}$.
- Compact heat exchanger: $d_h = 1 - 6 \text{ mm}$.
- Meso heat exchanger: $d_h = 100 \text{ }\mu\text{m} - 1 \text{ mm}$.
- Micro heat exchanger: $d_h = 1-100 \text{ }\mu\text{m}$.

[Kandlikar (2002)] recommended the following ranges of hydraulic diameters to distinguish different channels:

- Conventional channels: $d_h > 3 \text{ mm}$.
- Minichannels: $d_h = 200 \text{ }\mu\text{m} - 3 \text{ mm}$.
- Microchannels: $d_h = 10 - 200 \text{ }\mu\text{m}$.

[Kandlikar and Grande (2003)] explained this classification and refined it. The transition between conventional channels and minichannels is associated with the techniques applied to make the channels. Indeed, the channels of 3 mm hydraulic diameter or larger are made with the conventional techniques whereas narrower channels are formed as narrow fin passages, as for plate heat exchangers. The transition between minichannels and microchannels is imposed by the major changes in fabrication technology warranted below $200 \text{ }\mu\text{m}$. The range under $200 \text{ }\mu\text{m}$, termed as microchannel, is influenced by the rarefaction effects for gases and was divided by [Kandlikar and Grande (2003)] as follows:

- Transitional microchannels: $d_h = 10 - 1 \text{ }\mu\text{m}$.
- Transitional nanochannels: $d_h = 1 - 0.1 \text{ }\mu\text{m}$.
- Molecular nanochannels: $0.1 \text{ }\mu\text{m} > d_h$.

These definitions are arbitrary and are only based on geometrical considerations, independently from the type of fluid and its properties. They do not take into account the influence of channel size on the physical mechanisms, e.g. the effect of reduced pressure on bubble sizes and flow transitions. Furthermore these

criteria do not take in consideration the properties of the test fluid. For a more general definition, some approaches were developed to represent fluid flow in mini- and microchannel and to reach a better classification criterion between hydraulic diameters.

3.1.2 Bubble departure diameter approach

Such a macro-to-micro transition criterion can be related to the bubble departure diameter. [Jacobi and Thome (2002)] chose the bubble departure diameter as their transition criterion. They considered a macrochannel as one in which the bubbles are much smaller than the channel diameter, and a microchannel will be loosely identified as one in which the bubbles are constrained by the channel size. In other words, their macro-to-micro transition was assumed to be reached when the diameter of a growing bubble reaches the internal diameter of the tube before detachment. As a first approximation, the bubble departure diameter in nucleate pool boiling without cross-flow can be used.

The [Fritz (1935)] correlation gives the detachment diameter d_{bub} as:

$$d_{\text{bubbles}} = 0.0208 \cdot \beta \cdot \left[\frac{\sigma}{g \cdot (\rho_L - \rho_V)} \right] \quad (3.1)$$

where β is the contact angle in degrees ($^\circ$). [Jensen and Memmel (1986)] reported twelve widely quoted correlations to predict bubble departure diameters in nucleate pool boiling which can be used to determine the macro-to-micro transition.

3.1.3 Confinement number approach

In the microscale, the influence of gravity is surpassed by that of surface tension. Hence, no stratified flow can exist if the tube diameter is sufficiently small. [Kew and Cornwell (1997)] proposed the Confinement number Co as a criterion, defined as:

$$Co = \frac{1}{d_h} \cdot \sqrt{\frac{\sigma}{g \cdot (\rho_L - \rho_V)}} \quad (3.2)$$

Co represents the ratio between surface tension forces and gravity forces. The authors set the threshold at $Co = 0.5$, where $Co > 0.5$ is for microscale and $Co < 0.5$ is for macroscale. The threshold becomes smaller when the saturation pressure increases. The transition diameter can be rewritten as:

$$d_{\text{th}} = 2 \cdot l_{\text{cap}} \quad (3.3)$$

where the capillary length is given as:

$$l_{\text{cap}} = \sqrt{\frac{\sigma}{g \cdot (\rho_L - \rho_V)}} \quad (3.4)$$

Based on their flow visualizations and film thickness uniformity/nonuniformity measurements for R-134a, R-236fa and R-245fa during flow boiling in small channels of 1.03, 2.20 and 3.04 mm inner diameter, [Ong and Thome(2011a)] found that the gravity forces were more dominant when $Co < 0.34$ but weak when $Co > 1.0$.

The threshold diameter (d_{th}), that is the threshold below which there are deviations from macroscale flows, and the critical diameter (d_{crit}) representing the transition criterion to microscale can be written as follows:

$$d_{th} = 2.94 \cdot l_{cap} \quad (3.5)$$

$$d_{crit} = 1 \cdot l_{cap} \quad (3.6)$$

[Cheng and Wu (2006b)] used the Bond number to define transition criteria. The Bond number is a common macro-to-microscale transition criterion for two-phase flow and heat transfer derived from the confinement number approach. The Bond number, Bd , scales the ratio between gravity and surface tension forces for a tube of diameter d_h and among various definitions, is often written as:

$$Bd = \frac{g \cdot (\rho_L - \rho_V) \cdot d_h^2}{\sigma} \quad (3.7)$$

They classified phase change heat transfer in channels according to the Bond number as follows:

- microscale if $Bd < 0.05$, the effect of gravity can be neglected
- mesoscale if $0.05 < Bd < 3$, surface tension effect becomes dominant and gravitational effect is small
- macroscale if $Bd > 3$, the surface tension is small in comparison with gravitational force

The diameters of transition proposed by [Cheng and Wu (2006b)] can be expressed as following:

$$d_{th} = 1.73 \cdot l_{cap} \quad (3.8)$$

$$d_{crit} = 0.224 \cdot l_{cap} \quad (3.9)$$

From the analysis of the microscale flow pattern data of [Triplett et al. (1999)] for air-water in a 1.1 mm channel, [Ullmann and Brauner (2007)] suggested that the Eötvös number played a major role in flow pattern transitions and the disappearance of stratified flows. Hence, this number appears to be a good candidate to be used as a criterion for defining the two-phase macro-to-microchannel transition. The Eötvös number is expressed as:

$$Eö = \frac{g \cdot (\rho_L - \rho_V) \cdot l_c^2}{8 \cdot \sigma} \quad (3.10)$$

where l_c is the characteristic length. The practical difference between Bd and $Eö$ is that in the definition of Bd the hydraulic diameter is used. In the Eötvös number, l_c is often replacing by d_h . They recommended the macro-to-microchannel threshold to occur at an Eötvös number of about 0.02. The transition diameter can be written as:

$$d_{th} = 0.4 \cdot l_{cap} \quad (3.11)$$

Their observations, based on the flow regime with respect to the hydraulic diameter d_h resulted in the following classifications:

- $d_h < d_{th}$: Gravity forces are insignificant compared to surface tension factors and no stratified flow exists as in microscale.
- $d_h > d_{th}$: Gravity forces are dominant and the flow regimes are similar to macroscale flow.

[Harirchian and Garimella (2010)] developed a new transition criterion based on the fact that bubble confinement depends on channel size and on the mass flux since the bubble diameters varies with flow rate. Using FC-77 flow visualizations, they divided their experimental values into two groups: confined and unconfined flow. They correlated their transition between confined and unconfined flow:

$$\text{Bd}^{0.5} \cdot \text{Re}_{\text{LO}} = \frac{1}{\mu_L} \cdot \left(\frac{g \cdot (\rho_L - \rho_V)}{\sigma} \right)^{0.5} \cdot G \cdot d_h^2 = 160 \quad (3.12)$$

[Harirchian and Garimella (2010)] defined the convective confinement number expressed as $\text{Bd}^{0.5} \cdot \text{Re}_{\text{LO}}$. Their analysis resulted in the following classification:

- for $\text{Bd}^{0.5} \cdot \text{Re}_{\text{LO}} < 160$, confined flow corresponding to microchannel
- for $\text{Bd}^{0.5} \cdot \text{Re}_{\text{LO}} > 160$, unconfined flow corresponding to macrochannel

This criterion seems able to predict the confined and unconfined nature of the flow for experimental observations in literature having water, dielectric liquids and refrigerants as working fluids. The threshold diameter can be rewritten as follows (see [Baldassari and Marengo (2013)]):

$$d_{th} = \frac{160}{\text{Re}_{\text{LO}}} \cdot l_{cap} \quad (3.13)$$

3.1.4 Young-Laplace equation approach

[Li and Wang (2003)] conducted an analysis to predict the influence of tube size on two-phase flow regimes for flow condensing in mini/microchannels. They studied the gravitational effect on the transition from symmetric flow (where gravity can be ignored) to asymmetric flow (where gravity cannot be ignored). Based on the Young-Laplace equation, they proposed the following critical and threshold values of the tube diameter (d_{crit} and d_{th}) as a function of the capillary length (l_{cap}) as:

$$d_{crit} = 0.224 \cdot l_{cap} \quad (3.14)$$

$$d_{th} = 1.75 \cdot l_{cap} \quad (3.15)$$

Their critical diameter is similar to the bubble departure diameter in the Fritz equation above if the contact angle is set to 10° . Their threshold diameter differs from that of [Kew and Cornwell (1997)] only by the value of the multiplier (1.75 rather than 2).

Table 3.1: Summary of the threshold diameter expressions and the values of Eötvos number corresponding.

Authors	Diameters	Eötvos number
[Kew and Cornwell (1997)]	$d_{th} = 1.73 \cdot l_{cap}$	Eö = 4
[Ong and Thome(2011a)]	$d_{th} = 2.94 \cdot l_{cap}$ $d_{crit} = 1 \cdot l_{cap}$	Eö = 8.65 Eö = 1
[Cheng and Wu (2006b)]	$d_{th} = 1.73 \cdot l_{cap}$ $d_{crit} = 0.224 \cdot l_{cap}$	Eö = 3 Eö = 0.05
[Ullmann and Brauner (2007)]	$d_{th} = 0.4 \cdot l_{cap}$	Eö = 0.02
[Harirchian and Garimella (2010)]	$d_{th} = (160 / Re_{LO}) \cdot l_{cap}$	Eö = $(160 / Re_{LO})^2$
[Li and Wang (2003)]	$d_{th} = 1.75 \cdot l_{cap}$ $d_{crit} = 0.224 \cdot l_{cap}$	Eö = 3.06 Eö = 0.05

Their observations, based on the flow regime with respect to the hydraulic diameter d_h resulted in the following classifications:

- $d_h < d_{crit}$: Gravity forces are insignificant compared to surface tension factors as in microscale. Annular, elongated bubble and bubble flow regimes are symmetrical (equivalent to $Co > 4.46$)
- $d_{crit} < d_h < d_{th}$: Gravity and surface tension forces are equally dominant. A slight stratification of the flow distribution is observed (equivalent $0.57 < Co < 4.46$)
- $d_{th} < d_h$: Gravity forces are dominant and the flow regimes are similar to macroscale flow (equivalent to $Co < 0.57$)

Hence, this is apparently the first proposition for macro-to-miniscale and mini-to-microscale threshold criteria which can be applicable to adiabatic flows and flow boiling.

3.1.5 Comparison of the macro-to-micro transition thresholds

Table 3.1 summarizes the expressions of the transition threshold diameters previously quoted as well as the transition values of Eötvos number. Figure 3.1 displays a comparison of the threshold diameter calculated from several macro-to-microscale criteria evaluated for R-245fa as a function of saturation temperature. In conclusion, there is still a significant difference of opinions with respect to the two-phase macro-to-microscale transition. As an example, a channel of diameter $d_h = 3.0$ mm (diameter that will be used further on) belongs either to macrochannel at high saturation temperature or to macrochannel or minichannel (according to the criterion of [Ong and Thome(2011a)]) at low saturation temperature.

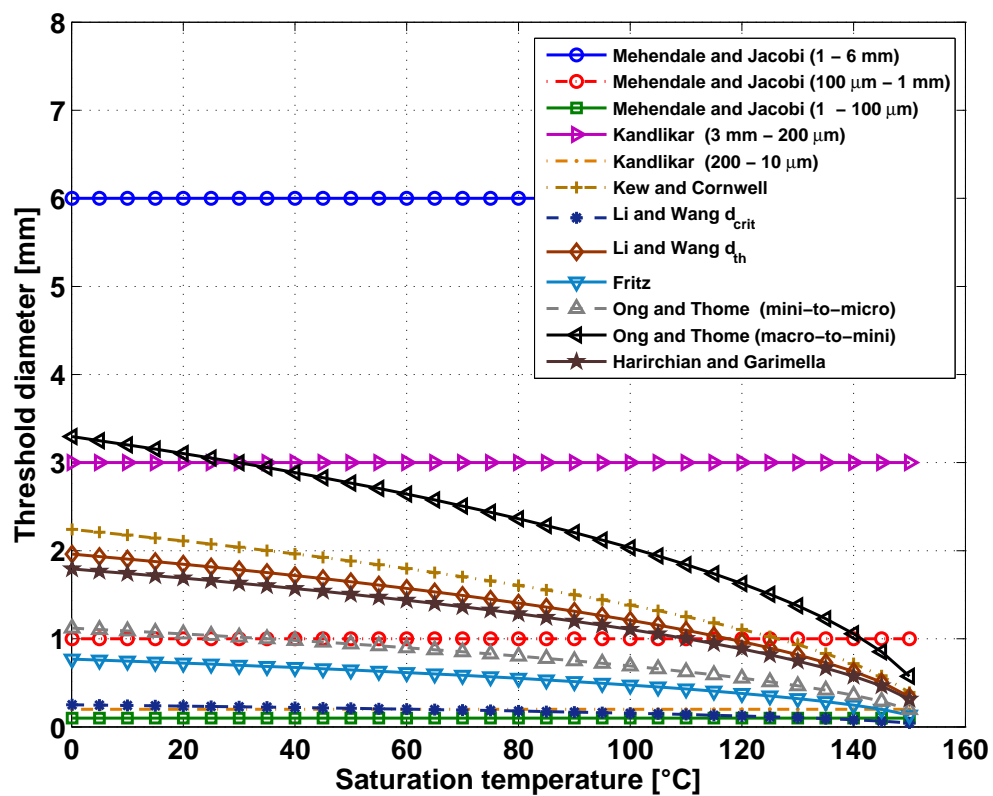


Figure 3.1: Comparison of selected macro-to-microscale transition criteria for R-245fa as a function of saturation temperature (The threshold diameter of [Harirchian and Garimella (2010)] was calculated from Eq. (3.13) with $Re_{LO} = 100$).

3.2 Flow patterns

One of the most important features of two-phase flows is the variety of flow patterns that can be encountered. The study of two-phase flow patterns describes how the liquid and vapor phases are distributed. Heat transfer coefficients and pressure drops are closely related to the two-phase flow structure of the fluid, and by consequence, two-phase flow pattern prediction is always required for a correct description of two-phase thermohydraulics. In this section, some techniques developed to characterize the flow patterns will be presented and described. Next, the flow patterns encountered in macrochannels and in mini-/microchannels will be described and, in the last part, a survey of two-phase flow patterns maps will be presented. This review will draw attention to the following main points:

- the existing techniques to characterize the two-phase flow patterns, their advantages and their drawbacks
- the most commonly flow structures observed in macro-, mini-, and microchannels
- the influence of saturation temperature on the flow patterns
- the influence of saturation temperature, heat flux, and mass velocity on the flow regime transitions

3.2.1 Two-phase flow pattern characterization techniques

The conventional experimental techniques to characterize the two-phase flow patterns can be classified into two types: contact measurement and non-contact measurement. For contact measurement, [Serizawa et al. (1975)] pioneered detailed experiments in bubbly flow using hot-film anemometers and studied liquid turbulent structure. An improved system of conductance probes was used by [Barnea et al. (1980)] to identify the flow patterns in two-phase horizontal, near horizontal and upward flows. The limit of these techniques is the requirement of the greatest accuracy, because the sensor is set up in the flow region.

Furthermore, in order to increase the objectivity, indirect methods were developed dealing with the statistical analysis of fluctuations in measured pressure or void fraction. [Rouhani and Sohal (1983)] confirmed the correlation between flow regime and the fluctuation characteristics of the two-phase flow properties using mathematical and statistical models to analyze these fluctuations. [Matsui (1984)], [Matsui (1986)] and [Olivier et al. (2007)] investigated the differential pressure fluctuations to characterize the flow regime transitions. [Canière et al. (2010)] developed a capacitive void fraction sensor to study the flow pattern mapping of horizontal refrigerant two-phase flow in macroscale tubes. Figure 3.2 represents three typical sensor signals for a slug flow, an intermittent flow, and an annular flow.

For the non-contact measurement, optical methods, X-rays and ultrasounds were used. On one hand, some techniques dealing with opaque channel were developed. [Jones and Zuber (1975)] used a X-rays void fraction measurement system to obtain statistical measurements in normally fluctuating air-water. [Xu and Xu (1998)] developed an ultrasonic facility for tomographic imaging of gas/liquid two-phase flows. On the other hand, for transparent channels, some techniques

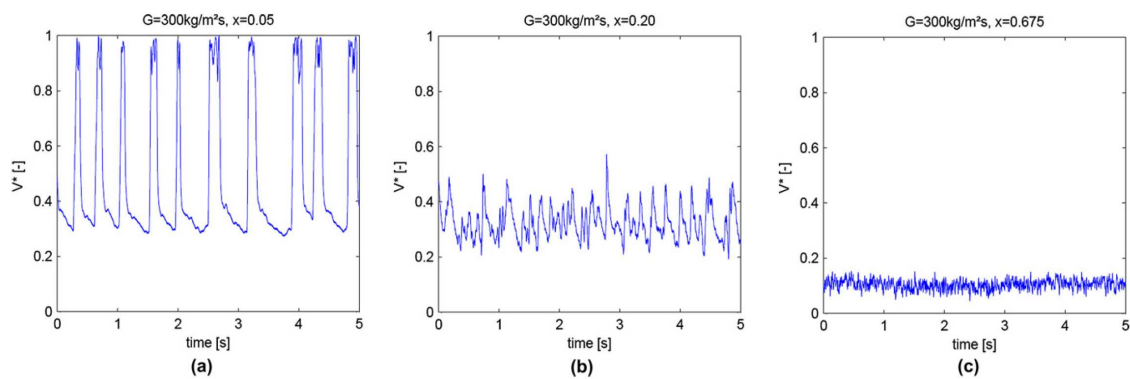


Figure 3.2: Capacitive void fraction signals of R-410A at $T_{\text{sat}} = 15^{\circ}\text{C}$ obtained by [Canière et al. (2010)]: (a) slug flow, (b) intermittent flow, and (c) annular flow.

were elaborated. The earlier experimental results were mostly based on a qualitative approach using direct observations from high speed photography or video technique: [Hewitt and Roberts (1969)] with vertical flows, [Baker (1954)], [Taitel and Dukler (1976)] and [Suo and Griffith (1963)] for horizontal flows. More recently, [Serizawa et al. (2002)] visualized gas-liquid two-phase flow patterns with a microscope for air-water flow in circular tubes of 20, 25 and 100 μm diameters and for steam-water flow in a 50 μm .

The best approach to identify the flow patterns is to quantitatively define criteria typical of each two-phase flow pattern. For instance, [Wojtan et al. (2005a)] used measurements and trends observed in the void fraction to determine the flow patterns. They applied the technique developed by [Ursenbacher et al. (2004)]. Later, [Revellin et al. (2006)] chose the bubbles frequency, the coalescence rates, and the mean bubble length as criteria to identify the flow patterns. For this, they developed an optical measurement method using two laser diodes and photodiodes, as shown in Fig. 3.3. More recently, [Sempértegui-Tapia et al. (2013)] used a similar technique.

Some of these techniques were optimized to obtain the bubble characteristics: the bubble velocity, the bubble frequency, the percentage of small bubbles and the mean bubble length. [Agostini et al. (2008)] investigated the velocity of elongated vapor bubbles exiting two horizontal micro-evaporator channels with refrigerant R-134a. Experimental video sequence with tube diameters of 509 and 790 μm were obtained with a high-speed high-definition digital video camera. [Revellin et al. (2008)] used the optical measurement method for two-phase flow pattern characterization developed by [Revellin et al. (2006)] to determine the frequency of bubbles generated in a microevaporator, the coalescence rates of these bubbles and the distribution of their length as well as their mean velocity. [Arcanjo et al. (2010)] investigated the bubbles velocity and frequency with R-134a and R-245fa evaporating in a stainless steel tube with diameter of 2.32 mm. [Revellin et al. (2008)] and [Arcanjo et al. (2010)] concluded that the bubble velocity increases with increasing mass velocity and vapor quality. Figure 3.4 presents the results of [Revellin et al. (2008)] on the influence of mass velocity and vapor quality on bubble velocity. They also noted that the frequency of bubbles passes through a peak with increasing the vapor quality from 0, as shown in Fig. 3.5. Moreover, they observed that the frequency peak value increased with increasing the mass velocity.

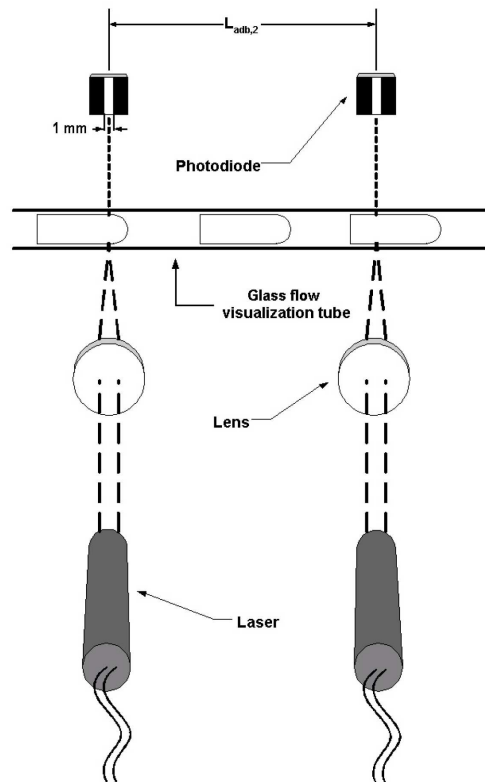


Figure 3.3: Schematic of the laser instrumentation developed by [Revellin et al. (2006)].

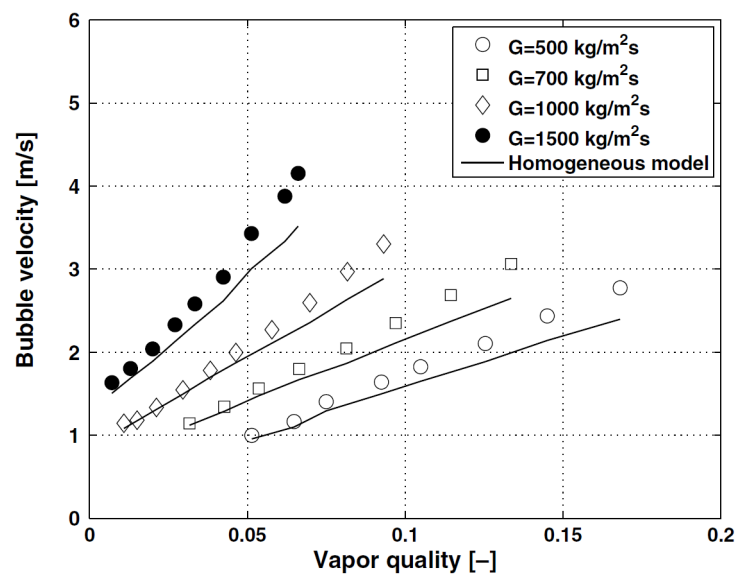


Figure 3.4: Elongated bubble velocity as a function of vapor quality for $T_{\text{sat}} = 35^\circ\text{C}$ with R-134a flowing in a 0.5 mm microchannel (from [Revellin et al. (2008)]).

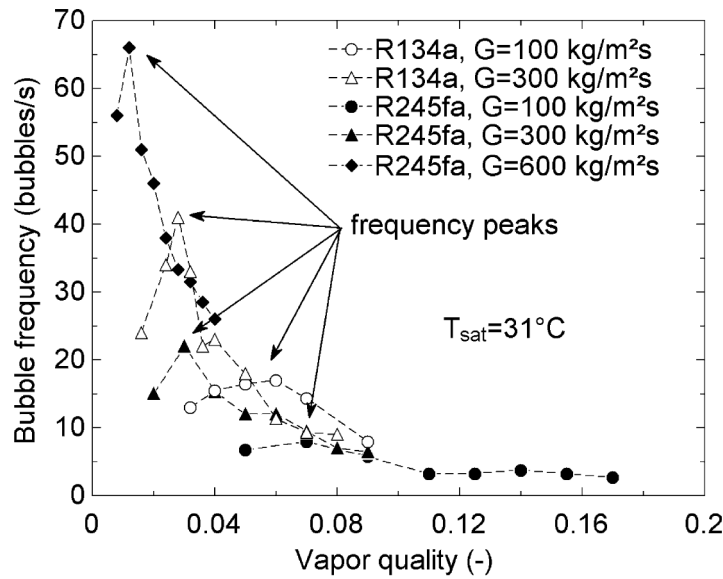


Figure 3.5: Frequency of bubbles as a function of vapor quality for various mass velocities and $T_{sat}=31^{\circ}\text{C}$ with R-134a and R-245fa in a 2.32 mm inner diameter tube (from [Arcanjo et al. (2010)]).

Only a few articles dealing with flow pattern characterization by image processing are available in the literature. [Zhang et al. (2010)] proposed a method for pattern recognition of gas-liquid two-phase flow regimes based on improved local binary pattern (LBP) operator (operator used to measure the local contrast in texture analysis). [Ong and Thome(2011a)] developed an image processing method to determine the liquid film thicknesses at the top and bottom of a tube. [Hanafizadeh et al. (2011)] analyzed vertical air-water flows by means of an image processing technique based on the binarization of pictures derived from films recorded with a high-speed video camera. Their final processed images of different flow regimes in air-water, two-phase flow in minichannel are represented on Fig. 3.6. This method is unable to determine bubble frequency, percentage of small bubbles and velocity.

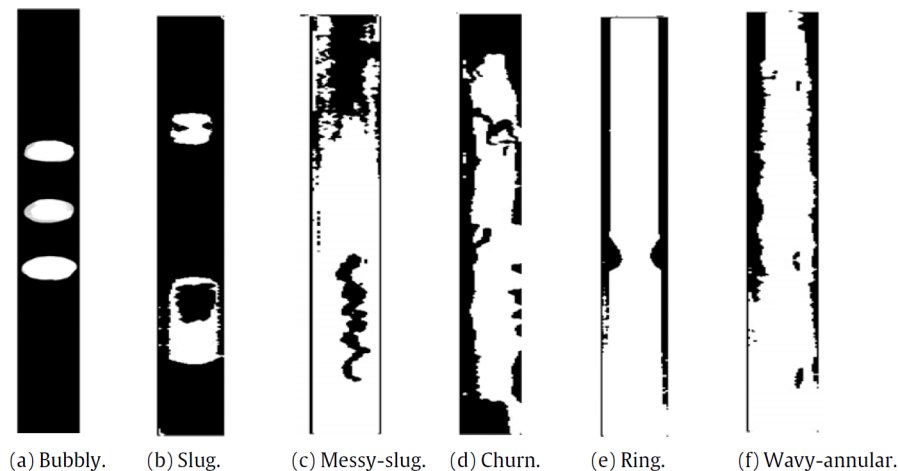


Figure 3.6: Final processed images of different two-phase flow regimes in a 2.0 mm inner diameter channel for air-water provided by [Hanafizadeh et al. (2011)].

3.2.2 Experimental studies on flow regimes

The respective distribution of liquid and vapor phases in a two-phase flow is an important aspect of its description. Their distributions exhibit commonly observed flow structures, which are defined as two-phase flow patterns that have particular identifying characteristics. Here below, various studies on flow pattern characterization dealing with macro-, mini-, and microchannel flows are reported. At the end of this section, a few publications dealing with the influence of saturation temperature are also reported.

The first study on flow patterns in minichannels was seemingly performed by [Suo and Griffith (1963)], who identified different flow patterns using channels of 1.03 mm and 1.60 mm inner diameter: bubbly/slug flow, slug flow, and annular flow. They used heptane or water as liquid phase, while using helium or nitrogen as gas phase. A relatively comprehensive summary and representation of gas-liquid flow patterns was provided by [Wambsganss et al. (1991)].

[Kew and Cornwell (1997)], [Cornwell and Kew (1993)] and [Cornwell and Kew (1995)] conducted experiments with R-113 in a 1.2 mm \times 0.9 mm rectangular channel. They identified three different flow regimes in their study: isolated bubbles flow, confined bubbles flow and slug/annular flow. These three flow regimes are schematically represented on Fig. 3.7. Many authors also observed these three basic flow patterns: [Damianidis and Westwater (1987)], [Mertz et al. (1996)], [Kasza et al. (1997)] and [Sheng and Palm (2000)]. [Mertz et al. (1996)] investigated evaporation in single- and multichannel test sections with water and R-141b in small vertical channels that were from 1 to 3 mm wide with aspect ratios up to 3. [Damianidis and Westwater (1987)] studied air-water two-phase flow in a 1.0 mm inner tube diameter, and [Sheng and Palm (2000)] investigated flow boiling of water in vertical glass tubes with diameter ranging from 1.0 to 4.0 mm.

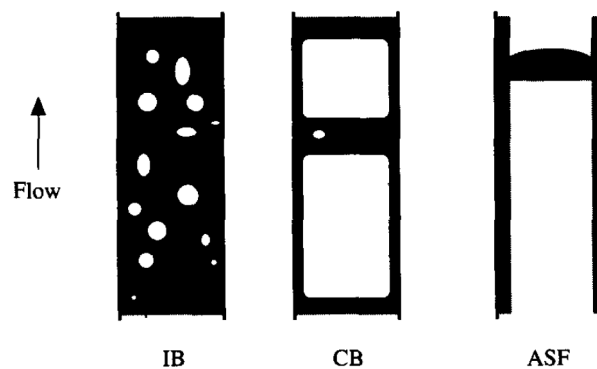


Figure 3.7: Schematic proposed by [Kew and Cornwell (1997)] showing flow regimes results with R-113 in a 1.2 mm \times 0.9 mm rectangular channel: IB - isolated bubble, CB - coalescing bubble, and ASF - annular slug flow.

Additional flow patterns were named by other authors to describe microchannel two-phase flows. [Kuwahara et al. (2000)] performed flow boiling experiments with R-134a in a 1.2 mm horizontal tube with mass velocities ranging from 80 to 1260 kg/m²·s. The flow patterns observed through the glass tube section in the ranges of vapor quality of $x = 0.008$ -0.975 at a constant pressure of 0.92 bar were: bubble flow, plug flow, slug flow, wavy-annular flow and annular flow. [Yang and Shieh (2001)] performed experimental investigation of two-phase flow patterns for

refrigerant R-134a and air-water in horizontal tubes with inner diameter from 1.0 to 3.0 mm. They reported six distinct flow regimes, as shown on Fig. 3.8: bubbly flow, plug flow, wavy flow, slug flow, annular flow and dispersed flow.

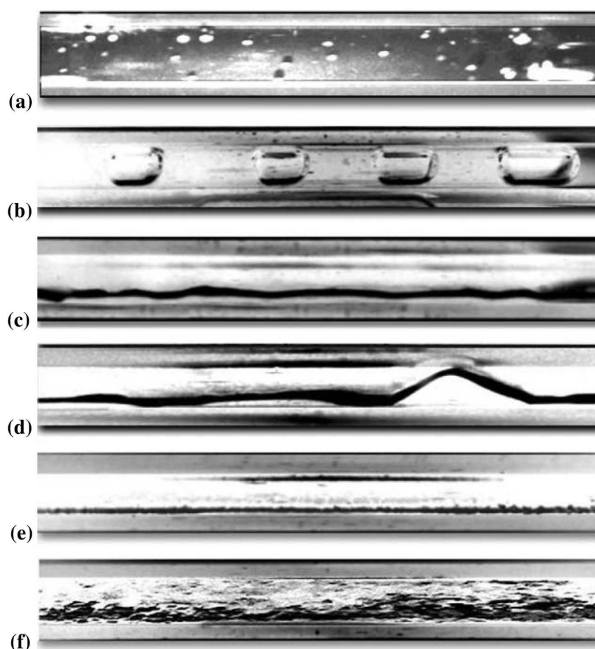


Figure 3.8: Photographs of air-water flow patterns in a 3.00 inner diameter tube visualized by [Yang and Shieh (2001)]: (a) bubbly flow, (b) plug flow, (c) wavy flow, (d) slug flow, (e) annular flow, and (f) dispersed flow.

More recently, [Revellin et al. (2006)] investigated flow boiling of R-134a at 30°C in a 0.5 mm glass channel and reported, using a new optical measurement method, four flow patterns: bubbly flow, slug flow, semi-annular flow and annular flow. They observed collision of bubbles which is a one-dimensional phenomenon caused by the small dimension of the channel. The bubble coalescence rates were observed to be an important phenomenon controlling the flow pattern transition in microchannels. From their observations, they also defined two other regimes: isolated bubbles and coalescing bubbles. [Revellin and Thome (2007a)] performed new experiments in 0.5 mm and 0.8 mm diameter glass channels using R-134a and R-245fa at 26, 30 and 35°C saturation temperatures. They observed the same flow patterns as in the previous study ([Revellin et al. (2006)]). [Tibiricá and Ribatski (2010)] characterized flow patterns for R-134a and R-245fa as working fluids in a 2.3 mm inner diameter tube at three different saturation temperatures: 22, 31 and 41°C. [Ong and Thome(2011a)] presented experimental two-phase flow pattern observations for channel with inner diameters of 1.03, 2.20 and 3.04 mm with R-134a, R-236fa and R-245fa. They observed flow patterns similar to those reported by [Revellin et al. (2006)] and they grouped together, for a seek of simplicity, “wavy-annular” and “smooth-annular” into “annular flow”. [Arcanjo et al. (2010)] performed two-phase flow pattern visualizations and measurements of elongated bubble velocity, frequency, and length. Their tests were run for R-134a and R-245fa evaporating in a 2.32 mm inner diameter tube with mass velocities ranging from 50 to 600 kg/m²·s and saturation temperatures of 22, 31, and 41°C.

They identified the following flow patterns: bubbly, elongated bubbles, churn, and annular flows. Many other research works dealing with two-phase flow visualizations are available in the literature: [Saisorn and Wongwises(2010a)], [Saisorn et al. (2010b)], [Saisorn et al. (2011)], [Galvis and Culham (2012)], [Harirchian and Garimella (2012)], [Celata et al. (2012)], [Zeguai et al. (2013)], and [Sempértegui-Tapia et al. (2013)]. In conclusion, there is no consensus on two-phase flow regime definitions and a multitude of names are available in the literature. In order to clarify this situation, [Thome et al. (2013)] defined five primary flow regimes (bubbly flow, slug flow, annular flow, stratified flow and mist flow) and assumed other flow patterns as subregimes or transition modes between these major flow regimes.

In order to investigate the effect of the channel diameter on the flow patterns, [Chung and Kawaji (2004)] performed experiments of two-phase flow with nitrogen gas and water in several circular channels of 530, 250, 100 and 50 μm diameter. For channels of 250 and 530 μm , the flow patterns observed were consistent with those appearing in minichannels of 1.0 mm: bubbly flow, slug flow, churn flow, slug-annular flow and annular flow. For channels of 50 and 100 μm , essentially only slug was identified under the flow conditions investigated. [Revellin et al. (2006)] provided a comparison of elongated bubbles in 2.0, 0.8 and 0.5 mm channels to demonstrate that gravity has essentially no buoyancy effect for the 0.5 mm channel as shown in Fig. 3.9. In the 2.0 mm channel, the difference in film thickness at the top compared to that at the bottom is notable. Similarly, the film thickness in the 0.790 mm channel is not uniform above and below the bubble. In contrast, in the 0.509 mm channel, the film is quite uniform.

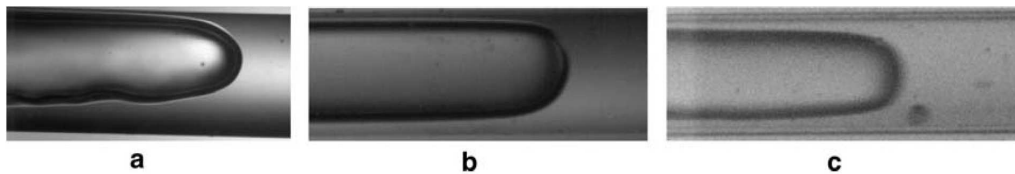


Figure 3.9: Elongated bubble for three different channel diameters: (a) 2.0 mm channel, (b) 0.8 mm channel, and (c) 0.5 mm channel. From [Revellin et al. (2006)].

Concerning stratification effect, [Triplett et al. (1999)] highlighted the role of surface tension which becomes more important in smaller diameter channels. In their investigations, stratified flow never occurred for gas-liquid flows in circular microchannels with 1.10 and 1.45 mm inner diameters, and with semi-triangular (triangular with one corner smoothed) cross-sections with hydraulic diameters of 1.09 and 1.49 mm. Surface tension was dominant and, slug and churn flow patterns occurred over extensive ranges of parameters. On the other hand, [Kasza et al. (1997)] presented a detailed study on flow visualization and reported stratified flow at very low flow rates, in their case 21 $\text{kg}/\text{m}^2\cdot\text{s}$ with water in a large rectangular flow channel of 2.5×6.0 mm.

Regarding dryout and mist flow regimes, some authors have used heat transfer coefficient measurements to identify these flow patterns. As a matter of fact, the process of evaporation in horizontal tubes during the transition from annular to mist flow is accompanied by the inception of the dryout at the top of the tube, while the onset of the dryout is accompanied by a drastic drop of the heat transfer coefficient relative to that prior to dryout. These phenomena were observed

by [Mori et al. (2000)] (see Fig. 3.10), [Mastrullo et al. (2012)] and [Wojtan et al. (2005a)]. These latters provided a schematic of the flow patterns during dryout shown on Fig. 3.11. As you can see on the figure, dryout occurs first at the top of the tube where the liquid film is thinner, denoted as vapor quality x_{di} (section A-A), and then progresses downward around the perimeter (section B-B) until reaching the bottom (section C-C) at the vapor quality x_{de} . [Wojtan et al. (2005a)] called the regime between x_{di} and x_{de} "dryout".

[Mori et al. (2000)] and [Wojtan et al. (2005a)] proposed prediction methods for both, vapor quality of dryout inception, x_{di} , and vapor quality of dryout completion, x_{de} . [Katto (1984)], and [Sun and Groll (2002)] also provided correlations to predict the vapor quality of dryout inception. For carbon dioxide, [Cheng et al. (2006a)] and [Cheng et al. (2008)] used the same method to identify dryout and mist flow regimes. [Kim and Mudawar (2013a)] proposed a correlation for dryout incipience quality from their database consisting of 997 dryout data points for mini/microchannels from 26 sources. They highlighted the effects of working fluid, heat flux, channel diameter, and saturation pressure on dryout incipience quality using their correlation.

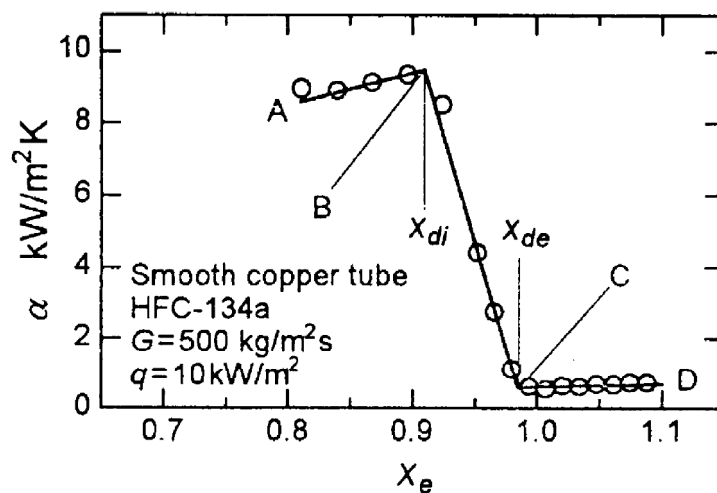


Figure 3.10: Representation of heat transfer coefficient in the neighborhood of dry-out from [Mori et al. (2000)].

A few publications available in the literature deal with high saturation temperatures or high reduced pressures. [Mastrullo et al. (2012)] performed flow visualizations in a horizontal smooth tube of 6.00 mm for carbon dioxide and R-410A, varying the reduced pressure from 0.57 to 0.64 (saturation temperature in the range of 7-12°C) and 0.19 to 0.52 (saturation temperature in the range of 5-42°C), respectively. They observed four flow patterns: slug flow, intermittent flow, annular flow and dryout flow.

3.2.3 Flow pattern maps

Flow pattern maps are used to predict the local two-phase flow configuration and also to identify the transition from one flow pattern to another. The flow pattern maps available in the literature were first developed for petrochemical industry, subsequently, the adiabatic flow pattern maps were developed as general flow pattern maps. In recent years, a number of flow pattern maps were developed for

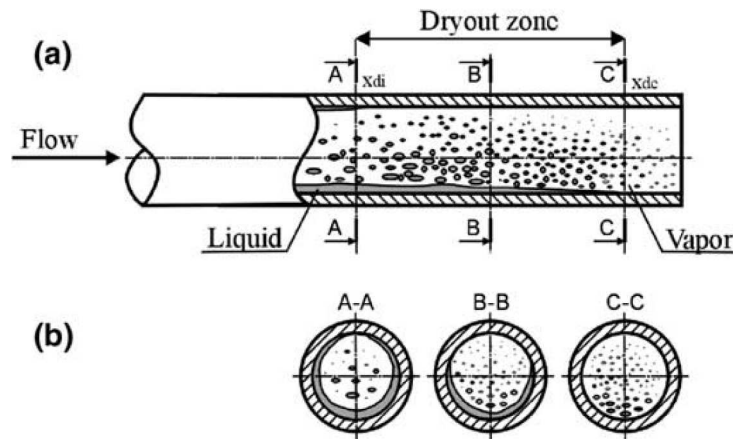


Figure 3.11: Schematic proposed by [Wojtan et al. (2005a)] of (a) dryout zone during evaporation in a horizontal tube and (b) cross sections: A-A onset of dryout in annular flow, B-B dryout, and C-C end of dryout and beginning of mist flow.

specific conditions (new fluids, small diameter tubes, evaporation or condensation, and compact heat exchanger geometries). Here below, the most common flow pattern maps for macroscale and for mini- and microscale are presented.

3.2.3.1 Macroscale flow pattern maps

One of the first flow pattern map for horizontal tubes was proposed by [Baker (1954)] and developed for flow of oil and gas in large diameter pipes. This adiabatic flow pattern map is based upon the superficial gas and liquid velocities relative to water-air mixtures. [Hewitt and Roberts (1969)] proposed a widely quoted adiabatic flow pattern map for vertical upflow. [Sato et al. (1971)] and [Sato et al. (1972)] proposed a diabatic flow pattern map based on observations for evaporating flow boiling experiments in horizontal channels. They based their map upon flow rate and vapor quality.

For large diameter, [Mandhane et al. (1974)] provided a generalized flow pattern map for air-water system (Fig. 3.12) which was quite representative of other flow conditions as well. [Ishii (1975)] developed a map with three flow patterns: separated, disperse and mixed. [Taitel and Dukler (1976)] proposed one of the most widely quoted flow pattern map for the prediction of the transition between two-phase flow regimes for adiabatic flow in horizontal tubes. This map is based on their analytical analysis of the flow transition mechanisms together with empirical selection of several parameters.

[Kattan et al. (1998a)] developed a flow pattern map for smaller diameter tubes typical of heat exchangers. This map is a modification of the [Steiner (1993)] map, which itself is a modification of [Taitel and Dukler (1976)] map and it includes a method for predicting the onset of the dryout at the top of the tube in evaporating annular flows. The axes of this map are the vapor quality, x , and the mass velocity, G , which are typical parameters related to flow boiling. The intermittent-to-annular transition occurs at a fixed value of vapor quality of 0.34.

Thome and co-workers added some improvements to this initial flow pattern map by increasing their experimental database. [El Hajal et al. (2003)] flow pattern map incorporated a newly defined method to calculate the vapor void fraction us-

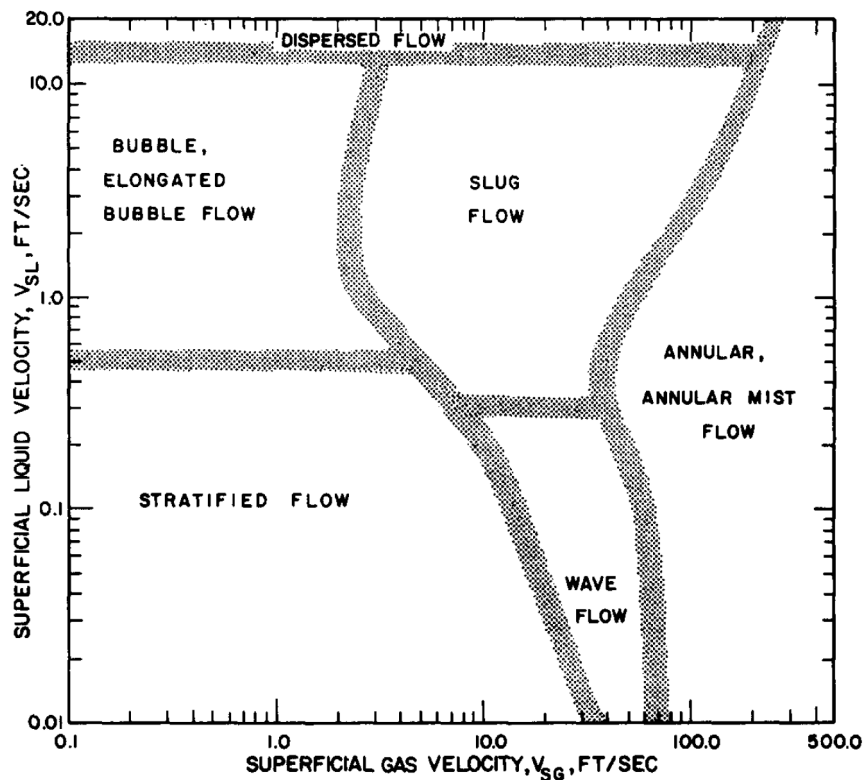


Figure 3.12: Flow pattern map of [Mandhane et al. (1974)] for air-water.

ing Rouhani-Axelsson model. For an inner diameter of 14.00 mm, [Zurcher et al. (2002)] proposed a modification of [Kattan et al. (1998a)] flow pattern map for two substitute refrigerants (R-134a and R-407C) and for one natural refrigerant (R-717, ammonia) in which the transition line between annular and intermittent flow to stratified flow was modified.

[Wojtan et al. (2005a)] modified the [Kattan et al. (1998a)] flow pattern map to develop a significantly new version of the map. Based on their void fraction measurements, the stratified-wavy region was divided into three subzones: slug, slug/stratified-wavy and stratified-wavy. This map incorporates annular-to-dryout and dryout-to-mist flow transition curves. It also takes into account the influence of the heat flux on the annular-to-dryout and dryout-to-mist flow transition curves using a non-dimensional ratio (\dot{q}/\dot{q}_{crit}). This influence was the reason to modify the approach of [Mori et al. (2000)]. This flow pattern map is represented on Fig. 3.13.

[Barbieri et al. (2008)] modified the [Kattan et al. (1998a)] flow pattern map with a new intermittent-to-annular transition line. They investigated the flow boiling of R-134a in smooth brass tubes of inner diameters varying from 6.2 mm to 12.6 mm at a saturation temperature of 5°C. They used two non-dimensional groups: the liquid Froude number, Fr_L , and the Lockhart-Martinelli parameter, X . [Cheng et al. (2008)] flow pattern map based on the flow boiling heat transfer mechanisms for horizontal tubes was developed specifically for carbon dioxide. This flow pattern map is applicable to a wide range of conditions: hydraulic diameters from 0.8 to 10 mm, mass velocities from 170 to 570 kg/m²·s, heat fluxes from 5 to 32 kW/m² and saturation temperatures from -28 to 25 °C (reduced pressures from 0.21 to 0.87). [Canière et al. (2010)] proposed flow pattern maps for R-410A and R-134a in a smooth tube with an inner diameter of 8 mm at a saturation temperature

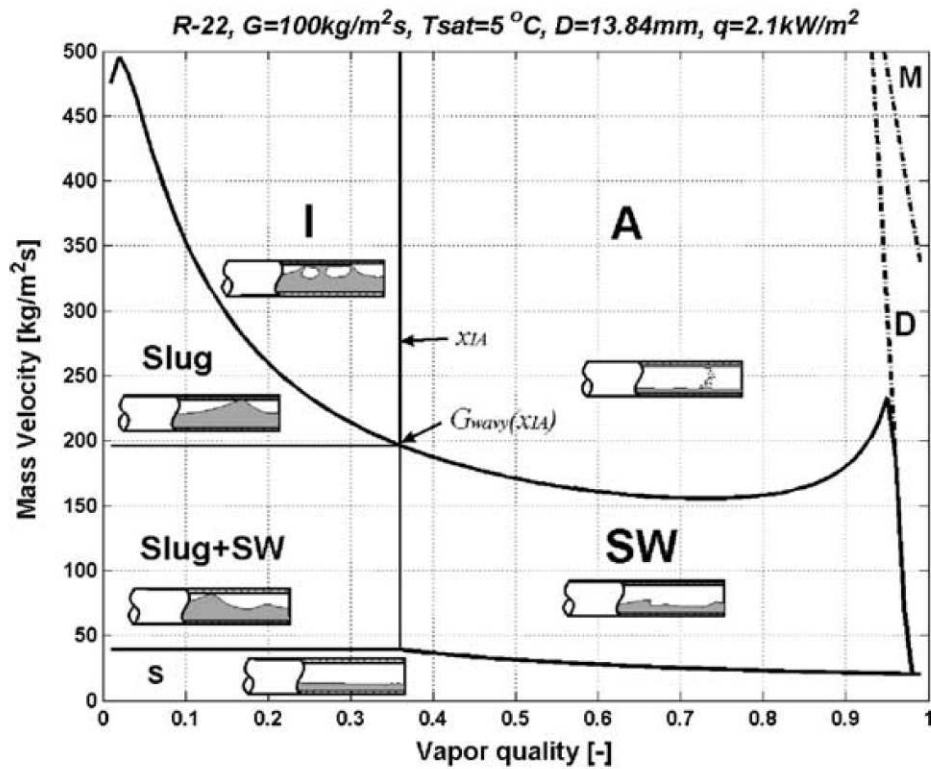


Figure 3.13: Flow pattern map developed by [Wojtan et al. (2005a)] for R-22 at $T_{\text{sat}} = 5^{\circ}\text{C}$ in a 13.84 inner tube diameter at $G = 100 \text{ kg/m}^2$ and $q = 2.1 \text{ kW/m}^2$.

of 15°C . The mass velocity ranged from 200 to $500 \text{ kg/m}^2\cdot\text{s}$. They found that the intermittent-to-annular flow transition occurred at slightly higher vapor qualities for R-410A compared to the prediction of [Barbieri et al. (2008)]. They obtained an excellent agreement with R-134a. Recently, [Mastrullo et al. (2012)] proposed a new flow pattern map with new easy-to-use correlations to explicitly illustrate the effect of reduced pressure.

3.2.3.2 Mini- and microscale flow pattern maps

The first microscale flow pattern map, as far we know, was developed by [Suo and Griffith (1963)]. Subsequently, [Triplett et al. (1999)] developed a flow pattern map based upon the superficial gas and liquid velocities for air-water in a 1.1 mm inner diameter circular tube. The flow pattern map provided by [Coleman and Garimella (1999)] and [Coleman and Garimella (2000)] for R-134a with diameter ranging from 1.3 to 5.5 mm used a x - G format.

[Akbar et al. (2003)] proposed a flow pattern map based on the observations of air-water flows in circular and near-circular channels with hydraulic diameters less than or equal to 1.0 mm. They used a log-log format for their flow pattern map with the vapor superficial Weber number, We_{SV} , and the liquid superficial Weber number We_{SL} . This map is suggested for use only when Bond number is less than 0.3.

[Revellin et al. (2006)] detected the transitions between several flow patterns from their tests in a 0.5 mm glass channel using saturated R-134a at 30°C (7.7 bar). The associated flow pattern map is shown on Fig. 3.14. It is compared to

a macroscale map developed by [Kattan et al. (1998a)]. There are two main differences between both maps:

- the microscale transition to annular flow is a function of the mass flux, whereas it happens at a fix vapor quality for macroscale
- the microscale transition to annular flow happens at lower vapor quality than in macroscale channels for high mass fluxes

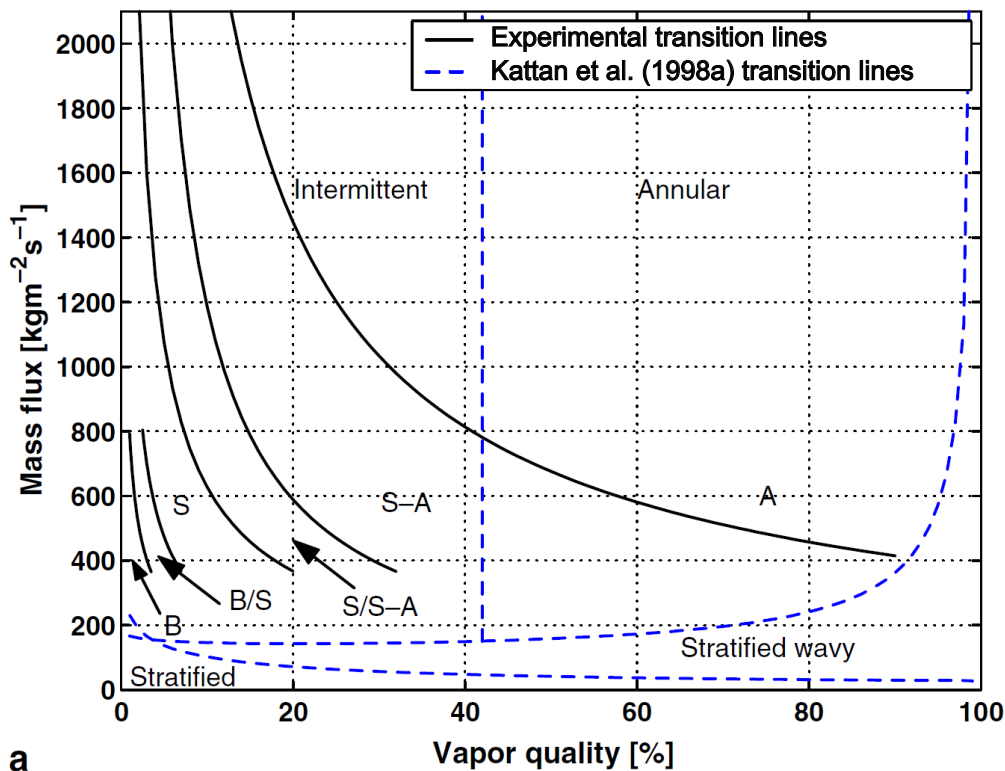


Figure 3.14: Comparison between [Revellin et al. (2006)] and [Kattan et al. (1998a)] flow pattern maps for R-134a with $d_h = 0.5$ mm and $T_{\text{sat}} = 30^\circ\text{C}$ (A: annular flow; B: bubbly; B/S: bubbly/slug flow; S: slug flow; S/S-A: slug/semi-annular flow; S-A: semi-annular flow).

Rather than segregating the observations into the traditional flow regimes of an adiabatic map, [Revellin and Thome (2007c)] developed flow pattern maps which classify flows into three types: (i) the isolated bubble regime, (ii) the coalescing bubble regime, and (iii) the annular regime. Their database includes data for two refrigerants (R-134a and R-245fa), two channel diameters (0.509 and 0.790 mm), and three saturation temperatures (26, 30, and 35°C). Figure 3.15 shows an example of this flow pattern map.

[Ullmann and Brauner (2007)] recently proposed a microscale flow pattern map derived from an analysis of the mechanisms controlling each flow pattern transition and tailored to small diameter channels. Based on the flow pattern observations of [Triplett et al. (1999)], they made significant modifications in the well-known macroscale transition criteria. Their flow pattern map describes five flow regimes: dispersed bubble, bubble, slug, aerated slug and annular.

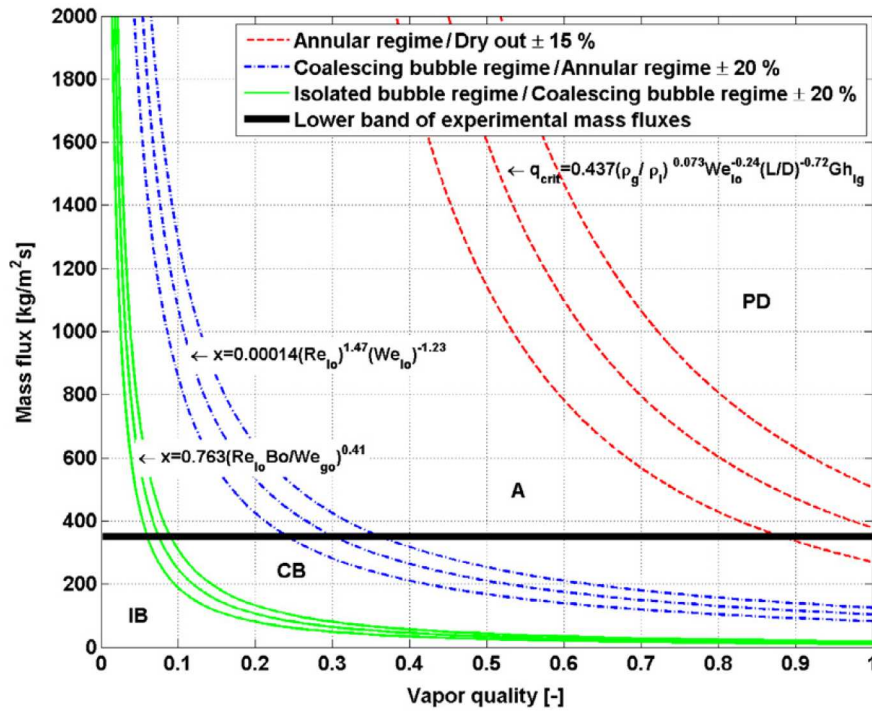


Figure 3.15: Diabatic coalescing bubble map of [Revellin and Thome (2007c)] for evaporating flow in circular uniformly heated microchannels for R-134a with $d_f = 0.5$ mm and $T_{\text{sat}} = 30^\circ\text{C}$ (IB: isolated bubble regime, CB: coalescing bubble regime, A: annular regime, and PD: post dryout regime).

[Ong and Thome(2011a)] modified the flow pattern map developed by [Ong and Thome (2009)] to predict both the macroscale and the microscale flow patterns. They focused their experiments on the macro-to-microscale transition with inner tube diameters ranging from 1.03 to 3.04 mm with R-134a, R-236fa and R-245fa whereas the flow pattern map of [Ong and Thome (2009)] was developed only for 1.030 mm inner diameter tube. They proposed a flow pattern map including new dimensionless numbers accounting for the gravity, inertia and surface tension effects. The introduction of the Froude number, Fr , accounts for the inertia and gravity forces while the Confinement number, Co , accounts for the confined bubble effect as a function of the capillary length.

[Arcanjo et al. (2010)] compared their experimental data of flow visualization with R-245fa to the flow pattern map data of [Revellin et al. (2006)] and [Ong and Thome (2009)]. They investigated the influence of the saturation temperature on the ability of the flow pattern maps of [Revellin et al. (2006)] and [Ong and Thome (2009)] to predict the experimental flow patterns. Figure 3.16 shows that the experimental intermittent-to-annular transitions are dependent on saturation temperature whereas the intermittent-to-annular transition lines of [Revellin et al. (2006)] and [Ong and Thome (2009)] do not take into account the effect of the saturation temperature.

More recently, [Costa-Patry and Thome (2012)] proposed a new flow pattern map from their experimental results for several multi-microchannel evaporators. They proposed a new correlation for the coalescing bubble-to-annular flow transition which takes into account the influence of the heat flux. They used two dimensionless numbers: the boiling number, Bo , and the Confinement number, Co .

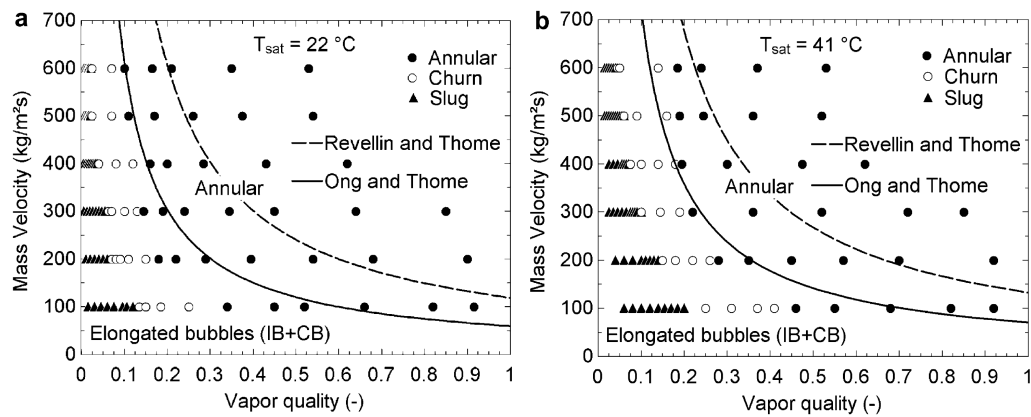


Figure 3.16: Comparison between the experimental data of [Arcanjo et al. (2010)] and the predictive methods (lines) by [Ong and Thome (2009)] and by [Revellin et al. (2006)] with R-245fa in a 2.32 mm inner diameter channel at (a) $T_{\text{sat}} = 22^\circ\text{C}$ and (b) $T_{\text{sat}} = 41^\circ\text{C}$.

The two-phase flow patterns were widely investigated since 1954 and the first flow pattern map developed by [Baker (1954)]. Previous works also indicate that the influence of some parameters (hydraulic diameter, heat flux) was much more investigated than that of other parameters, among which the saturation temperature.

3.2.4 Conclusions

Among the numerous techniques developed to determine regimes that can take place during two-phase flows, the techniques using detailed physical information of the flow are the most promising. The image processing technique represents the most convenient technique to implement for a laboratory disposing of a high speed high resolution video camera. This technique has to be coupled with the measurement of the heat transfer coefficient to characterize the dryout inception.

Even if many authors seem to use different names, six flow regimes seem to be commonly recognized in the literature: bubbly flow, slug flow, annular flow, stratified flow, dryout flow and mist flow. These six primary flow regimes are schematically represented on Fig. 3.17. Other flow patterns are subregimes or transition modes between these major flow regimes.

To date, only few studies have been carried out to investigate the effect of saturation temperature on the two-phase flow structure. Nevertheless, some results on the influence of saturation temperature on the bubble dynamics suggest that the saturation temperature may be an important factor. The transitions to annular flow and to dryout flow may be strongly influenced by the saturation temperature. The results of [Revellin et al. (2008)] and [Arcanjo et al. (2010)] on the influence of saturation temperature on the elongated bubbles characteristics, shown on Fig. 3.18, tend to corroborate its major role. Therefore, the study of two-phase flow and the development of new flow pattern maps valid at high saturation temperature should be one goal of the present research work.

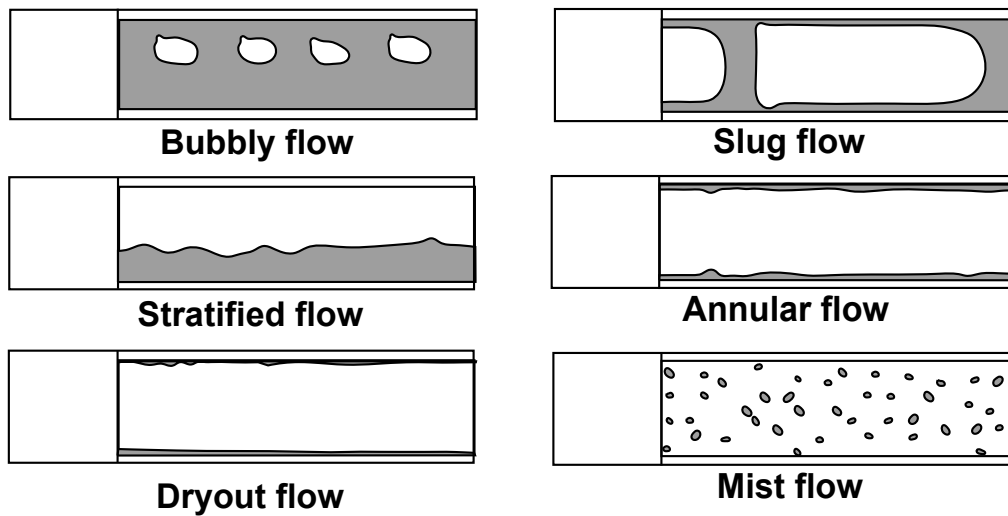


Figure 3.17: Schematic of the 6 primary flow regimes commonly recognized in the literature.

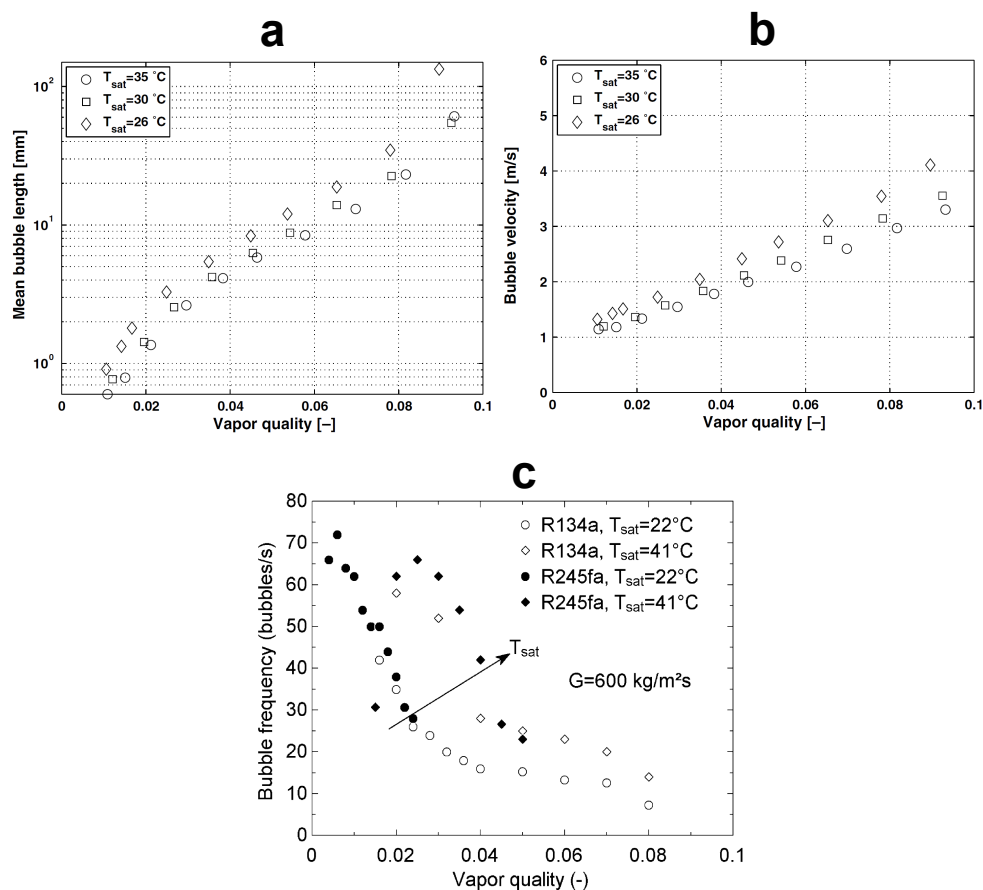


Figure 3.18: Influence of saturation temperature on elongated bubbles characteristics: (a) elongated bubble velocity as a function of vapor quality for R-134a flowing in a 0.5 mm inner diameter tube at $G = 1000 \text{ kg/m}^2\text{s}$ from [Revellin et al. (2008)], (b) elongated bubble length as a function of vapor quality for R-134a flowing in a 0.5 mm inner diameter tube at $G = 1000 \text{ kg/m}^2\text{s}$ from [Revellin et al. (2008)], and (c) elongated bubble frequency as a function of vapor quality from [Arcanjo et al. (2010)].

3.3 Pressure drop

The reliable prediction of pressure drop in two-phase flows is an important prerequisite to accurate optimization of thermal systems. The total pressure drop of a fluid is due to the variation of potential and kinetic energy of the fluid and to the friction on the channel walls or between the phases. Thus, the total pressure drop ΔP_{total} is the sum of the static pressure drop (elevation head) ΔP_{static} , the momentum pressure drop (acceleration) ΔP_{mom} , and the frictional pressure drop ΔP_{frict} :

$$\Delta P_{\text{total}} = \Delta P_{\text{static}} + \Delta P_{\text{mom}} + \Delta P_{\text{frict}} \quad (3.16)$$

For a horizontal tube (i.e. the configuration of interest in the next chapters), there is no change in static head, i.e. $\Delta P_{\text{static}} = 0$. The momentum pressure drop reflects the change in kinetic energy of the flow due to the flashing or diabatic effect. When measuring two-phase pressure drops in horizontal tubes, the frictional pressure drop is obtainable by subtracting the momentum pressure drop from the measured total pressure drop. The frictional pressure drop results from the shear stress between the flowing fluid and the channel wall and between the phases of the fluid itself.

A concise summary of experimental researches on two-phase flow pressure drop is presented below and considers only two-phase pressure drop studies for horizontal channels with different sizes: macro-, mini-, and microchannels. The objective is to illustrate typical trends observed in the literature. This review draws attention to the following main points:

- the difference between two-phase flow pressure drop in macrochannels and microchannels
- the effect of the nature of flow pattern on the two-phase flow pressure drop
- the effect of mass flux, reduced pressure, and saturation temperature on the two-phase flow pressure drop
- the range of saturation temperature used during the two-phase flow pressure drop studies

3.3.1 Experimental studies for pressure drop in straight tubes

Frictional two-phase pressure drops in internal geometries have been experimentally investigated over the last three decades by several authors. Figure 3.19 presents the number of data points published in the open literature (122 articles for 23 refrigerants since 1980) only for refrigerants flow boiling. We see that R-245fa was not a favorite fluid in the past. Actually, it regained some interest during the last decades because of its possible application for electronic cooling and air conditioning (see [Zyhowski et al. (2002)]).

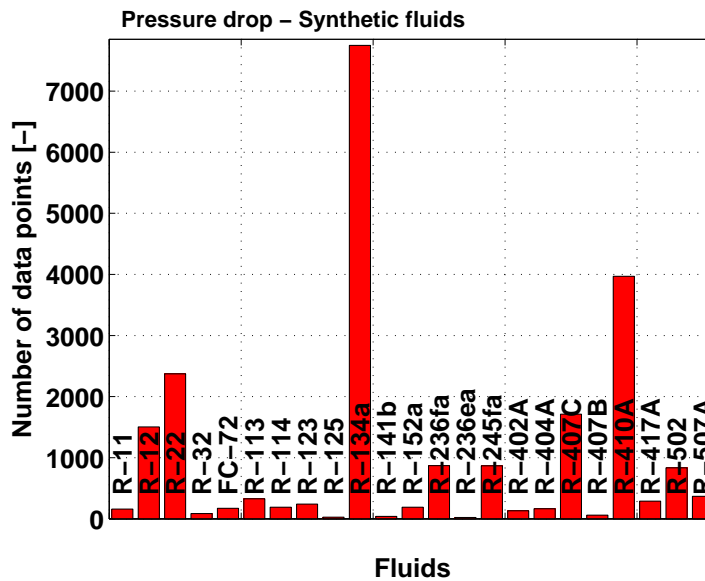


Figure 3.19: Number of pressure drop data points (22363 data points in total) for each refrigerant published in 122 articles since 1980 for flow boiling ([Charnay et al. (2011)]).

3.3.1.1 Pressure drop studies in macrochannels

[Kuo and Wang (1996)] reported diabatic and adiabatic experimental pressure drop data for R-22 and R-407C in a microfin tube with inner diameter of 9.52 mm. They investigated the effect of mass velocity on the pressure drop. They observed from their results that the pressure drop increased significantly with increasing the mass velocity and the vapor quality. All the studies quoted in this section corroborate these trends. So, the effects of mass velocity and vapor quality are clearly established and hence typical representation of these effects on the two-phase flow pressure drop in macrochannels can be plotted. These effects are schematically represented on Fig. 3.20.

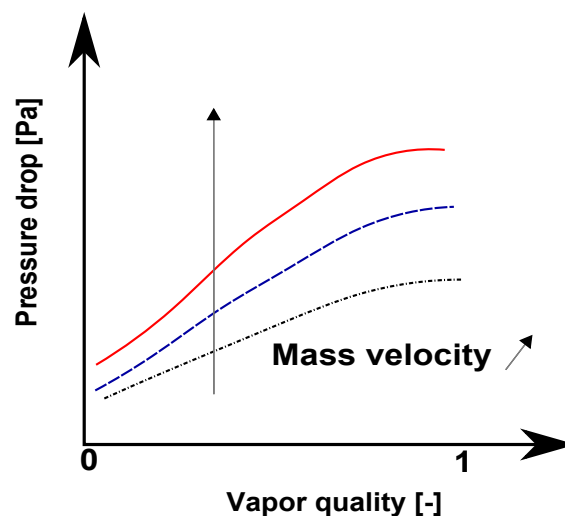


Figure 3.20: Schematic of the typical trends of two-phase flow pressure drop observed in macrochannels: influence of the mass velocity and the vapor quality.

[Zhang and Webb (2001)] investigated the two-phase pressure drop characteristics for R-134a, R-22, and R-404A flowing in a multiport extruded aluminium tube with hydraulic diameter of 2.13 mm, and in two copper tubes having inside diameters of 6.25 and 3.25 mm, respectively. They studied the influence of the saturation temperature on the pressure drop. The saturation temperature ranged from 20 to 65°C. They noted a decrease of the two-phase flow pressure drop with increasing the saturation temperature as represented on their results on Fig. 3.21. This influence of the saturation temperature on the pressure drop was also observed by [Wang et al. (2001)], [Wongsa-ngam et al. (2004)], [Park and Hrnjak (2007)], [De Rossi et al. (2009)], [Oh and Son (2011)], and [Padilla et al. (2011)]. Typical representation of the results available in the literature on the influence of saturation temperature is represented on Fig. 3.22.

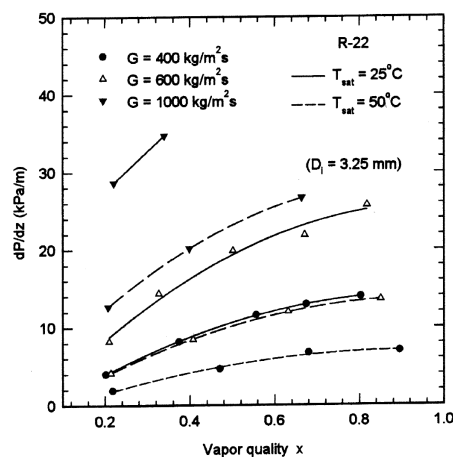


Figure 3.21: R-22 two-phase flow pressure drop measured by [Zhang and Webb (2001)] in a 3.25 mm inner diameter tube.

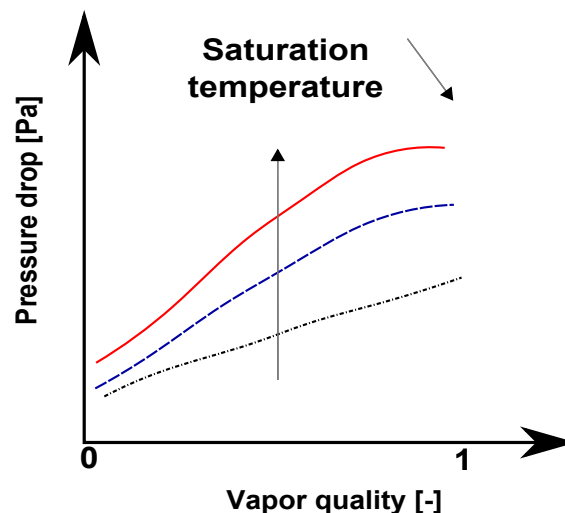


Figure 3.22: Schematic of the typical trends of two-phase flow pressure drop observed in macrochannels: influence of the saturation temperature.

[Ould Didi et al. (2002)] provided pressure drop data points for five refrigerants (R-134a, R-123, R-402A, R-404A and R-502) flowing in two horizontal test sections of 10.92 and 12.00 mm inner diameters. In their study, the saturation temperature ranged from -1.3 to 30.7°C. They classified their data by flow pattern using

the [Kattan et al. (1998a)] flow pattern map. They segregated their database into annular flow, intermittent flow, and stratified-wavy flow. They found that the best correlation for annular flow was that of [Müller-Steinhagen and Heck (1986)], the best for intermittent flow was that of [Grønnerud (1979)], and the best for stratified-wavy flow was that of [Grønnerud (1979)]. [Greco and Vanoli (2006)] used the same flow pattern map to determine the flow regimes. They provided two-phase flow pressure drop data obtained with several refrigerants (R-22, R-507, R-404A, R-134a, R-407C, and R-410A) in a horizontal, smooth, stainless steel tube with an inner diameter of 6.00 mm. The experimental tests were carried out at an almost constant saturation pressure of 7.0 bar (saturation temperature ranging from -28 to 25°C). They investigated the effect of the kind of flow regimes on the pressure drop:

- intermittent flow: a slight increase of the pressure drop when increasing the vapor quality with some anomalies
- annular flow: a stiff increase of the pressure drop when increasing the vapor quality
- mist flow: a decrease of the pressure drop when increasing the vapor quality

In the same spirit, [Quibén and Thome (2007a)] investigated the trends of vapor quality versus the vapor quality. They provided experimental data on two-phase flow pressure drop of R-134a, R-22 and R-410A in horizontal channels with two different sizes (8.0 and 13.8 mm). They noted two distinct behaviors over the range of vapor quality (see Fig. 3.23):

- an increase of the pressure drop when increasing the vapor quality until a maximum value
- a falloff of the pressure drop after the maximum value until the complete evaporation

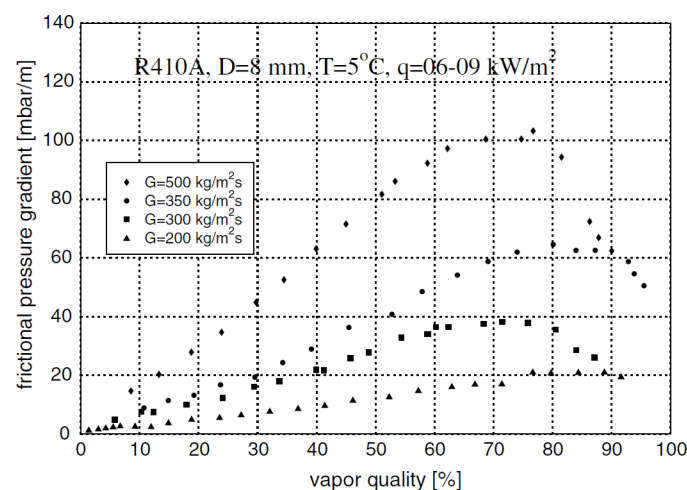


Figure 3.23: Frictional pressure gradients versus vapor quality for different mass velocities. From [Quibén and Thome (2007a)].

They identified two distinct configurations: (i) the location of the peaks was near to the onset of dryout at the top of the tube or (ii) the peak occurred before the onset of the dryout. For the second configuration, they associated the appearance of this peak with the damping out of interfacial waves (as the annular film thins) to explain this phenomenon. They compared their database to the correlations of [Grønnerud (1979)] and [Müller-Steinhagen and Heck (1986)]. Only 40 % of the data were captured within $\pm 20\%$ by the [Grønnerud (1979)] correlation whereas that of [Müller-Steinhagen and Heck (1986)] provided the best accuracy, but with only 50% of the data captured within $\pm 20\%$. [Mauro et al. (2007)] compared their database obtained for a 6.00 mm inner diameter horizontal smooth tube and for different refrigerants (R-22, R-507, R-404A, R-407C, R-410A, R-417A and R-507A) and different experimental conditions (saturation temperature ranging from -18.4 to 46.2°C) to four correlations and to the phenomenological model of [Quibén and Thome (2007b)] developed from the previous database. They statistically showed that the method of [Grønnerud (1979)] and that developed by [Quibén and Thome (2007b)] were equally accurate.

[Filho et al. (2004)] provided pressure drop results of R-134a under convective boiling conditions in horizontal smooth and microfinned copper tubes. Experiments were carried out at a saturation temperature of 5°C with different inner diameters ranging from 6.24 to 8.76 mm for smooth tubes and from 6.40 to 8.92 mm for microfinned tubes. They investigated the influence of inner tube diameter and they concluded that pressure drop decreased with increasing inner tube diameter. This trend was confirmed later by [Quibén and Thome (2007a)] and [Padilla et al. (2011)]. The typical trend of evolution of the pressure drop with the quality for various channel diameters is schematically depicted on Fig. 3.24. The correlation of [Jung et al. (1989)] was found to be the best prediction correlation for smooth tube. [De Rossi et al. (2009)] reached the same conclusion when comparing their experimental database to several predictive methods for pressure drops. Their database was obtained with R-134a flowing inside a 6.00 mm inner diameter, smooth and horizontal stainless steel tube with a saturation temperature ranging from -8.9 to 19.9°C .

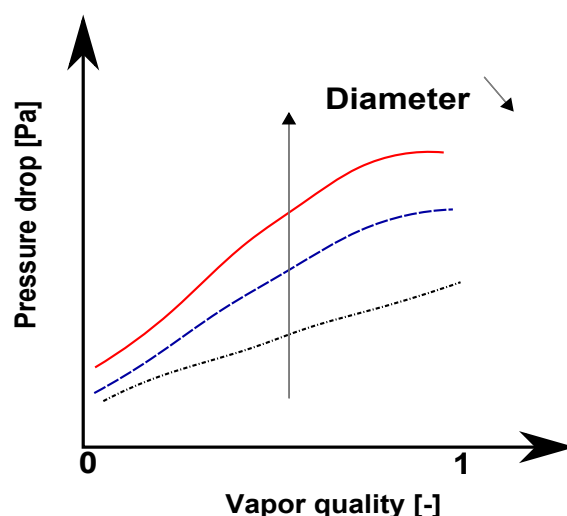


Figure 3.24: Schematic of the typical trends of two-phase flow pressure drop observed in macrochannels: influence of the inner tube diameter.

[Park and Hrnjak (2007)] measured the two-phase flow pressure drop in a 6.1 mm inner diameter horizontal smooth tube for CO₂, R-410A and R-22. This study was performed at two different saturation temperatures of -15 and -30°C. The pressure drop measured for CO₂ was much lower than that of R-22 and R-410A at identical conditions. They found that the correlation of [Müller-Steinhagen and Heck (1986)] was the best at predicting their data. [Padilla et al. (2011)] found the same results when comparing their 819 experimental pressure drop data to several correlations. Their database was obtained during two-phase flow of refrigerants HFO-1234yf, R-134a and R-410A in horizontal straight tubes. The inner diameter ranged from 7.90 to 10.85 mm and the saturation temperature from 4.8 to 20.7°C. The best accuracy was given by the correlation of [Müller-Steinhagen and Heck (1986)] with around 90% of the data predicted within a $\pm 30\%$ error band.

[Oh and Son (2011)] reported flow boiling pressure drop data of CO₂ in a 4.57 mm inner diameter horizontal tube. The saturation temperature ranged from 0 to 40°C. They compared their database against the correlations of [Chisholm (1973)], [Friedel (1979)], [Jung et al. (1989)] and, [Choi et al. (1999)]. They concluded by noting that none of the empirical correlations assessed in their study were able to predict correctly the pressure drop of CO₂.

Table 3.2 summarizes the experimental conditions corresponding to the previous quoted studies.

3.3.1.2 Pressure drop studies in mini- and microchannels

Pressure drop in small diameter tubes was studied by a number of investigators. [Lazarek and Black (1982)] investigated the pressure drop for saturated boiling of R-113 in a round tube with an internal diameter of 3.1 mm. They conducted systematic experiments to evaluate the three components of pressure drop (i.e. momentum, static, and frictional pressure drop). They correlated their database to predict each component of the pressure drop.

[Tran et al. (2000)] provided two-phase flow pressure drop measurements with three refrigerants (R-134a, R-12, and R-113) at six different saturation pressures ranging from 1.38 to 8.56 bar (saturation temperature ranging from 5.5 to 63.9°C) and in two sizes of circular channels (2.46 and 2.92 mm inner diameters) and one rectangular channel (4.06 × 1.7 mm). They observed an increase of the pressure drop when the vapor quality and the mass velocity increased. These results are similar to those measured in macrochannels and shown on Fig. 3.20. They also investigated the influence of the saturation temperature on the two-phase pressure drop of R-134a (saturation temperatures ranging from 11.9°C to 32.8°C) and R-12 (saturation temperatures ranging from 16.8°C to 34.0°C). The pressure drop was higher at a lower saturation temperature. For R-134a, they observed that a decrease in saturation temperature of 50% caused an increase in two-phase flow pressure drop of about 60%. This observation was similar to that made in macroscale conditions reported on Fig. 3.22. These observations indicated a similar behavior in macro- and minichannels. [Yun and Kim (2004)] corroborated these results from two-phase pressure drop data of CO₂ flowing in circular channels with inner diameters of 2.0 and 0.98 mm and rectangular channels with hydraulic diameters ranging from 1.08 to 1.54 mm and saturation temperatures varying from 0 to 10°C. [Tran et al. (2000)] evaluated five correlations developed for macrochannels: they were all found unable to predict the pressure drop in minichannels in any of these test conditions. These authors developed a correlation taking into account the effects of surface tension and channel size.

Table 3.2: Summary of experimental two-phase flow pressure drop studies in macrochannels (C: circular; F: finned; H: horizontal; M: multiport channel; S: smooth).

Author	Fluid	Geometry	d_h [mm]	Length [mm]	\dot{q} [kW/m ²]	G [kg/m ² ·s]	T_{sat} [°C]	x [-]
[Kuo and Wang (1996)]	R-22/R-407	H - F - C	9.52	1300	6-14	100-300	1.66 - 6.04	0.1-0.9
[Zhang and Webb (2001)]	R-134a/R-22/R-404A	H - S - C/M	2.13-6.25	560-914	0	200-1000	20 - 65	0.2-0.89
[Ould Didi et al. (2002)]	R-134a/R-123/R-402A/R-404A/R-502	H - S - C	10.92-12.00	3013	0	100-500	-1.3 - 30.7	0.04-1
[Haberschill et al. (2003)]	R-22/R-407C	H - S/F - C	6.50-11.98	1000	10-30	100-300	10.31 - 16.41	0-1
[Wongsa-ngam et al. (2004)]	R-134a	H - S/F - C	5.43-8.12	2500	10	400-800	10 - 20	0.1-0.95
[Filho et al. (2004)]	R-134a	H - S/F - C	6.24-8.92	1500	0	70-1100	5	0.5-0.95
[Greco and Vanoli (2006)]	R-22/R-507/R-404A/R-134a/R-407C	H - S - C	6	6000	11.7-36.8	280-1080	-28 - 25	0-1
[Park and Hrnjak (2007)]	CO ₂ /R-410A/R-22	H - S - C	6.1	150	0	100-400	-30 - -15	0.1-0.8
[Quibén and Thome (2007a)]	R-134a/R-22/R-410A	H - S - C	8.00-13.8	980-2035	0-57.5	70-700	5	0-1
[Mauro et al. (2007)]	(*)	H - S - C	6	6000	5-42	190-1150	-18.4 - 46.2	0.2-98
[De Rossi et al. (2009)]	R-134a	H - S - C	6	1000-1200	0	197-472	-8.8 - 19.9	0.05-0.94
[Oh and Son (2011)]	CO ₂	H - S - C	4.57	4200	10-40	200-1000	10 - 40	0-1
[Padilla et al. (2011)]	HFO-1234yf/R-134a/R-410A	H - S - C	7.90-10.85	1000	0	187-1702	4.8-20.7	0.04-0.98

(*) R-22/R-134a/R-404A/R-407C/R-410A/R-417A/R-507A

[Cavallini et al. (2005)] provided two-phase flow pressure drop characteristics of three refrigerants (R-236ea, R-134a, and R-410A) flowing in a 1.4 mm hydraulic diameter multiport minichannel tube. The choice of these three refrigerants allowed to vary an important parameter, namely the reduced pressure. Indeed, the saturation temperature was fixed at 40°C which corresponds to a reduced pressures of 0.096, 0.25, and 0.49 for R-236ea, R-134a, and R-410A, respectively. For a fixed set of operating conditions (except pressure), R-410A (with the highest reduced pressure) presented a significantly lower pressure drop in comparison with R-236ea and R-134a. The low pressure fluid R-236ea showed the highest pressure drop among the three fluids. Figure 3.25 shows typical trends regarding the influence of reduced pressure on the pressure drop. In addition, [Cavallini et al. (2005)] compared their database against several correlations. The statistical analysis indicated that the correlations assessed in their study were not able to predict the pressure drop data of R-410A: all the correlations overpredicted their experimental values. On the contrary, the pressure drop data for the refrigerants R-236ea and R-134a was well predicted by the correlation of [Müller-Steinhagen and Heck (1986)]. [Ducoulombier et al. (2011)] also compared their database to several correlations and that one of [Müller-Steinhagen and Heck (1986)] gave the best prediction. Their database was obtained from two-phase flow pressure drop measurements of carbon dioxide in a single horizontal stainless steel tube having a 0.529 mm inner diameter. Experiments were carried out for four saturation temperatures of -10, -5, 0, and 5°C.

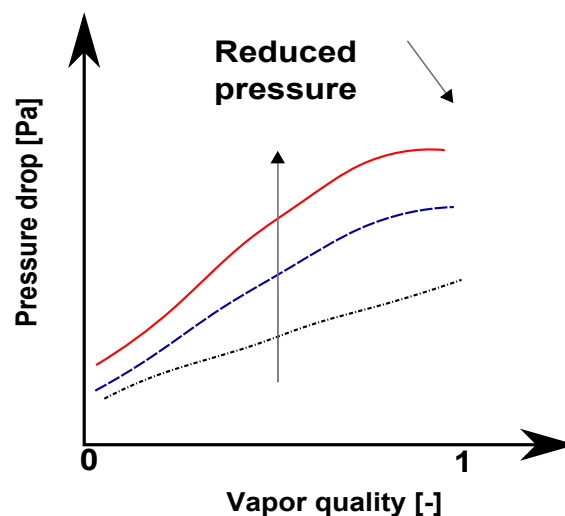


Figure 3.25: Schematic of typical trends of the influence of reduced pressure on the two-phase flow pressure drop.

[Yun et al. (2006)] investigated the two-phase flow pressure drop of R-410A in rectangular microchannels whose hydraulic diameters were 1.36 and 1.44 mm. The saturation temperatures were fixed at 0, 5, and 10°C. On the one hand, they studied the influence of the hydraulic diameter with a comparison between their results and those of [Chang et al. (2000)] obtained in a 5.0 mm inner diameter tube. The pressure drops increased with decreasing the hydraulic diameter as represented on Fig. 3.24. On the other hand, they investigated the influence of the saturation temperature on the two-phase pressure drop. They observed a decrease of the pressure drops with an increase of the saturation temperature as observed by [Chang et al. (2000)] for a larger diameter tube.

[Revellin and Thome (2007b)] measured the two-phase pressure drops over a

wide range of experimental test conditions in microchannels of two different diameters (0.509 and 0.790 mm) and for two refrigerants (R-134a and R-245fa). In general, their results depicted the expected trend (i.e. the higher the mass flux, the higher the vapor quality, the higher the two-phase pressure drop). However, for mass velocities of 1000 and 1200 kg/m²·s, they observed a change in the trend which corresponded to a change in the flow patterns with the transition from wavy annular to smooth annular, represented on Fig. 3.26. [Ducoulombier et al. (2011)] confirmed this observation with carbon dioxide. [Revellin and Thome (2007b)] also studied the influence of the saturation temperature on the pressure drop from tests performed at three different saturation temperatures (26, 30, and 35°C) and found the expected trend (i.e. the higher the saturation temperature, the lower the two-phase pressure drop). Finally, they confirmed the strong influence of the diameter on the two-phase frictional pressure drop and corroborated the results of [Yun et al. (2006)].

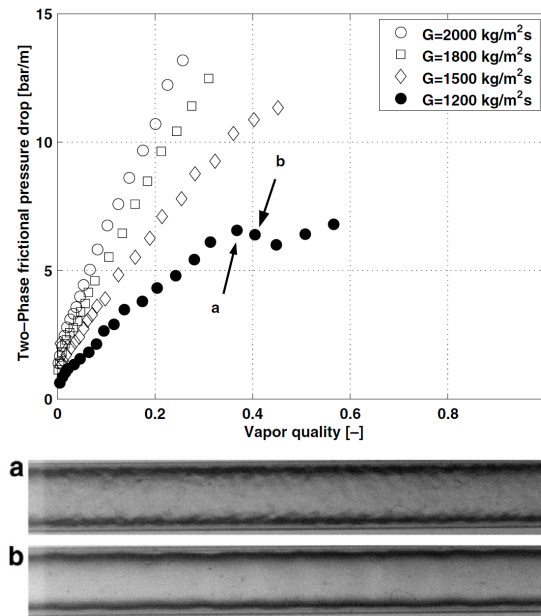


Figure 3.26: Two-phase frictional pressure drop as a function of the vapor quality for R-134a, $d_h=0.509\text{mm}$ and $T_{\text{sat}}=30^\circ\text{C}$ and the corresponding flow patterns at the locations (a) and (b): (a) wavy annular and (b) smooth annular flow. From [Revellin and Thome (2007b)].

[Tibiricá et al. (2011a)] presented experimental flow boiling pressure drop results of R-134a in a horizontal smooth tube with an internal diameter of 2.32 mm. The saturation temperature was fixed at 31°C. They corroborated the influence of the mass velocity and vapor quality on the pressure drop. They also compared their database against some of the most quoted prediction correlations. The predictive correlation of [Cioncolini et al. (2009)] worked the best to predict the data. [Tibiricá and Ribatski (2011b)] used the same test section to provide flow boiling pressure drop results of R-245fa at two different saturation temperatures (31 and 41°C). Five frictional pressure drop correlations were assessed against the experimental database and they concluded by noting that the [Cioncolini et al. (2009)] method was found to work the best.

Table 3.4 summarizes the experimental conditions corresponding to the previous quoted studies for mini- and microchannels.

3.3.2 Two-phase pressure drop prediction method

The empirical correlations are commonly used in modeling two-phase pressure drop. The main reason is that minimum knowledge of the systems characteristics is required. Thus, empirical correlations are easy to implement and often they provide good accuracy in the range of the experimental conditions on which the methods are based. As a consequence, one of the principal disadvantages of this approach is that they are limited by the range of their underlying database. Another important disadvantage of the empirical approach is that no single correlation is able to provide an acceptable accuracy for general sense. Two principle concepts in empirical methods are assumed: the homogeneous and the separated flow models. More recently, another approach, more phenomenological, taking into account the flow pattern effects was developed. Below, the most quoted empirical correlations are presented as well as the most quoted flow pattern based two-phase pressure drop models.

3.3.2.1 Homogeneous flow model

The homogeneous flow model provides the simplest technique for analyzing two-phase flows. In the homogeneous model, both liquid and vapor phases are assumed to move at the same velocity. This ideal-fluid obeys the conventional equations of a single-phase fluid and is characterized by suitably averaged properties of the liquid and vapor phase.

The frictional pressure drop for a steady flow in a channel with a constant cross sectional area is:

$$\left(\frac{dP}{dz}\right)_{\text{frict}} = \frac{2 \cdot f_{\text{TP}} \cdot G^2}{d_h \cdot \rho_{\text{TP}}} \quad (3.17)$$

In Eq. (3.17), ρ_{TP} is the two-phase mixture density given by:

$$\rho_{\text{TP}} = \left(\frac{x}{\rho_V} + \frac{1-x}{\rho_L}\right)^{-1} \quad (3.18)$$

and f_{TP} is the two-phase friction factor defined as:

$$f_{\text{TP}} = \frac{16}{\text{Re}_{\text{TP}}} \text{ for } \text{Re}_{\text{TP}} < 2000 \quad (3.19)$$

$$f_{\text{TP}} = \frac{0.079}{\text{Re}_{\text{TP}}^{0.25}} \text{ for } \text{Re}_{\text{TP}} > 2000 \quad (3.20)$$

where the two-phase Reynolds number (Re_{TP}) is :

$$\text{Re}_{\text{TP}} = \frac{G \cdot d_h}{\mu_{\text{TP}}} \quad (3.21)$$

In the homogeneous model, there are some common expressions for the viscosity of two-phase gas-liquid flow. The expressions available for the two-phase liquid-gas viscosity are mostly of an empirical nature as a function of vapor quality (x). A non-exhaustive list of two-phase viscosity definitions available in the literature is given in Table 3.3. The two definitions proposed by [Awad and Muzychka (2008)] were developed by analogy to the effective thermal conductivity using the Maxwell-Eucken No 1 definition and the Maxwell-Eucken No 2 definition, respectively. These definitions of two-phase viscosity are available in the paper of [Hashin and Shtrikman (1962)].

Table 3.3: Two-phase viscosities proposed by several authors used in the homogeneous flow models.

Authors	Definitions
[McAdams et al. (1942)]	$\mu_{TP} = \left(\frac{x}{\mu_V} + \frac{1-x}{\mu_L} \right)^{-1}$
[Cicchitti et al. (1960)]	$\mu_{TP} = x \cdot \mu_V + (1-x) \cdot \mu_L$
[Dukler et al. (1964)]	$\mu_{TP} = \rho_{TP} \cdot \left(x \cdot \frac{\mu_V}{\rho_V} + (1-x) \cdot \frac{\mu_L}{\rho_L} \right)$
[Beattie and Whalley (1982)]	$\mu_{TP} = \theta \cdot \mu_V + (1-\theta) \cdot (1+2.5 \cdot \theta) \cdot \mu_L$ $\theta = \left[1 + \left(\frac{\rho_V}{\rho_L} \right) \cdot \left(\frac{1-x}{x} \right) \right]^{-1}$
[Lin et al. (1991)]	$\mu_{TP} = \frac{\mu_L \cdot \mu_V}{\mu_V + x^{1.4} \cdot (\mu_L - \mu_V)}$
[Fourar and Bories (1995)]	$\mu_{TP} = \rho_{TP} \cdot \left(\sqrt{x \cdot \nu_V} + \sqrt{(1-x) \cdot \nu_L} \right)^2$
[Davidson et al. (1943)]	$\mu_{TP} = \mu_L \cdot \left[1 + x \cdot \left(\frac{\rho_L}{\rho_V} - 1 \right) \right]$
[García et al. (2003)]	$\mu_{TP} = \frac{\mu_L \cdot \rho_V}{x \cdot \rho_L + (1-x) \cdot \rho_V}$
[Awad and Muzychka (2008)] No 1	$\mu_{TP} = \mu_L \cdot \frac{2 \cdot \mu_L + \mu_V - 2 \cdot (\mu_L - \mu_V) \cdot x}{2 \cdot \mu_L + \mu_V + (\mu_L - \mu_V) \cdot x}$
[Awad and Muzychka (2008)] No 2	$\mu_{TP} = \mu_V \cdot \frac{2 \cdot \mu_V + \mu_L - 2 \cdot (\mu_V - \mu_L) \cdot (1-x)}{2 \cdot \mu_V + \mu_L + (\mu_V - \mu_L) \cdot (1-x)}$

An extension of the homogeneous two-phase model was proposed by [Bankoff (1960)] which takes into account some two-dimensional effects. He derived expressions for the axial variation of velocity and void fraction in a tube. The assumption was that the axial variation could be determined using a power law function. The two-phase frictional pressure drop is expressed as a function of a two-phase multiplier as follows:

$$\left(\frac{dP}{dz}\right)_{\text{frict}} = \left(\frac{dP}{dz}\right)_{\text{LO}} \cdot \Phi_{\text{TP}}^{7/4} \quad (3.22)$$

The liquid only frictional pressure gradient is:

$$\left(\frac{dP}{dz}\right)_{\text{LO}} = \frac{2 \cdot f_{\text{LO}} \cdot G^2}{d_h \cdot \rho_L} \quad (3.23)$$

with

$$f_{\text{LO}} = \frac{0.079}{\text{Re}_{\text{LO}}^{0.25}} \text{ with } \text{Re}_{\text{LO}} = \frac{G \cdot d_h}{\mu_L} \quad (3.24)$$

In Eq. (3.22), the two-phase multiplier is expressed by:

$$\Phi_{\text{TP}} = \frac{1}{1-x} \cdot \left[1 - \gamma \cdot \left(1 - \frac{\rho_V}{\rho_L}\right)\right]^{3/7} \cdot \left[1 + x \cdot \left(\frac{\rho_L}{\rho_V}\right) - 1\right] \quad (3.25)$$

where

$$\gamma = \frac{0.71 + 2.35 \cdot \left(\frac{\rho_V}{\rho_L}\right)}{1 + \left(\frac{1-x}{x}\right) \cdot \left(\frac{\rho_V}{\rho_L}\right)} \quad (3.26)$$

This method was derived using 375 data points for steam-water mixtures in horizontal and vertical tubes in a range of mass velocity from 950 to 1220 kg/m²·s, pressure from 0.1 to 172.3 bar and is applicable to vapor quality from 0 to 0.9.

3.3.2.2 Empirical models based on the separated flow model

The separated flow model considers the two-phases to be artificially separated into two streams, one liquid and one vapor, each flowing in its own duct.

3.3.2.2.1 The Φ_L^2, Φ_V^2 based methods

The first of these analyses was performed by [Lockhart and Martinelli (1949)] from data for horizontal two-phase flow of two-component (benzene-air, kerosene-air, water-air, and various oils-air) systems at low pressures (close to atmospheric) with a range of saturation temperature from 15.5 to 29.5°C and a range of inner tube diameters from 1.49 to 25.83 mm.

Table 3.4: Summary of experimental two-phase flow pressure drop studies in mini- and microchannels (C: circular; F: finned; H: horizontal; M: multiport; R: rectangular; S: smooth).

Author	Fluid	Geometry	d_h [mm]	Length [mm]	\dot{q} [kW/m ²]	G [kg/m ² ·s]	T_{sat} [°C]	x [-]
[Lazarek and Black (1982)]	R-113	H - S - C	3.1	123	0	125-750	48 - 80	0-0.6
[Tran et al. (2000)]	R-134a/R-12/R-113	H - S - C/R	2.40-2.92	412-914	2.2-129	33-832	5.5 - 63.9	0.02-0.95
[Yun and Kim (2004)]	CO ₂	H - S - C/R	0.98 - 2.0	400-1200	5-48	100-3570	0-10	0.2-0.9
[Cavallini et al. (2005)]	R-236ea/R-134a/R-410A	H - S - M	1.4	1130	0	200-1400	40	0.25-0.81
[Yun et al. (2006)]	R-410A	H - S - R	1.36-1.44	/	10-20	200-400	0-10	
[Revellin and Thome (2007b)]	R-134a/R-245fa	H - S - C	0.509-0.790	100	0	210-2094	26 - 35	0-0.95
[Tibiricá et al. (2011a)]	R-134a	H - S - C	2.32	/	10-55	100-600	31	0.2-0.99
[Tibiricá and Ribatski (2011b)]	R-245fa	H - S - C	2.32	/	0-55	100-700	31 - 41	0.1-0.99
[Ducoulombier et al. (2011)]	CO ₂	H - S - C	0.529	191	0	200-1400	-10 - 5	0-1

They demonstrated that four flow regimes can exist during two-phase flow: (i) liquid and gas both turbulent (**tt**), (ii) liquid laminar and gas turbulent (**lt**), (iii) liquid turbulent and gas laminar (**tl**), and (iv) liquid and gas both laminar (**ll**).

There are two basic postulates stated for the analysis of the pressure drop:

- the static pressure drop for the liquid phase must equal the static pressure drop of the vapor phase regardless of the flow pattern,
- the volume occupied by the liquid plus the volume occupied by the gas at any instant must equal the total volume of the pipe.

These postulates suggest that the flow pattern does not change along the tube length, thus they eliminate from consideration slug flow in which alternate slugs of liquid and gas move down the tube.

In the final model, the two-phase frictional pressure drop based on a two-phase multiplier for the liquid phase, or the vapor phase, respectively, is:

$$\left(\frac{dP}{dz}\right)_{\text{frict}} = \left(\frac{dP}{dz}\right)_V \cdot \Phi_{V,tt}^2 \quad (3.27)$$

$$\left(\frac{dP}{dz}\right)_{\text{frict}} = \left(\frac{dP}{dz}\right)_L \cdot \Phi_{L,tt}^2 \quad (3.28)$$

where the terms $\left(\frac{dP}{dz}\right)_V$ and $\left(\frac{dP}{dz}\right)_L$ represent the frictional two-phase pressure drop that would exist if the flow as a vapor or liquid, respectively, were assumed to flow alone in the entire cross-section of the tube, are expressed as:

$$\left(\frac{dP}{dz}\right)_V = \frac{2 \cdot f_V \cdot G^2 \cdot x^2}{d_h \cdot \rho_V} \quad (3.29)$$

$$\left(\frac{dP}{dz}\right)_L = \frac{2 \cdot f_L \cdot G^2 \cdot (1-x)^2}{d_h \cdot \rho_L} \quad (3.30)$$

The single-phase friction factors of the liquid (f_L) and the vapor (f_V) and the Reynolds numbers are calculated using the classical definition with their respective physical properties:

$$f_V = \frac{0.079}{\text{Re}_V^{0.25}} \text{ where } \text{Re}_V = \frac{G \cdot d_h \cdot x}{\mu_V} \quad (3.31)$$

$$f_L = \frac{0.079}{\text{Re}_L^{0.25}} \text{ where } \text{Re}_L = \frac{G \cdot d_h \cdot (1-x)}{\mu_L} \quad (3.32)$$

The resulting graphical correlation is shown on Fig. 3.27 where Φ (not Φ^2) is plotted as a function of X . All flow regimes were correlated in this manner and the corresponding Φ_V^2 and Φ_L^2 can be related to the Lockhart-Martinelli parameter by relationships of the forms:

$$\Phi_V^2 = 1 + C \cdot X + X^2 \quad (3.33)$$

$$\Phi_L^2 = 1 + \frac{C}{X} + \frac{1}{X^2} \quad (3.34)$$

where the Lockhart-Martinelli parameter is defined as:

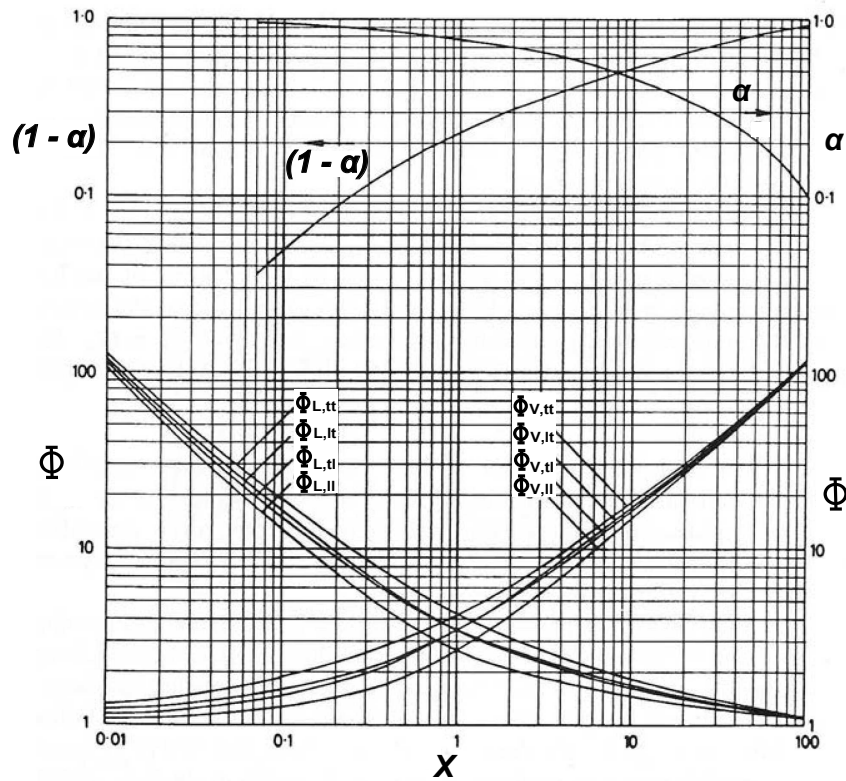


Figure 3.27: [Lockhart and Martinelli (1949)] correlation.

Table 3.5: Values of C to fit the empirical curves of [Lockhart and Martinelli (1949)].

	Liquid	Gas	C
(tt)	turbulent	turbulent	20
(lt)	laminar	turbulent	12
(tl)	turbulent	laminar	10
(ll)	laminar	laminar	5

$$X = \left(\frac{1-x}{x} \right)^{0.9} \cdot \left(\frac{\rho_V}{\rho_L} \right)^{0.5} \cdot \left(\frac{\mu_L}{\mu_V} \right)^{0.1} \quad (3.35)$$

and C takes the values given in Table 3.5.

Several authors modified the parameter C in Eqs. (3.33) and (3.34) from their database. For instance, [Mishima and Hibiki (1996)] measured the frictional pressure drop for air-water flows in capillary tubes with inner diameters in the range from 1 to 4 mm and modified the constant C as a function of the tube diameter:

$$C = 21 \cdot \left(1 - e^{-0.319 \cdot d_h} \right) \quad (3.36)$$

This model is applicable for vertical and horizontal round tubes as well as rectangular channels. [Zhang et al. (2010)] modified the expression of C proposed by [Mishima and Hibiki (1996)] for minichannel. They used the non-dimensional Laplace constant La^* (also called Confinement number Co) defined as :

Table 3.6: Empirical constants of [Lee and Lee (2001)].

Liquid	Gas	A	q	r	s	X	Re_L
laminar	laminar	6.833×10^{-8}	-1.317	0.719	0.557	0.776 - 14.176	175 - 1480
laminar	turbulent	6.135×10^{-2}	0	0	0.726	0.303 - 1.426	293-1506
turbulent	laminar	3.627	0	0	0.174	3.276 - 79-415	2606 - 17642
turbulent	turbulent	0.408	0	0	0.451	1.309 - 14.781	2675-17757

$$La^* = \frac{\left[\frac{\sigma}{g \cdot (\rho_L - \rho_V)} \right]^{0.5}}{d_h} \quad (3.37)$$

They correlated the parameter C by the following equation for adiabatic liquid-vapor two-phase flow:

$$C = 21 \cdot \left[1 - e^{\left(\frac{-0.142}{La^*} \right)} \right] \quad (3.38)$$

The applicable ranges of this model are as follows: $0.014 \leq d_h \leq 6.25$ mm, $Re_L \leq 2000$, and $Re_V \leq 2000$.

[Sun and Mishima (2009)] proposed two expressions of C for both laminar and turbulent flow regimes. They collected 2092 data points from 18 published papers. The hydraulic diameter ranged from 0.506 to 12 mm. Based on the database, they found that C was strongly affected not only by La^* but also by Re_L in laminar flow. For turbulent flow, [Sun and Mishima (2009)] modified C but also the expression of Φ_L^2 .

In the same spirit, [Lee and Lee (2001)] proposed a model for the two-phase pressure drop through horizontal rectangular channels with small heights by modifying the parameter C as presented in Eq. (3.39).

$$C = A \cdot \zeta^q \cdot \psi^r \cdot Re_{LO}^s \quad (3.39)$$

where

$$\zeta = \frac{\mu_L^2}{\rho_L \cdot \sigma \cdot d_h} \quad (3.40)$$

and

$$\psi = \frac{\mu_L \cdot J}{\sigma} \quad (3.41)$$

where J is the superficial velocity and A , q , r , and s are constants which take different value for each different flow regime (Table 3.6).

[Lee and Mudawar (2005)] measured the two-phase pressure drop across a microchannel heat sink. The micro-channels were formed by machining 231 μm wide \times 713 μm deep groves into the surface of a copper block. They took into

account that typical microchannel operating conditions rarely produced turbulent liquid flow. Therefore, they proposed two correlations for C based on the flow regimes of the liquid and vapor:

$$C_{ll} = 2.16 \cdot \text{Re}_{LO}^{0.047} \cdot \text{We}_{LO}^{0.6} \quad (3.42)$$

$$C_{lt} = 1.45 \cdot \text{Re}_{LO}^{0.25} \cdot \text{We}_{LO}^{0.23} \quad (3.43)$$

[Yamamoto et al. (2007)] proposed a correlation to predict the frictional pressure drop of carbon dioxide in minichannels. They found that the parameter C was dependent on the vapor quality and the mass velocity. More recently, [Pamitran et al. (2010)] investigated the two-phase flow pressure drop of R-22, R-134a, R-410A, R-290 and CO₂ in horizontal tubes of 0.5, 1.5 and 3.0 mm inner diameters. Experimental data were obtained over a heat flux range from 5 to 40kW/m², a mass velocity range from 50 to 600 kg/m²·s, a saturation temperature range from 0 to 15°C, and a quality up to 1. Their experimental results showed that pressure drop was a function of mass velocity, inner tube diameter, surface tension, density and viscosity, and therefore, they developed a factor C as a function of the two-phase Weber number (We_{TP}) and two-phase Reynolds number (Re_{TP}). The expression of C is:

$$C = 0.003 \cdot \text{We}_{TP}^{-0.433} \cdot \text{Re}_{TP}^{1.23} \quad (3.44)$$

where

$$\text{Re}_{TP} = \frac{G \cdot d_h}{\mu_{TP}} \quad (3.45)$$

with μ_{TP} is calculated using the model of [Beattie and Whalley (1982)] given in Table 3.3. The two-phase Weber number is calculated from the following equation:

$$\text{We}_{TP} = \frac{G^2 \cdot d_h}{\rho_{TP} \cdot \sigma} \quad (3.46)$$

with

$$\rho_{TP} = \epsilon \cdot \rho_V + (1 - \epsilon) \cdot \rho_L \quad (3.47)$$

3.3.2.2.2 The Φ_{LO}^2, Φ_{VO}^2 based method

Because the Lockhart-Martinelli multipliers were determined from experiments at atmospheric pressure in the previous model, [Martinelli and Nelson (1948)] extended the region of validity of the procedure up to the critical pressure. In this model, the frictional pressure drop is determined by using a two-phase multiplier factor from the frictional pressure drop of the single-phases, considering the liquid and the vapor phase flowing alone (LO stands for “liquid only” and VO for “vapor only”) in the channel with the total mass flow rate. [Martinelli and Nelson (1948)] proposed the following expression for the two-phase frictional pressure drop:

$$\left(\frac{dP}{dz} \right)_{\text{frict}} = \left(\frac{dP}{dz} \right)_{LO} \cdot \Phi_{LO}^2 \quad (3.48)$$

where $\left(\frac{dP}{dz} \right)_{LO}$ is:

$$\left(\frac{dP}{dz}\right)_{LO} = f_{LO} \cdot \frac{2 \cdot G^2}{d_h \cdot \rho_L} \quad (3.49)$$

with

$$f_{LO} = \frac{16}{\text{Re}_{LO}} \text{ for } \text{Re}_{LO} = \frac{G \cdot d_h}{\mu_L} < 2000 \quad (3.50)$$

$$f_{LO} = 0.079 \cdot \text{Re}_{LO}^{-0.25} \text{ for } \text{Re}_{LO} > 2000 \quad (3.51)$$

They assumed in their model that the relationship between Φ_{LO}^2 and Φ_L^2 was:

$$\Phi_{LO}^2 = \Phi_L^2 \cdot (1 - x)^{1.8} \quad (3.52)$$

where Φ_L^2 is calculated by Eq. (3.34) for atmospheric pressure. From their experimental tests, they determined in graphical form the function between the two-phase multiplier Φ_L^2 and the Lockhart-Martinelli parameter X .

Several authors extended the model of [Martinelli and Nelson (1948)] for different experimental conditions by modifying Φ_{LO}^2 . [Jung et al. (1989)] proposed a correlation based on 600 pressure data points obtained for pure and mixed refrigerants (R-22, R-114, R-12, and R-152a). The mass velocity ranged from 230 to 720 kg/m²·s for annular flow only. They replaced Φ_{LO}^2 in Eq. (3.48) by:

$$\Phi_{LO}^2 = 12.82 \cdot X^{-1.47} \cdot (1 - x)^{1.8} \quad (3.53)$$

with X calculated with Eq. (3.35).

[Friedel (1979)] proposed another correlation for the two-phase frictional pressure gradient multiplier defined as:

$$\Phi_{LO}^2 = E + \frac{3.24 \cdot F \cdot H}{\text{Fr}^{0.045} \cdot \text{We}^{0.035}} \quad (3.54)$$

In Eq. (3.54), the Froude number (Fr) and the Weber number (We) are defined, respectively as:

$$\text{Fr} = \frac{G^2}{g \cdot d_h \cdot \rho_H^2} \quad (3.55)$$

$$\text{We} = \frac{G^2 \cdot d_h}{\sigma \cdot \rho_H} \quad (3.56)$$

where homogeneous density (ρ_H) in this method is defined as:

$$\rho_H = \left(\frac{x}{\rho_V} + \frac{1-x}{\rho_L} \right)^{-1} \quad (3.57)$$

The factors H , F and E are calculated by Eqs. (3.58), (3.59), and (3.60), respectively.

$$H = \left(\frac{\rho_L}{\rho_V} \right)^{0.91} \cdot \left(\frac{\mu_V}{\mu_L} \right)^{0.19} \cdot \left(1 - \frac{\mu_V}{\mu_L} \right)^{0.7} \quad (3.58)$$

$$F = x^{0.78} \cdot (1 - x)^{0.224} \quad (3.59)$$

$$E = (1 - x)^2 + x^2 \cdot \frac{\rho_L \cdot f_{VO}}{\rho_V \cdot f_{LO}} \quad (3.60)$$

This correlation is applicable to vertical upflow and to horizontal flow. This method is known to work well when $\mu_L/\mu_V < 1000$, which is the case for many working fluids and operating conditions typical of engineering application of two-phase flows, and for mass velocity less than $2000 \text{ kg/m}^2 \cdot \text{s}$.

[Zhang and Webb (2001)] modified the correlation of [Friedel (1979)] to predict two-phase pressure drop of R-134a, R-22, and R-404A flowing in a multi-port extruded aluminium tube with hydraulic diameter of 2.13 mm, and in two copper tubes having inside diameter of 6.25 and 3.25 mm, respectively. They used the reduced pressure ($P_{\text{red}} = P_{\text{sat}}/P_{\text{crit}}$) to replace the non-dimensional groups of density and viscosity ratios in the associated terms in the Friedel correlation and did not use the We and Fr numbers. Their expression for the two-phase multiplier is:

$$\Phi_{LO}^2 = (1 - x)^2 + 2.87 \cdot x^2 \cdot P_{\text{red}}^{-1} + 1.68 \cdot x^{0.8} \cdot (1 - x)^{0.25} \cdot P_{\text{red}}^{-1.64} \quad (3.61)$$

The method of [Grønnerud (1979)] was developed specifically for refrigerants by using around 1000 data points for R-12 and R-717 in a 26.2 mm inner diameter horizontal tube. This method is for vapor qualities from 0 to 1 and the following two-phase multiplier was proposed:

$$\Phi_{LO}^2 = 1 + \left(\frac{dP}{dz} \right)_{\text{frict}} \cdot \left[\left(\frac{\rho_L}{\rho_V} \right) \cdot \left(\frac{\mu_L}{\mu_V} \right)^{-0.25} - 1 \right] \quad (3.62)$$

The frictional pressure gradient depends on the Froude number and is given as:

$$\left(\frac{dP}{dz} \right)_{\text{frict}} = f_{\text{Fr}} \cdot [x + 4 \cdot (x^{1.8} - x^{10} \cdot f_{\text{Fr}}^{0.5})] \quad (3.63)$$

When applying this expression, if the liquid Froude number $\text{Fr}_L \geq 1$, then the friction factor $f_L = 1.0$, or if $\text{Fr}_L < 1$, then:

$$f_{\text{Fr}} = \text{Fr}_L^{0.3} + 0.0055 \cdot \left(\ln \frac{1}{\text{Fr}_L} \right)^2 \quad (3.64)$$

where

$$\text{Fr}_L = \frac{G^2}{g \cdot d_h \cdot \rho_L^2} \quad (3.65)$$

This method was derived in a range of mass velocities from 20 to $1600 \text{ kg/m}^2 \cdot \text{s}$, and saturation temperatures from -45.0 to 5.0°C .

[Chisholm (1973)] transformed the graphical procedure of [Baroczy (1965)] into equations to provide a more convenient correlation for predicting local pressure gradients during the turbulent flow of two-phase mixtures in smooth tubes. He proposed the following equation for the calculation of the frictional pressure drop. The two-phase multiplier is expressed as:

Table 3.7: Values of B for the correlation of [Chisholm (1973)] for smooth tubes.

Y [-]	G [kg/m ² ·s]	B [-]
≤ 9.5	≤ 500	4.8
≤ 9.5	$500 < G < 1900$	$\frac{2400}{G}$
≤ 9.5	≥ 1900	$\frac{55}{G^{0.5}}$
$9.5 < G < 28$	≤ 600	$\frac{520}{Y \cdot G^{0.5}}$
$9.5 < G < 28$	> 600	$\frac{21}{Y}$
> 28		$\frac{15000}{Y^2 \cdot G^{0.5}}$

$$\Phi_{LO}^2 = 1 + (Y^2 - 1) \cdot \left[B \cdot x^{\frac{2-n}{2}} \cdot (1-x)^{\frac{2-n}{2}} + x^{2-n} \right] \quad (3.66)$$

where the exponent n is equal to 0.25 and the Chisholm parameter Y is given by:

$$Y^2 = \frac{(dP/dz)_{VO}}{(dP/dz)_{LO}} \quad (3.67)$$

The values of the parameter B are given in Table 3.7.

[Yoon et al. (2004)] investigated the pressure drop of carbon dioxide in a 7.53 mm inner diameter horizontal smooth tube. The saturation temperature ranged from -4 to 20°C and mass flux from 200 to 530 kg/m²·s. They included the surface tension in the two-phase flow pressure drop correlation by using the Weber number which is the ratio of inertia forces and surface tension forces. Their frictional two-phase multiplier is based on the approach of [Chisholm (1973)] and it is expressed as:

$$\Phi_{LO}^2 = 1 + a \cdot (Y^2 - 1) \cdot \left[\frac{B}{We_{VO}} \cdot x^{0.875} \cdot (1-x)^{0.875} + x^{1.75} \right] \quad (3.68)$$

The constant a was found equal to 4.2 by a least square fitting. This correlation is applicable for flow boiling of carbon dioxide in smooth channels.

[Tran et al. (2000)] developed a pressure drop correlation on the basis of Chisholm method. The definitions of B and Y were modified to better reflect the physics of

flow boiling in small tubes in which the channel size, fluid physical properties, mass velocity, pressure, and quality are important factors. The new frictional two-phase multiplier is expressed as:

$$\Phi_{LO}^2 = 1 + (4.3 \cdot Y^2 - 1) \cdot \left[Co \cdot x^{0.875} \cdot (1-x)^{0.875} + x^{1.75} \right] \quad (3.69)$$

where Co is the dimensionless confinement number calculated with Eq. (3.70).

$$Co = \frac{1}{d_h} \cdot \sqrt{\frac{\sigma}{g \cdot (\rho_L - \rho_V)}} \quad (3.70)$$

This correlation is applicable for smooth tubes in the range of experimental conditions used by [Tran et al. (2000)] in their study (see Table 3.4).

Contrary to the previous correlations, [Chawla (1968)] suggested the following method based on the vapor pressure gradient and not the liquid pressure gradient:

$$\left(\frac{dP}{dz} \right)_{\text{frict}} = \left(\frac{dP}{dz} \right)_{VO} \cdot \Phi_{VO} \quad (3.71)$$

$\left(\frac{dP}{dz} \right)_{VO}$ is calculated with:

$$\left(\frac{dP}{dz} \right)_{VO} = f_{VO} \cdot \frac{2 \cdot G^2}{d_h \cdot \rho_V} \quad (3.72)$$

where

$$f_{VO} = \frac{16}{Re_{VO}} \text{ for } Re_{VO} = \frac{G \cdot d_h}{\mu_V} < 2000 \quad (3.73)$$

$$f_{VO} = 0.079 \cdot Re_{VO}^{-0.25} \text{ for } Re_{VO} > 2000 \quad (3.74)$$

In Eq. (3.71), the two-phase multiplier is:

$$\Phi_{VO} = x^{1.75} \cdot \left[1 + s \cdot \left(\frac{1-x}{x} \right) \cdot \left(\frac{\rho_V}{\rho_L} \right) \right]^{2.375} \quad (3.75)$$

where the slip ratio s is:

$$s = \frac{u_V}{u_L} = \frac{1}{9.1 \cdot \left[\frac{1-x}{x} \cdot (Re_{VO} \cdot Fr_H)^{-0.167} \cdot \left(\frac{\rho_L}{\rho_V} \right)^{-0.9} \cdot \left(\frac{\mu_L}{\mu_V} \right)^{-0.5} \right]} \quad (3.76)$$

where Fr_H and Re_{VO} are calculated by using the following expressions:

$$Fr_H = \frac{G^2}{g \cdot d_h \cdot \rho_{TP}^2} \text{ with } \rho_{TP} = \left(\frac{x}{\rho_V} + \frac{1-x}{\rho_L} \right)^{-1} \quad (3.77)$$

$$Re_{VO} = \frac{G \cdot d_h}{\mu_V} \quad (3.78)$$

This method was derived from 88 data points for R-11 in horizontal tubes in a range of mass velocity from 20 to 200 kg/m²·s, saturation temperature from 0.0 to 20.0°C, inner diameter from 6 to 25 mm and is applicable to vapor qualities from 0.10 to 0.95.

[Müller-Steinhagen and Heck (1986)] proposed a model for the prediction of frictional pressure drop for two-phase flow in pipes. This method was developed from 7851 data points obtained for several mixtures (air-water, steam-water, hydrocarbons-air, oils-air, R-11, R-12, R-22, Neon, and N₂) in horizontal tubes and 1462 data points in vertical tubes including air-water, steam-water, R-12, and argon combinations. The channel diameter ranged from 4 to 392 mm. This correlation is simple and more convenient to use than other methods. The two-phase frictional pressure drop is expressed as:

$$\left(\frac{dP}{dz}\right)_{\text{frict}} = F \cdot (1 - x)^{1/3} + B \cdot x^3 \quad (3.79)$$

where the factor F is:

$$F = A + 2 \cdot (B - A) \cdot x \quad (3.80)$$

The factors A and B are the frictional pressure gradients for all liquid $\left(\frac{dP}{dz}\right)_{\text{LO}}$ and all vapor flow $\left(\frac{dP}{dz}\right)_{\text{VO}}$, respectively. $\left(\frac{dP}{dz}\right)_{\text{LO}}$ is given by Eq. (3.49) and $\left(\frac{dP}{dz}\right)_{\text{VO}}$ Eq. (3.72).

3.3.2.3 Phenomenological model

In general, the methods that follow an empirical approach do not account for flow pattern effects on the process, which are particularly important at low flow rates (stratification effects) and high vapor quality (dryout effects). Furthermore, they do not use the actual velocities of liquid and vapor phases by introduction of the local void fraction in the method. Conversely, two-phase pressure drop models developed following a phenomenological approach are theory based methods as the interfacial structure is taken into account.

[Quibén and Thome (2007b)] provided a phenomenological model that is physically based on several simplified interfacial two-phase flow structures. The corresponding interfacial flow structures are determined using the [Wojtan et al. (2005a)] flow pattern map. The model treats each flow regime separately and then insures a smooth transition at the transition boundary, in agreement with the experimental observations. The [Quibén and Thome (2007b)] model was developed from the database presented by [Quibén and Thome (2007a)] for R-22, R-410A and R-134a during flow boiling in horizontal tube. The model was based on diameters comprised between 8 to 13.8 mm over the entire range of vapor quality. The complete set of equations will not be given here due to their length and complexity but the calculating procedure is given by [Quibén and Thome (2007b)]. Below, the calculation procedure for the annular flow regime is presented and described:

$$\left(\frac{dP}{dz}\right)_{\text{frict}} = f_{\text{annular}} \cdot \frac{2 \cdot G^2 \cdot x^2}{d_h \cdot \rho_V \cdot \epsilon^2} \quad (3.81)$$

where the friction factor is calculated by:

$$f_{\text{annular}} = 0.67 \cdot \left[\frac{1 - \epsilon}{4} \right]^{1.2} \cdot \left[\frac{g \cdot d_h \cdot (1 - \epsilon)^2 \cdot (\rho_L - \rho_V)}{16 \cdot \sigma} \right]^{-0.4} \cdot \left(\frac{\mu_V}{\mu_L} \right)^{0.08} \cdot \text{We}_L^{-0.034} \quad (3.82)$$

and the Weber number is given by:

$$\text{We}_L = \frac{\rho_L \cdot u_L^2 \cdot d_h}{\sigma} \quad (3.83)$$

The void fraction calculation used is given by the [Steiner (1993)] version of the [Rouhani and Axelsson (1970)] expression and is as follows:

$$\epsilon = \frac{x}{\rho_V} \cdot \left[(1 + 0.12 \cdot (1 - x)) \cdot \left(\frac{x}{\rho_V} + \frac{1 - x}{\rho_L} \right) + \frac{1.18 \cdot (1 - x) \cdot [g \cdot \sigma \cdot (\rho_L - \rho_V)]^{0.25}}{G \cdot \rho_L^{0.5}} \right]^{-1} \quad (3.84)$$

Based on a statistical comparison, they concluded that the two-phase frictional pressure drop flow pattern map based model successfully predicted their experimental database and reproduced the numerous trends observed in the data.

[Revellin and Haberschill (2009)] developed a simple linear function to predict the two-phase pressure drop based on an explicit expression for the vapor quality corresponding to the maximum pressure drop (x_M). According to the theory of [Quibén and Thome (2007b)], the maximum occurs either in the annular flow regime (x_{M1}), or at the annular-to-dryout transition (x_{M2}), or at the annular-to-mist flow transition (x_{M3}) depending on the conditions. To determine the transitions between each regime, the authors used the flow pattern map of [Wojtan et al. (2005a)]. The expressions of x_{M1} , x_{M2} , and x_{M3} are:

$$x_{M1} = -\frac{a_2}{3 \cdot a_3} + 2 \cdot \sqrt{\frac{-p_1}{3}} \cdot \cos \left[\frac{1}{3} \cdot \arccos \left(\frac{-p_2}{2} \cdot \sqrt{\frac{27}{-p_1^3}} \right) + \frac{4 \cdot \pi}{3} \right] \quad (3.85)$$

$$x_{M2} = 0.58 \cdot e \left[0.52 - 0.23 \cdot \text{We}_V^{0.17} \cdot \text{Fr}_V^{0.37} \cdot \left(\frac{\rho_V}{\rho_L} \right)^{0.25} \cdot \left(\frac{\dot{q}}{\dot{q}_{\text{crit}}} \right)^{0.70} \right] \quad (3.86)$$

$$x_{M3} = 0.61 \cdot e \left[0.57 - 0.0058 \cdot \text{We}_V^{0.38} \cdot \text{Fr}_V^{0.15} \cdot \left(\frac{\rho_V}{\rho_L} \right)^{0.09} \cdot \left(\frac{\dot{q}}{\dot{q}_{\text{crit}}} \right)^{0.27} \right] \quad (3.87)$$

Finally, according to [Quibén and Thome (2007b)], x_M is based on flow regimes and is retained as:

$$x_M = \min(x_{M1}, x_{M2}, x_{M3}) \quad (3.88)$$

The procedure to calculate the parameters a_2 , a_3 , p_1 , and p_2 is described in the article of [Revellin and Haberschill (2009)].

As a first approximation, the authors developed a simple mathematical function to predict the frictional pressure drop. They assumed a linear variation of the pressure drop as a function of x for $0 \leq x < x_M$ and another linear variation of the pressure drop as a function of x for $x_M \leq x \leq 1$. As a result, the approximation was:

- For $0 \leq x < x_M$

$$\left(\frac{dP}{dz}\right)_{\text{frict}} = \left[\left(\frac{dP}{dz}\right)_{\text{LO}} - \left(\frac{dP}{dz}\right)_{\text{max}}\right] \cdot \frac{x}{x_M} - \left(\frac{dP}{dz}\right)_{\text{LO}} \quad (3.89)$$

- For $x_M \leq x \leq 1$

$$\left(\frac{dP}{dz}\right)_{\text{frict}} = \left[\left(\frac{dP}{dz}\right)_{\text{VO}} - \left(\frac{dP}{dz}\right)_{\text{max}}\right] \cdot \frac{x-1}{x_M-1} - \left(\frac{dP}{dz}\right)_{\text{VO}} \quad (3.90)$$

[Cheng et al. (2008)] collected 387 two-phase flow pressure drop data points of CO₂. The inner tube diameters ranged from 0.8 to 7 mm, the saturation temperature from -25 to 20°C, and the mass velocity from 190 to 2000 kg/m²·s. The database was compared to several empirical pressure drop models: [Chisholm (1973)], [Friedel (1979)], [Grønnerud (1979)], [Müller-Steinhagen and Heck (1986)], [Yoon et al. (2004)], and the flow pattern based model of [Quibén and Thome (2007b)]. None of these models was able to predict the CO₂ pressure drop data well.

Therefore, they proposed a new flow pattern based phenomenological model specific to carbon dioxide by modifying the [Quibén and Thome (2007b)] model. To determine the flow regimes, they extended the flow pattern map of [Cheng et al. (2006a)] to a wider range of conditions. The complete set of equations will not be given here but the calculating procedure is given by [Cheng et al. (2008)]. Below, the calculation procedure for the annular flow regime is presented. The CO₂ frictional pressure drop model is calculated by Eq. (3.81) where f_{annular} is expressed as:

$$f_{\text{annular}} = 3.128 \cdot \text{Re}_V^{-0.454} \cdot \text{We}_L^{-0.0308} \quad (3.91)$$

More recently, [Cioncolini et al. (2009)] proposed a two-phase frictional pressure drops model during annular flow. This model is based on the vapor core Weber number, capable of providing physical insight into the flow. The databank contains 3908 data points for eight different gas-liquid combinations and 22 different tube diameters, covering microscale and macroscale channel from 0.517 to 31.7 mm in diameter. They proposed to different friction factors for macroscale and microscale, respectively. This model is not described here but it is detailed in the article of [Cioncolini et al. (2009)].

3.3.3 Conclusions

This concise review highlights the influence of the flow parameters (mass velocity and vapor quality), the working fluids, the geometry and the saturation conditions. The general trends on the influence of G , x , T_{sat} and d_h on the two-phase pressure drop were clearly determined and are schematically represented on Figs. 3.20, 3.22, and 3.24, respectively. The literature analysis also reveals that there is no distinct trend of variation of pressure drop with these parameters in mini and in microchannels. On the contrary, this review underlines the fact that the two-phase flow regime plays a major role on the pressure drop.

Moreover, no pressure drop data were published for saturation temperature higher than 80°C. Figure 3.28 shows the distribution of data points according to the reduced pressure and saturation temperature for pressure drop studies published since 1980 ([Charnay et al. (2011)]). As can be seen in the figure, there is no data in the saturation temperature range encountered in ORC systems that are the initial motivation of the present PhD thesis.

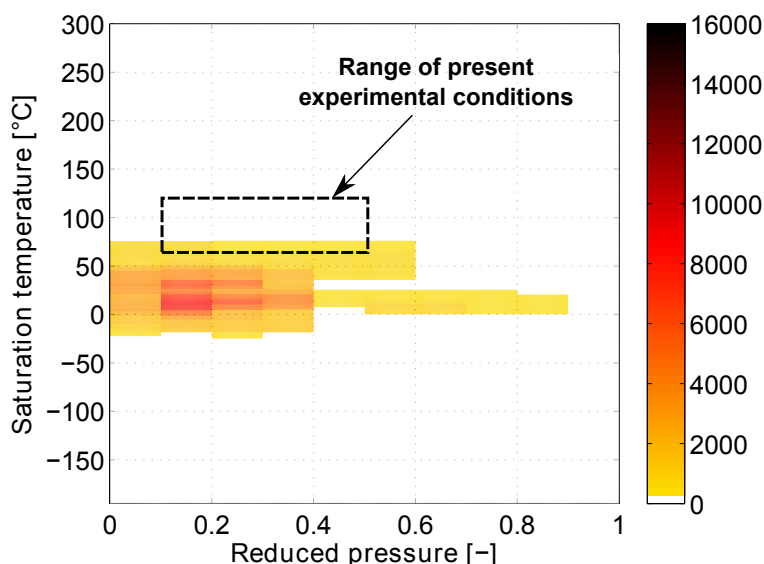


Figure 3.28: Distribution of data points published in 122 articles since 1980 for pressure drop studies with respect to saturation temperature and reduced pressure ([Charnay et al. (2011)]).

In addition, despite numerous theoretical and experimental investigations done in the past, no general model is available to reliably predict two-phase pressure drops. Indeed, these models still have very large standard, mean and average deviations. Figure 3.29 displays a comparison among several two-phase pressure drop prediction methods for R-245fa in a 3.00 mm inner tube diameter at 500 kg/m²·s for two different saturation temperatures: 40°C and 120°C. The discrepancies observed can be explained by considering that two-phase flow includes all the complexities of single-phase flow like non-linearities, transition to turbulence, and instabilities plus additional two-phase characteristics like motion and deformation of the interface and interactions between phases. Moreover, the empirical approach is the most widely used. This approach is restricted by its underlying database whereas the phenomenological approach requires an in-depth knowledge of the flow patterns. In conclusion, it is very risky to extrapolate these methods at saturation temperature higher than 80°C, where no data are available.

This is why, among others, the present PhD thesis aims (i) at providing new pressure drop data at high saturation temperature and (ii) at assessing the existing correlations and models against this new data set. The ranges of reduced pressure and saturation temperature investigated during the present study are represented on Fig. 3.28 with the stippled zone.

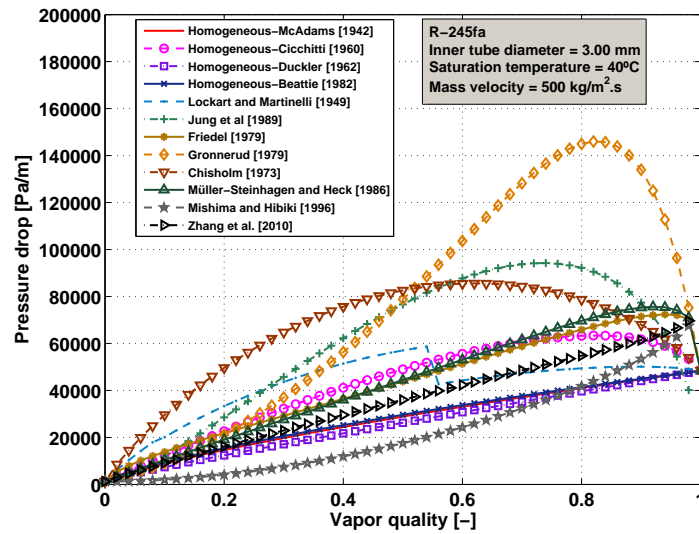
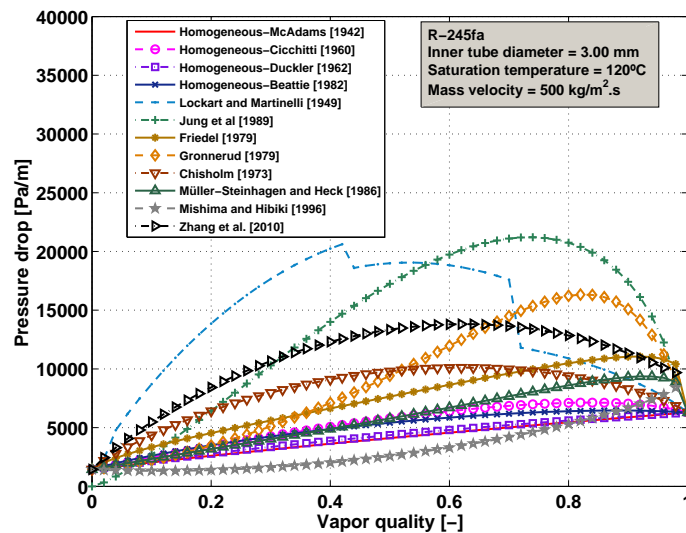
(a) $T_{\text{sat}} = 40^\circ\text{C}$ (b) $T_{\text{sat}} = 120^\circ\text{C}$

Figure 3.29: Comparison among several two-phase pressure drop prediction methods for R-245fa in a 3.00 mm inner tube diameter at $500 \text{ kg/m}^2\cdot\text{s}$ for two different saturation temperatures: 40°C and 120°C .

3.4 Heat transfer coefficient

3.4.1 Experimental studies on flow boiling heat transfer

Experimentally, two mechanisms were assumed to govern flow boiling heat transfer in macrochannels: (i) the nucleate boiling and (ii) the convective boiling. Nucleate boiling is related to the formation of bubbles at the tube wall, whereas, convective boiling is related to conduction and convection through a thin liquid film with evaporation at the liquid-vapor interface. These boiling mechanisms are often assumed when trying to describe flow boiling, for simplicity, to be independent the one from the other. In fact, it is indeed well known (see [Collier and Thome (1994)]) that these mechanisms can coexist when the vapor quality increases.

These mechanisms were experimentally related to the heat transfer coefficient:

- when nucleate boiling is dominant, the heat transfer coefficient is independent of the mass velocity and vapor quality, dependent on the heat flux and sensitive to the saturation pressure level.
- when convective boiling is dominant, the heat transfer coefficient is independent of the heat flux and dependent on the mass flux and vapor quality.
- when both nucleate and convective boiling are of the same order of importance, the heat transfer coefficient is dependent on the heat flux, mass velocity and vapor quality.

A concise summary of experimental researches on two-phase heat transfer coefficients is presented below for different geometries: macrochannels, minichannels and microchannels. Figure 3.19 presents the number of data points published in the open literature (130 articles for 22 refrigerants since 1980) only for refrigerants during flow boiling heat transfer studies. As shown in the figure, R-245fa is ranked as the fourth most studied refrigerant since 1980 (with about 3600 data points) after R-134a, R-410A, and R-22. These figures confirm a resurgence of interest for R-245fa during the last decades.

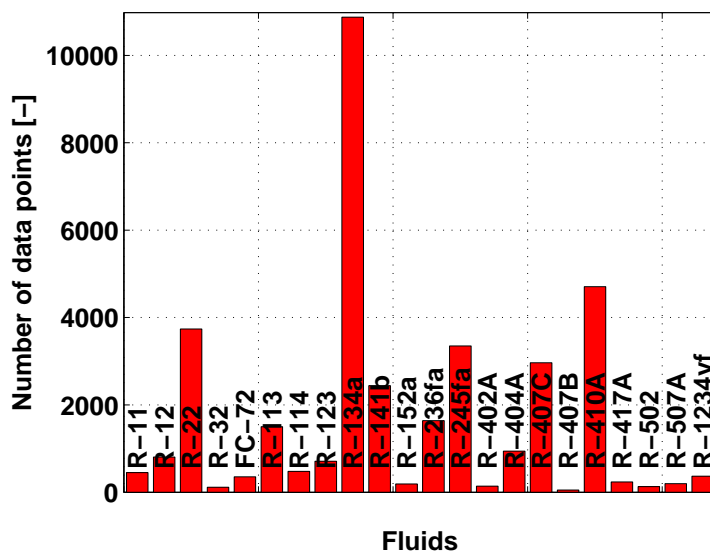


Figure 3.30: Number of flow boiling heat transfer coefficient data points (28416 data points in total) for each refrigerant published in 130 articles since 1980 for flow boiling ([Charnay et al. (2011)]).

The objective is not to describe all the works that were published on this topic but rather to describe those sufficient to illustrate typical trends observed in the literature. This review draws attention to three main points:

- the different mechanisms that govern flow boiling heat transfer.
- the difference between flow boiling heat transfer in macrochannels and microchannels.
- the effect of the temperature on the heat transfer coefficient.

3.4.1.1 Flow boiling heat transfer studies in macrochannels

During the five last decades, flow boiling of refrigerants in tubes has been intensely investigated especially in sight of refrigeration applications. The first part of this review focuses on experimental studies of flow boiling heat transfer in circular macroscale tubes to illustrate the typical trends observed in such geometry. [Hambræus (1991)] reported a heat transfer investigation during flow boiling of R-134a inside a 12.00 inner diameter horizontal tube. The heat transfer coefficients were dependent on mass velocity and heat flux indicating that nucleate boiling and convective boiling were both present.

[Wang et al. (1998)] studied phase-change heat transfer coefficient characteristics for R-22 and R-410A flowing inside a smooth tube with a 6.54 mm inner diameter. They noticed two different trends according to the mass velocity:

- For a mass velocity of $100 \text{ kg/m}^2\cdot\text{s}$, the effect of heat flux was very pronounced for both R-22 and R-410A and the heat transfer coefficients did not increase with the vapor quality. These trends were the clue for a predominance of nucleate boiling in the heat transfer mechanisms.
- For a mass velocity of $400 \text{ kg/m}^2\cdot\text{s}$, the heat transfer coefficients increased with the vapor quality. The flow regime visualized was annular flow pattern and the heat transfer was dominated by convective boiling.

[Kattan et al. (1998b)] presented an experimental study on flow boiling heat transfer for five refrigerants (R-134a, R-123, R-402A, R-404A and R-502) evaporating inside horizontal tubes with two diameters: 12.00 mm and 10.92 mm. They observed a significant increase in the heat transfer coefficient with heat flux. They defined three different trends:

- At low vapor quality (from 8 to 15%), they observed a maximum in heat transfer coefficients which could correspond to a change in flow pattern or a change in the respective contribution of nucleate boiling and convective boiling to the overall heat transfer.
- For intermediate vapor quality, the heat transfer coefficient decreased monotonically with increasing vapor quality at the lowest mass flow rate, in their case $100 \text{ kg/m}^2\cdot\text{s}$.
- At high vapor quality, they observed a decrease of the heat transfer coefficient which was caused by the transition from annular flow to annular flow with partial dry-out.

[Jabardo and Bandarra Filho (2000)] performed experiments on flow boiling in horizontal tube with an inner diameter of 12.7 mm for three refrigerants: R-22, R-134a and R-404A. Figure 3.31 shows their results on the influence of heat flux and mass velocity on the heat transfer coefficient. They also found out new trends in connection to the effects of heat flux and mass velocity. They found that nucleate boiling effects could persist at high vapor quality, especially for higher heat fluxes. They compared their experimental data to the correlations of [Jung et al. (1989)] and [Kandlikar (1990)]. Both correlations overpredicted the experimental heat transfer coefficient.

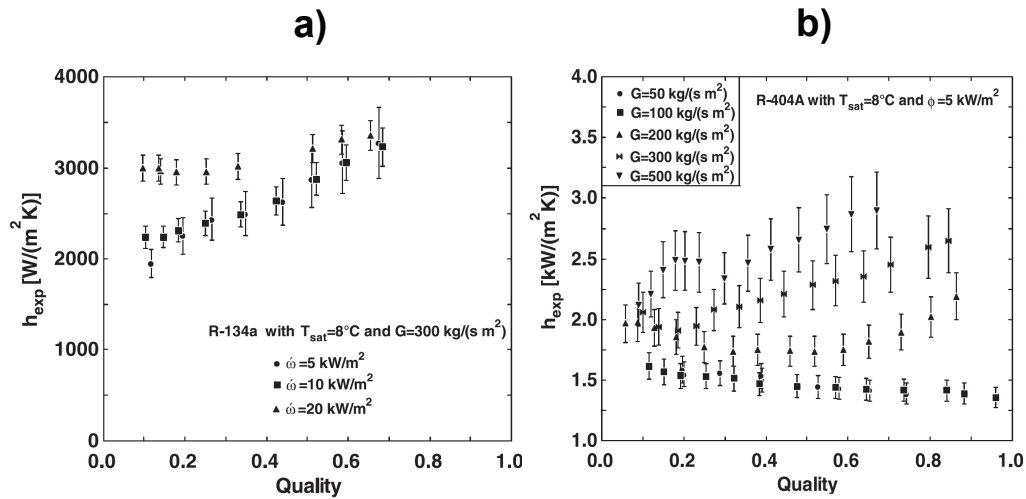


Figure 3.31: Influence of (a) heat flux and (b) mass velocity on the heat transfer coefficient observed by [Jabardo and Bandarra Filho (2000)].

Table 3.8: Summary of experimental flow boiling heat transfer studies in macrochannels.

Author	Fluid	Geometry	d_h [mm]	\dot{q} [kW/m ²]	G [kg/m ² ·s]	T_{sat} [°C]	x [-]	TYPE
[Hambraeus (1991)]	R-134A	circular	12.0	2-10	60-300	-6.0	0-1.0	A
[Wang et al. (1998)]	R-22/R-410A	circular	6.54	2.5-20	100-400	2.0	0-0.95	A
[Ebisu and Torikoshi (1998)]	R-410A/R-22/R-407C	circular	7.0	7.5	150-300	5.0	0-0.9	A
[Kattan et al. (1998b)]	R-134a/R-123/R-402A/R-404A/R-502	circular	10.9 - 12.0	0.4-37.0	100-500	-1.3-30.7	0.02-1.0	A
[Jabardo and Bandarra Filho (2000)]	R-22/R-134a/R-404A	circular	5-20		50-500	8.0 - 15.0	0.05-0.95	A
[Park and Hrnjak (2007)]	CO ₂ /R-410A/R-22	circular	6.1	5-15	100-400	-30.0 - -15.0	0.1-0.8	A

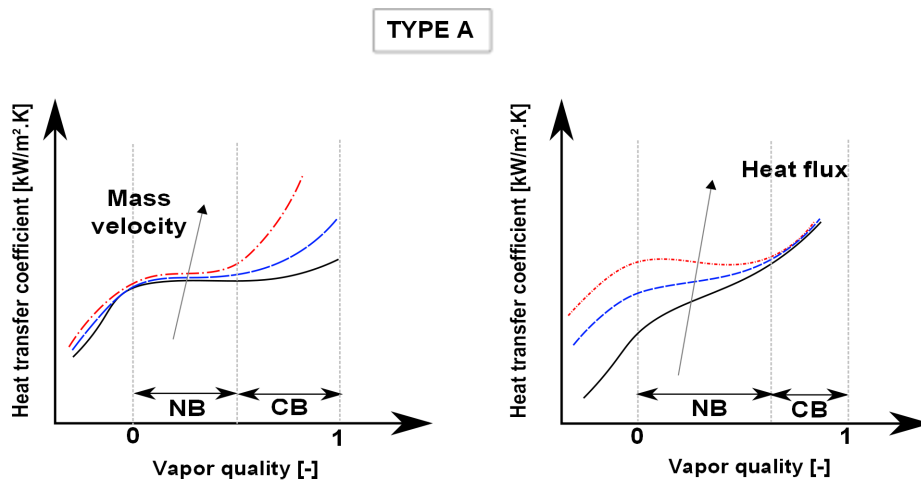


Figure 3.32: Schematic of the typical trends of heat transfer coefficient observed with nucleate and convective boiling dominant regions (NB: Nucleate Boiling and CB: Convective Boiling).

[Park and Hrnjak (2007)] investigated flow boiling heat transfer with R-410A and carbon dioxide in a 6.1 mm inner diameter horizontal smooth tube. The heat transfer trends of carbon dioxide revealed the predominance of nucleate boiling, i.e. dependence upon the heat flux and independence upon the mass velocity and the vapor quality. Nucleate and convective boiling heat transfer mechanisms are active for R-410A flow boiling heat transfer (influence of heat flux, mass flux and quality).

The experimental conditions of these studies are reported in Table 3.8. In conclusion, for macrochannels, nucleate and convective boiling mechanisms are coupled. At low vapor quality, nucleate boiling is dominant whereas at higher vapor quality, convective boiling becomes predominant. Typical representations of the results available in the literature are represented on Fig. 3.32 and this kind of characteristic curve will be referred to as being of “type A” in the following.

3.4.2 Heat transfer studies in mini- and microchannels

Flow boiling heat transfer inside channels having hydraulic diameters smaller than 3 mm, identified here as minichannels, has become in recent years a major research topic in the thermal fluid science field. Most of this interest was driven by the industrial demand for compact devices capable of dissipating extremely high heat flux. Despite the enormous benefits that can represent these minichannels, they are still under development and require deeper investigations. During the last decade, great efforts have been made to identify the main parameters governing microscale flow boiling heat transfer. The upcoming literature review is based on a classification of the dominant heat transfer mechanism: (i) studies with nucleate boiling dominance, (ii) studies showing no predominance of nucleate or convective boiling and (iii) studies with convective boiling dominance.

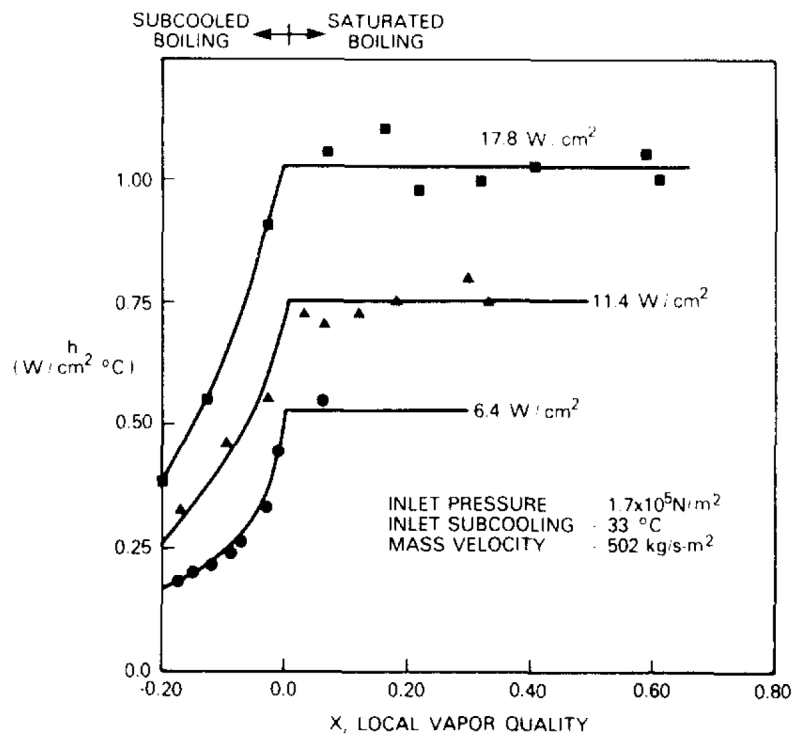


Figure 3.33: Heat transfer coefficient measured by [Lazarek and Black (1982)] as a function of vapor quality for various heat fluxes.

3.4.2.1 Experimental studies with nucleate boiling dominance

[Lazarek and Black (1982)] experimentally investigated R-113 flow boiling heat transfer in a vertical circular channel of 3.1 mm. The experiments indicated that the flow boiling heat transfer coefficient was independent of vapor quality and strongly dependent on heat flux, as shown on Fig. 3.33. They concluded from their results that the nucleate boiling mechanism was dominant during their tests.

The same conclusion was reached by [Tran et al. (1996)], [Bao et al. (2000)], [Lin et al. (2001)], [Yu et al. (2002)], [Choi et al. (2007a)] and [Saisorn et al. (2010b)].

Recently, [Bortolin et al. (2011)] confirmed these features with R-245fa in a 0.96 mm diameter single circular channel at $31^\circ C$. [Ali et al. (2011)] presented an experimental study of flow boiling heat transfer with R-134a in minichannel. The experimental results showed that the heat transfer coefficient increased with heat flux, while mass velocity and vapor quality had no considerable effect.

[Basu et al. (2011)] also investigated flow boiling of R-134a but in horizontal circular microtubes with a diameter ranging from 0.50 mm to 1.60 mm. The measured heat transfer coefficients increased with increasing heat flux and saturation pressure but were independent of mass flux. The effects of vapor quality on heat transfer coefficients were less pronounced and varied depending on the quality.

From flow visualization with a high-speed video camera and a microscope optics, [Kasza et al. (1997)] provided a model of the dominant flow regimes during nucleate boiling in a small horizontal channel. Figure 3.34 shows these flow regimes.

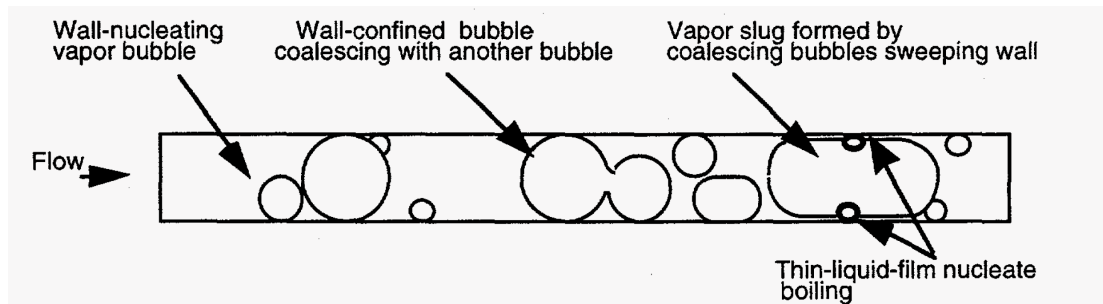


Figure 3.34: Schematic of flow regimes during nucleate boiling in a horizontal small channel proposed by [Kasza et al. (1997)].

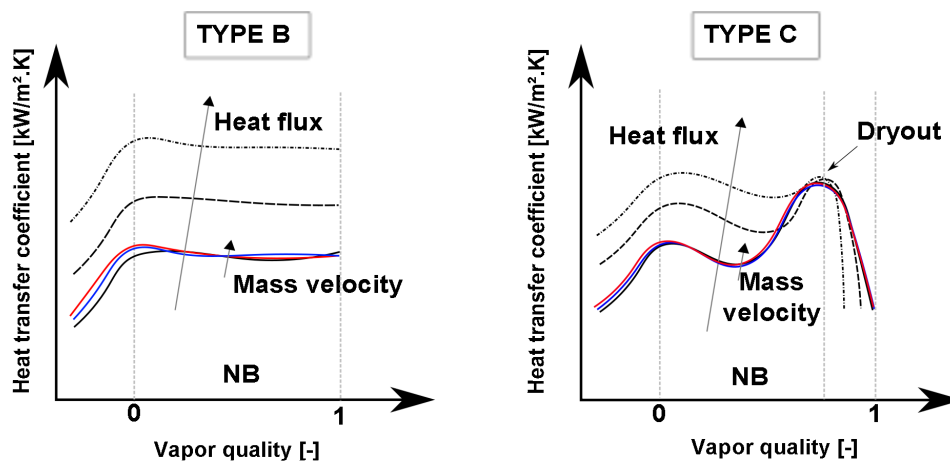


Figure 3.35: Schematic of the typical trends observed for heat transfer coefficient in the case of nucleate boiling dominance (NB: Nucleate Boiling).

From these studies and the graphs they display, two typical curves for the case of nucleate boiling dominance can be drawn, as shown on Fig. 3.35. Two representations are necessary (Fig. 3.35, characteristic curves of type “B” and “C”) to better transcribe the heat transfer coefficient trends in nucleate boiling heat transfer dominant region. Table 3.9 summarizes the experimental conditions as well as the typical curves corresponding to the previous quoted studies. The effects of heat flux and mass velocity are also represented on these graphs.

3.4.2.2 Experimental studies showing both nucleate and convective boiling

[Cornwell and Kew (1993)] conducted experiments in two sets of parallel channels. Their results indicated that the flow boiling in such small channels exhibits fully developed nucleate boiling characteristics in the isolated bubble region at lower qualities. At higher qualities, for annular flow region, convective effects are dominant. These characteristics are similar to those observed for the large diameter tubes.

[Wambsganss et al. (1993)] investigated the flow boiling of R-113 in a 2.92 mm inner diameter tube and observed a heat transfer sensitivity to both heat flux and mass flux. Their results indicated the contributions of both nucleate boiling and convective boiling heat transfer mechanisms.

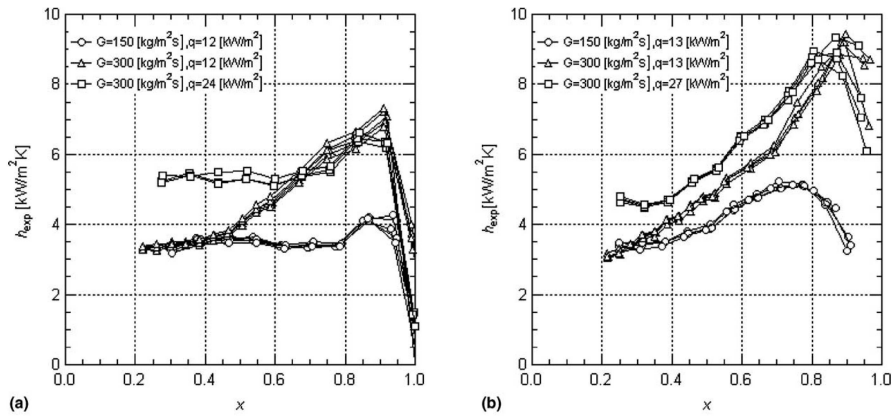


Figure 3.36: Effect of heat flux and mass flux on heat transfer coefficient observed by [Saitoh et al.(2005)] for two different diameter channels: (a) 3.1 mm and (b) 1.12 mm.

[Saitoh et al.(2005)] described an increase of the heat transfer coefficient with increasing mass flux or heat flux indicating the presence of both nucleate and convective boiling mechanisms as represented on Fig. 3.36. They also highlighted the influence of inner diameter: its increase reduced the contribution of forced convective boiling to the heat transfer.

[Ong and Thome (2009)] performed flow boiling heat transfer experiments with R-134a, R-236fa and R-245fa in a 1.03 mm inner diameter circular channel. The local heat transfer coefficients displayed a heat flux and a mass flux dependency.

Table 3.9 summarizes the experimental conditions of the previously quoted works. Figure 3.32 represents the general trends described in this section which are similar to those for macroscale studies. The relation between the type of curve and the original work is also given in Table 3.9.

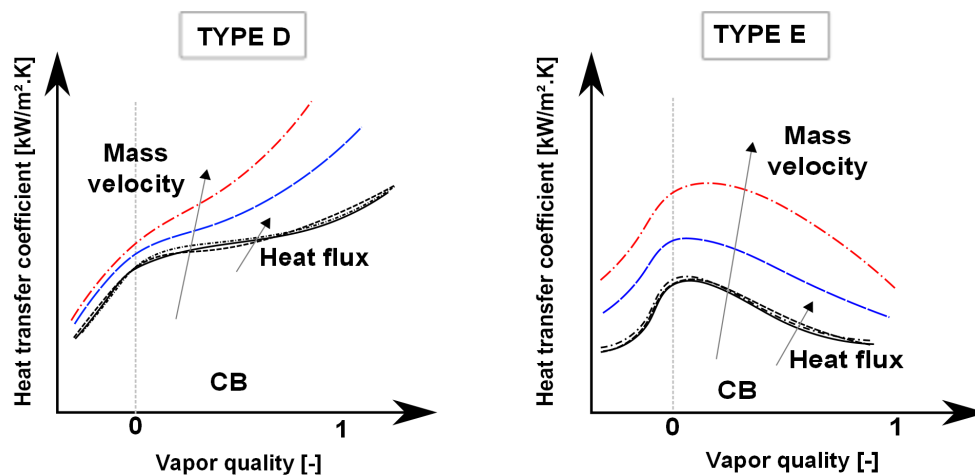


Figure 3.37: Schematic of the typical trends of heat transfer coefficient when convective boiling is dominant (CB: Convective Boiling).

3.4.2.3 Experimental studies with convective boiling dominance

[Lee and Lee (2001)] performed experiments with R-113 during flow boiling through horizontal rectangular channels with low aspect ratios. The quality range was from 0.15 to 0.75 and the flow pattern appeared to be mainly annular. The heat transfer coefficients increased with the mass flux and the local quality, whereas the effect of the heat flux appeared to be minor. Convective boiling was therefore the dominant heat transfer regime.

[Qu and Mudawar (2003)] provided flow boiling heat transfer experiments in microchannel heat sinks for water at 30°C and 60°C. They pointed out the existence of an abrupt transition to annular flow near the point of zero vapor quality and revealed the dominance of convective boiling corresponding to annular flow.

[Ong and Thome (2011b)] completed their first study ([Ong and Thome (2009)]) with two other diameters of 2.20 mm and 3.04 mm for the same refrigerants. Experimentally, they observed that the flow boiling heat transfer coefficients were a significant function of the type of two-phase flow pattern. Furthermore, the monotonically increasing heat transfer coefficients with vapor quality signified convective boiling as the dominant heat transfer mechanism.

For each investigation, the experimental conditions are summarized in Table 3.9. As for the case of nucleate boiling dominance, two representations are necessary to better transcribe the heat transfer coefficient trends when convective boiling heat transfer is dominant (Fig. 3.37, curves of type “D” and “E”).

Table 3.9: Summary of experimental flow boiling heat transfer studies in minichannels and microchannels.

	Author	Fluid	Geometry	d_h [mm]	\dot{q} [kW/m ²]	G [kg/m ² ·s]	T_{sat} [°C]	x [-]	TYPE
Nucleate boiling dominant region	[Lazarek and Black (1982)]	R-113	circular	3.1	14-380	125-750	55-97	0-0.6	/
	[Tran et al. (1996)]	R-12	circ./rect.	2.4	3.6-129	44-832	16-34	0-0.95	B
	[Bao et al. (2000)]	R-11/R-123	circular	1.95	5-200	50-1800	5-15	0-0.9	B
	[Lin et al. (2001)]	R-141b	circ./rect.	1.1-3.6	1-300	50-3500	31-68	0-1.0	C
	[Yu et al. (2002)]	Water	circular	2.98	/	50-200	120	0.15-1.0	B
	[Choi et al. (2007a)]	(*)	circular	1.5-3.0	20-40	200-600	10	0-1.0	C
	[Saisorn et al. (2010b)]	R-134a	circular	1.75	1-83	200-1000	31-50	0-0.95	B
	[Bortolin et al. (2011)]	R-245fa	circular	0.96	5-85	200-400	31	0.05-0.8	C
	[Ali et al. (2011)]	R-134a	circular	1.70	2-156	50-600	27-32	0-1	C
[Basu et al. (2011)]	R-134a	circular	0.5-1.6	0-350	300-1500	15-45	0-1	B	
Nucleate and convective dominant region	[Cornwell and Kew (1993)]	R-141b	circular	1.39-3.69	9.7-90.0	188-1480	/	0-0.95	A
	[Wambsganss et al. (1993)]	R-113	circular	2.92	8.8-90.75	50-300	/	0-0.9	A
	[Saitoh et al.(2005)]	R-134a	circular	0.51-3.1	5-39	150-450	5-15	0.1-1.0	A
	[Ong and Thome (2009)]	(**)	circular	1.03	2.3-250	200-1600	31	0-1.0	A
	[Charnay et al. (2013)]	R-245fa	circular	3.0	10-90	100-1500	60	0-1.0	A
Convective dominant region	[Lee and Lee (2001)]	R-113	rectangular	0.78-3.63	15	50-200	/	0.15-0.75	D
	[Qu and Mudawar (2003)]	Water	rectangular	0.35	/	135-402	104	0-0.2	E
	[Ong and Thome (2011b)]	(**)	channel	1.03-3.04	4.8-221.5	200-1290	31-35	0-1.0	D

(*) R-22/R-134a/CO₂ - (**) R-134a/R-236fa/R-245fa

3.4.2.4 Experimental studies on the influence of saturation temperature

Liquid-vapor phase-change phenomena at high saturation temperatures present specificities that are due to high vapor density, low surface tension, high vapor viscosity and low liquid viscosity. These conditions lead to flow boiling heat transfer characteristics quite different from those of conventional data (presented here-above). A few recent papers reported data on the influence of saturation temperature.

[[Greco and Vanoli \(2005\)](#)] investigated flow boiling heat transfer characteristics for R-410A and R-404A with saturation temperatures ranging from -15°C to 23.5°C and from -15°C to 15°C , respectively. Their experimental results indicated that for both fluids the heat transfer coefficients increased with increasing the saturation temperature for a constant mass velocity. For higher saturation temperature and low vapor quality regions, they observed also a decrease of the heat transfer coefficient with increasing vapor quality. For higher vapor quality region, the heat transfer coefficient increased again. In conclusion, the heat transfer coefficient resulted from the interaction between nucleate boiling and convective boiling.

[[Da Silva Lima et al. \(2009\)](#)] presented heat transfer results for R-134a at three saturation temperatures (5 , 10 and 15°C) flowing in a 6.00 mm inner diameter tube. At low vapor quality, they observed the same trends as those of [[Greco and Vanoli \(2005\)](#)] with a decrease of the heat transfer coefficients with the vapor quality. They noted the existence of a local minimum vapor quality, x_{\min} , which results of the competition between nucleate and convective boiling mechanisms. The local minimum vapor quality corresponded to their transition from slug flow regime to intermittent flow regime. After this minimum, the heat transfer coefficients increased until dryout inception indicating convective boiling dominant region.

[[Del Col \(2010\)](#)] focused on flow boiling of halogenated refrigerants at high saturation temperature in a horizontal tube. The database was characterized by saturation temperatures ranging from 25°C to 45°C . He observed that the experimental trends of heat transfer coefficients versus vapor quality were dependent on fluid and experimental conditions (especially the saturation temperature). The heat transfer coefficient increased with vapor quality (for R-134a), was roughly constant (for R-134a, R-22 and R-125) or even decreased with vapor quality (R-410A). Moreover, at lower vapor quality, the higher the saturation temperature, the larger the heat transfer coefficient, while, at higher vapor quality, the difference between high and low saturation temperature decreased and the curves merged together, as shown on Fig. 3.38. Similarities between R-410A and carbon dioxide heat transfer data were discussed in his work.

[[Tibiricá and Ribatski \(2010\)](#)] provided flow boiling heat transfer results for R-134a and R-245fa with saturation temperatures of 22 , 31 and 41°C . They found that the heat transfer coefficient was a strong function of heat flux, mass velocity and vapor quality. They confirmed the influence of saturation temperature observed in the previous study. With R-245fa, they noted that the heat transfer coefficient increased with saturation temperature for a larger vapor quality range. Other studies reported the same trends on the impact of saturation temperature: [[Agostini et al. \(2008\)](#)], [[Vakili-Farahani et al. \(2013\)](#)], [[Ong and Thome \(2011b\)](#)], [[Basu et al. \(2011\)](#)], [[Ali et al. \(2011\)](#)] and [[Grauso et al. \(2013\)](#)].

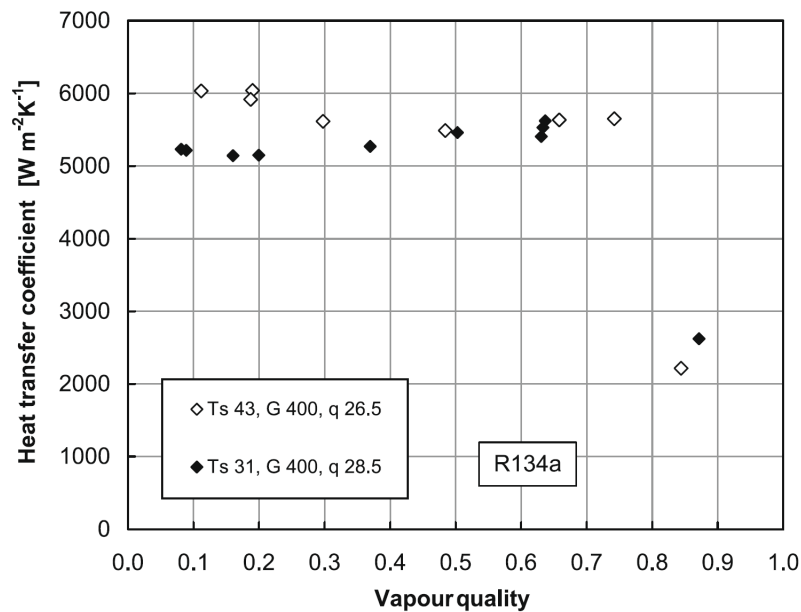


Figure 3.38: Influence of saturation temperature on the heat transfer coefficient with R-134a in a 8.0 mm inner diameter channel. From [Del Col (2010)].

At the opposite, [Saisorn et al. (2010b)] observed a decrease of the heat transfer coefficients with increasing saturation temperature across their experimental range of vapor quality as shown on Fig. 3.39. They studied flow boiling of R-134a in a circular minichannel with an inner diameter of 1.75 mm for three different saturation temperatures of 31, 40 and 50°C. They called for a physical explanation that an increase of saturation temperature contributes to a thinner liquid film on the tube wall which can be easily broken. A similar trend regarding the effect of the saturation temperature on heat transfer coefficients was also reported by [Choi et al. (2007b)] (for carbon dioxide) and [Kaew-On and Wongwises (2009)] (for R-410A with saturation temperature ranging from 10 to 30°C).

These two different trends are schematically represented with typical curves on Fig. 3.40 where the curves of type “F” correspond to papers reporting an increase of the heat transfer coefficient with increasing saturation temperature, whereas the curve of type “G” correspond to the opposite trends. For each paper, this information is reported as well as the experimental conditions in Table 3.10.

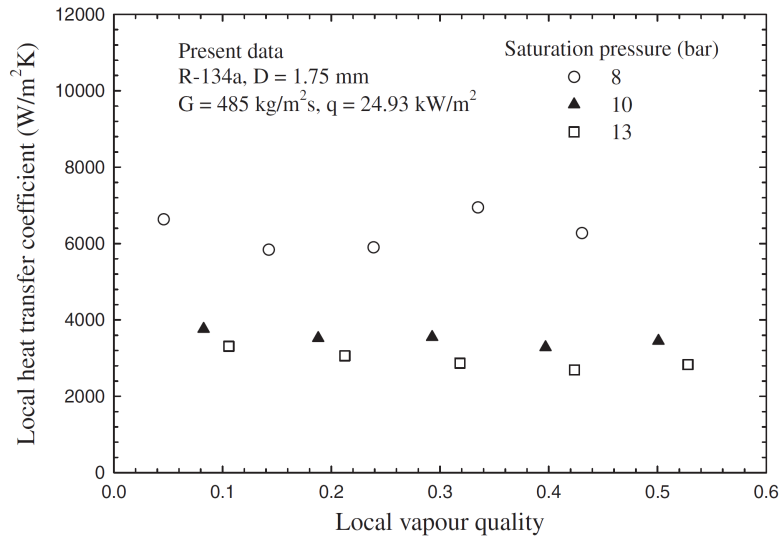


Figure 3.39: Influence of saturation temperature on the heat transfer coefficient. From [Saisorn et al. (2010b)].

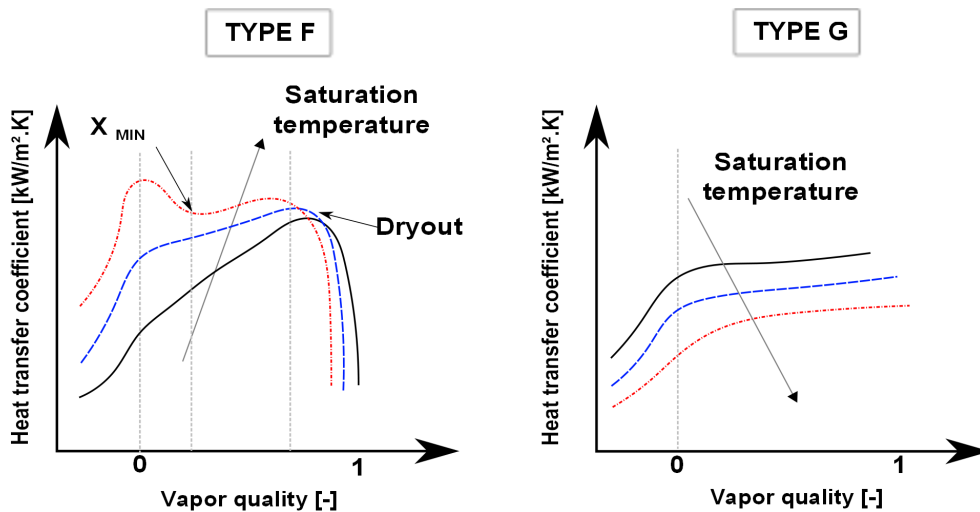


Figure 3.40: Schematic of the typical heat transfer coefficient trends with the influence of saturation temperature.

Table 3.10: Summary of experimental flow boiling heat transfer studies on the influence of saturation temperature.

Author	Fluid	Geometry	d_h [mm]	\dot{q} [kW/m ²]	G [kg/m ² ·s]	T_{sat} [°C]	x [-]	TYPE
[Greco and Vanoli (2005)]	R-410A/R-404A	circular	6.0	11-39	290-1100	-15-23.5	0-1.0	F
[Da Silva Lima et al. (2009)]	R-134a	circular	13.84	7.5-17.5	300-500	5-20	0.01-0.99	F
[Del Col (2010)]	(*)	circular	8.0	9-53	200-600	25-45	0-1.0	F
[Tibiricá and Ribatski (2010)]	R-134a/R-245fa	circular	2.3	5-55	50-700	31-68	0.05-0.99	F
[Agostini et al. (2008)]	R-245fa	rectangular	0.336	36-1900	281-1501	24-44	0.15-1.0	F
[Vakili-Farahani et al. (2013)]	R-245fa/R-1234ze	rectangular	1.3-1.45	3-107	50-400	30-70	0-1.0	F
[Ong and Thome (2011b)]	(**)	channel	1.03-3.04	4.8-221.5	200-1290	31-35	0-1.0	F
[Ali et al. (2011)]	R-134a	circular	1.70	2-156	50-600	27-32	0-1.0	F
[Basu et al. (2011)]	R-134a	circular	0.5-1.6	0-350	300-1500	15-45	0-1.0	F
[Grauso et al. (2013)]	CO ₂ /R-410A	circular	6.0	5-20	150-500	5-42	0-1.0	F
[Saisorn et al. (2010b)]	R-134a	circular	1.75	1-83	200-1000	31-50	0-0.95	G
[Choi et al. (2007b)]	CO ₂	circular	1.5-3	20-40	200-600	-10-10	0-1.0	G
[Kaew-On and Wongwises (2009)]	R-410A	rectangular	3.48	5-14.25	200-400	10-30	0-1.0	G

(*) R-22/R-134a/R-125/R-410A - (**) R-134a/R-236fa/R-245fa

3.4.3 Two-phase flow boiling heat transfer prediction methods

In spite of the enormous number of research works undertaken to date, the prediction of flow boiling heat transfer coefficients remains essentially empirical due to the complex hydrodynamic and heat transfer processes. A number of methods have been developed to predict the heat transfer coefficient in horizontal and vertical smooth tubes for natural and synthetic refrigerants. A summary of an extensive literature survey on flow boiling heat transfer prediction models or correlations will be presented below. Firstly, the prediction models and correlations will be classified into two groups: (i) pre-dryout and (ii) post-dryout heat transfer prediction methods.

Then, for pre-dryout, prediction methods will be classified according to their theoretical background as follows:

- asymptotic approach
- Nusselt-type correlations
- enhancement-factor approach
- phenomenological approach

Several pool boiling correlations are also included in the pre-dryout methods.

For post-dryout heat transfer, fewer prediction models or correlations are available, they will hence all be grouped together. Moreover, some prediction methods developed exclusively or not for carbon dioxide will be evaluated for both pre-dryout and post-dryout regions.

3.4.3.1 Pre-dryout heat transfer prediction methods

The pre-dryout region gathers intermittent flow and annular flow regimes and ends by the inception of the dryout at the top of the tube at the location where the heat transfer coefficient begins to decrease sharply.

3.4.3.1.1 Pool boiling correlations

[[Bertsch et al. \(2008\)](#)] proposed an assessment of several predictive correlations by comparing them against 10 independent data sets from the published literature covering a range of hydraulic diameter from 0.16 to 2.01 mm. They found that the correlation of [[Cooper \(1984\)](#)] provided the lowest deviation between predictions and measurements for their database and that the correlation of [[Gorenflo\(1993\)](#)] resulted in smaller deviations from the experimental database than most of the flow boiling correlations. This is remarkable in view of the fact that these correlations were developed specifically for pool boiling and do not contain any effects of mass velocity or vapor quality. They concluded by noting that these good agreements could indicate a dominance of the nucleate boiling heat transfer mechanism. Moreover, several published works, such as those of [[Gungor and Winterton \(1986\)](#)], [[Liu and Winterton \(1991\)](#)], [[Yun et al. \(2005\)](#)], and [[Bertsch et al. \(2009\)](#)] recommended the correlation of [[Cooper \(1984\)](#)] for nucleate flow boiling.

Comparisons between experimental results and the heat transfer coefficients predicted by pool boiling correlations appear to be promising and have to be performed. Nucleate pool boiling correlations are generally formulated as follows:

$$\alpha_{\text{nb}} \propto \dot{q}^n \quad (3.92)$$

[Stephan and Abdelsalam (1980)] proposed four specific correlations according to the following fluid classes: water, organics, refrigerants and cryogenes. The organic fluid correlation is the most widely quoted:

$$\alpha_{\text{nb}} = 0.0546 \cdot \left[\left(\frac{\rho_V}{\rho_L} \right)^{1/2} \cdot \left(\frac{\dot{q} \cdot d_{\text{bubbles}}}{\lambda_L \cdot T_{\text{sat}}} \right) \right]^{0.67} \cdot \left(\frac{h_{\text{LV}} \cdot d_{\text{bubbles}}^2}{a_L^2} \right)^{0.248} \cdot \left(\frac{\rho_L - \rho_V}{\rho_L} \right)^{-4.33} \cdot \left(\frac{\lambda_L}{d_{\text{bubbles}}} \right) \quad (3.93)$$

[Cooper (1984)] proposed a form of pool boiling correlation including the molecular mass of the fluid (M) and the reduced pressure ($P_{\text{red}} = P/P_{\text{crit}}$). The [Cooper (1984)] correlation covers reduced pressure from 0.001 to 0.9. The expression of this correlation is:

$$\alpha_{\text{nb}} = 55 \cdot P_{\text{red}}^{0.12} \cdot (-\log_{10} P_{\text{red}})^{-0.55} \cdot M^{-0.5} \cdot \dot{q}^{0.67} \quad (3.94)$$

[Gorenflo(1993)] proposed a correlation to specifically include the effect of reduced pressure and that also included the effect of surface roughness expressed as follows:

$$\alpha_{\text{nb}} = \alpha_0 \cdot F_{\text{PF}} \cdot \left(\frac{\dot{q}}{\dot{q}_0} \right)^{0.9-0.3 \cdot P_{\text{red}}^{0.3}} \cdot \left(\frac{R_p}{R_{p0}} \right)^{0.133} \quad (3.95)$$

where F_{PF} is a pressure correction factor and R_p is the surface roughness.

[Jung et al. (2003)] developed a correlation based upon the database obtained for eight pure refrigerants (R-123, R-11, R-142b, R-134a, R-12, R-22, R-125, and R-32) following both the Cooper and the Stephan and Abdelsalam approaches. The final form of the correlation is:

$$\alpha_{\text{nb}} = 10 \cdot \left(\frac{\lambda_L}{d_{\text{bubbles}}} \right) \cdot \left[\frac{\dot{q} \cdot d_{\text{bubbles}}}{\lambda_L \cdot T_{\text{sat}}} \right]^{C_1} \cdot P_{\text{red}}^{0.1} \cdot (1 - T_{\text{red}})^{-1.4} \cdot \left(\frac{\nu_L}{a_L} \right)^{-0.25} \quad (3.96)$$

In Eq. (3.96), ν_L is the liquid kinetic viscosity, a_L is the liquid thermal diffusivity and T_{red} is the reduced temperature (T/T_{crit}). The exponent C_1 is calculated by:

$$C_1 = 0.855 \cdot \left(\frac{\rho_V}{\rho_L} \right)^{0.309} \cdot P_{\text{red}}^{-0.437} \quad (3.97)$$

[Ribatski and Jabardo (2003)] introduced the surface roughness and material effects into a correlation for nucleate pool boiling of halocarbon refrigerants (R-11, R-123, R-12, R-134a, and R-22). The reduced pressure ranged from 0.008 to 0.260. Three materials were considered: copper, brass and stainless steel.

$$\alpha_{\text{nb}} = B \cdot \left(\dot{q}^{0.9-0.3 \cdot P_{\text{red}}^{0.2}} \right) \cdot P_{\text{red}}^{0.45} \cdot [-\log(P_{\text{red}})]^{-0.8} \cdot R_p^{0.2} \cdot M^{-0.5} \quad (3.98)$$

where B is an empirical constant accounting for wall material effect.

[Yun et al. (2005)] generated a pool boiling heat transfer correlation specific to carbon dioxide from a power law form of heat flux and reduced pressure.

3.4.3.1.2 Asymptotic approach

In the asymptotic approach, flow boiling models consider two heat transfer mechanisms to be important: (i) nucleate boiling heat transfer (α_{nb}) and (ii) convective boiling heat transfer (α_{cb}). These two main heat transfer mechanisms are combined to obtain the heat transfer coefficient (α_{TP}) in the following power law form:

$$\alpha_{TP} = [(\alpha_{nb})^n + (\alpha_{cb})^n]^{1/n} \quad (3.99)$$

[Chen (1963)] and [Chen (1966)] proposed the first flow boiling model for evaporation in vertical tubes. He assumed a simple addition of the respective contribution by setting $n=1$ but introduced two dimensionless factors, a nucleate boiling suppression factor (S) and a two-phase multiplier factor (F). The model is expressed as:

$$\alpha_{TP} = S \cdot \alpha_{nb} + F \cdot \alpha_L \quad (3.100)$$

The suppression factor accounts for the smaller effective superheat due to forced convection as compared to that in a nucleate pool boiling, hence the nucleation of boiling sites is partially suppressed and the contribution of nucleate boiling is reduced. The factor F reflects the increase in convective heat transfer contribution due to the presence of vapor phase. The nucleate pool boiling correlation of [Forster and Zuber (1955)] is used to calculate α_{nb} as:

$$\alpha_{nb} = 0.00122 \cdot \left[\frac{\lambda_L^{0.79} \cdot c_{p,L}^{0.45} \cdot \rho_L^{0.49}}{\sigma^{0.5} \cdot \mu_L^{0.29} \cdot h_{LV}^{0.24} \cdot \rho_V^{0.24}} \right] \cdot \Delta T_{sat}^{0.24} \cdot \Delta P_{sat}^{0.75} \quad (3.101)$$

whereas the single-phase heat transfer (α_L) is calculated by the turbulent flow correlation of [Dittus and Boetler (1930)] defined as:

$$\alpha_L = 0.023 \cdot \text{Re}_L^{0.8} \cdot \text{Pr}_L^{0.4} \cdot \left(\frac{\lambda_L}{d_h} \right) \quad (3.102)$$

A modified form of this boiling model was developed by [Gungor and Winterton (1986)] from a large database of 3693 points from the literature including data for R-11, R-12, R-22, R-113, R-114 and water. They replaced the enhancement factor (F) by a two-phase convection multiplier (E) which is dependent upon the boiling number (Bo) and the Lockhart-Martinelli parameter (X). The suppression factor (S) is correlated as a function of the Lockhart-Martinelli parameter and the liquid Reynolds number (Re_L). They introduced S_{hor} and E_{hor} which take into account the orientation of the tube. The expression for α_{TP} is:

$$\alpha_{TP} = S \cdot S_{hor} \cdot \alpha_{nb} + E \cdot E_{hor} \cdot \alpha_L \quad (3.103)$$

From the previous model, [Del Col (2010)] proposed a tool for practical applications from his database obtained for flow boiling of halogenated refrigerants at high saturation temperature (from 25°C to 45°C) in a horizontal smooth tube. He proposed to multiply the heat transfer calculated by the model of [Gungor and Winterton (1986)] by a factor of 1.2.

[Kandlikar (1990)] expressed the two-phase flow boiling heat transfer coefficient as the larger value of the convective and the nucleate boiling contributions. He used the Boiling number (Bo) to represent the nucleate boiling contribution

and not a pool boiling correlation. The single-phase heat transfer coefficient considering the liquid phase flowing alone in the tube (α_{LO}) is used in the following expressions to predict the nucleate boiling and convective boiling components:

$$\alpha_{TP,nb} = \left(0.6683 \cdot C_V^{-0.2} \cdot (1-x)^{0.8} \cdot f_2(Fr_{LO}) + 1058.0 \cdot Bo^{0.7} \cdot (1-x)^{0.8} \cdot F_f \right) \cdot \alpha_{LO} \quad (3.104)$$

$$\alpha_{TP,cb} = \left(1.136 \cdot C_V^{-0.9} \cdot (1-x)^{0.8} \cdot f_2(Fr_{LO}) + 667.2 \cdot Bo^{0.7} \cdot (1-x)^{0.8} \cdot F_f \right) \cdot \alpha_{LO} \quad (3.105)$$

where F_f is the fluid-dependent parameter and Fr_{LO} is the Froude number considering the liquid phase flowing alone in the complete cross-section of the tube. C_V is the convective number defined as:

$$C_V = \left(\frac{1-x}{x} \right)^{0.8} \cdot \left(\frac{\rho_V}{\rho_L} \right)^{0.5} \quad (3.106)$$

α_{LO} is calculated from the [Gnielinski (1976)] correlation as:

$$\alpha_{LO} = \frac{(f_F/8) \cdot (Re_{LO} - 1000) \cdot Pr_L}{1 + 12.7 \cdot (f_F/8)^{1/2} \cdot (Pr_L^{2/3} - 1)} \cdot \left(\frac{\lambda_L}{d_h} \right) \quad (3.107)$$

with f_F is the Fanning friction factor.

The [Chen (1963)] model is based on the assumption that two-phase flow convective heat transfer can be described by the [Dittus and Boetler (1930)] correlation. The validity of this assumption is quite questionable when used for other conditions since the [Dittus and Boetler (1930)] correlation is applicable only for turbulent flow.

[Lee and Lee (2001)] re-examined the Chen process to predict the heat transfer coefficient for the laminar flow in rectangular minichannels. They modified the multiplier factor (F) as a function of the aspect ratio and the two-phase frictional multiplier calculated by [Lockhart and Martinelli (1949)].

[Kandlikar and Balasubramanian (2004)] modified the [Kandlikar (1990)] model to circular minichannels by using the laminar single-phase heat transfer coefficient for all liquid flow and the nucleate boiling as the dominant part of the original model.

In the same spirit, [Zhang et al. (2004)] modified the Chen model to extend it to a wide range of flow conditions, e.g. liquid-laminar and gas-turbulent such as often occurs in minichannels. They proposed another definition of the factor F as a function of the two-phase friction multiplier defined by [Chisholm (1967)] (ϕ_L^2) whereas, initially, [Chen (1963)] defined this factor as a function of the turbulent-turbulent Lockhart-Martinelli parameter. The general form proposed by [Chen (1963)] was expressed as:

$$F = 1 + C \cdot \left(\frac{1}{X} \right)^n \quad (3.108)$$

where the Lockhart-Martinelli parameter is calculated by:

$$X = \left(\frac{f_L}{f_V} \right)^{0.5} \cdot \left(\frac{1-x}{x} \right) \cdot \left(\frac{\rho_V}{\rho_L} \right)^{0.5} \quad (3.109)$$

[Zhang et al. (2004)] provided another expression of F as a function of the turbulent two-phase friction multiplier (ϕ_L^2) leading to:

$$F = C \cdot (\phi_L^2)^m \quad (3.110)$$

In Eq. (3.110), ϕ_L^2 is calculated by a general form for four conditions according to [Chisholm (1967)]:

$$\phi_L^2 = 1 + \frac{C}{X} + \frac{1}{X^2} \quad (3.111)$$

In Eq. (3.111), the values of the Chisholm parameter (C) depends on liquid-vapor flow conditions and X .

For laminar flow, the convective heat transfer correlation of [Dittus and Boetler (1930)] was replaced by a single-phase laminar flow equation. The authors used the correlation of [Forster and Zuber (1955)] to calculate the nucleate pool boiling coefficient.

[Choi et al. (2007a)] proposed a boiling heat transfer coefficient model from a database obtained with R-22, R-134a, and carbon dioxide. Using the model of [Zhang et al. (2004)], they replaced the factors S and F with the following expressions:

$$F = 0.042 \cdot \phi_L^2 + 0.958 \quad (3.112)$$

$$S = 469.1689 \cdot (\phi_L^2)^{-0.2093} \cdot Bo^{0.7402} \quad (3.113)$$

They modified the Lockhart-Martinelli parameter to take into account the important effect of quality, density ratio and viscosity ratio:

$$X = \left(\frac{\mu_L}{\mu_V} \right)^{1/8} \cdot \left(\frac{1-x}{x} \right)^{7/8} \cdot \left(\frac{\rho_V}{\rho_L} \right)^{1/2} \quad (3.114)$$

[Choi et al. (2007b)] proposed a specific carbon dioxide flow boiling heat transfer coefficient model based on their database. In both studies proposed by Choi et al., the [Dittus and Boetler (1930)] correlation was used to determine the liquid heat transfer coefficient (α_{LO}) and the [Cooper (1984)] correlation for the nucleate boiling heat transfer coefficient. They defined two coefficients F and S for the specific carbon dioxide prediction method.

[Saitoh et al. (2007)] modified the model of [Chen (1963)] to predict the flow boiling heat transfer coefficient of R-134a over a wide range of tube diameters. They used a vapor Weber number (We_V) to take into account the effect of tube diameter on the fluid flow conditions. They used the [Stephan and Abdelsalam (1980)] correlation to calculate α_{nb} . They proposed another expression of factor F for forced convective boiling heat transfer expressed as:

$$F = 1 + \frac{(1/X)^{1.05}}{1 + We_V^{0.4}} \quad (3.115)$$

The factor S for suppression of nucleate boiling is expressed as a function of Re_{TP} defined as $Re_{TP} = Re_L \cdot F^{1.25}$:

$$S = \frac{1}{1 + 0.4 \cdot (Re_{TP} \cdot 10^{-4})^{1.4}} \quad (3.116)$$

Table 3.11: Experimental conditions used to develop the asymptotic models with $n = 2$ (see Eq. (3.92)) (A: annuli, C: circular, H: horizontal R: rectangular, and V: vertical).

Reference	Fluid	Geometry	d_h [mm]	P_{sat} [bar]	T_{sat} [°C]	G [kg/m ² ·s]	\dot{q} [kW/m ²]	x [-]
[Chen (1963)]	water, methanol, cyclohexane, pentane, heptane, benzene	V - C	/	0.55-34.8	/	/	/	0.01-0.71
[Gungor and Winterton (1986)]	water, R-12, R-22, R-11, R-113, R-114, ethylen glycol	V,H - A,C	2.95-32	0.08-202.6	-0.7-365	12.4-61518	0.35-91534	0-1
[Kandlikar (1990)]	water, R-11, R-12, R-22, R-113, R-114, R-152, neon, nitrogen	V,H - C	4.6-32	0.4-64.2	/	13-8179	0.0003-2.28	0-0.99
[Kandlikar and Balasubramanian (2004)]	R-113, R-141b, R-123	H, V - C	0.19-2.92	/	/	50-300	5.46-90.75	0-0.98
[Lee and Lee (2001)]	R-113	H - R	0.8-3.6	/	/	50-200	15	0.15-0.75
[Zhang et al. (2004)]	water, R-11, R-12, R-113	H, V - C, R	0.78-6	1.01-12.1	34-190	23.4-2939	2.95-2511	/
[Choi et al. (2007a)]	R-22, R-134a, carbon dioxide	H - C	1.5-3.0	4.15-45.0	10	200-600	10-40	0-1
[Choi et al. (2007b)]	carbon dioxide	H - C	1.5-3.0	26.5 - 45.0	-10 - 10	200-600	10-40	0-1
[Saitoh et al. (2007)]	R-134a	H - C	0.51-3.1	3.5-4.9	5-15	150-450	5-39	0.2-1
[Pamitran et al. (2007)]	R-410A	H - C	1.5-3.0	10.95	10	300-600	10-30	0-1
[Bertsch et al. (2009)]	water, R-134a, R-236fa, R-245fa, R-11, R-123, R-134a, FC-77, R-113, R-141b, nitrogen, R-12	H, V - C, R	0.16-2.91	/	-194 - 97	20-3000	0-115	0-1
[Ducoulombier et al. (2011)]	carbon dioxide	H - C	0.529	26.5 - 34.8	-10 - 0	200-1200	10-30	0-1
[Fang (2013)]	carbon dioxide	H - C	0.529 - 7.75	10 - 67	-30 - 28.6	97.5 - 1400	3.93 - 40	0-1

[Pamitran et al. (2007)] developed a boiling heat transfer prediction model for R-410A. They specifically took into account the mass transfer resistance during convective boiling and the mixture effect on nucleate boiling as this refrigerant is a binary mixture.

[Bertsch et al. (2009)] proposed a heat transfer model for saturated flow boiling in small channels. They used Eq. (3.94) to calculate α_{nb} and replaced α_L by $\alpha_{L,TP}$ calculated as:

$$\alpha_{L,TP} = \alpha_L \cdot (1 - x) + \alpha_L \cdot x \quad (3.117)$$

In Eq. (3.117), α_L is calculated from the [Hausen (1943)] correlation for developing laminar flow. They chose a formulation for the suppression factor considering a linear decrease of the nucleate boiling heat transfer coefficient with increasing the vapor quality and expressed as:

$$S = 1 - x \quad (3.118)$$

They modified also the enhancement factor F leading to the following expression:

$$\alpha_{TP} = \alpha_{nb} \cdot (1 - x) + \alpha_{cb,TP} \cdot \left[1 + 80 \cdot (x^2 - x^6) \cdot e^{-0.6 \cdot Co} \right] \quad (3.119)$$

More recently, [Ducoulombier et al. (2011)] developed a prediction model for carbon dioxide flow boiling heat transfer coefficient. The heat transfer coefficient corresponds to the larger value of the heat transfer coefficient corresponding to convective boiling (α_{cb}) or the heat transfer coefficient referring to nucleate boiling (α_{nb}). Their expressions for α_{cb} and α_{nb} are given by:

$$Bo > 1.1 \cdot 10^{-4} : \alpha_{cb} = \left(1.47 \cdot 10^4 \cdot Bo + 0.93 \cdot \left(\frac{1}{X} \right)^{2/3} \right) \cdot \alpha_L \quad (3.120)$$

$$Bo < 1.1 \cdot 10^{-4} : \alpha_{cb} = \left(1 + 1.80 \cdot \left(\frac{1}{X} \right)^{0.986} \right) \cdot \alpha_L \quad (3.121)$$

$$\alpha_{nb} = 131 \cdot P_{red}^{-0.0063} \cdot (-\log_{10} P_{red})^{-0.55} \cdot M^{-0.5} \cdot \dot{q}^{0.58} \quad (3.122)$$

Based on their carbon dioxide database of 2956 experimental data points, [Fang (2013)] developed a new carbon dioxide specific model which is given as:

$$\alpha_{TP} = \frac{0.00061 \cdot (S + F) \cdot Re_L \cdot Fa^{0.11} \cdot Pr_L^{0.4}}{\ln \left(\frac{1.024 \cdot \mu_{L,f}}{\mu_{L,w}} \right)} \quad (3.123)$$

They proposed two factors (S and F) and defined a new dimensionless number (Fa) expressed as:

$$Fa = \frac{(\rho_L - \rho_V) \cdot \sigma}{G^2 \cdot d_h} \quad (3.124)$$

This dimensionless number is associated with the formation and departure of bubbles.

Table 3.11 summarizes the experimental conditions for the development of the asymptotic models developed with $n = 2$ (see Eq. (3.92)).

Table 3.12: Experimental conditions used to develop the asymptotic models with $n = 3$ (see Eq. (3.92)) (A: annuli, C: circular, H: horizontal R: rectangular, and V: vertical).

Reference [-]	Fluid [-]	Geometry [-]	d_h [mm]	P_{sat} [bar]	T_{sat} [°C]	G [kg/m ² ·s]	\dot{q} [kW/m ²]	x [-]
[Kutateladze (1961)]	water	/	/	/	/	/	/	/
[Liu and Winterton (1991)]	water, R-12, R-22, R-11, R-113, R-114, ethylen glycol, butanol, ethanol	H - C, A	2.95-32	/	/	12-8180	0.34-2620	0-0.948
[Yoon et al. (2004)]	carbon dioxide	H - C	7.53	31.3 - 57.3	-4 - 20	200 - 530	12 - 20	0-0.7

[Kutateladze (1961)] used $n = 2$ for the weighting between both contribution. This method has the feature over the simple addition method that nucleate boiling is further suppressed once the convective boiling contribution ($F \cdot \alpha_{cb}$) is appreciably larger than the nucleate boiling contribution ($S \cdot \alpha_{nb}$).

$$\alpha_{TP} = \left[(S \cdot \alpha_{nb})^2 + (F \cdot \alpha_{cb})^2 \right]^{1/2} \quad (3.125)$$

In Eq. (3.125), α_{nb} and α_{cb} are calculated by the correlations of [Dittus and Boetler (1930)] and [Cooper (1984)], respectively. [Liu and Winterton (1991)] used this approach and modified the factors (F and S) to provide a flow boiling model for vertical and horizontal flow in tubes and annuli. [Yoon et al. (2004)] adapted the factors for carbon dioxide flow boiling.

Table 3.12 summarizes the range of experimental conditions used during the development of the asymptotic models based on $n = 3$ (see Eq. (3.92)).

[Steiner and Taborek (1992)] proposed a prediction model of the heat transfer coefficient during flow boiling in vertical tubes from an asymptotic approach using an exponent n equal to 3. This model was developed from data obtained for flow boiling in vertical circular channels of several refrigerants: water, R-11, R-12, R-22, R-113, benzene, n-pentane, n-heptane, cyclohexane, methanol, ethanol, n-butanol, nitrogen, hydrogen, helium, and ammonia.

$$\alpha_{TP} = \left[(S \cdot \alpha_{nb})^3 + (F \cdot \alpha_{cb})^3 \right]^{1/3} \quad (3.126)$$

3.4.3.1.3 Enhancement-factor approach

[Schrock and Grossman (1962)] developed a correlation based on a fit of their data points for water in a vertical tube. This correlation is based on an enhancement ratio Ψ that refers to single-phase heat transfer coefficient of flowing liquid:

$$\Psi = \frac{\alpha_{TP}}{\alpha_{LO}} \quad (3.127)$$

In this equation, the correlation of [Dittus and Boetler (1930)] is used to calculate α_{LO} with the liquid only Reynolds number (Re_{LO}). For saturated flow boiling in vertical and horizontal tubes, [Shah (1982)] proposed another enhancement correlation with another mode of calculation of the two-phase enhancement factor given by:

$$\Psi = \frac{\alpha_{TP}}{\alpha_L} = \max(\Psi_{nb}, \Psi_{cb}) \quad (3.128)$$

[Shah (1982)] defined a dimensionless number N which is used to determine the appropriate set of equations to calculate Ψ_{nb} and Ψ_{cb} .

3.4.3.1.4 Nusselt-type correlations

[Lazarek and Black (1982)] proposed an empirical prediction method for the heat transfer coefficient during flow boiling in a minichannel. The heat transfer coefficient was expressed with a Nusselt-type correlation, i.e. as a function of the liquid only Reynolds number and the Boiling number. They correlated their 728 saturated boiling heat transfer coefficient measurements using a least squares data fitting algorithm to obtain the following form:

$$\alpha_{TP} = 30 \cdot \text{Re}_{LO}^{0.857} \cdot \text{Bo}^{0.714} \cdot \left(\frac{\lambda_L}{d_h} \right) \quad (3.129)$$

This prediction method is independent of the vapor quality. Indeed, nucleate boiling was the predominant heat transfer mechanism during the experiments (independence from the vapor quality).

[Tran et al. (1996)] developed a correlation with the same approach from their data points for the nucleate boiling dominant heat transfer region (selection of their data with a wall superheat larger than 2.75 K). In this correlation, Re_{LO} is replaced with the Weber number (We) to eliminate viscous effects in favor of surface tension as:

$$\alpha_{TP} = 840000 \cdot (\text{Bo}^2 \cdot We_L)^{0.3} \cdot \left(\frac{\rho_L}{\rho_V} \right)^{-0.4} \quad (3.130)$$

[Warrier et al. (2002)] compared is heat transfer data for FC-84 to the correlations of [Lazarek and Black (1982)], [Kandlikar (1990)], [Liu and Winterton (1991)] and [Tran et al. (1997)]. The latter was the only one able to show a correct trend (a decrease of the heat transfer coefficient with increasing vapor quality) but the correlation did not correctly predict the two-phase heat transfer coefficient. Therefore, they proposed another correlation expressed as a function of Boiling number (Bo) and the liquid single-phase heat transfer coefficient (α_L):

$$\alpha_{TP} = \left(1 + 6 \cdot \text{Bo}^{1/16} - 5.3 \cdot (1 - 855 \cdot \text{Bo}) \cdot x^{0.65} \right) \cdot \alpha_L \quad (3.131)$$

[Sun and Mishima (2009)] developed a correlation based on the [Lazarek and Black (1982)] correlation, taking into account the effect of Weber number:

$$\alpha_{TP} = \frac{6 \cdot \text{Re}_{LO}^{1.05} \cdot \text{Bo}^{0.54}}{\text{We}_{LO}^{0.191} \cdot (\rho_L/\rho_V)^{0.142}} \cdot \frac{\lambda_L}{d_h} \quad (3.132)$$

Besides, [Kew and Cornwell (1997)] modified the [Lazarek and Black (1982)] correlation to adapt it to their database where convective boiling is the dominant heat transfer mechanism (highlighted by the dependence of the heat transfer coefficient on the vapor quality). Their correlation is expressed as a function of the liquid only Reynolds number (Re_{LO}), the Boiling number (Bo) and the vapor quality (x):

$$\alpha_{TP} = 30 \cdot \text{Re}_{LO}^{0.857} \cdot \text{Bo}^{0.714} \cdot \left(\frac{1}{1-x} \right)^{0.143} \cdot \left(\frac{\lambda_L}{d_h} \right) \quad (3.133)$$

Table 3.13 summarizes the experimental conditions for the development of these Nusselt-type correlations.

3.4.3.1.5 Phenomenological approach

[Kattan et al. (1998b)] developed a phenomenological model based on the two-phase flow structure. To determine the flow structure, they used their own two-phase flow pattern map for horizontal evaporating flows. The model covers fully stratified flows, stratified-wavy flows, intermittent flows, annular flows and annular flows with partial dryout. Plug and slug flows are classified as intermittent flows. This model does not predict the two-phase flow boiling heat transfer for bubbly flow and mist flow regimes. The heat transfer coefficients are calculated

from the evaluation of wet and dry perimeters, which are geometrically related to the flow structure:

$$\alpha_{TP} = \frac{d_h \cdot \theta_{dry} \cdot \alpha_V + d_h \cdot (2\pi - \theta_{dry}) \cdot \alpha_{wet}}{2 \cdot \pi \cdot d_h} \quad (3.134)$$

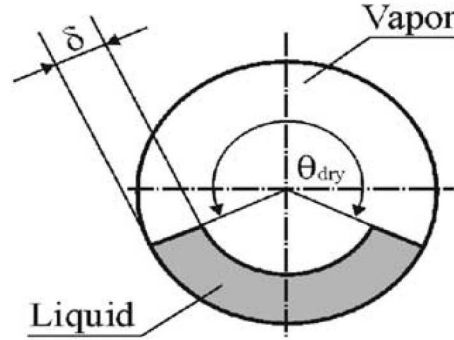


Figure 3.41: Annular flow with partial dry-out by [Thome et al. (2004a)].

In eq. (3.134), the heat transfer coefficient is viewed as a weighted average of two heat transfer coefficients, namely one for the area of the tube which is dry and one for the area which is wet shown on Fig 3.41. Here, α_V is the vapor heat transfer coefficient calculated from the [Dittus and Boetler (1930)], while α_{wet} is the heat transfer coefficient for the liquid fluid calculated from an asymptotic expression using an exponent of three.

θ_{dry} is the angle of the tube wall that is assumed to be constantly dry for stratified flows and annular flows with partial dryout. For annular and intermittent flows, the tube perimeter is always wet and the dry angle is equal to 0. The authors proposed a dry angle value for the stratified flow before the dryout inception and another for the region after the dryout inception.

α_{wet} is calculated with the following asymptotic expression that combines the nucleate boiling and convective boiling contributions:

$$\alpha_{wet} = (\alpha_{nb}^3 + \alpha_{cb}^3)^{1/3} \quad (3.135)$$

The correlation of [Cooper (1984)] is used to calculate the nucleate boiling heat transfer coefficient. Besides, [Kattan et al. (1998b)] proposed from their database a correlation to predict the convective boiling heat transfer coefficient assuming the annular ring of liquid more realistically as a film flow rather than as a tubular flow:

$$\alpha_{cb} = 0.0133 \cdot \left[\frac{4 \cdot G \cdot (1-x) \cdot \delta}{(1-\epsilon) \cdot \mu_L} \right]^{0.69} \cdot \left[\frac{c_{p,L} \cdot \mu_L}{\lambda_L} \right]^{0.4} \cdot \frac{\lambda_L}{\delta} \quad (3.136)$$

In Eq. (3.136), ϵ is the void fraction predicted by the drift flux void fraction model of [Rouhani and Axelsson (1970)] for vertical tubes that was modified by [Steiner (1993)] for horizontal tubes. δ is the annular liquid film thickness.

Table 3.13: Experimental conditions used to develop the Nusselt-type correlations (A: annuli, C: circular, H: horizontal R: rectangular, and V: vertical).

Reference [-]	Fluid [-]	Geometry [-]	d_h [mm]	P_{sat} [bar]	T_{sat} [°C]	G [kg/m ² ·s]	\dot{q} [kW/m ²]	x [-]
[Lazarek and Black (1982)]	R-113	V - C	3.1	1.3-4.1	55-97	125-750	14-380	0-0.6
[Tran et al. (1997)]	R-12, R-113	H - C, R	2.4-2.92	5.1-8.2	16-33	44-832	3.6-129	0-0.94
[Yu et al. (2002)]	water	H - C	2.98	2	120	50-200	10-300	0.15-1
[Warrier et al. (2002)]	FC-84	H - R	0.75	/	/	557-1600	0-60	0.03-0.55
[Sun and Mishima (2009)]	water, carbon dioxide, R-11, R-12, R-123, R-134a, R-141b, R-22, R-404a, R-407c, R-410a	H, V - C, R	0.21-6.5	/	/	44-1500	5-109	0-1
[Kew and Cornwell (1997)]	R-141b	H - C	1.39-3.69	/	/	/	/	/

[Thome and El Hajal (2004c)] updated the heat transfer model of [Kattan et al. (1998b)] to the case of flow boiling of carbon dioxide in horizontal tubes. They found necessary to first correct the nucleate pool boiling correlation to better describe the behavior of CO₂ at high reduced pressures and secondly to include a boiling suppression factor on the nucleate boiling heat transfer coefficient to capture the trends in the flow boiling data. [Thome and El Hajal (2004c)] modified the [Kattan et al. (1998b)] model by replacing Eq. (3.135) with the following expression:

$$\alpha_{\text{wet}} = \left((S \cdot \alpha_{\text{nb,CO}_2})^3 + \alpha_{\text{cb}}^3 \right)^{1/3} \quad (3.137)$$

In Eq. (3.137), $\alpha_{\text{nb,CO}_2}$ is determined from the [Cooper (1984)] pool boiling correlation as:

$$\alpha_{\text{nb,CO}_2} = 0.71 \cdot \alpha_{\text{nb}} + 3970 \quad (3.138)$$

The boiling suppression factor S was determined from their whole carbon dioxide database resulting in the following expression:

$$S = \frac{(1-x)^{1/2}}{0.121 \cdot \text{Re}_L^{0.225}} \quad (3.139)$$

[Wojtan et al. (2005b)] extended the model of [Kattan et al. (1998b)] from their database and their flow pattern map. The previous model did not predict the heat transfer coefficient for stratified-wavy flow with accuracy. In consequence, stratified-wavy region was divided into three subzones: slug, slug/stratified-wavy and stratified-wavy. They proposed equations to calculate the dry angle for these three subzones.

[Thome et al. (2004a)] and [Dupont et al. (2004)] presented a phenomenological model to predict the two-phase flow boiling heat transfer coefficient during intermittent flows in microchannels. They proposed a model for flow boiling which is interpreted as a sequence of three steps as represented on Fig. 3.42 (this model is referred to as “three zones model”). At a given location, the process proceeds as follows: (i) a liquid slug passes, (ii) an evaporating elongated bubble passes and (iii) if the thin evaporating film of the bubble dries out before the arrival of the next liquid slug, then a vapor slug passes.

The cycle then repeats itself upon arrival of the next liquid slug. Thus, either a liquid slug and elongated bubble pair or a liquid slug, elongated bubble and vapor slug triplet passes at this given point at a frequency that is a function of the formation rate of bubbles upstream. The heat transfer coefficient is expressed as a time-average of the successive heat transfer coefficients for the three passages:

$$\alpha_{\text{TP}}(z) = \frac{t_L}{\tau} \cdot \alpha_L(z) + \frac{t_{\text{film}}}{\tau} \cdot \alpha_{\text{film}}(z) + \frac{t_V}{\tau} \cdot \alpha_V(z) \quad (3.140)$$

In Eq. (3.140), α_L and α_V are calculated from an expression of the mean heat transfer coefficient as a function of Reynolds number using the [Churchill and Usagi (1972)] asymptotic method with $n=4$. The three zone model has three adjustable parameters which are difficult to predict theoretically: (i) δ_{min} , the minimum thickness of the liquid film at dryout, (ii) C_{δ_0} , a correction factor on the prediction of the initial film thickness δ_0 and (iii) f , the pair frequency.

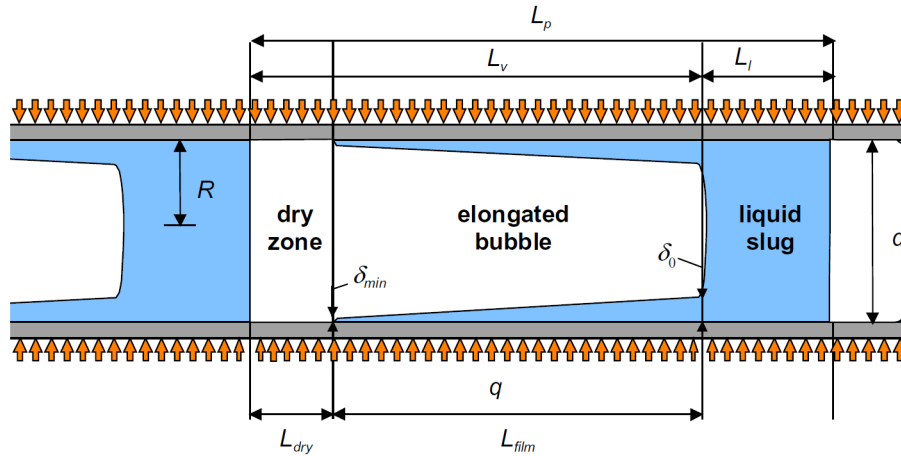


Figure 3.42: Three-zone heat transfer model for elongated bubble flow regime in microchannels developed by [Thome et al. (2004a)].

[Cioncolini and Thome (2011)] provided an algebraic model of turbulence in adiabatic and evaporative annular two-phase flow, focusing in particular on momentum and convective boiling heat transfer through the annular liquid film. This turbulence model is part of unified annular flow modeling suite that includes methods to predict the entrained liquid fraction and the fractional pressure gradient (see [Cioncolini and Thome (2010a)], [Cioncolini et al. (2010b)] and [Cioncolini and Thome (2012a)]).

Table 3.14 presents the ranges of experimental conditions used to develop these models based on the phenomenological approach.

3.4.3.2 Dryout and post-dryout prediction methods

The regime of post-dryout heat transfer is encountered when the heated wall becomes dry before complete evaporation, i.e. during dryout and mist flow regimes. Figure 3.11 shows a representation of these flow regimes. Empirical methods for predicting heat transfer in these flow regimes have been reported. On the one hand, some prediction methods can be classified as simple modifications of single-phase heat transfer correlation ([Dittus and Boetler (1930)] or [Gnielinski (1976)]). [Dougall and Roshenow (1963)] proposed the following correlation to predict the heat transfer coefficient only in mist flow regime assuming homogeneous flow:

$$\alpha_{TP} = 0.023 \cdot \text{Re}_{V,H}^{0.8} \cdot \text{Pr}_V^{0.4} \cdot \frac{\lambda_V}{d_h} \quad (3.141)$$

In Eq. (3.141), $\text{Re}_{V,H}$ is the homogeneous vapor Reynolds number. [Groeneveld (1973)] corrected the homogeneous approach where the definition of the Reynolds number is not consistent with homogeneous flow theory. [Groeneveld (1973)] added a multiplying factor y defined as:

$$y = 1 - 0.1 \cdot \left[\left(\frac{\rho_L}{\rho_V} - 1 \right) \cdot (1 - x) \right]^{0.4} \quad (3.142)$$

The final expression for two-phase flow boiling heat transfer coefficient during mist flow proposed by [Groeneveld (1973)] is:

$$\alpha_{TP} = 0.00327 \cdot \left(\frac{G \cdot d_h}{\mu_V} \cdot \left[x + \frac{\rho_V}{\rho_L} \cdot (1 - x) \right] \right)^{0.901} \cdot \text{Pr}_V^{1.32} \cdot y^{-1.50} \cdot \frac{\lambda_V}{d_h} \quad (3.143)$$

[Ünal and Gasselt (1983)] conducted experiments on post-dryout heat transfer in a non-uniformly heated steam generator tube. Based on the experimental database and existing literature data on uniformly heated tubes, they provided a correlation for the estimation of post-dryout heat transfer coefficient. More recently, [Sindhuja et al. (2010)] modified the [Ünal and Gasselt (1983)] correlation in order to better fit their database for ternary refrigerant mixtures.

[Wojtan et al. (2005b)] extended the model of [Kattan et al. (1998b)] from their database and their flow pattern map for both dryout and mist flow regimes. Based on their experimental data, [Wojtan et al. (2005b)] modified the correlation of [Groeneveld (1973)] for the prediction of the mist flow heat transfer coefficients during evaporation of refrigerants as follows:

$$\alpha_{TP,mist} = 0.0117 \cdot \text{Re}_{V,H}^{0.79} \cdot \text{Pr}_V^{1.06} \cdot y^{-1.83} \cdot \frac{\lambda_V}{d_h} \quad (3.144)$$

For the dryout region, the heat transfer coefficient decreases sharply and then becomes nearly constant in value for mist flow, they proposed the linear interpolation equation to calculate the heat transfer coefficient:

$$\alpha_{TP,dryout} = \alpha_{TP}(x_{di}) - \frac{x - x_{di}}{x_{de} - x_{di}} \cdot [\alpha_{TP}(x_{di}) - \alpha_{TP,mist}(x_{de})] \quad (3.145)$$

In Eq. (3.145), x_{di} and x_{de} are the vapor qualities for the dryout inception and completion, respectively. $\alpha_{TP}(x_{di})$ is the heat transfer coefficient calculated by Eq. (3.134) at dryout inception vapor quality. $\alpha_{TP,mist}(x_{de})$ is the heat transfer coefficient determined by Eq. (3.144) at the completion dryout vapor quality.

Besides, [Saitoh et al. (2007)] proposed a correlation to predict the heat transfer coefficient in the post-dryout region based on the summation of two terms: (i) the heat transfer coefficient by the [Dittus and Boetler (1930)] correlation in the vapor phase (α_V) and (ii) the pre-dryout heat transfer coefficient in the liquid phase calculated by the [Saitoh et al. (2007)] correlation ($\alpha_{TP,pre}$).

$$\alpha_{TP,mist} = (1 - A_{dryout}) \cdot \alpha_{TP,pre} + A_{dryout} \cdot \alpha_V \quad (3.146)$$

In Eq. (3.146), A_{dryout} is the ratio of the dry portion around the entire perimeter of the tube.

[Yoon et al. (2004)] developed a correlation to predict the post-dryout heat transfer coefficient for carbon dioxide flow boiling. They estimated the heat transfer coefficient after the critical quality as the sum of the liquid and vapor heat transfer coefficients for the wet and dry portion so.

Table 3.15 summarizes the experimental conditions for the development of these correlations and models for post-dryout heat transfer coefficient.

Table 3.14: Experimental conditions used to develop the prediction models based on the phenomenological approach (A: annuli, C: circular, H: horizontal R: rectangular, and V: vertical).

Reference [-]	Fluid [-]	Geometry [-]	d_h [mm]	P_{sat} [bar]	T_{sat} [°C]	G [kg/m ² ·s]	\dot{q} [kW/m ²]	x [-]
[Kattan et al. (1998b)]	R-134a, R-402A, R-404A, R-502, R-123, R-407C, ammonia	H - C	10.92 - 12	1.12 - 8.87	-1.3 - 30.7	16.3 - 500	440 - 71600	0.01 - 0.1
[Thome and El Hajal (2004c)]	carbon dioxide	H - C	0.19 - 10.06	17 - 64	-25 - 25	85 - 1440	5 - 36	0 - 0.91
[Wojtan et al. (2005b)]	R-22, R-410A	H, C	8 - 13.84	5.84-9.34	5	70-700	2-57.5	0.01-0.99
[Thome et al. (2004a)]	R-113, R-12, R-134a, R-11, R-123, R-141b, carbon dioxide	H - C, R	0.77-3.1	1.24-57.66	5.23-81.59	50-564	5-178	0.01-0.99
[Cioncolini and Thome (2011)]	R-22, R-32, R-134a, R-290, R-600a, water, R-12, R-245fa	H, V - C	1.03 - 14.4	1 - 72	/	123 - 3925	3 - 736	0.19-0.94

3.4.4 Conclusions

In conclusion, the first part of this section allowed to show that heat transfer mechanisms are strongly dependent on the flow parameters (mass velocity, heat flux and vapor quality), the working fluid, the geometry and the saturation temperature. It clearly appears that (i) heat transfer is driven by two main mechanisms: nucleate boiling and convective boiling and (ii) there are no data available for saturation temperature higher than 100°C. Figure 3.43 shows from a color scale the number of data points available in the literature as a function of the reduced pressure and saturation temperature. This graph highlights the lack of information for saturation temperature higher than 100°C.

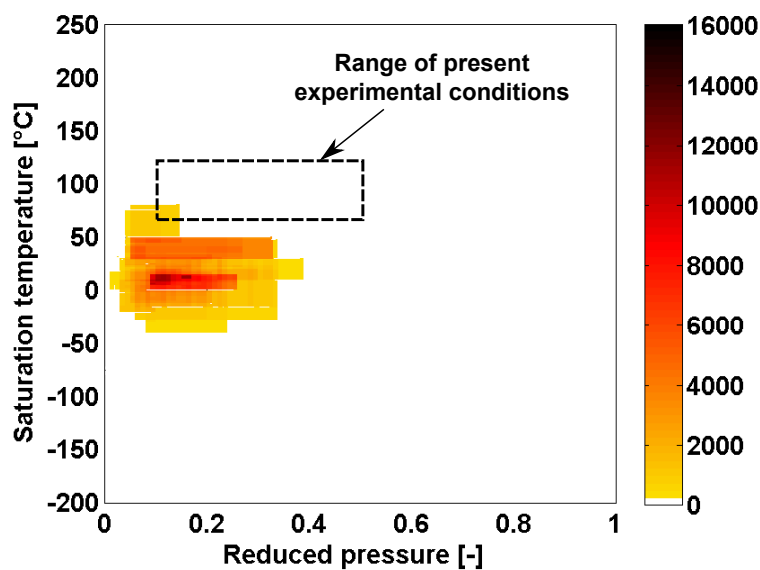


Figure 3.43: Distribution of data points published (28416 data points) in 130 articles since 1980 for heat transfer studies with respect to saturation temperature and reduced pressure([Charnay et al. (2011)]).

The second part permitted to present a state-of-the-art on two-phase phase flow boiling heat transfer predictions tools. It is clearly shown that almost all the correlations or models remain essentially empirical due to the complex hydrodynamic and heat transfer processes. The Tables 3.11, 3.12, 3.13, 3.14, and 3.15 emphasized that the range of applicability of these tools does not exceed 100°C. Figure 3.44 displays a comparison between several flow boiling heat transfer prediction methods for R-245fa in a 3.00 mm inner diameter tube at 500 kg/m²·s and 50 kW/m² for two different saturation temperatures: 40°C and 120°C. These graphs highlight the discrepancies which can exist from one method to another. Figure 3.44(b) shows that these discrepancies increase when these methods are extrapolated up to high saturation temperature.

The main objective of this investigation is to provide accurate data on flow boiling heat transfer coefficient at high saturation temperatures to better understand the relative importance of the various heat transfer mechanisms in these conditions and to assess the correlations and models at high saturation temperature. The ranges of reduced pressure and saturation temperature during the experiments are represented on Fig. 3.43 with the stippled zone.

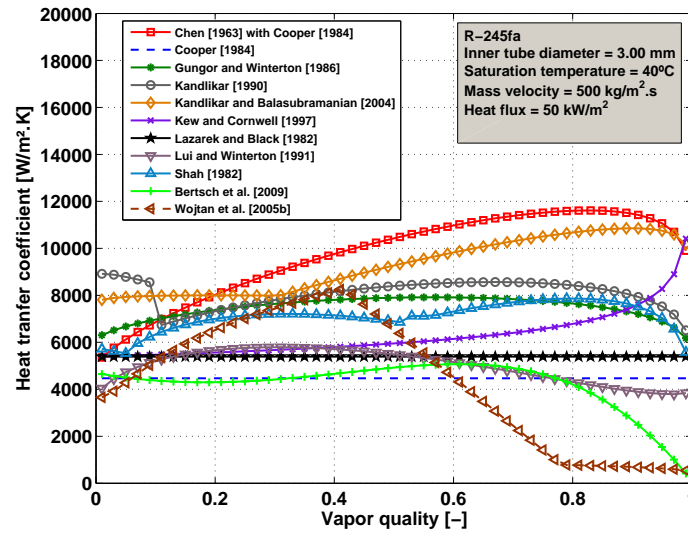
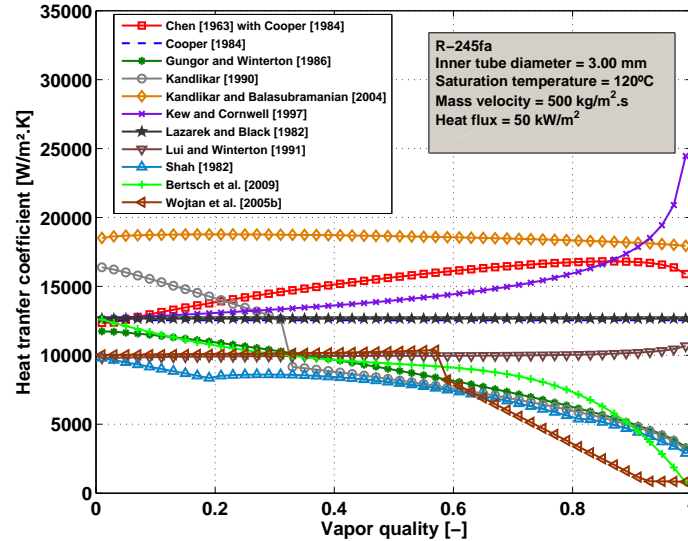
(a) $T_{\text{sat}} = 40^{\circ}\text{C}$ (b) $T_{\text{sat}} = 120^{\circ}\text{C}$

Figure 3.44: Comparison among several flow boiling heat transfer prediction methods for R-245fa in a 3.00 mm inner tube diameter at 500 kg/m².s and 50 kW/m² for two different saturation temperatures: 40°C and 120°C.

3.5 Conclusions on the state-of-the-art review

A state-of-the-art review related to the existing studies on flow visualization, flow pattern map, pressure drop, and heat transfer during flow boiling of refrigerants has been carried out. Each section, previously presented, draws up its own conclusion available in sections 3.2.4, 3.3.3, and 3.4.4, respectively. The effect of the high saturation temperature has, so to say, never been studied so far for T_{sat} higher than 100°C. However, some works investigated the influence of saturation temperature on flow boiling. With their limited range of saturation temperature, the authors concluded by noting that the two-phase flow patterns and their transitions, the two-phase flow pressure drop, and the two-phase flow boiling heat transfer coefficients were strongly influenced by the saturation temperature.

In addition, this literature review enables the elaboration of the research plan in order to answer to the problem of the evaporator design of the Organic Rankine Cycle:

- Development of a quantitative method coupled with a method of analysis of heat transfer coefficient to characterize the flow regimes.
- Visualization of the flow patterns and drawing of flow pattern maps.
- Measurements of the pressure drop, parametric analysis, assessment of the existing correlations and models for two-phase pressure drop, and analysis of their domains of applicability.
- Measurements of the heat transfer coefficient, parametric analysis, assessment of the existing correlations and models for two-phase flow boiling heat transfer coefficient, and analysis of their domains of applicability.

Table 3.15: Experimental conditions used to develop the prediction correlations and models for post-dryout heat transfer coefficient (A: annuli, C: circular, H: horizontal R: rectangular, and V: vertical).

Reference [-]	Fluid [-]	Geometry [-]	d_h [mm]	P_{sat} [bar]	T_{sat} [°C]	G [kg/m ² ·s]	\dot{q} [kW/m ²]	x [-]
[Dougall and Roshenow (1963)]	/	/	/	/	/	/	/	/
[Groeneveld (1973)]	/	V, H - A, C	2.5 - 25	34 - 215	/	700 - 5300	120 - 2100	0 - 0.9
[Ünal and Gasselt (1983)]	/	V - C, A	/	/	/	/	/	/
[Wojtan et al. (2005b)]	R-22, R-410A	H, C	8 -13.84	5.84-9.34	5	70-700	2-57.5	0.01-0.99
[Saitoh et al. (2007)]	R-134a	H - C	0.51-3.1	3.5-4.9	5-15	150-450	5-39	0.2-1
[Yoon et al. (2004)]	carbon dioxide	H - C	7.53	31.3 - 57.3	-4 - 20	200 - 530	12 - 20	0-0.7
[Sindhuja et al. (2010)]	R-407C	V - C	12.7	17 - 35	/	1200 - 2000	50 - 80	0.22 - 0.73

Chapter 4

Description of the experiments

This chapter describes the conceptualization, construction, components assembly and commissioning of the experimental setup used during the present PhD work. It was built in such a way that flow visualizations, flow boiling heat transfer coefficient measurements, and two-phase flow pressure drop measurements could be done on the same system. In parallel, an image processing method to characterize the two-phase flow regimes, to determine the bubbles frequency and to measure the velocity of bubbles was developed.

4.1 Description of the experimental test facility

An experimental test facility was developed in order to control the fluid characteristics at inlet of the test sections, i.e. mass flow rate, inlet subcooling and saturation pressure.

The working fluid is R-245fa as one motivation behind the present work lies in Organic Rankine Cycles. This refrigerant exhibits a high stability and high critical point ($T_{\text{crit}}=154.05$ °C and $P_{\text{crit}}=36.4$ bar) so that it may be boiled at relatively high temperature. Although R-245fa is non-ozone depleting (due to its lack of chlorine) and therefore regarded as “environmentally friendly”, R-245fa is however a global warming gas with a global warming potential (GWP) of 950-1020 $\text{kg}_{\text{eq.CO}_2}/\text{kg}$. Table 4.1 summarizes the main properties of R-245fa. Previous studies promoted to use R-245fa as operating fluid in ORC systems. For instance, [Zhang et al. (2011)] ranked R-245fa as one of the best operating fluids for ORC systems according to the thermal efficiency and exergy efficiency. Besides, considering safety levels and environmental impacts, [Wang et al. (2011)] defined R-245fa as the most suitable working fluids for an engine waste heat recovery application.

Table 4.1: R-245fa properties (ALT: Atmosphere Life Time - GWP: Global Warming Potential - ODP: Ozone Depletion Potential).

P_{crit} [bar]	T_{crit} [°C]	M [g/mol]	GWP [$\text{kg}_{\text{eq.CO}_2}/\text{kg}$]	ODP [-]	ALT [year]
36.4	154.05	134.05	950-1020	0	7.6

The test facility used in the present study is shown schematically in Fig. 4.1. The test bench was designed with three optional methods for controlling the flow through the test sections: either by controlling the rotational velocity of the pump, or by actionning a by-pass valve, or by actionning a microvalve placed at the inlet of the test section. Liquid R-245fa is pumped by a gear pump and then passes through a filter/dryer, a Coriolis-type flowmeter, a microvalve, the test section, and a condenser which is a plate heat exchanger. A controlled-temperature reservoir allows to fix the saturation pressure in the loop. Two K-type thermocouples were installed to measure the liquid and vapor phase temperatures and a pressure transducer measures the saturation pressure inside the reservoir. The microvalve at the inlet of the test section avoids oscillations when boiling starts in the test section, as it induces an increase in the pressure drop in the loop.

4.2 Description of the test section

The test section, presented in Fig. 4.2, consists of three parts: (i) a 2000 mm spirally-shaped stainless steel tube (called preheater) whose inner and outer diameters (d_{inner} and d_{outer}) are 3.00 and 5.99 mm respectively, (ii) a 185 mm (l_{evap}) stainless steel horizontal tube (called evaporator) with the same inner and outer diameters as those of the preheater, (iii) a glass tube whose inner and outer diameters are 2.96 and 5.95 mm respectively.

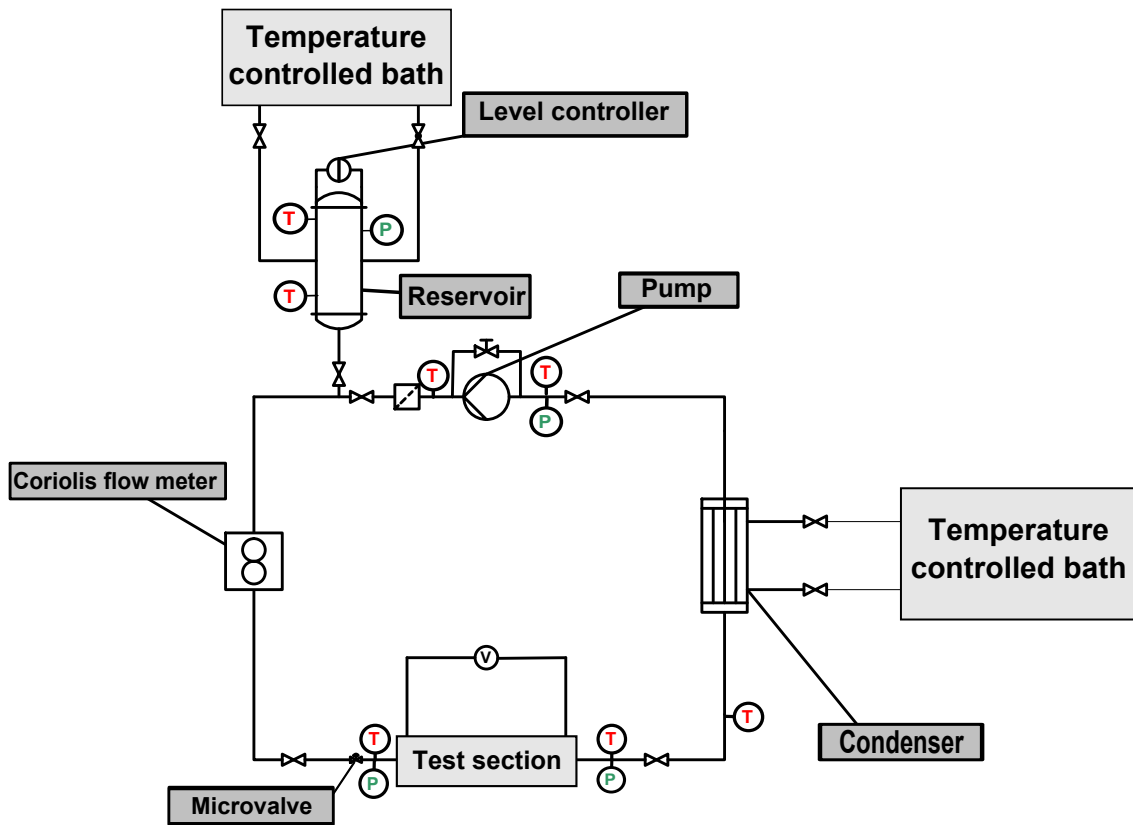


Figure 4.1: Schematic of the test facility.

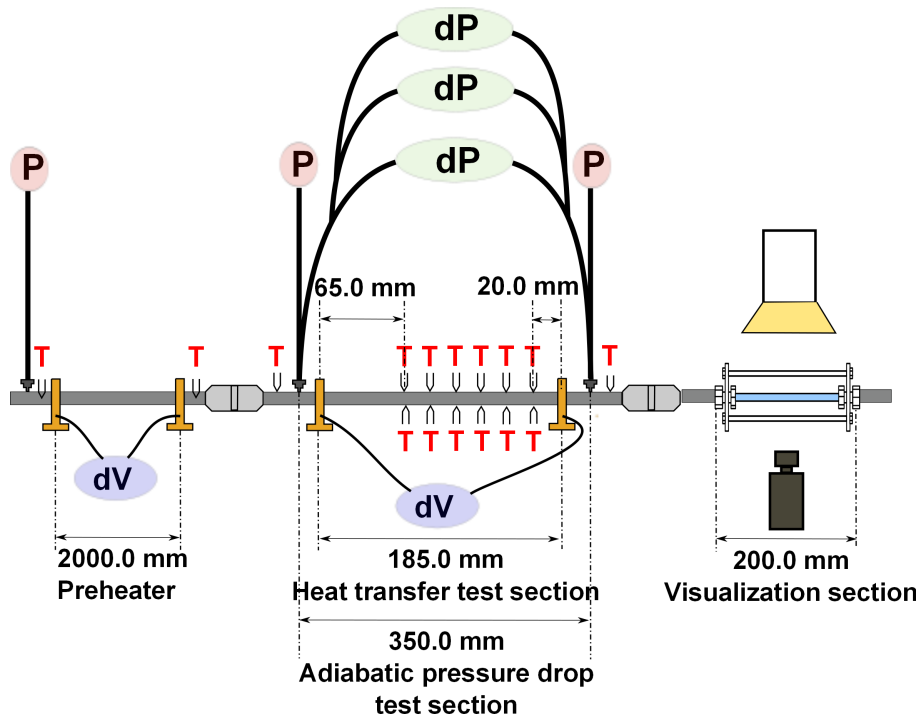


Figure 4.2: Schematic of the test section.

The flow boiling heat transfer test section corresponds to the evaporator. The control of the vapor quality at the heat transfer test section inlet is ensured by the preheater. The test section is heated by Joule effect, by means of two copper clamps that are connected electrically to a power supply. In addition, during the experiments, the preheater and evaporator heat fluxes (\dot{q}_{ph} and \dot{q}_{evap}) were recalculated with a direct voltage measurement on the external wall of the tube. For electrical insulation, the preheater and the evaporator are separated by a 30 mm tube made of peek resin. To measure the temperature at the inlet and outlet of the preheater, two 0.5 mm K-type thermocouples are used and two pressure transducers are installed at the inlet and outlet of the heat transfer test section. Two 80 μm K-type thermocouples are installed at the top of the tube at the inlet and the outlet of the evaporator.

As shown in Fig. 4.3, twelve 80 μm K-type thermocouples are strapped on a Kapton layer for electrical insulation at six positions along the channel: six thermocouples are placed at the top of the evaporator and six at the bottom. For each position y , the distances between the evaporator inlet and the thermocouple (l_y) are indicated on Fig. 4.4. As represented on Fig. 4.4, the stainless steel tubes are thermally insulated by a silicone tube whose thickness is 10 mm and a 10 mm thick layer of glass fibres.

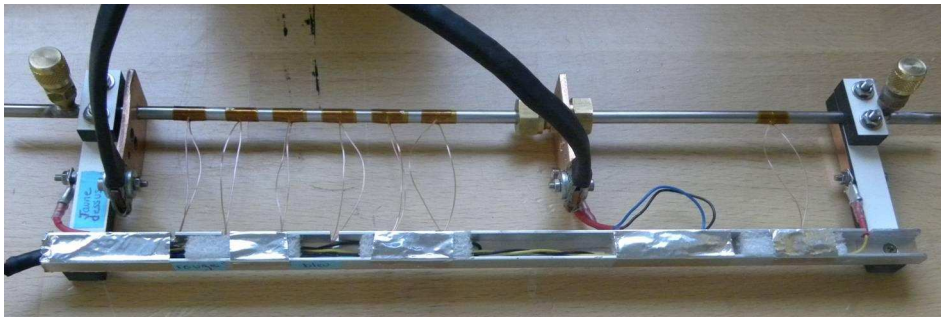


Figure 4.3: Image of the heat transfer test section before thermal insulating (i.e. evaporator).

The two-phase pressure drop values were directly obtained from the differential pressure transducers under adiabatic conditions. As a consequence, the measurements of pressure drop and heat transfer coefficients could not be performed simultaneously. The desired vapor quality at the inlet of the test section was obtained by adjusting the power of the preheater. The length between the two pressure tap locations ($l_{\Delta P}$) was 350 mm. In order to investigate a wide range of flow conditions with the best accuracy as possible, a selection of sensors was used depending on the level of the pressure drop being measured. Three differential pressure transducers were used:

- Keller KE23D differential pressure transducer: 0 - 5 bar
- Keller KE23D differential pressure transducer: 0 - 200 mbar
- Rosemount 3551S differential pressure transducer: 0 - 50 mbar

The differential pressure transducers were placed at levels higher than the test section, and the capillary tubes were positioned vertically. Two valves were placed

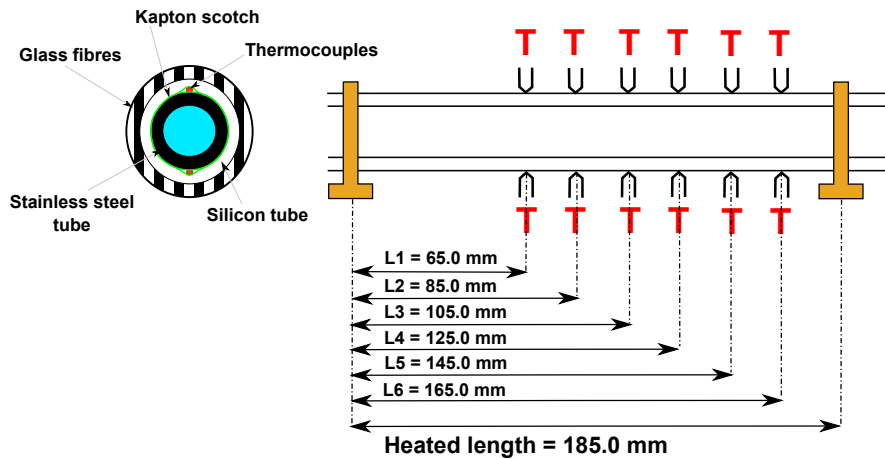


Figure 4.4: Schematic view of the evaporator (right) and thermocouple locations (left).

at the inlet and the outlet of each sensor in order to isolate it when the pressure drop was higher than their operating range.

The experimental setup, as described above, is completely monitored using a computer. Signals from the thermocouples, pressure transducers, mass flowmeter and power supplies are collected by a computerized data acquisition system. The entire acquisition system includes: (i) computer, (ii) a graphical data acquisition program written under LabView environment (National Instruments, 2006), and (iii) one Keithley Data Acquisition model 2701 with two slot cards allowing for multiple measurements up to 40 channels. Besides, this LabView program allows to remote control of the two power supplies and the two controlled-temperature reservoir.

4.3 Measurements and accuracy

In this section, the different measurement techniques, calibration methods, and the experimental accuracy will be detailed. This section introduces the root-sum-square (RSS) combination, the basic form used for combining uncertainty contributions in multiple-sample analysis. The term δX_i refers to the uncertainty in X_i in a general and nonspecific way: whatever is being dealt with at the moment (for example, fixed errors, random errors, or uncertainties). The systematic component was determined through a calibration or taken from the instrumentation documentation. Table 4.2 lists the uncertainty for each type of measurement.

Consider a variable X , which has a known uncertainty δX . The form for representing this variable and its uncertainty is:

$$X = X_{i(\text{measured})} \pm \delta X_i \quad (4.1)$$

The result R of the experiment is assumed to be calculated from a set of measurements using a data interpretation program (by hand or by computer) represented by:

Table 4.2: Sensors used for the instrumentation of the experimental setup.

Equipment	Range	Incertitude
K-Type thermocouple	-30 - 300 °C	± 0.25 °C
Keller PAA33 absolute pressure transducer	0-35 bar	± 0.07 bar
Keller KE23D differential pressure transducer	0-5 bar	± 0.01 bar
Keller KE23D differential pressure transducer	0-200 mbar	± 0.4 mbar
Rosemount 3551S differential pressure transducer	0-50 mbar	± 0.05 mbar
Micro Motion Coriolis type mass flowmeter	0-108 kg/h	± 0.1 %
Sorensen DCS 8-350 power supply	0-8 V	± 12 mV
	0-350 A	± 1400 mA
Sorensen SGA 60-250 power supply	0-60 V	± 60 mV
	0-250 A	± 1000 mA

$$R = R(X_1, X_2, X_3, X_4, \dots, X_N) \quad (4.2)$$

The effect of the uncertainty in a single measurement on the calculated result, if only that one measurement was in error would be:

$$\delta R_{X_i} = \frac{\partial R}{\partial X_i} \cdot \delta X_i \quad (4.3)$$

The partial derivative of R with respect to X_i is the sensitivity coefficient for the result R with respect to the measurement X_i . When several independent variables are used in the function R , the individual terms are combined by a root-sum-square method. The general formulation for error propagation, presented in [Taylor (2000)], is expressed as:

$$\delta R = \sqrt{\sum_1^N \left(\frac{\partial R}{\partial X_i} \cdot \delta X_i \right)^2} \quad (4.4)$$

Each term represents the contribution made by the uncertainty in one variable, δX_i , to the overall uncertainty in the result, δR . Each term has the same form: the partial derivative of R with respect to X_i multiplied by the uncertainty interval for that variable.

4.3.1 Tube diameter

Tube diameters (for both stainless steel tube and glass tube) have been measured with a digital vernier caliper (Mitutoyo serie 500) with a resolution of ± 0.02 mm. The measurements of stainless steel tube inner and outer diameters have been carried out on two samples chosen among the same tube used in the test section fabrication. The diameter has been measured 8 times in total for each tube, at different locations. The results are determined using the Student's distribution with 7 degrees of freedom and 95% confidence interval.

$$d_{\text{inner}} = 3.00 \pm 0.03 \text{ mm} \quad (4.5)$$

$$d_{\text{outer}} = 5.99 \pm 0.03 \text{ mm} \quad (4.6)$$

The procedure has been repeated for the glass tube with measurements on two different samples chosen among the numerous tubes bought and 8 measurements have been made for each diameter.

$$d_{\text{inner}} = 2.96 \pm 0.03 \text{ mm} \quad (4.7)$$

$$d_{\text{outer}} = 5.95 \pm 0.03 \text{ mm} \quad (4.8)$$

4.3.2 Tube lengths

Tube lengths are measured with an error less than 0.1 mm. This uncertainty comes directly from the measurement instruments.

$$\delta l = \pm 0.1 \text{ mm} \quad (4.9)$$

4.3.3 Temperature

Different K-type thermocouples were used in the experimental facility: (i) six 0.5 mm K-type thermocouples made by Serv'Instrumentation and (ii) sixteen 80 μm K-type thermocouples made in the CETHIL laboratory. Two cold junctions thermocouple box made in the CETHIL laboratory were used to ensure a stable reference temperature. Preliminary calibration of the thermocouples was performed to determine the actual deviation. For this purpose, the thermocouples were placed in a thermal bath next to a platinum probe and the temperature of the bath was varied from 10 to 130°C. A second degree polynomial equation was then applied to correct the measurement. The thermocouple systematic error was $\pm 0.25^\circ\text{C}$.

$$\delta T = \pm 0.25 \text{ }^\circ\text{C} \quad (4.10)$$

4.3.4 Absolute pressure and differential pressure

Absolute pressure measurements were made using Keller PAA33 transducers with a range from 0 to 35 bar. The nominal uncertainty given by the manufacturer is $\pm 0.2\%$ in overall measure range (i.e. ± 70 mbar). This nominal uncertainty includes the hysteresis errors, the linearity as a function of scale limit values and the repeatability as well.

$$\delta P = \pm 0.07 \text{ bar} \quad (4.11)$$

Three differential pressure transducers were used during the present investigation to measure the pressure drop along the evaporator. Two of them were made by Keller and the last one by Rosemount. Each sensor was calibrated by the manufacturers. The uncertainty given by Rosemount (for Rosemount 3551S1CD) is $\pm 0.10\%$ of the full scale, i.e. ± 0.05 mbar. For the two others transducers, the nominal uncertainty given by Keller is $\pm 0.2\%$ in overall measure range.

4.3.5 Fluid properties

Fluid properties and the vapor pressure curve were obtained with REFPROP (NIST Standard Reference Database 23, Version 7.0) from a temperature measurement applying a linear regression. Regressions of 4th order were used to calculate σ , μ_L , μ_V , λ_L , and λ_V whereas linear regressions of 6th order were used to calculate $c_{p,L}$,

$c_{p,V}$, h_L , h_V , ρ_L and ρ_V . For instance, the linear regression of 6th order is expressed as:

$$X = a_0 + a_1 \cdot T + a_2 \cdot T^2 + a_3 \cdot T^3 + a_4 \cdot T^4 + a_5 \cdot T^5 + a_6 \cdot T^6 \quad (4.12)$$

and the corresponding uncertainty is:

$$\delta X = [a_1 + 2 \cdot a_2 \cdot T + 3 \cdot a_3 \cdot T^2 + 4 \cdot a_4 \cdot T^3 + 5 \cdot a_5 \cdot T^4 + 6 \cdot a_6 \cdot T^5] \cdot \delta T \quad (4.13)$$

The coefficients a_0 , a_1 , a_2 , a_3 , a_4 , a_5 , and a_6 for the R-245fa enthalpy are given in Table 4.3.

Table 4.3: Coefficients for the R-245fa enthalpy calculations.

	a_0	a_1	a_2	a_3	a_4	a_5	a_6
h_L	200313.8	1252.49	2.746	-0.04234	0.000578	-0.000003767	-0.0000001043
h_V	404436.2	811.42	-2.758	0.06702	0.000915	0.000006013	-0.00000001678

For example, for a given saturation temperature of 100°C, the results for the enthalpies for R-245fa are $h_L = 341310 \text{ J/kg} \pm 0.10\%$ and $h_V = 476770 \text{ J/kg} \pm 0.04\%$.

4.3.6 Mass flow and mass velocity

The nominal uncertainty of the Micromotion Elite CMF010M Coriolis type mass flowmeter is $\pm 0.1\%$ of the measurement. The definition of the mass velocity was introduced in section 2.5.1. It can be expressed for a circular pipe as:

$$G = \frac{4 \cdot \dot{m}}{\pi \cdot d_{\text{inner}}^2} \quad (4.14)$$

The uncertainty for G is:

$$\delta G = \sqrt{\left(\frac{4}{\pi \cdot d_{\text{inner}}^2} \cdot \delta \dot{m}\right)^2 + \left(\frac{-8 \cdot \dot{m}}{\pi \cdot d_{\text{inner}}^3} \cdot \delta d_{\text{inner}}\right)^2} \quad (4.15)$$

The mass velocity ranges from 96.4 kg/m²·s to 1509.6 kg/m²·s. Thus the uncertainties for these extreme values of G are:

$$G = 96.4 \pm 2.0 \text{ kg/m}^2 \cdot \text{s} \quad (4.16)$$

$$G = 1509.6 \pm 30.3 \text{ kg/m}^2 \cdot \text{s} \quad (4.17)$$

4.3.7 Heat flux

The heat powers delivered to the preheater and the evaporator ($\dot{Q}_{\text{inner,ph}}$ and $\dot{Q}_{\text{inner,evap}}$) are calculated from the measurements of the voltage (U) and the intensity (I). The thermal insulation is assumed ideal with no heat loss to the surroundings. This assumption will be tested by evaluating the energy balances for both preheater and evaporator, presented in section 4.5.1. The heat powers are determined with the following expressions:

$$\dot{Q}_{\text{inner,ph}} = I_{\text{ph}} \cdot U_{\text{ph}} \quad (4.18)$$

$$\dot{Q}_{\text{inner,evap}} = I_{\text{evap}} \cdot U_{\text{evap}} \quad (4.19)$$

The corresponding uncertainties for $\dot{Q}_{\text{inner,ph}}$ and $\dot{Q}_{\text{inner,evap}}$ are:

$$\delta\dot{Q}_{\text{inner,ph}} = \sqrt{(I_{\text{ph}} \cdot \delta U_{\text{ph}})^2 + (U_{\text{ph}} \cdot \delta I_{\text{ph}})^2} \quad (4.20)$$

$$\delta\dot{Q}_{\text{inner,evap}} = \sqrt{(I_{\text{evap}} \cdot \delta U_{\text{evap}})^2 + (U_{\text{evap}} \cdot \delta I_{\text{evap}})^2} \quad (4.21)$$

The accuracy given by the manufacturer is ± 60 mV and ± 1000 mA for the preheater (Sorensen SGA 60–250) and ± 12 mV and ± 1400 mA for the evaporator (Sorensen DCS 8–350).

The heat fluxes imposed at the evaporator and the preheater are expressed as:

$$\dot{q}_{\text{ph}} = \frac{\dot{Q}_{\text{inner,ph}}}{\pi \cdot d_{\text{inner}} \cdot l_{\text{ph}}} \quad (4.22)$$

$$\dot{q}_{\text{evap}} = \frac{\dot{Q}_{\text{inner,evap}}}{\pi \cdot d_{\text{inner}} \cdot l_{\text{evap}}} \quad (4.23)$$

The uncertainties for the heat fluxes were calculated with the following expressions:

$$\delta\dot{q}_{\text{ph}} = \sqrt{\left(\frac{1}{\pi \cdot d_{\text{inner}} \cdot l_{\text{ph}}} \cdot \delta\dot{Q}_{\text{inner,ph}}\right)^2 + \left(\frac{-\dot{Q}_{\text{inner,ph}}}{\pi \cdot l_{\text{ph}} \cdot d_{\text{inner}}^2} \cdot \delta d_{\text{inner}}\right)^2 + \left(\frac{-\dot{Q}_{\text{inner,ph}}}{\pi \cdot d_{\text{inner}} \cdot l_{\text{ph}}^2} \cdot \delta l_{\text{ph}}\right)^2} \quad (4.24)$$

$$\delta\dot{q}_{\text{evap}} = \sqrt{\left(\frac{1}{\pi \cdot d_{\text{inner}} \cdot l_{\text{evap}}} \cdot \delta\dot{Q}_{\text{inner,evap}}\right)^2 + \left(\frac{-\dot{Q}_{\text{inner,evap}}}{\pi \cdot l_{\text{evap}} \cdot d_{\text{inner}}^2} \cdot \delta d_{\text{inner}}\right)^2 + \left(\frac{-\dot{Q}_{\text{inner,evap}}}{\pi \cdot d_{\text{inner}} \cdot l_{\text{evap}}^2} \cdot \delta l_{\text{evap}}\right)^2} \quad (4.25)$$

Table 4.4 presents the heat power and the heat flux with their respective uncertainties calculated for both preheater and evaporator from two situations: at low heat flux and at high heat flux.

Table 4.4: Uncertainties on heat power and heat flux.

		U [V]	I [A]	\dot{Q} [W]	$\delta\dot{Q}$ [W]	\dot{q} [W/m ²]	$\delta\dot{q}$ [W/m ²]
Preheater	Low flux	1.75	13.08	40.4	± 2.3	2142	± 120
	High flux	14.63	183.89	2690.3	± 18.4	142725	± 1728
Evaporator	Low flux	0.41	43.29	17.3	± 0.8	9931	± 450
	High flux	0.91	96.25	87.6	± 1.8	50234	± 1106

4.4 Data reduction

In this section, the calculations used to determine the vapor quality (x), the heat transfer coefficient (α), and the frictional pressure drop (Δ_{frict}) are detailed.

Firstly, the vapor quality data reduction method is introduced taking into account the fact that two different situations may occur at the inlet of the evaporator:

- the fluid enters into the evaporator as subcooled liquid: **configuration A**.
- the fluid enters into the evaporator as saturated two-phase flow: **configuration B**.

For each situation, the vapor quality is calculated at different positions: (i) at the inlet of the evaporator, (ii) at the position y , and (iii) at the outlet of the evaporator.

Subsequently, the heat transfer coefficient data reduction method is detailed for both single-phase flow and flow boiling. Finally, the frictional pressure drop data reduction method is presented.

4.4.1 Vapor quality under configuration B

4.4.1.1 Inlet vapor quality under configuration B

With the **configuration B**, the fluid enters into the preheater as subcooled liquid and the boiling starts into the preheater. Figure 4.5 shows a schematic view of the preheater under this configuration.

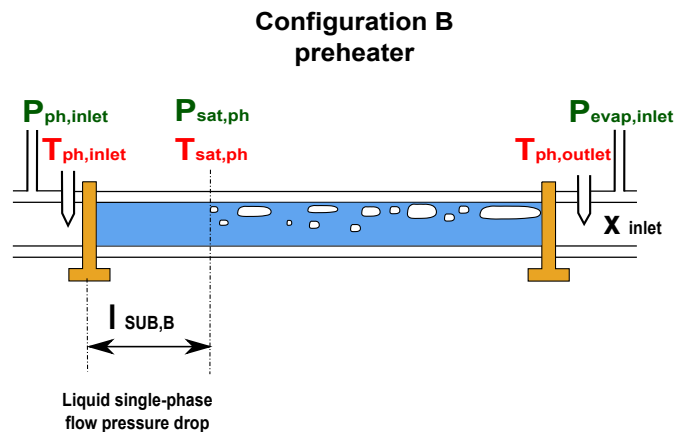


Figure 4.5: Schematic view of the preheater in configuration B.

The vapor quality at the inlet of the evaporator (x_{inlet}) is expressed in terms of the local enthalpy as follows:

$$x_{\text{inlet}} = \frac{h_{L,\text{inlet,ph}} + \frac{\dot{Q}_{\text{inner,ph}}}{\dot{m}} - h_{L,\text{sat,ph}}}{h_{LV,\text{outlet,ph}}} \quad (4.26)$$

where $h_{L,\text{inlet,ph}}$ is the specific enthalpy of the liquid deduced from $T_{\text{ph,inlet}}$ and $P_{\text{ph,inlet}}$. $h_{L,\text{sat,ph}}$ is the specific enthalpy of the saturated liquid calculated at $T_{\text{sat}}(P_{\text{sat,ph}})$. $h_{LV,\text{outlet,ph}}$ is the latent heat of vaporization determined at $T_{\text{sat}}(P_{\text{evap,inlet}})$.

Figure 4.6 presents the variation of the latent heat of vaporization as a function of the reduced pressure for an extreme case in terms of pressure drop along the preheater ($\Delta P = 1.5$ bar). The variation of h_{LV} is calculated from the following equation:

$$\Delta h_{LV,\text{outlet,ph}} = \frac{h_{LV}(P_{\text{ph,inlet}}) - h_{LV}(P_{\text{evap,inlet}})}{h_{LV}(P_{\text{evap,inlet}})} \quad (4.27)$$

This variation is lower than 3% over the range of reduced pressure investigated in the present study, therefore the variation of the latent heat of vaporization along the preheater is negligible and the definition of the vapor quality (Eq. (4.26)) is confirmed.

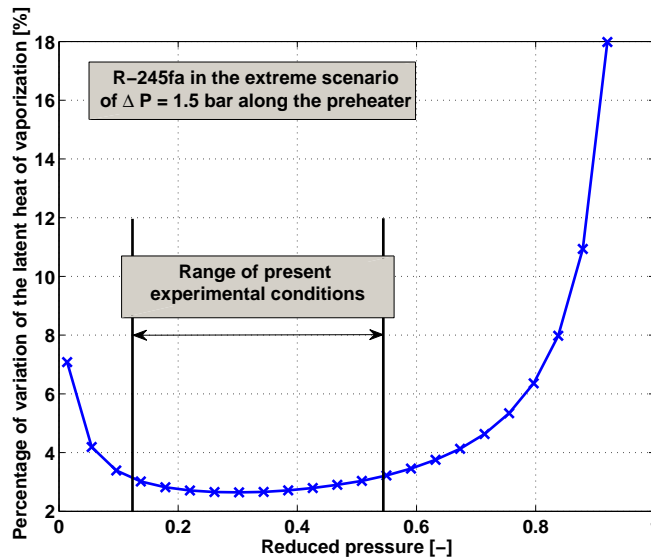


Figure 4.6: Variation of R-245fa latent heat of vaporization as a function of the reduced pressure in the extreme case of a pressure drop along the preheater equal to 1.5 bar.

In order to calculate x_{inlet} , a computational algorithm was used to calculate $P_{\text{sat,ph}}$ required to determine $h_{L,\text{sat,ph}}$. In the computational algorithm, presented in Fig. 4.7, the subcooled length, $l_{\text{SUB,B}}$ is calculated by the following energy balance equation:

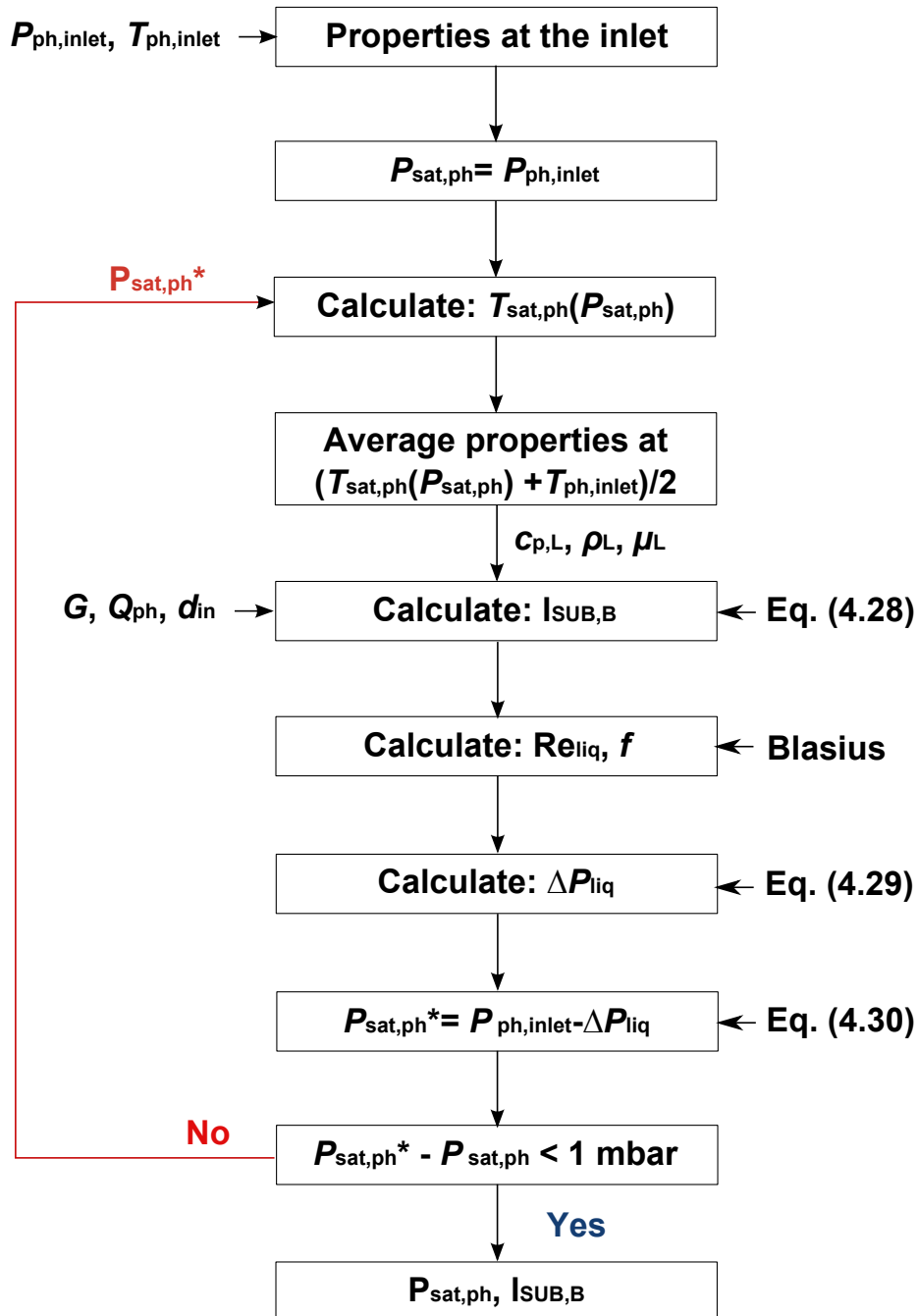


Figure 4.7: Computational algorithm of the single-phase flow pressure drop and the subcooled length for R-245fa flowing under configuration B.

$$l_{\text{SUB,B}} = \frac{\dot{m} \cdot c_{p,L}}{\dot{q}_{\text{inner,ph}} \cdot \pi \cdot d_{\text{inner}}} \cdot (T_{\text{sat,B}}(P_{\text{ph,inlet}}) - T_{\text{ph,inlet}}) \quad (4.28)$$

and the single-phase flow pressure drop is calculated from averaged properties with the following expression:

$$\Delta P_{L,\text{ph}} = \frac{G^2}{2 \cdot \rho_L} \cdot 4 \cdot f \cdot \frac{l_{\text{SUB,B}}}{d_{\text{inner}}} \quad (4.29)$$

where f is the friction factor calculated with the Blasius correlation. Then, $P_{\text{sat,ph}}$ is obtained by:

$$P_{\text{sat,ph}} = P_{\text{ph,inlet}} - \Delta P_{L,\text{ph}} \quad (4.30)$$

The calculation continues until the difference between two successive iterations is greater than 1 mbar.

The uncertainty of x_{inlet} is determined from the following equation:

$$\begin{aligned} \delta x_{\text{inlet}}^2 = & \left(\frac{1}{h_{LV,\text{outlet,ph}}} \cdot \delta h_{L,\text{inlet,ph}} \right)^2 + \left(\frac{1}{\dot{m} \cdot h_{LV,\text{outlet,ph}}} \cdot \delta \dot{Q}_{\text{inner,ph}} \right)^2 + \left(-\frac{\dot{Q}_{\text{inner,ph}}}{\dot{m}^2 \cdot h_{LV,\text{outlet,ph}}} \cdot \delta \dot{m} \right)^2 \\ & + \left(-\frac{1}{h_{LV,\text{outlet,ph}}} \cdot \delta h_{L,\text{sat,ph}} \right)^2 + \left(-\frac{x_{\text{inlet}}}{h_{LV,\text{outlet,ph}}} \cdot \delta h_{LV,\text{outlet,ph}} \right)^2 \end{aligned} \quad (4.31)$$

where $\delta h_{L,\text{inlet,ph}}$, $\delta h_{L,\text{sat,ph}}$, $\delta h_{LV,\text{outlet,ph}}$ are calculated from Eq. (4.13) with the coefficients given in Table 4.3 and the appropriate temperatures. The uncertainty on the measured temperatures is $\pm 0.25^\circ\text{C}$ whereas for deduced temperatures, the uncertainties are calculated by error propagation on a case-by-case basis.

4.4.1.2 Vapor quality at each position y under configuration B

With the configuration B, the fluid enters into the evaporator as saturated two-phase flow and the thermodynamic vapor quality at each position y in the saturated region x_y is expressed as follows:

$$x_y = x_{\text{inlet}} + \frac{\dot{Q}_{\text{inner,evap}} \cdot l_y}{\dot{m} \cdot h_{LV,y}} \quad (4.32)$$

where l_y is the distance between the inlet of the evaporator and the position y and $h_{LV,y}$ is the latent heat of vaporization calculated at $T_{\text{sat},y}$ which is deduced from the saturation pressure at the position y :

$$T_{\text{sat},y} = T_{\text{sat}}(P_{\text{sat},y}) \quad (4.33)$$

with the saturation pressure at the position y calculated from the following equation:

$$P_{\text{sat},y} = P_{\text{evap,inlet}} - (\Delta P_{\text{total}}) \cdot \left(\frac{l_y}{l_{\text{evap}}} \right) \quad (4.34)$$

where ΔP_{total} is the pressure drop measured along the evaporator which is assumed to be linear as the vapor quality difference between the evaporator inlet and

outlet remains low ($\Delta x < 0.3$). $P_{\text{evap,inlet}}$ is the absolute pressure measured at the inlet of the evaporator (see Fig. 4.2).

The uncertainty on x_y is estimated by the following expression:

$$\begin{aligned} \delta x_y^2 = & \delta x_{\text{inlet}}^2 + \left(\frac{l_y}{\dot{m} \cdot l_{\text{evap}} \cdot h_{\text{LV},y}} \cdot \delta \dot{Q}_{\text{inner,evap}} \right)^2 + \left(\frac{\dot{Q}_{\text{inner,evap}}}{\dot{m} \cdot l_{\text{evap}} \cdot h_{\text{LV},y}} \cdot \delta l_y \right)^2 \\ & + \left(-\frac{\dot{Q}_{\text{inner,evap}} \cdot l_y}{\dot{m}^2 \cdot l_{\text{evap}} \cdot h_{\text{LV},y}} \cdot \delta \dot{m} \right)^2 + \left(-\frac{\dot{Q}_{\text{inner,evap}} \cdot l_y}{\dot{m} \cdot l_{\text{evap}}^2 \cdot h_{\text{LV},y}} \cdot \delta l_{\text{evap}} \right)^2 + \left(-\frac{\dot{Q}_{\text{inner,evap}} \cdot l_y}{\dot{m} \cdot l_{\text{evap}} \cdot h_{\text{LV},y}^2} \cdot \delta h_{\text{LV},y} \right)^2 \end{aligned} \quad (4.35)$$

where $\delta \dot{Q}_{\text{inner,evap}}$ is calculated from Eq. (4.21), δl_y and δl_{evap} are equal to ± 0.1 mm, and $\delta \dot{m}$ is equal to $\pm 0.1\%$. $\delta h_{\text{LV},y}$ is calculated from $\delta T_{\text{sat},y}$.

4.4.1.3 Outlet vapor quality under configuration B

With the configuration B, x_{outlet} is expressed by the following expression:

$$x_{\text{outlet}} = x_{\text{inlet}} + \frac{\dot{Q}_{\text{inner,evap}}}{h_{\text{LV,evap,outlet}} \dot{m}} \quad (4.36)$$

where $h_{\text{LV,evap,outlet}}$ is the latent heat of vaporization calculated at $T_{\text{sat}}(P_{\text{evap,outlet}})$.

4.4.2 Vapor quality under configuration A

4.4.2.1 Inlet vapor quality under configuration A

With the configuration A, the fluid enters into the evaporator as subcooled liquid and the boiling starts into the evaporator, thus, the vapor quality at the inlet of the evaporator (x_{inlet}) is equal to 0.

$$x_{\text{inlet}} = 0 \quad (4.37)$$

Figure 4.8 shows a schematic view of the evaporator in configuration A.

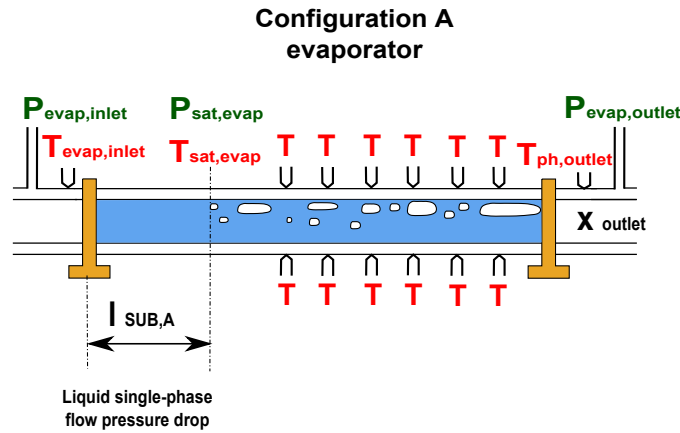


Figure 4.8: Schematic view of the evaporator in configurations A.

4.4.2.2 Vapor quality at position y under configuration A

The thermodynamic vapor quality at each position y in the saturated region, x_y is expressed as:

$$x_y = \frac{h_{L,\text{inlet,evap}} + \frac{\dot{Q}_{\text{inner,evap}}}{\dot{m}} \cdot \frac{l_y}{l_{\text{evap}}} - h_{\text{sat,evap}}}{h_{LV,y}} \quad (4.38)$$

where $h_{L,\text{inlet,evap}}$ is the specific enthalpy of the liquid deduced from $T_{\text{evap,inlet}}$ and $P_{\text{evap,inlet}}$. $h_{\text{sat,evap}}$ is the specific enthalpy of the saturated liquid calculated at $T_{\text{sat}}(P_{\text{sat,evap}})$.

In order to determine $T_{\text{sat}}(P_{\text{sat,evap}})$ necessary to deduce $h_{\text{sat,evap}}$, the subcooled length, $l_{\text{SUB,A}}$, must be evaluated. The procedure used to determine the subcooled length into the preheater under configuration B was adapted to configuration A. Firstly, the subcooled length is calculated by the following energy balance:

$$l_{\text{SUB,A}} = \frac{\dot{m} \cdot c_{p,L}}{\dot{q}_{\text{inner,evap}} \cdot \pi \cdot d_{\text{inner}}} \cdot (T_{\text{sat}}(P_{\text{sat,evap}}) - T_{\text{evap,inlet}}) \quad (4.39)$$

The saturation pressure at the end of the subcooled length, i.e. at the beginning of the two-phase flow ($P_{\text{sat,evap}}$) is calculated taking into account the single-phase pressure drop:

$$P_{\text{sat,evap}} = P_{\text{evap,inlet}} - \Delta P_{L,\text{evap}} \quad (4.40)$$

where the single-phase flow pressure drop along $l_{\text{SUB,A}}$ ($\Delta P_{L,\text{evap}}$) is calculated with the following expression:

$$\Delta P_{L,\text{evap}} = \frac{G^2}{2 \cdot \rho_L} \cdot 4 \cdot f \cdot \frac{l_{\text{SUB,A}}}{d_{\text{inner}}} \quad (4.41)$$

In Eq. (4.38), $h_{LV,y}$ is the latent heat of vaporization calculated at $T_{\text{sat},y}$. This temperature is deduced from the following expression:

$$T_{\text{sat},y} = T_{\text{sat}}(P_{\text{sat},y}) \quad (4.42)$$

where the saturation pressure at any location y ($P_{\text{sat},y}$) is calculated by Eq. (4.43):

$$P_{\text{sat},y} = P_{\text{sat,evap}} - (\Delta P_{\text{total}} - \Delta P_L) \cdot \left(\frac{l_y - l_{\text{SUB,A}}}{l_{\text{evap}} - l_{\text{SUB,A}}} \right) \quad (4.43)$$

where ΔP_{total} is the pressure drop measured along the evaporator, ΔP_L is the liquid phase pressure drop calculated, l_y is the distance between the inlet of the evaporator and the thermocouple y and l_{evap} is the evaporator length. In this definition, the two-phase flow pressure drop is assumed to be linear as the vapor quality difference between the evaporator inlet and outlet remains low ($\Delta x < 0.3$).

The equation to estimate the uncertainty on x_y is similar to Eq. (4.31) but also takes into account the uncertainties on l_y and l_{evap} .

4.4.2.3 Outlet vapor quality under configuration A

With the configuration A, the thermodynamic vapor quality at the outlet of the evaporator, x_{outlet} is expressed as:

$$x_{\text{outlet}} = \frac{h_{L,\text{inlet,evap}} + \frac{\dot{Q}_{\text{inner,evap}}}{\dot{m}} - h_{\text{sat,evap}}}{h_{LV,\text{evap,outlet}}} \quad (4.44)$$

where $h_{L,\text{inlet,evap}}$ is the specific enthalpy of the liquid deduced from $T_{\text{evap,inlet}}$ and $P_{\text{evap,inlet}}$. $h_{\text{sat,evap}}$ is the specific enthalpy of the saturated liquid calculated at $T_{\text{sat}}(P_{\text{sat,evap}})$. $h_{LV,\text{evap,outlet}}$ is the latent heat of vaporization calculated at $T_{\text{sat}}(P_{\text{evap,outlet}})$. $P_{\text{evap,outlet}}$ is measured at the outlet of the evaporator by an absolute pressure transducer as represented in Fig. 4.2.

4.4.3 Heat transfer coefficient

4.4.3.1 Single-phase heat transfer coefficient

The heat transfer coefficient during liquid flow is calculated from the following expression:

$$\alpha_{L,\text{mean},y} = \frac{\dot{q}_{\text{evap}}}{T_{\text{wall,inner},y} - T_{f,y}} \quad (4.45)$$

where \dot{q}_{evap} is the imposed heat flux at the evaporator.

The mean inner wall temperature at each position y ($T_{\text{wall,inner},y}$) is calculated as:

$$T_{\text{wall,inner},y} = \frac{T_{\text{wall,inner},y,\text{bottom}} + T_{\text{wall,inner},y,\text{top}}}{2} \quad (4.46)$$

where $T_{\text{wall,inner},y,\text{bottom}}$ and $T_{\text{wall,inner},y,\text{top}}$ are the inner wall temperatures at the bottom and at the top of the tube respectively. These temperatures are calculated from those measured at the outer surface of the tube, both at the bottom and at the top ($T_{\text{wall,outer},y,\text{bottom}}$ and $T_{\text{wall,outer},y,\text{top}}$). For example, at the top position y , $T_{\text{wall,inner},y,\text{top}}$ is calculated with the equation below:

$$T_{\text{wall,inner},y,\text{top}} = T_{\text{wall,outer},y,\text{top}} + \frac{\dot{q}_{\text{evap}}''}{4 \cdot \lambda_{\text{ss}}} \cdot (r_{\text{outer}}^2 - r_{\text{inner}}^2) - \left(\frac{\dot{q}_{\text{evap}}''}{2 \cdot \lambda_{\text{ss}}} \cdot r_{\text{outer}}^2 \right) \cdot \ln \left(\frac{r_{\text{outer}}}{r_{\text{inner}}} \right) \quad (4.47)$$

where \dot{q}_{evap}'' is the volumetric heat flux at the evaporator, λ_{ss} is the thermal conductivity of the stainless steel tube and r_{outer} and r_{inner} are the outer and the inner radii respectively.

In Eq. (4.45), $T_{f,y}$ is the temperature of the fluid at the position y calculated from the following energy balance:

$$T_{f,y} = T_{\text{evap,inlet}} + \frac{\dot{Q}_{\text{inner,evap}}}{\dot{m} \cdot c_{p,L}} \cdot \frac{l_y}{l_{\text{evap}}} \quad (4.48)$$

The uncertainty on $\alpha_{L,\text{mean},y}$ is calculated from the following equation:

$$\delta\alpha_{L,\text{mean},y} = \sqrt{\left(\frac{\delta\dot{q}_{\text{evap}}}{T_{\text{wall,inner},y} - T_{f,y}}\right)^2 + \left(-\frac{q_{\text{evap}} \cdot \delta T_{\text{wall,inner},y}}{(T_{f,y} - T_{\text{wall,inner},y})^2}\right)^2 + \left(\frac{q_{\text{evap}} \cdot \delta T_{f,y}}{(T_{\text{wall,inner},y} - T_{f,y})^2}\right)^2} \quad (4.49)$$

where $\delta\dot{q}_{\text{evap}}$ is calculated from Eq. (4.25), $\delta T_{\text{wall,inner},y}$ and $\delta T_{f,y}$ are obtained by applying the error propagation method to Eqs. (4.47) and (4.48), respectively.

4.4.3.2 Flow boiling heat transfer coefficient

The flow boiling heat transfer coefficient at each position y ($\alpha_{\text{mean},y}$) is calculated from the following equation:

$$\alpha_{\text{mean},y} = \frac{\dot{q}_{\text{evap}}}{T_{\text{wall,inner},y} - T_{\text{sat},y}} \quad (4.50)$$

The mean inner wall temperature at each position y ($T_{\text{wall,inner},y}$) is calculated by Eq. (4.46) and $T_{\text{wall,inner},y,\text{bottom}}$ and $T_{\text{wall,inner},y,\text{top}}$ are calculated with Eq. (4.47).

The saturation temperature at each position y ($T_{\text{sat},y}$) is deduced for both configurations from the saturation pressure:

$$T_{\text{sat},y} = T_{\text{sat}}(P_{\text{sat},y}) \quad (4.51)$$

According to the configuration A or B, the saturation pressure at any location y ($P_{\text{sat},y}$) is calculated from Eqs. (4.43) or (4.34), respectively.

The uncertainty on $\alpha_{\text{mean},y}$ is calculated from the following equation:

$$\delta\alpha_{\text{mean},y} = \sqrt{\left(\frac{\delta\dot{q}_{\text{evap}}}{T_{\text{wall,inner},y} - T_{\text{sat},y}}\right)^2 + \left(-\frac{q_{\text{evap}} \cdot \delta T_{\text{wall,inner},y}}{(T_{\text{sat},y} - T_{\text{wall,inner},y})^2}\right)^2 + \left(\frac{q_{\text{evap}} \cdot \delta T_{\text{sat},y}}{(T_{\text{wall,inner},y} - T_{\text{sat},y})^2}\right)^2} \quad (4.52)$$

4.4.4 Frictional pressure drop

The two-phase pressure drops for flows inside horizontal tubes are the sum of two contributions: the momentum pressure drop ΔP_{mom} and the frictional pressure drop ΔP_{frict} :

$$\Delta P_{\text{total}} = \Delta P_{\text{mom}} + \Delta P_{\text{frict}} \quad (4.53)$$

The momentum pressure drop is expressed as follows:

$$\Delta P_{\text{mom}} = G^2 \cdot \left\{ \left[\frac{(1-x)^2}{\rho_L \cdot (1-\epsilon)} + \frac{x^2}{\rho_V \cdot \epsilon} \right]_{\text{outlet}} - \left[\frac{(1-x)^2}{\rho_L \cdot (1-\epsilon)} + \frac{x^2}{\rho_V \cdot \epsilon} \right]_{\text{inlet}} \right\} \quad (4.54)$$

The variation of vapor quality between the inlet and the outlet of the test section due to the pressure drop provokes a so-called flashing (increase of the vapor quality

due to expansion). The flashing effect may easily be calculated using the relation developed by [Revellin et al. (2012)], which is expressed (for constant properties) as follows:

$$\Delta x = -\frac{v_{LV} \cdot T_{\text{sat}} \cdot c_{x,TP} + h_{LV} \cdot v_{TP}}{h_{LV}^2} \cdot \Delta P_{\text{total}} \quad (4.55)$$

where $c_{x,TP}$ corresponds to the specific heat capacity of the two-phase flow at constant vapor quality, calculated by the following relation:

$$c_{x,TP} = x \cdot c_{x,V} + (1 - x) \cdot c_{x,L} \quad (4.56)$$

The two-phase specific volume is defined as:

$$v_{TP} = x \cdot v_V + (1 - x) \cdot v_L \quad (4.57)$$

The void fraction (ϵ) can be calculated by the [Steiner (1993)] version of the drift flux model of [Rouhani and Axelsson (1970)]:

$$\epsilon = \frac{x}{\rho_V} \cdot \left[(1 + 0.12 \cdot (1 - x)) \cdot \left(\frac{x}{\rho_V} + \frac{1 - x}{\rho_L} \right) + 1.18 \cdot \frac{(1 - x)}{G} \cdot \left(\frac{g \cdot \sigma \cdot (\rho_L - \rho_V)}{\rho_L^2} \right)^{0.25} \right]^{-1} \quad (4.58)$$

where the vapor quality is calculated as:

$$x = \frac{x_{\text{inlet}} + x_{\text{outlet}}}{2} \quad (4.59)$$

where x_{inlet} is calculated with Eq. (4.26) and x_{outlet} is expressed as:

$$x_{\text{outlet}} = x_{\text{inlet}} + \Delta x \quad (4.60)$$

According to Eqs. (4.54) and (4.53), the momentum pressure drop is subtracted from the total pressure to obtain the two-phase frictional pressure drop. The uncertainty on ΔP_{frict} is calculated from the following equation:

$$\delta \Delta P_{\text{frict}} = \delta \Delta P_{\text{total}} + \delta \Delta P_{\text{mom}} \quad (4.61)$$

where $\delta \Delta P_{\text{total}}$ corresponds to the uncertainty of the sensor and $\delta \Delta P_{\text{mom}}$ is estimated from Eq. (4.54).

4.5 Validation of the test section for single-phase flows

4.5.1 Energy balance

In order to estimate the heat losses to the surrounding environment, the overall heat balance of the system was checked for various heat fluxes and mass velocities. The fluid temperature rise along the heated length provides the heat input into the refrigerant (Q_{outer}), and is calculated by:

$$\dot{Q}_{\text{outer}} = \dot{m} \cdot c_{p,L} \cdot (T_{f,\text{outlet}} - T_{f,\text{inlet}}) \quad (4.62)$$

where $T_{f,\text{inlet}}$ and $T_{f,\text{outlet}}$ are the temperatures of the fluid at the inlet and the outlet respectively for either the preheater or the evaporator. The uncertainty is obtained with the following equation:

$$\delta\dot{Q}_{\text{outer}} = \sqrt{(\dot{m} \cdot \Delta T \cdot \delta c_{p,L})^2 + (c_{p,L} \cdot \Delta T \cdot \delta\dot{m})^2 + (c_{p,L} \cdot \dot{m} \cdot 2 \cdot \delta T)^2} \quad (4.63)$$

where $\Delta T = T_{f,\text{outlet}} - T_{f,\text{inlet}}$.

The measured \dot{Q}_{outer} was compared with the heat input to the test section, \dot{Q}_{inner} (calculated as $U \times I$). Figs. 4.9(a) and 4.9(b) represent the energy balance for the preheater and the evaporator respectively along with the uncertainty bars. The heat losses rate is around 7% and 4% for the preheater and the evaporator, respectively. From these preliminary tests, one should consider that the energy balance for both is validated.

4.5.2 Heat transfer test section validation

Concerning the validation of the heat transfer test section, Fig. 4.10 represents the comparison between the experimental Nusselt numbers and the predicted Nusselt numbers calculated with the [Shah and London (1978)] correlation for laminar flow in the thermal entry region and with the [Gnielinski (1976)] correlation for turbulent flow.

The experimental Nusselt number is calculated from the following expression:

$$\text{Nu}_{\text{exp}} = \frac{\alpha_{L,\text{mean},y} \cdot d_{\text{inner}}}{\lambda_{L,\text{mean}}} \quad (4.64)$$

where $\alpha_{L,\text{mean},y}$ is the single-phase flow heat transfer coefficient calculated by Eq. (4.45) and $\lambda_{L,\text{mean}}$ is the mean liquid thermal conductivity of R-245fa. The uncertainty on the experimental Nusselt number is expressed as:

$$\delta\text{Nu}_{\text{exp}} = \sqrt{\left(\frac{d_{\text{inner}}}{\lambda_{L,\text{mean}}} \cdot \delta\alpha_{L,\text{mean},y}\right)^2 + \left(\frac{\alpha_{L,\text{mean},y}}{\lambda_{L,\text{mean}}} \cdot \delta d_{\text{inner}}\right)^2 + \left(-\frac{\alpha_{L,\text{mean},y} \cdot d_{\text{inner}}}{\lambda_{L,\text{mean}}} \cdot \delta\lambda_{L,\text{mean}}\right)^2} \quad (4.65)$$

The [Gnielinski (1976)] correlation is expressed as follows:

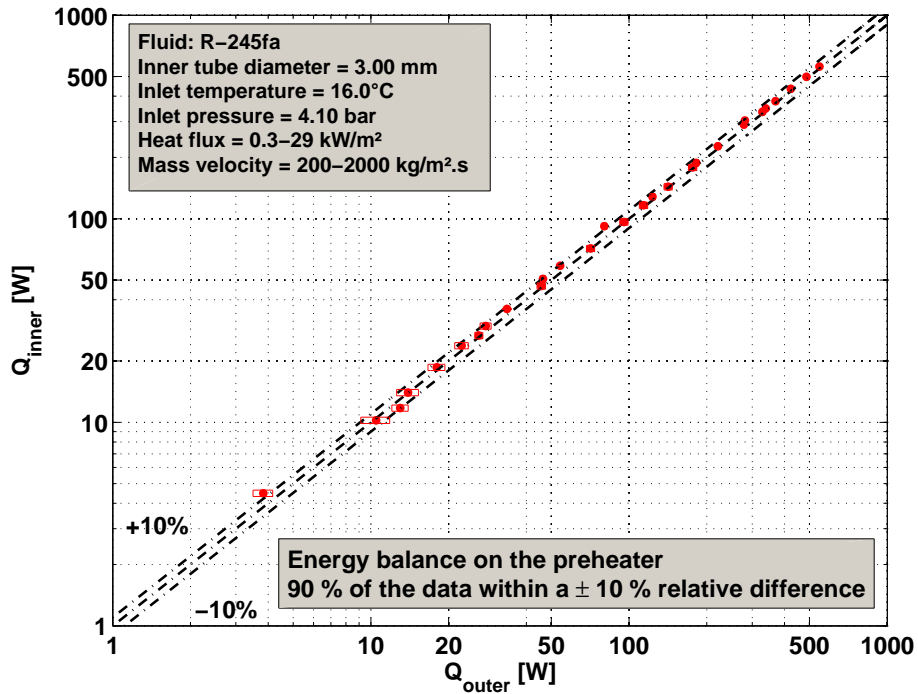
$$\text{Nu} = \frac{(f/8) \cdot (\text{Re}_L - 1000) \cdot \text{Pr}_L}{1 + 12.7 \cdot (f/8)^{1/2} \cdot (\text{Pr}_L^{2/3} - 1)} \quad (4.66)$$

The graph indicates a good agreement with these correlations as the Mean Absolute Error (MAE) is around 5 % and as this deviation is within the uncertainty range. However, the results were overestimated by these correlations. This validation concerns the twelve thermocouples.

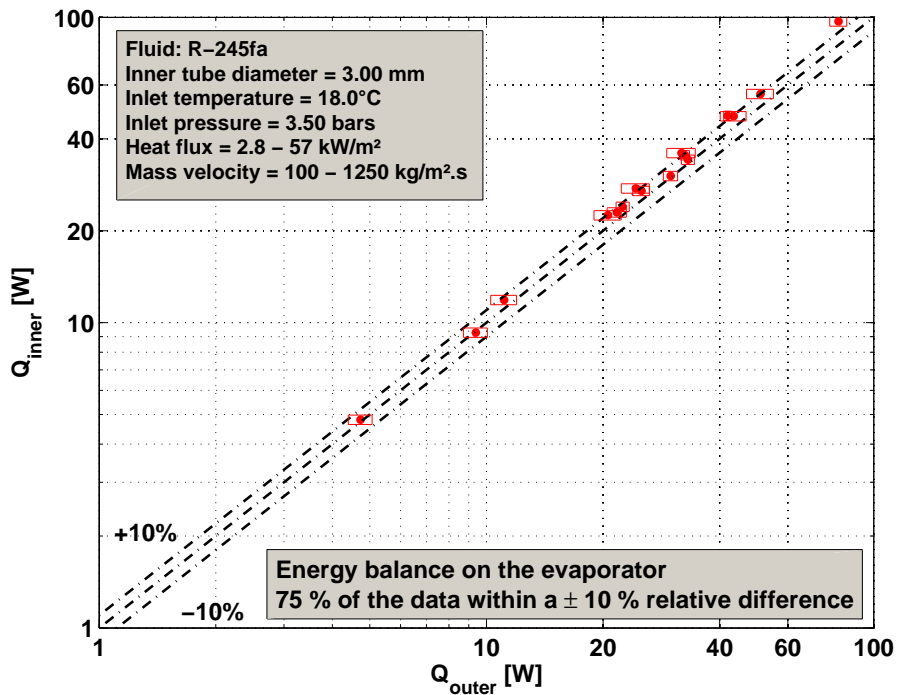
4.5.3 Pressure drop test section validation

The last single-phase flow validation deals with the pressure drop test section. The experimental friction factor was deduced from the following expression:

$$f = \frac{\Delta P \cdot d_{\text{inner}} \cdot \rho_L}{2 \cdot l_{\Delta P} \cdot G^2} \quad (4.67)$$



(a) Preheater.



(b) Evaporator.

Figure 4.9: Energy balance: single-phase validation

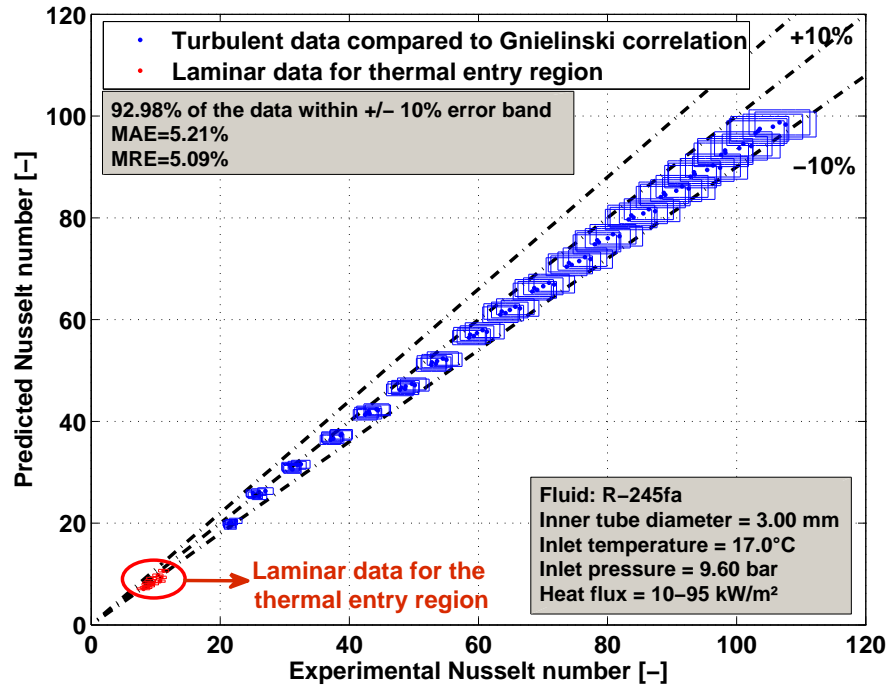


Figure 4.10: Comparison between experimental Nusselt numbers and predicted Nusselt number.

where ΔP is the pressure drop measured and $l_{\Delta P}$ is the length between the two pressure taps.

The uncertainty of the experimental friction factor is calculated from:

$$\delta f = \sqrt{\left(\frac{\partial f}{\partial \Delta P} \cdot \delta \Delta P\right)^2 + \left(\frac{\partial f}{\partial d_{\text{inner}}} \cdot \delta d_{\text{inner}}\right)^2 + \left(\frac{\partial f}{\partial \rho_L} \cdot \delta \rho_L\right)^2 + \left(\frac{\partial f}{\partial l_{\Delta P}} \cdot \delta l_{\Delta P}\right)^2 + \left(\frac{\partial f}{\partial G} \cdot \delta G\right)^2} \quad (4.68)$$

Then, this value of friction factor is compared with the theoretical value calculated by two different correlations: the Blasius correlation and the [Churchill (1977)] correlation. The [Churchill (1977)] correlation is valid for laminar, transition, and turbulent flow regimes. This correlation is expressed as:

$$f_{\text{Churchill}} = 2 \cdot \left[\left(\frac{8}{\text{Re}} \right)^{12} + \frac{1}{(A + B)^{3/2}} \right]^{1/12} \quad (4.69)$$

where A and B are calculated with the following equations:

$$A = \left[2.457 \cdot \ln \frac{1}{\left(\frac{7}{\text{Re}} \right)^{0.9} + \frac{0.27 \cdot R_p}{d_{\text{inner}}}} \right]^{16} \quad (4.70)$$

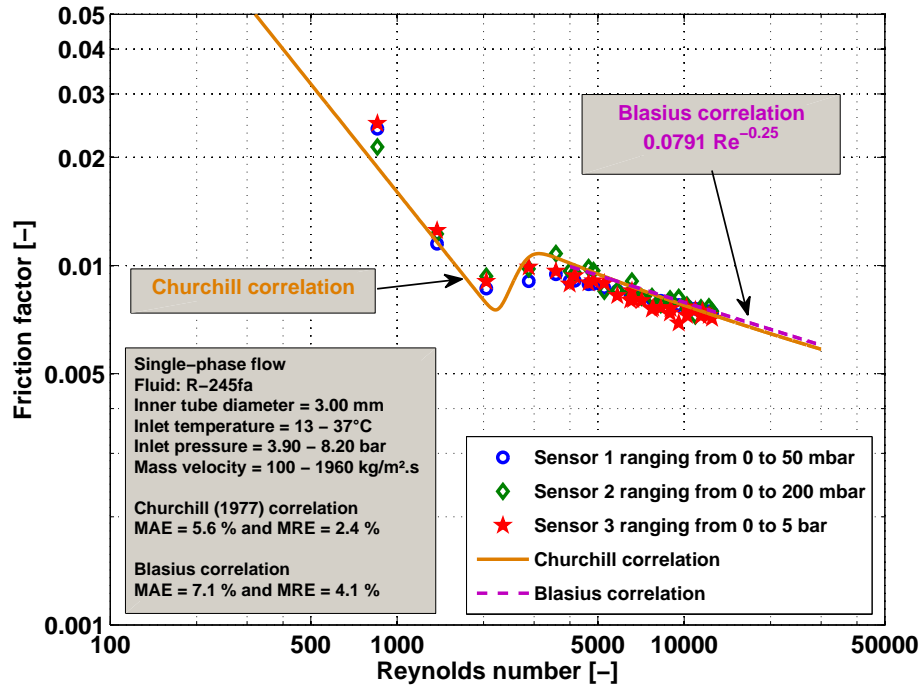


Figure 4.11: Comparison between experimental friction factors and predicted friction factors.

$$B = \left(\frac{37530}{Re} \right)^{16} \quad (4.71)$$

The Blasius correlation is valid for Reynolds numbers ranging from 4000 to 100000 and it is expressed as:

$$f_{\text{Blasius}} = 0.079 \cdot Re^{-0.25} \quad (4.72)$$

Figure 4.11 shows a comparison between the experimental friction factor and the predicted friction factor calculated by the Blasius and [Churchill (1977)] correlations. The graph indicates a good agreement with these correlations as the Mean Absolute Error (MAE) is around 5 % and 7 % for the [Churchill (1977)] and Blasius correlations, respectively. This validation concerns the three differential pressure transducers. The uncertainties bars are not plotted for a better readability of the graph. They are however plotted in Fig. 4.12.

Figure 4.12 shows a comparison between the experimental pressure drop and the predicted pressure drop with the correlation of [Churchill (1977)] for the three pressure drop transducers. The uncertainties on the measurements are represented with the horizontal bars. The difference between the sensors is relatively low and the deviation from the predicted values is within the uncertainty range.

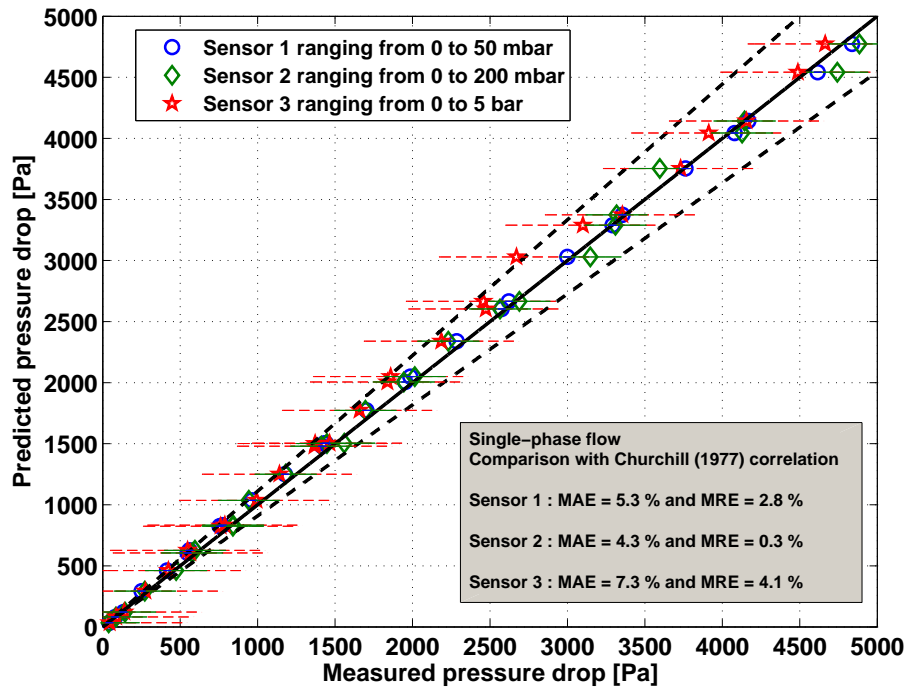


Figure 4.12: Comparison between experimental pressure drop measured by the three different sensors and the pressure drop calculated by [Churchill (1977)].

Table 4.5: Optical measurement conditions.

Parameter	Range	Units
Frame rate	3000	frames/s
Shutting speed	1/402000	s
Acquisition time	2	s
Frame size	128x1024	pixel
Grayscale value	0 - 255	

4.6 Image processing method

4.6.1 Description of the technique

4.6.1.1 General description

An optical method to characterize the two-phase flow regimes, to determine the bubbles frequency and to measure the velocity of bubbles was developed. Two instruments were used to visualize the two-phase flow: a high-speed image acquisition system and an image processing program written under Matlab environment. The experimental setup (Fig. 4.13) consists of a high-speed camera system (*PHOTRON FASTCAM 1024 PCI model 100K*). The main parameters of the image acquisition are summarized in Table. 4.5. The recording speed of 3000 frames/s was found to be a good trade-off between file size and image quality. The light system used for the visualization is provided through an adjustable light source behind the visualization glass tube.

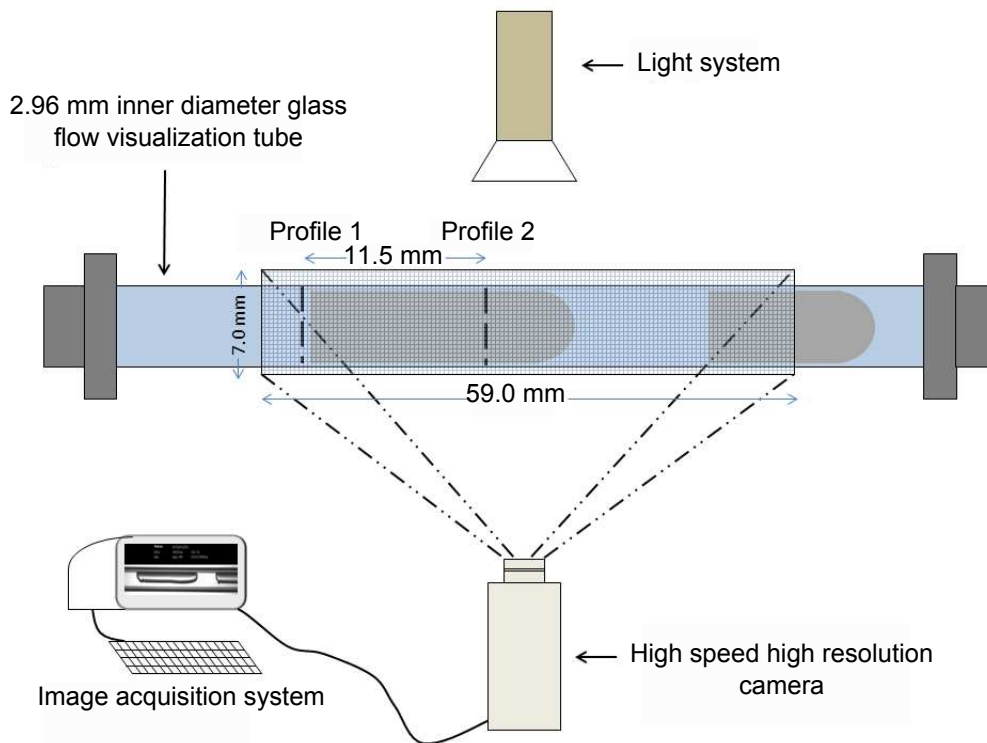


Figure 4.13: Diagram of the image acquisition system.

The size of the image is 128×1024 pixels. Each pixel has a grayscale value ranging from 0 to 255. Note that the grayscale used here is inverted from the traditional grayscale. Indeed, in the present study, a grayscale value equal to 0 corresponds to the white color and a grayscale value equal to 255 corresponds to the black color, as shown Fig. 4.14. This choice has been made to improve the distinction between the two phases and to have a grayscale value of the liquid phase close to 0 and a grayscale value of the vapor phase close to 255.

To characterize the flow configuration along the cross section, a profile line is placed from the top to the bottom position of the inner diameter, as represented in Fig. 4.15 (profile 1). This choice can be justifiable when only one bubble passes the profile at a time. This profile line has been placed as close as possible to the entrance of the glass tube. Indeed, the vapor quality entering the flow visualization

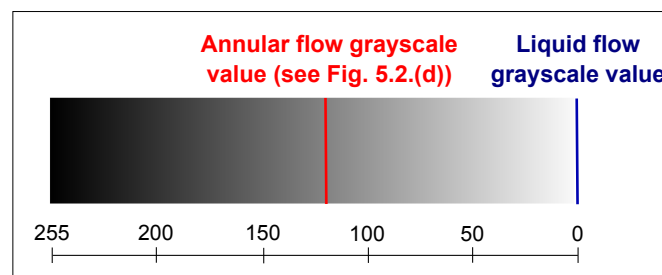


Figure 4.14: Grayscale value used in the image processing.

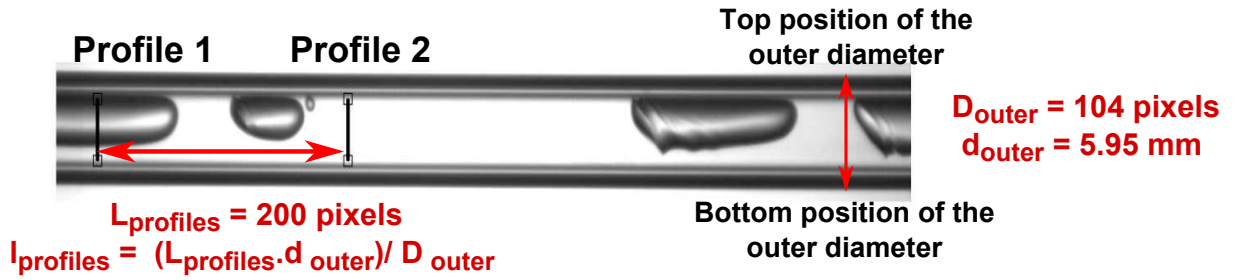


Figure 4.15: Profile positions and image information necessary for scale plan calculation.

section was determined at the outlet of the evaporator. In the present study, profile 1 was placed 2.9 mm from the entrance of the glass tube. For each image, the mean grayscale value along a profile is calculated from the grayscale values of each pixel along this profile. The acquisition time is 2 seconds and corresponds to 6 000 frames. Figure 4.16(a) shows the mean grayscale values as a function of time for a bubbly-slug flow regime.

All flow patterns, as for example the one shown for a bubbly-slug flow in Fig. 4.16(a), exhibit pulsed signals with peaks corresponding to the vapor phase and troughs corresponding to the liquid phase. To count the bubbles, a threshold line must be placed between the liquid and the vapor grayscale levels at a specific value. This value has been chosen according to Fig. 4.16(b) which represents the histogram of distribution of the signal in 5 particular grayscale ranges.

The threshold, in red line in Fig. 4.16(b), is placed 20 grayscale value after the first peak. Threshold is 25 in the present case. When the grayscale value is below the threshold, the presence of liquid is retained whereas a value greater than the threshold means the presence of vapor. [Revellin et al. (2006)] used two thresholds to distinguish between wavy annular flow and smooth annular flow. However, in the present study, these flow regimes are grouped together into annular flow, which explains why one threshold is necessary.

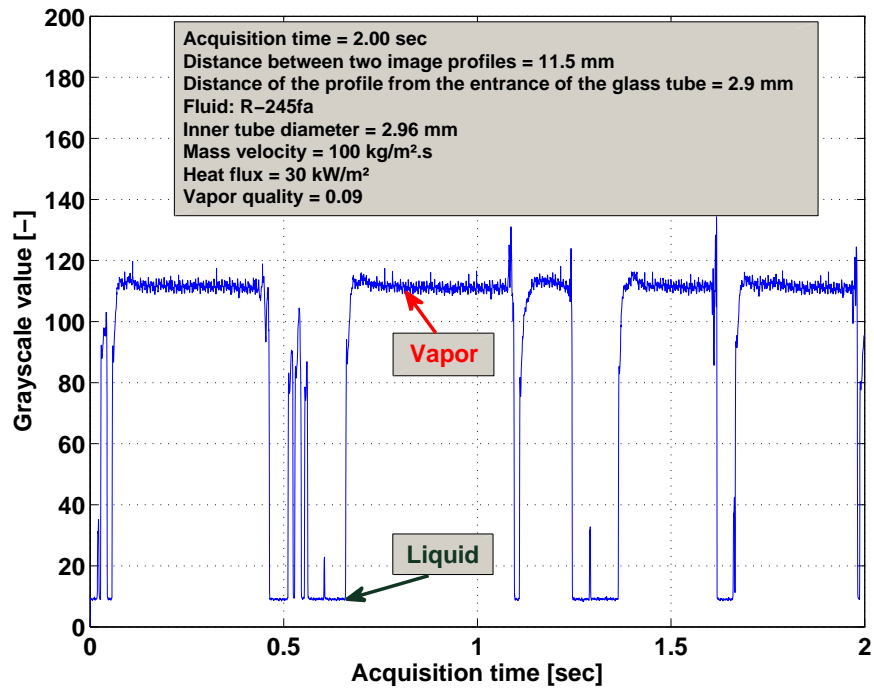
4.6.1.2 Bubble frequency

From the grayscale signal, the bubble frequency (average number of bubble passages per second) can be computed easily.

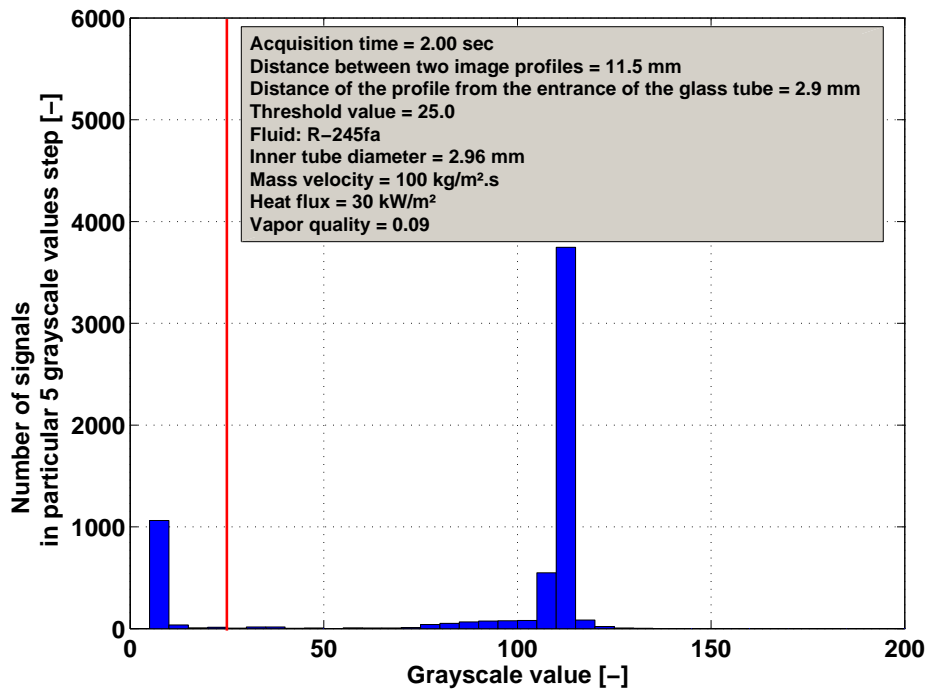
4.6.1.3 Bubble velocity

The method to determine the vapor bubble velocity is based on the presence of two profiles, as shown in Fig. 4.15 separated by a known distance, namely 11.5 mm in the present experiment. This distance (l_{profiles}) was calculated from the length in pixel (L_{profiles}) and a scale conversion factor (Sc [m/pixel]) that is the ratio between the tube outer diameter (5.95 mm) (d_{outer}) and the number of pixels required to display the cross-section of the tube (D_{outer}):

$$Sc = \frac{d_{\text{outer}}}{D_{\text{outer}}} \quad (4.73)$$



(a) Image diagram.



(b) Image histogram.

Figure 4.16: Example of (a) a grayscale signal and (b) a histogram of its distribution showing the chosen threshold for characterizing a bubbly slug flow: (a) Signal at profile 1 versus time and (b) histogram of 6,000 images segregated into 5 grayscale value steps.

The uncertainty of the scale conversion factor is calculated with the following expression:

$$\delta S_c = \sqrt{\left(\frac{1}{D_{\text{outer}}} \cdot \delta d_{\text{outer}}\right)^2 + \left(\frac{-d_{\text{outer}}}{D_{\text{outer}}^2} \cdot \delta D_{\text{outer}}\right)^2} \quad (4.74)$$

where δD_{outer} is equal to 2 pixels. Indeed, for a position deduced from the image processing program, the uncertainty is ± 1 pixel. From Fig. 4.15, the scale conversion factor is equal to:

$$S_c = 0.0572 \pm 0.0011 \text{ mm/pixel} \quad (4.75)$$

A normalized cross-correlation was used to determine the mean velocity of the bubbles, as the ratio of the distance between profiles 1 and 2 and the time corresponding to the peak of the cross-correlation function (mean transit time). Figure 4.17 shows an example of normalized cross-correlation. From time delay between the two signals defined by the peak correlation (t_{cc}), the mean bubble velocity was calculated.

$$u_{\text{bubbles}} = \frac{l_{\text{profiles}}}{t_{\text{cc}}} = \frac{S_c \cdot L_{\text{profiles}}}{t_{\text{cc}}} \quad (4.76)$$

The uncertainty of the bubbles velocity is defined from the following equation:

$$\delta u_{\text{bubbles}} = \sqrt{\left(\frac{L_{\text{profiles}}}{t_{\text{cc}}} \cdot \delta S_c\right)^2 + \left(\frac{S_c}{t_{\text{cc}}} \cdot \delta L_{\text{profiles}}\right)^2 + \left(\frac{-S_c \cdot L_{\text{profiles}}}{t_{\text{cc}}^2} \cdot \delta t_{\text{cc}}\right)^2} \quad (4.77)$$

where $\delta L_{\text{profiles}}$ is equal to 2 pixels and δt_{cc} is the error made when determining the peak location of the cross correlation. [Revellin (2005)] fixed this error at 1 data point, i.e. in the present investigation $\delta t_{\text{cc}} = 1/3000$ s. From the cross-correlation signal presented in Fig. 4.17, the peak is located at $t_{\text{cc}} = 62$ msec. Thus, the mean bubble velocity in these conditions is equal to:

$$u_{\text{bubbles}} = 0.184 \pm 0.006 \text{ m/s} \quad (4.78)$$

4.6.1.4 Percentage of small bubbles

Given the mean bubble velocity and the transit time of the front and back interface of each vapor bubble, its length can be determined. A vapor bubble is called a small bubble when its length is lower than the tube inner diameter (3.00 mm). During the tests, the percentage of small bubbles was calculated. An elongated bubble flow corresponds to a percentage of small bubbles close to 0.

4.6.2 Experimental validation of the optical method parameters

In order to fix the main parameters of the optical measurement method, an experimental validation was performed before running image processing. These main

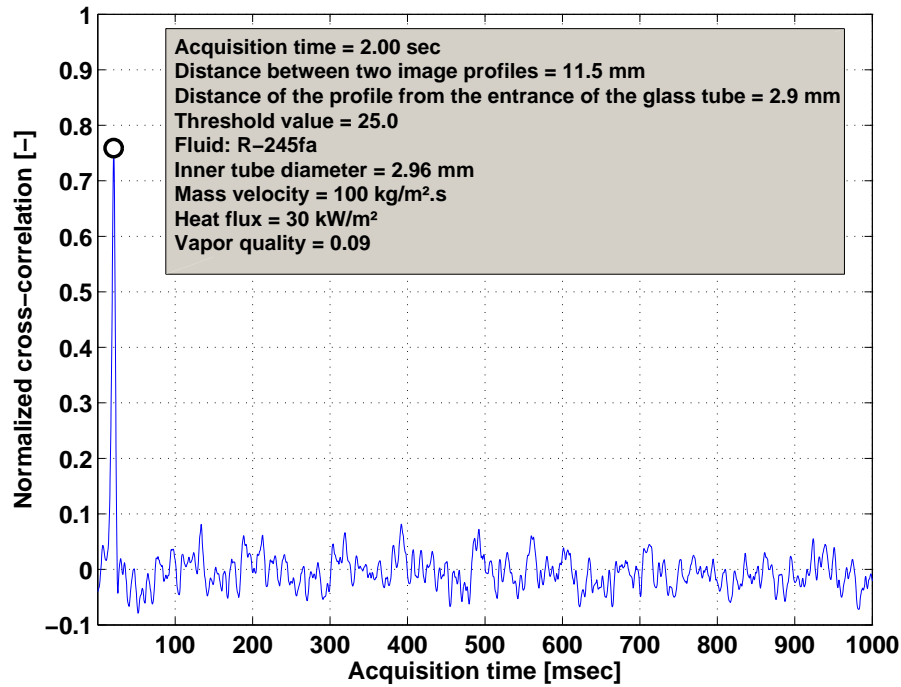


Figure 4.17: Example of normalized cross-correlation of grayscale value signals from the two profiles.

parameters are: the acquisition time and the distance between the two image profiles. Figures 4.18(a) and 4.18(b) represent the acquisition time validation for respectively the bubble velocity and the bubble frequency.

The chosen acquisition time is 2 seconds, value from which the bubble frequency and the bubble velocity are almost constant. Figure 4.18(c) shows the bubble velocity according to the distance between two image profiles. As can be seen, the distance has no effect on the bubble velocity and 11.5 mm has been selected. As a reminder, the threshold value is chosen from the histogram, as shown in Fig. 4.16(b), the position of profile 1 is driven by the obligation to be the closest from the glass tube entrance and the frame rate is chosen as a compromise of the file size and the image information.

4.7 Experimental procedures

Two distinct experimental procedures were used according to whether the tests were carried out under diabatic or adiabatic conditions. For the former, the heat transfer coefficients measurements and the flow pattern visualizations were performed simultaneously. Under these conditions, for one test, the mass velocity was fixed at the inlet of the preheater, the heat flux was imposed to the evaporator where the saturation temperature was also regulated. The vapor qualities at the position y (x_y) and at the outlet of the evaporator (x_{outlet}) were calculated as explained previously. These values of vapor quality were modified by adjusting the power of the preheater in order to cover a range from 0 to 1.

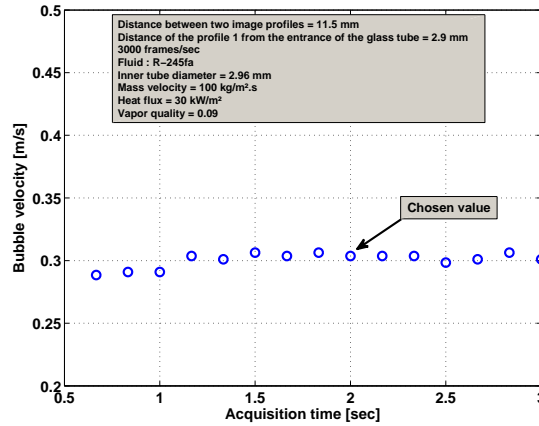
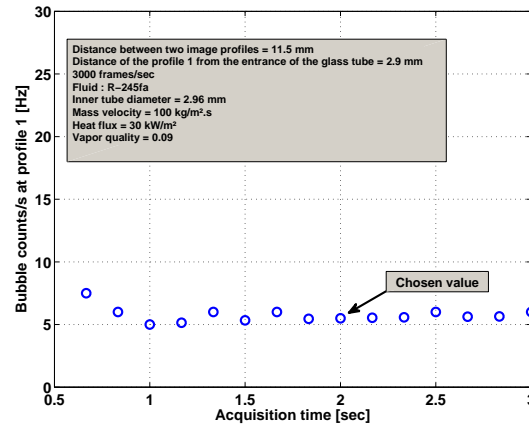
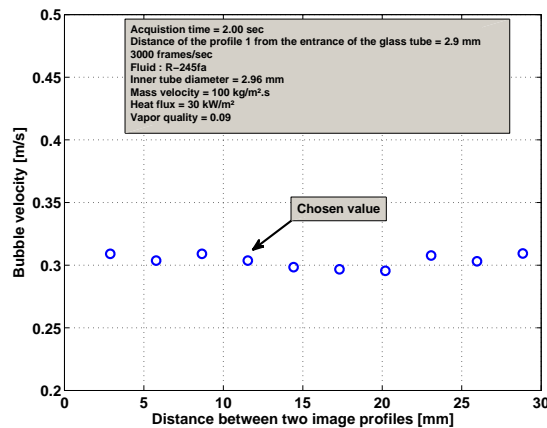
(a) Bubble velocity *vs.* acquisition time.(b) Bubble frequency *vs.* acquisition time.(c) Bubble velocity *vs.* $l_{profiles}$.

Figure 4.18: Method parameters validation for R-245fa with $d_{inner} = 3.00$ mm and $T_{sat} = 60$ °C: (a) bubble counts/s at profile 1 versus acquisition time : chosen value of acquisition time parameter, 2 seconds; (b) bubble velocity versus acquisition time : chosen value of acquisition time parameter, 2 seconds; (c) bubble frequency versus distance between two image profiles : chosen distance between two image profiles, 11.5 mm.

Table 4.6 summarizes the experimental conditions for the flow boiling experiments. For the heat transfer coefficients and flow patterns measurements, the experiments were carried out for seven mass velocities (100, 300, 500, 700, 1000, 1200 and 1500 kg/m²·s), for three heat fluxes (10, 30 and 50 kW/m²) and saturation temperatures of 60, 80, 100 and 120°C with R-245fa as the operating fluid. In addition, two tests were performed with 70 and 90kW/m² at 60°C. The diabatic experimental investigation entailed varying the vapor quality from 0 to 1 for a series of 86 configurations (characterized by a given G , a given \dot{q}_{evap} , and a given T_{sat}). The step of vapor quality was not fixed but rather progressive according to the observed phenomena. For instance, a focus was made on the flow regime transition zones.

Table 4.6: Experimental conditions for flow boiling experiments.

Parameter	Range
d_{inner} [mm]	3.00
d_{outer} [mm]	5.99
l_{evap} [mm]	185.0
\dot{q}_{ph} [kW/m ²]	0.5 - 20.0
\dot{q}_{evap} [kW/m ²]	0 - 90.0
G [kg/m ² ·s]	100 - 1500
T_{sat} [°C]	60 - 120
x [-]	0-1

Under adiabatic conditions, the pressure drop measurements were performed. The desired vapor quality at the inlet of the pressure drop test section (x_{inlet}) was obtained by adjusting the power of the preheater. The vapor quality ranged from 0 to 1. The saturation temperature was regulated at the inlet of the pressure drop test section and the mass velocity was imposed at the inlet of the preheater. The same ranges in G and T_{sat} as those studied for diabatic conditions were investigated in order to utilize the information obtained on the flow patterns. Table 4.7 summarizes these experimental conditions for the two-phase flow experiments. Finally, the campaign of adiabatic experiments entailed varying x_{inlet} from 0 to 1 for a series of 28 configurations (characterized by a given G , a given T_{sat}).

Table 4.7: Experimental conditions for two-phase flow experiments.

Parameter	Range
d_{inner} [mm]	3.00
d_{outer} [mm]	5.99
$l_{\Delta P}$ [mm]	350.0
G [kg/m ² ·s]	100 - 1500
T_{sat} [°C]	60 - 120
x [-]	0-1

4.8 Conclusions

A new multipurpose minichannel test facility has been built at the Centre Thermique de Lyon (CETHIL UMR-5008) to investigate the flow boiling of refrigerants at high saturation temperatures. A test section has been developed to perform flow visualizations, flow boiling heat transfer coefficient measurements, and two-phase flow pressure drop measurements. Single-phase flow validation has been carried out and the results valid the accuracy of the measurements. Furthermore, an optical measurement method based on image processing technique has been developed and perfected to quantitatively identify flow patterns, obtain bubble frequencies and lengths and measure bubble velocities.

Chapter 5

Flow patterns and bubble dynamics

In this chapter, a description of the two-phase flow patterns observed for R-245fa in a minichannel at high saturation temperature will be presented. The method to characterize them from objective criteria based on image processing and an appropriate analysis of the heat transfer coefficient will be developed. The effect of the heat flux, the mass velocity and the saturation temperature on the flow pattern will be introduced and discussed. Following this, a new diabatic flow pattern map at high saturation temperature will be presented. The flow patterns transition deduced from the experiments will be compared to predictions available in the literature. Additionally, measurements of the mean bubble velocity obtained from the image processing will be presented.

5.1 Flow pattern characterization

5.1.1 Visualization

From the image processing method described in section 4.6, four flow patterns can be quantitatively identified: bubbly flow, bubbly-slug flow, slug flow and annular flow. Figure 5.1 displays photos of these four flow patterns that were observed in our experimental test bench as described in section 4.2, especially, the 2.96 mm inner diameter tube used for visualization. Wavy-annular flow and smooth annular flow are grouped together in annular flow. This choice is driven by the will to stick to the five primary flow regimes (presented in Fig. 3.17) as recommended by [Thome et al. (2013)] for the sake of making future data usable by others.

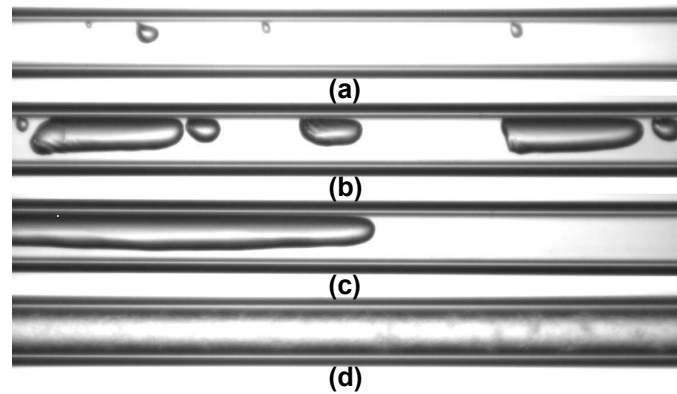


Figure 5.1: Flow pattern photos for R-245fa with $d_{\text{inner}} = 2.96$ mm and $T_{\text{sat}} = 60^\circ\text{C}$: (a) bubbly flow at $x = 0.01$, $G = 500$ kg/m²·s and $\dot{q} = 50$ kW/m²; (b) bubbly-slug flow at $x = 0.05$, $G = 300$ kg/m²·s and $\dot{q} = 50$ kW/m²; (c) slug flow at $x = 0.16$, $G = 100$ kg/m²·s and $\dot{q} = 30$ kW/m²; (d) annular flow at $x = 0.92$, $G = 500$ kg/m²·s and $\dot{q} = 50$ kW/m².

5.1.1.1 Flow pattern features

The identification of the flow regime was made from the signal diagram that was reduced to determine the bubble frequency and a percentage of bubbles considered as “small”. When a bubble is smaller in length than the internal diameter of the channel, it is classified as a “small bubble”; otherwise, it is defined here as an “elongated bubble”. The flow patterns and their transitions are defined as follows:

- *Bubbly flow* : In bubbly flow, the vapor phase is distributed as discrete bubbles in a continuous liquid phase and the bubbles are smaller in length than the diameter of the tube (Fig. 5.1(a)). This regime is considered to occur when the percentage of the small bubbles in the flow ranges from 95%¹ to 100% while a non-zero bubble frequency is measured. Figure 5.2(a) shows the grayscale value/time signal for this flow with the periodic passage of small bubbles.
- *Bubbly – Slug flow* : In bubbly-slug flow, bubbly flow (described above) and slug flow (described below) are both present as shown in Fig. 5.1(b). This

¹The transition thresholds for the percentage of small bubbles were fixed to 5% and 95% according to the experimental visualizations and the results. Note that a small variation of these threshold values (e.g. 1% and 99% as proposed by [Revellin et al. (2006)]) do not seem to influence the results.

regime is identified when the percentage of surviving small bubbles is in the range from 5%¹ to 95%¹ while a non-zero bubble frequency is measured. As a matter of fact, the term of surviving bubbles defines bubbles that are not yet coalesced into elongated bubbles. Figure 5.2(b) corresponds to the signal for this flow with some thin peaks (vapor bubbles) and large peaks (vapor slugs).

- *Slug flow* : In slug flow, the vapor bubbles are greater in length than the diameter of the tube, but the length can vary considerably. The nose of the bubble has a characteristic hemispherical cap and the vapor in the bubbles is separated from the tube wall by a thin film of liquid. The liquid flow is contained mostly in the liquid plugs which separate successive vapor bubbles (Fig. 5.1(c)). This flow pattern corresponds to a percentage of small bubbles ranging from 0% to 5%¹ while a non-zero bubble frequency is measured. Slug flow is assumed as predominant even if 5%¹ of the small bubbles survive. Indeed, few small bubbles can be present at the end of the vapor slug but are not representative of the flow regime. Figure 5.2(c) shows the grayscale value/time signal, the vapor slugs are clearly detectable.
- *Annular flow* : In annular flow, a liquid film flows on the tube wall with a continuous central vapor core (Fig. 5.1(d)). Liquid slugs are not present. Two types of annular flow were detected during the test, viz. wavy-annular flow and smooth annular flow. As justified before, both are grouped together into annular flow. Annular flow is characterized by a bubble frequency equal to 0 Hz. This type of signal is represented in Fig. 5.2(d).

From the results on the influence of the kind of flow patterns on the heat transfer coefficient (addressed in section 6.1), the choice to focus our attention on the transition to annular flow were made. In a consequence, bubbly flow, bubbly-slug flow, and slug flow were grouped together into intermittent flow.

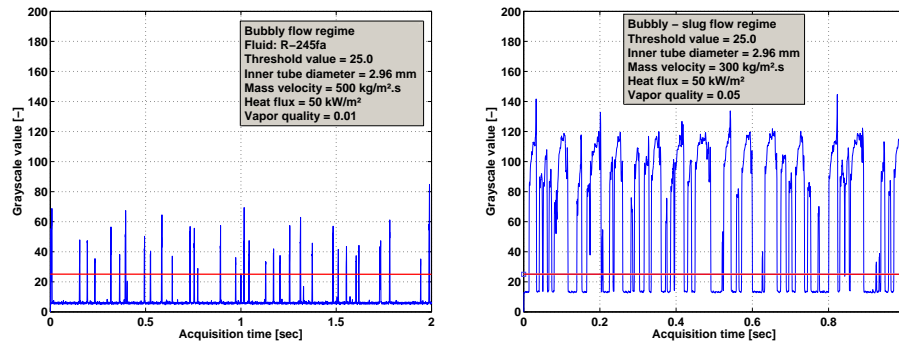
5.1.1.2 Characterization results

Figure 5.3 presents the two main flow patterns that were detected with the help of the optical measurement technique, i.e. intermittent flow ($f_{\text{bubbles}} = 131$ Hz) and annular flow ($f_{\text{bubbles}} = 0$ Hz), the former grouping together the bubbly, bubbly-slug and slug flow regimes. These visualizations have been carried out for a saturation temperature of 120°C, a heat flux of 50 kW/m² and a mass velocity of 500 kg/m²·s.

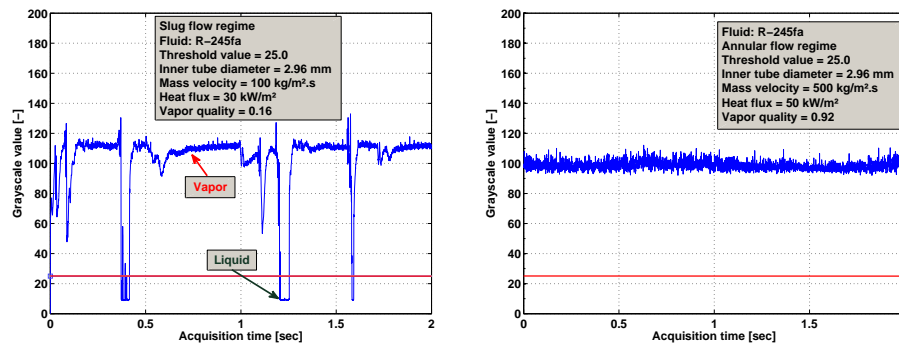
5.1.2 Dryout and mist flow regimes characterization

Apart from the intermittent and annular flow regimes identified by the optical measurement technique, two other flow regimes can be detected from the analysis of measurement of the inner wall temperatures and from the resulting heat transfer coefficient. Figure 5.4 shows the saturation temperature (almost constant over the range of vapor quality), the top and bottom inner wall temperatures and the mean heat transfer coefficient. A diagram of the flow regimes encountered along the evaporator is also proposed on Fig. 5.4 to better highlight the relation between heat transfer and flow regimes.

¹The transition thresholds for the percentage of small bubbles were fixed to 5% and 95% according to the experimental visualizations and the results. Note that a small variation of these threshold values (e.g. 1% and 99% as proposed by [Revellin et al. (2006)]) do not seem to influence the results.



(a) Bubbly flow at $x = 0.01$, $G = 500 \text{ kg/m}^2\cdot\text{s}$ and $\dot{q} = 50 \text{ kW/m}^2$. (b) Bubbly-slug flow at $x = 0.05$, $G = 300 \text{ kg/m}^2\cdot\text{s}$ and $\dot{q} = 50 \text{ kW/m}^2$.



(c) Slug flow at $x = 0.16$, $G = 100 \text{ kg/m}^2\cdot\text{s}$ and $\dot{q} = 30 \text{ kW/m}^2$. (d) Annular flow at $x = 0.92$, $G = 500 \text{ kg/m}^2\cdot\text{s}$ and $\dot{q} = 50 \text{ kW/m}^2$.

Figure 5.2: Flow pattern signals with thresholds for R-245fa with $d_{\text{inner}} = 2.96 \text{ mm}$ and $T_{\text{sat}} = 60 \text{ }^\circ\text{C}$.

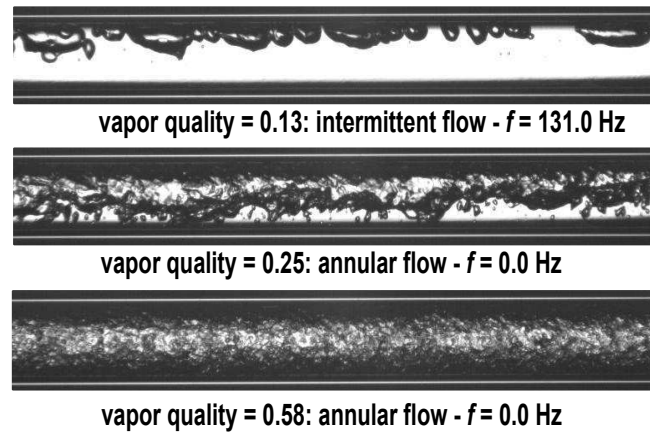


Figure 5.3: Influence of the vapor quality on the flow patterns for R-245fa in a 2.96 inner tube diameter at $T_{\text{sat}} = 120 \text{ }^\circ\text{C}$, $\dot{q} = 50 \text{ kW/m}^2$ and $G = 500 \text{ kg/m}^2\cdot\text{s}$.

In the intermittent and annular flow regimes, the channel walls are wetted by the liquid and the heat transfer coefficient is high. The top and bottom inner wall temperatures are nearly the same.

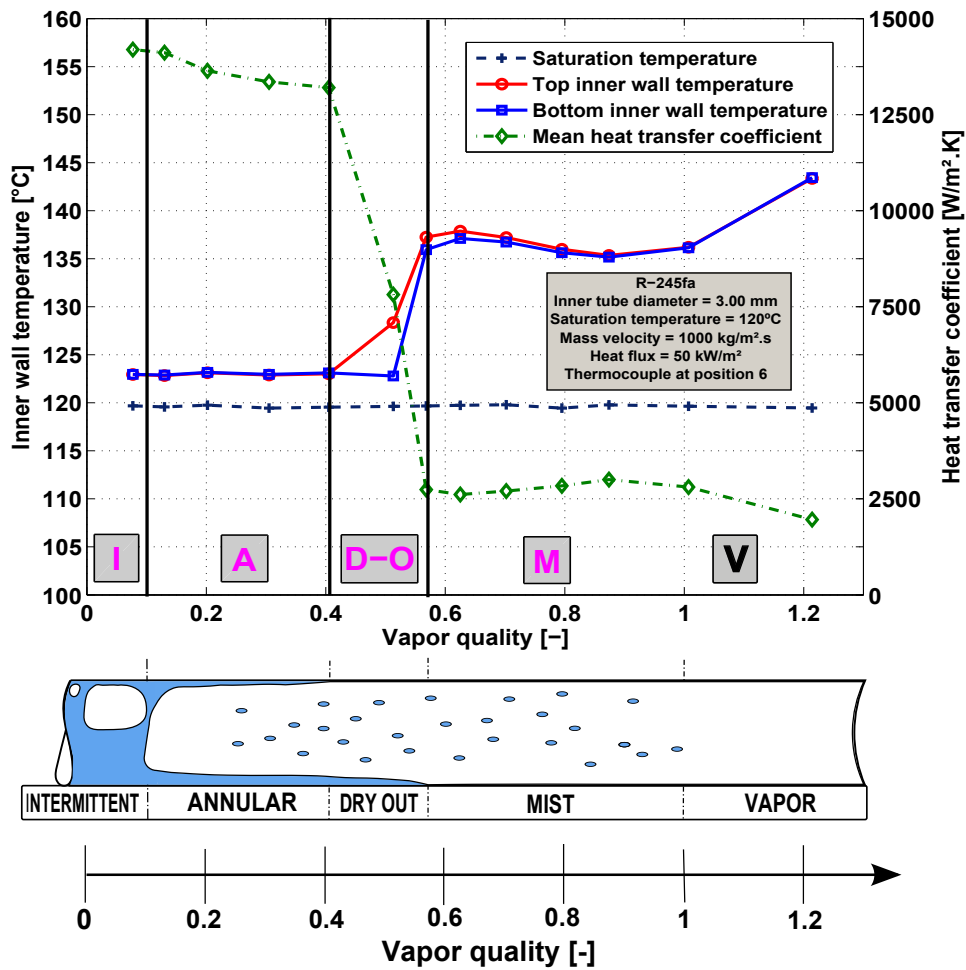


Figure 5.4: Temperatures and heat transfer coefficients as a function of vapor quality at 120°C with flow patterns (I: intermittent; A: annular; D-O: dryout; M: mist flow and V: vapor).

The steep increase in the inner wall temperatures at $x = 0.4$ results in a corresponding stiff decrease in the heat transfer coefficient that announces the occurrence of dryout. The heat transfer coefficient falls over a limited quality range and then becomes nearly constant in value. The vertical line at $x = 0.4$ indicates the inception point of dryout (x_{di}) at the top of the horizontal tube, where locally the heat transfer begins to fall as the annular film dries out. The vertical line at $x = 0.57$ indicates the location where dryout is complete (x_{de}) around the tube perimeter, and thus also where the deterioration of the heat transfer ends. The distinction of these two points is caused by the shift of the dryout position from the top to the bottom around and along the tube perimeter with increasing quality. Indeed, the inner wall temperature at the top starts to increase at lower vapor quality than inner wall temperature at the bottom. The dryout completion ($x = 0.57$) corresponds to the inception of the mist flow regime where the liquid film is entrained into the high velocity vapor core with or without redistribution on the channel walls. Similar results were reported by [Mori et al. (2000)] for R-134a and [Wojtan et al. (2005a)] for R-22 and R-410A.

Finally, based on the optical measurement technique and the analysis of the inner wall temperatures and the resulting heat transfer coefficients, it is possible to identify 4 main flow regimes which are:

- Intermittent flow (bubble frequency greater than 0 Hz)
- Annular flow (bubble frequency equal to 0 Hz)
- Dryout (major decrease of the heat transfer coefficient)
- Mist flow (heat transfer coefficient becomes nearly constant)

5.2 Flow regime transitions

This section presents an analysis of the parametric influence of the main flow parameters (mass velocity, heat flux, and vapor quality) and of the saturation temperature on the flow pattern transitions.

5.2.1 Intermittent-to-annular transition

5.2.1.1 Influence of mass velocity

The influence of the mass velocity on the flow regimes can be seen on Fig. 5.5 for a saturation temperature of 120°C, a heat flux of 50 kW/m² and a vapor quality of 0.32. When the mass velocity increases, the flow tends to be annular, i.e. a bubble frequency decreasing from 28.5 to 0 Hz. In addition, the liquid-vapor interface is more and more disturbed due to increasing shear stress.

In order to confirm the influence of the mass velocity made from the visualizations, the mean bubble frequency and the percentage of small bubbles were determined for different flow conditions. Figure 5.6(a) shows typical results of the bubble frequency vs. the vapor quality for a saturation temperature of 60°C, a heat flux of 50 kW/m² and three different mass velocities. In Fig. 5.6(a), each curve exhibits three different slopes which correspond to:

- an increase of the bubble frequency: the number of bubbles (small and/or elongated) increases quickly with the increase of the vapor quality until reaching a maximum value. This phenomenon could be partly linked to the bubbly

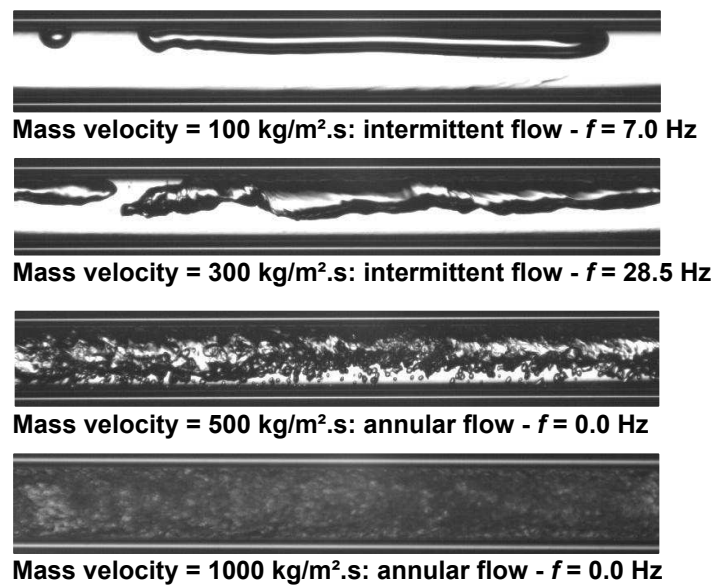


Figure 5.5: Influence of the mass velocity on the flow patterns for R-245fa in a 2.96 inner tube diameter at $T_{\text{sat}} = 120$ °C, $\dot{q} = 50$ kW/m² and $x = 0.32$.

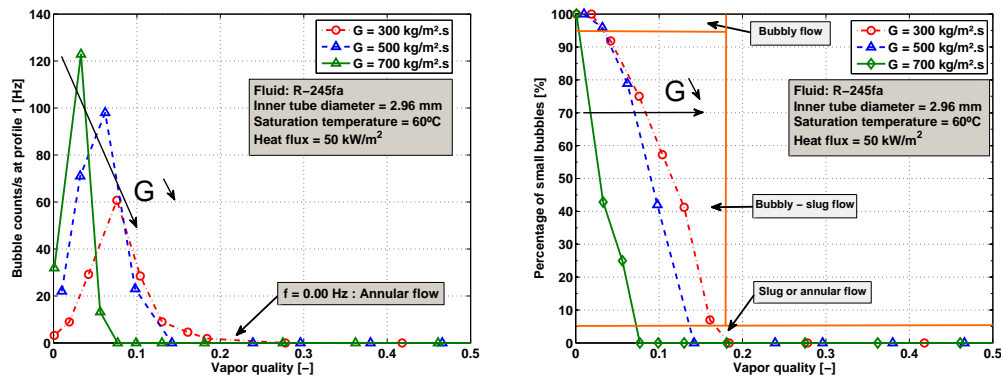
flow and the bubbly/slug flow regimes which are classified into intermittent flow as explained before in section 5.1.1.1.

- a decrease of the bubble frequency: the number of bubbles decreases from the maximum value to 0 Hz. The decrease of the number of bubbles is related to the coalescence. This decrease corresponds to bubbly-slug and slug flows.
- bubble frequency equal to 0 Hz which reveals the occurrence of annular flow.

Such a behavior was previously observed by [Revellin et al. (2008)] and [Arcanjo et al. (2010)] as shown in Fig. 3.5. In Fig. 5.6(a), in the rising frequency zone, for a given vapor quality, the higher the mass velocity, the larger the bubble frequency, whereas in the decreasing frequency zone, the bubble frequency decreases when the mass velocity increases. [Arcanjo et al. (2010)] suggested that such a behavior could be related to the increase of the turbulence intensity with the mass velocity and its effect on the bubble departure and elongated bubble growth and coalescence. Besides, the vapor quality corresponding to the maximum bubble frequency decreases when the mass velocity increases. This behavior can be explained by the fact that for a given vapor quality, the numbers of bubbles increases with increasing the mass velocity, so, it is logical that the beginning of the bubble coalescence occurs for lower vapor quality and consequently the decrease in the bubble frequency at lower vapor qualities.

Figure 5.6(b) shows the percentage of small bubbles as a function of the vapor quality for $T_{\text{sat}} = 60$ °C, $\dot{q} = 50$ kW/m² and different mass velocities. In this graph, the transition between bubbly flow, bubbly-slug flow, and slug-annular flow are represented, for further information, according to the percentage of small bubbles as following:

- from 95% to 100%: Bubbly flow;
- from 5% to 95%: Bubbly - slug flow;



(a) Effect of mass velocity on bubble frequencies. (b) Effect of mass velocity on percentage of small bubbles.

Figure 5.6: Influence of the mass velocity on the vapor bubble characteristic for R-245fa, $d_{\text{inner}} = 2.96$ mm, $T_{\text{sat}} = 60$ °C and $\dot{q} = 50$ kW/m².

- from 0% to 5%: Slug or annular flow.

At a given vapor quality, the lower the mass velocity, the larger the percentage of small bubbles. In Fig. 5.6(b), the curves show clearly that annular flow occurs for lower qualities when the mass velocity increases. Indeed, bubbly flow tends to disappear at high mass flux because small bubbles quickly coalesce to form elongated bubbles.

5.2.1.2 Influence of heat flux

The heat flux may also influence the flow regimes characteristics. Figure 5.7 shows the intermittent flow and annular flow regimes for three different heat fluxes for a saturation temperature of 120°C, a mass velocity of 500 kg/m²·s and a vapor quality of 0.20. As can be seen, the higher the heat flux, the greater the number of vapor slugs. This characteristic will have for sure an influence on the flow regime transitions.

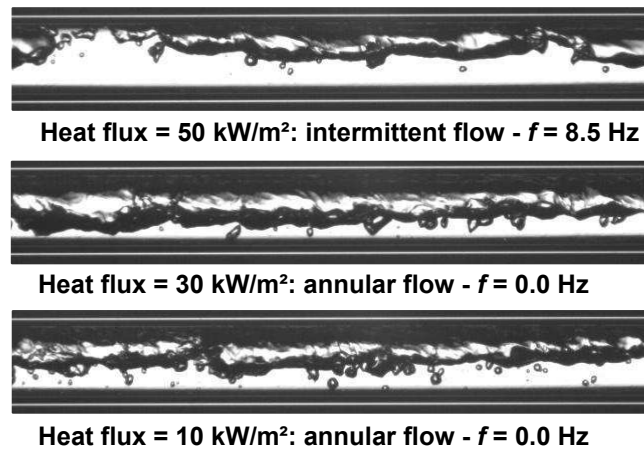
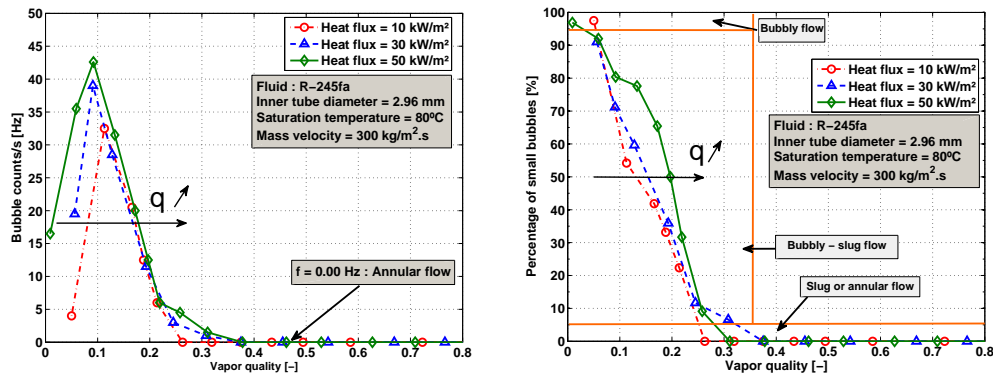


Figure 5.7: Influence of the heat flux on the flow patterns for R-245fa in a 2.96 inner tube diameter at $T_{\text{sat}} = 120$ °C, $G = 500$ kg/m²·s and $x = 0.20$.

Figure 5.8 shows the influence of the heat flux on the bubble frequency and the percentage of small bubbles for $T_{\text{sat}} = 80^\circ\text{C}$, $G = 300\text{ kg/m}^2\cdot\text{s}$, and three different heat fluxes (10, 30, and 50 kW/m^2). The trends of the bubble frequency as a function of the vapor quality are those expected and similar to those presented in Fig. 5.6(a). This graph confirms the observation made from the visualization, i.e. the higher the heat flux, the higher the bubble frequency. Figure 5.8(b) shows that, at a given vapor quality, the larger the heat flux, the greater the bubble frequency. Both figures indicate that the larger the heat flux, the larger the vapor quality for intermittent-to-annular transition. In conclusion, the results of the bubble frequency and the percentage of small bubbles confirm the observations made from the visualizations.



(a) Effect of heat flux on bubble frequencies. (b) Effect of heat flux on percentage of small bubbles.

Figure 5.8: Influence of the heat flux on the vapor bubble characteristic for R-245fa, $d_{\text{inner}} = 2.96\text{ mm}$, $T_{\text{sat}} = 80^\circ\text{C}$ and $G = 300\text{ kg/m}^2\cdot\text{s}$.

5.2.1.3 Influence of saturation temperature

Another parameter that may affect flow regimes is the saturation temperature. Figure 5.9 presents the observations of the flow regimes for 60, 80, 100 and 120°C at two different vapor qualities and for a given mass velocity of $500\text{ kg/m}^2\cdot\text{s}$ and heat flux of 50 kW/m^2 along with a schematic of the cross-section to better see the stratification effect.

Table 5.1: R-245fa properties at 60°C and 120°C

	ρ_L [kg/m ³]	ρ_V [kg/m ³]	μ_L [μPa.s]	μ_V [μPa.s]	σ [mN/m]
60°C	1237	25.7	265	12	9.59
120°C	998	119.7	125	15	2.64

As can be seen, the higher the saturation temperature, the thicker the liquid film thickness at the bottom, in other words the larger the stratification effect. Actually, the surface tension is divided by 3.6 when passing from 60 to 120°C (see Table 5.1) which explains the increasing tendency to stratification (gravity becoming predominant over surface tension effect when the saturation temperature increases). These results are in agreement with the approaches of [Kew and Cornwell (1997)], [Li

and Wang (2003)], and [Ong and Thome(2011a)] to predict the macro-to-microscale transition. Theoretically, when the saturation temperature increases, the threshold diameter decreases as shown in Fig. 3.1. Experimentally, the stratification effect, which is typical of the macroscale, increases with increasing the saturation temperature as shown in Fig. 5.9. Thus, the experimental results agree with the theory. Furthermore, the higher the temperature, the smaller and shorter the bubbles.

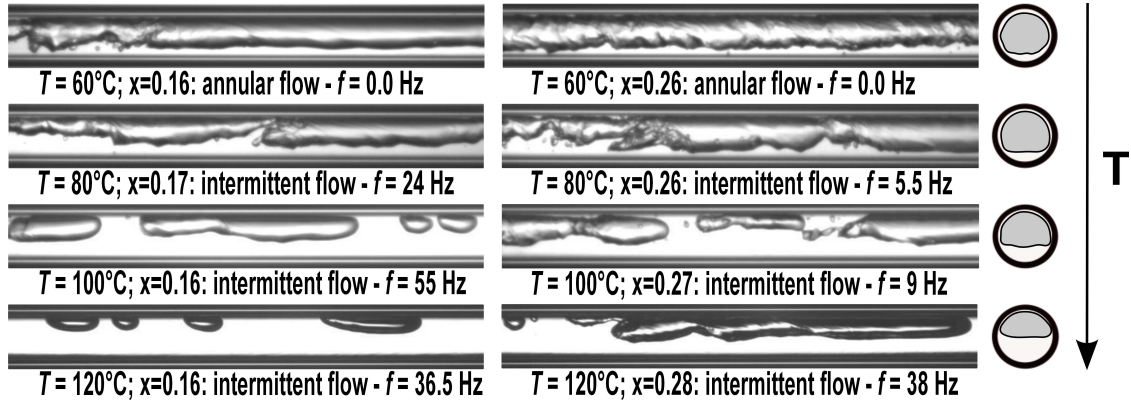


Figure 5.9: Influence of the saturation temperature on the flow patterns for R-245fa in a 2.96 inner tube diameter at $G = 500 \text{ kg/m}^2 \cdot \text{s}$ and $\dot{q} = 50 \text{ kW/m}^2$.

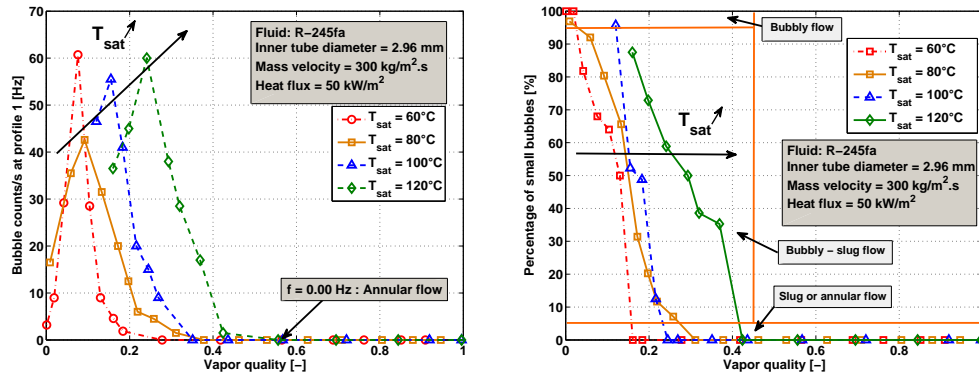
Figures 5.10 and 5.11 show the influence of the saturation temperature on the bubble frequency and the percentage of small bubbles at two different situations: (i) $\dot{q} = 50 \text{ kW/m}^2$ and $G = 300 \text{ kg/m}^2 \cdot \text{s}$ and (ii) $\dot{q} = 30 \text{ kW/m}^2$ and $G = 500 \text{ kg/m}^2 \cdot \text{s}$, respectively. Figures 5.10(b) and 5.11(b) corroborate the observation made from the visualization on the bubble size: the higher the temperature, the shorter the bubbles. This observation is directly related to the vapor density which passes from 25.7 kg/m^3 at 60°C to 119.5 kg/m^3 at 120°C (see Table 5.1).

According to Figs. 5.10(a) and 5.11(a), the vapor quality for the bubble frequency peak increases with increasing the saturation temperature. Furthermore, the intermittent-to-annular transition occurs for larger values of vapor quality when the saturation temperature increases. In general, the higher the saturation temperature, the larger the bubble frequency peak value. This observation is directly related to the decrease of surface tension with increasing the saturation temperature. During flow boiling, the bubble departure is given by a balance between surface tension forces, that act to keep the bubble attached to the wall, and buoyancy and drag forces that act in order to detach the bubble from the wall. As a consequence, by decreasing the surface tension, the bubble departure diameter decreases and the bubble frequency increases. [Taitel and Dukler (1976)] and [Arcanjo et al. (2010)] suggested that a decrease of the surface tension favored the breaking of bubbles by turbulence effects that may also result in an increase of the bubble frequency.

5.2.2 Annular-to-dryout transition

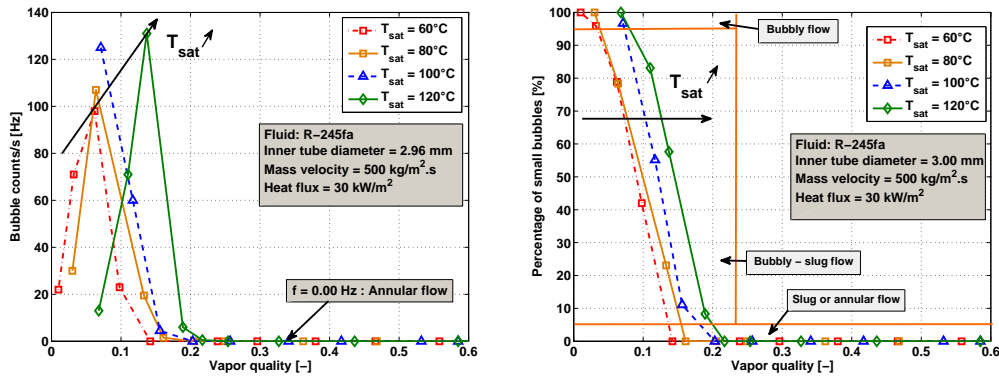
5.2.2.1 Influence of mass velocity

The mass velocity has also a significant influence on the inception and completion of dryout, as shown in Fig. 5.12 for a saturation temperature of 120°C . As can be seen, the higher the mass velocity, the lower the vapor quality at which dryout



(a) Effect of saturation temperature on bubble frequencies. (b) Effect of saturation temperature on percentage of small bubbles.

Figure 5.10: Influence of the saturation temperature on the vapor bubble characteristic for R-245fa, $d_{inner} = 2.96$ mm, $G = 300$ kg/m².s and $q = 50$ kW/m².



(a) Effect of saturation temperature on bubble frequencies. (b) Effect of saturation temperature on percentage of small bubbles.

Figure 5.11: Influence of the saturation temperature on the vapor bubble characteristic for R-245fa, $d_{inner} = 2.96$ mm, $G = 500$ kg/m².s and $q = 30$ kW/m².

occurs. In fact, the higher the mass velocity, the higher the shear stress and the higher the entrainment of droplets in the vapor core.

5.2.2.2 Influence of heat flux

Figure 5.13 presents the influence of the heat flux on the occurrence of dryout. The higher the heat flux, the lower the vapor quality at which dryout and mist flow start because the thinner the liquid film thickness. Such a behaviour was pointed out previously by [Wojtan et al. (2005a)].

5.2.2.3 Influence of saturation temperature

As shown in Fig. 5.9, the saturation temperature has a significant influence on the stratification. It is thus not surprising to see an increasing temperature difference between the top and the bottom of the tube as the saturation temperature increases (Fig. 5.14). When the temperature is equal to 80°C, there is almost no temperature difference because the liquid film exhibits almost the same thickness all around

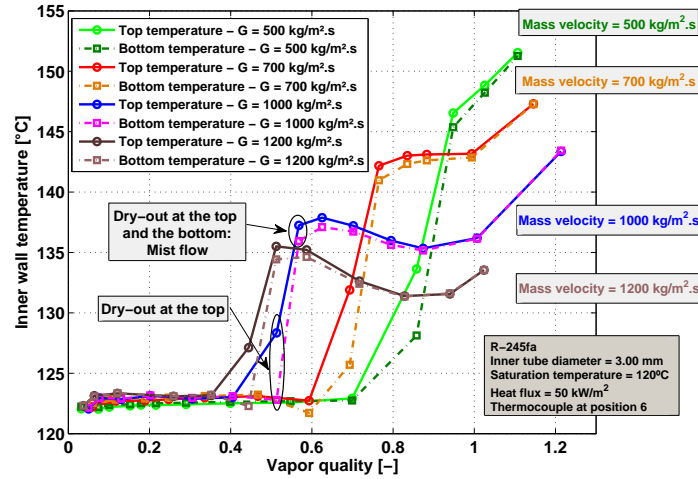


Figure 5.12: Influence of the mass velocity on the dryout.

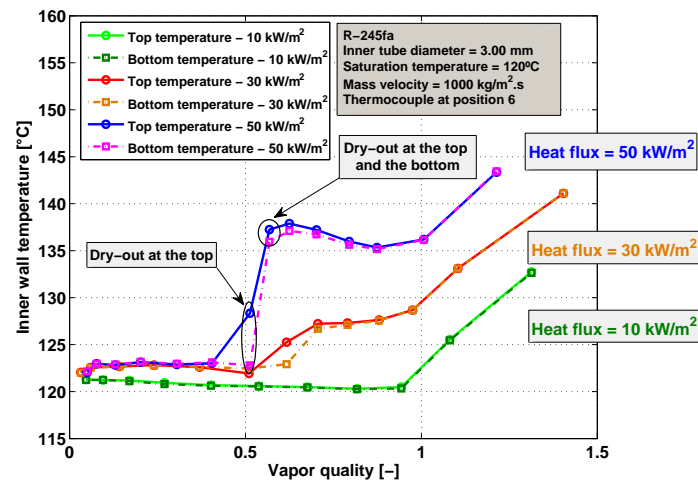


Figure 5.13: Influence of the heat flux on the wall temperature and detection of dryout.

the perimeter of the tube. On the contrary, at 120°C the liquid film is thinner at the top and dryout occurs first at the top. Moreover, as shown previously, when the saturation temperature increases, the surface tension decreases. As the surface tension decreases, it is easier to entrain the liquid film into the high velocity vapor core and the dryout inception is encountered at lower vapor quality.

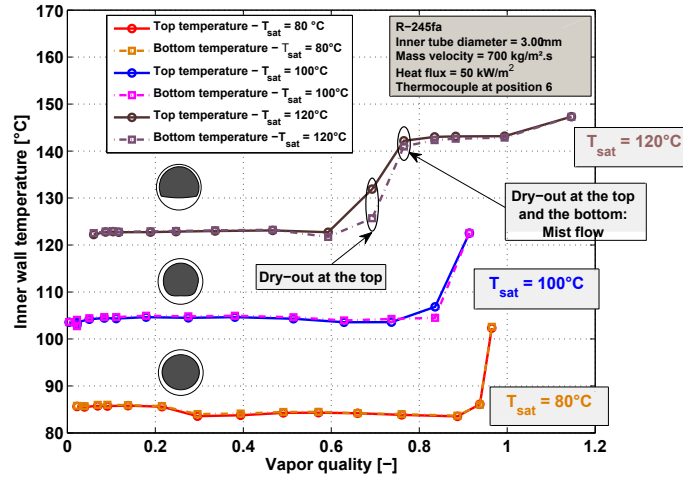


Figure 5.14: Influence of the saturation temperature on the dryout.

5.3 Flow pattern maps

Figures 5.15 and 5.16 present different flow pattern maps for four saturation temperatures (60, 80, 100 and 120°C) in two different formats: mass velocity vs. vapor quality and superficial liquid velocity vs. superficial vapor velocity, which are calculated from the test results as follows:

$$J_V = \frac{G \cdot x}{\rho_V} \quad (5.1)$$

$$J_L = \frac{G \cdot (1 - x)}{\rho_L} \quad (5.2)$$

The four main flow patterns described previously are encountered, i.e. intermittent flow, annular flow, dryout and mist flow regimes, with the exception of the map plotted for $T_{sat}=60^\circ\text{C}$, a temperature for which the dryout and mist flow regimes were not detected. It can be clearly observed that the inception of the dryout and mist flow regimes occurs at lower quality when the saturation temperature increases. As a matter of fact, the surface tension decreases with the increase of the saturation temperature, so that the liquid film is more easily entrained into the high velocity vapor core. Furthermore, when the mass velocity is larger, the intermittent flow regime takes place over a narrower range of vapor quality (consistently with Fig. 5.5) and mist flow regime occupies a wider range of vapor quality (consistently with Fig. 5.12). Notice that at 120°C and at a mass velocity of 100 kg/m²·s, the flow is almost always intermittent whereas at high mass velocities, the intermittent flow tends to disappear because bubbles and slugs quickly coalesce to form elongated bubbles that lead to annular flow.

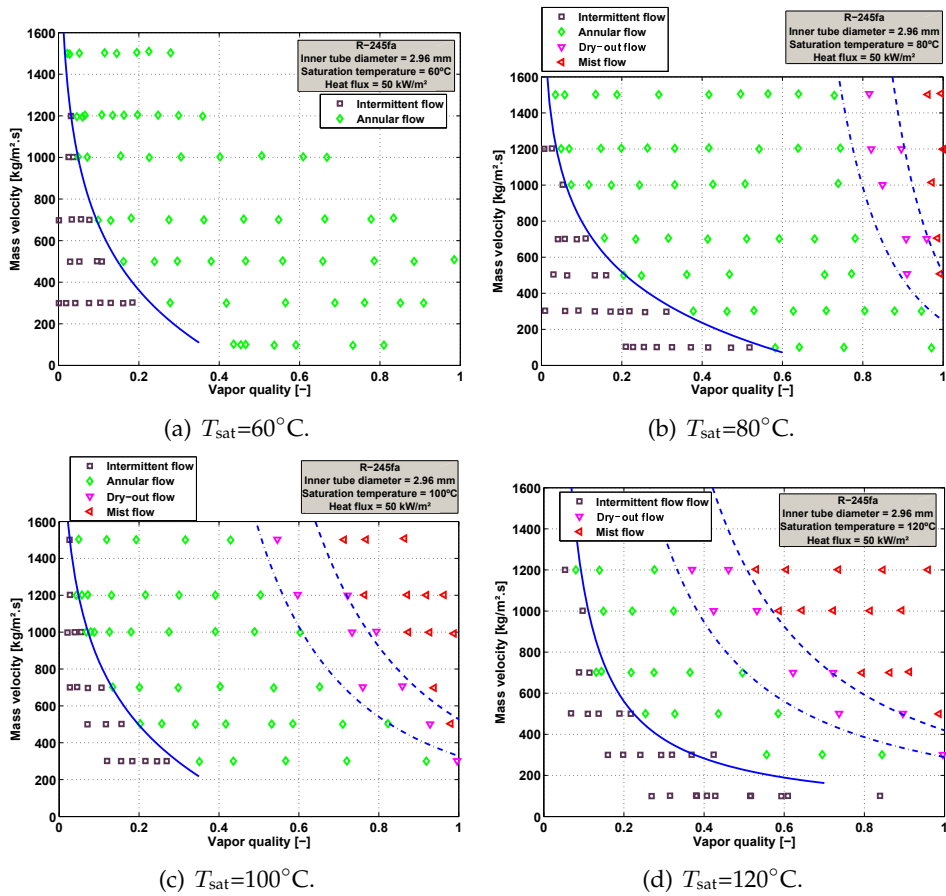


Figure 5.15: Flow pattern maps with transition lines for R-245fa and $\dot{q} = 50 \text{ kW/m}^2$ at four saturation temperatures.

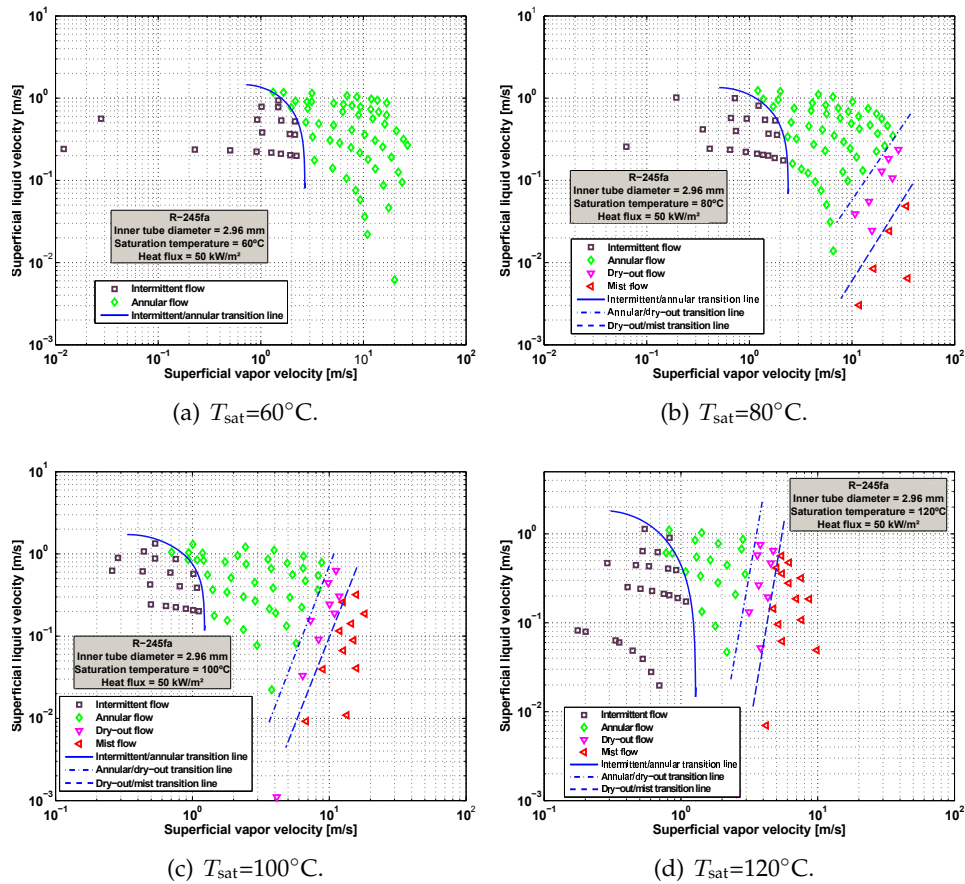


Figure 5.16: Flow pattern maps with transition lines for R-245fa and $\dot{q} = 50 \text{ kW/m}^2$ at four saturation temperatures.

The trend of the flow regime transitions looks like those encountered in microchannels ([Revellin and Thome (2007a)]). As a matter of fact, the most important observation to make about the flow patterns in the present study is that their intermittent-to-annular transitions are controlled primarily by the rate of coalescence as explained in [Charnay et al. (2013)]. The rate of coalescence was recognized to have a major influence on the intermittent-to-annular transition in the microscale (not the macroscale).

Figure 5.17 shows the influence of the heat flux on the flow pattern transitions. Whatever the saturation line temperature, the higher the vapor quality for which the intermittent-to-annular transition occurs. This influence was also observed by [Costa-Patry and Thome(2013)]. On the contrary, as shown in Fig. 5.18, the higher the heat flux, the lower the qualities for the annular-to-dryout and dryout-to-mist flow transitions. These results are consistent with those presented previously on the effect of the heat flux on the flow patterns.

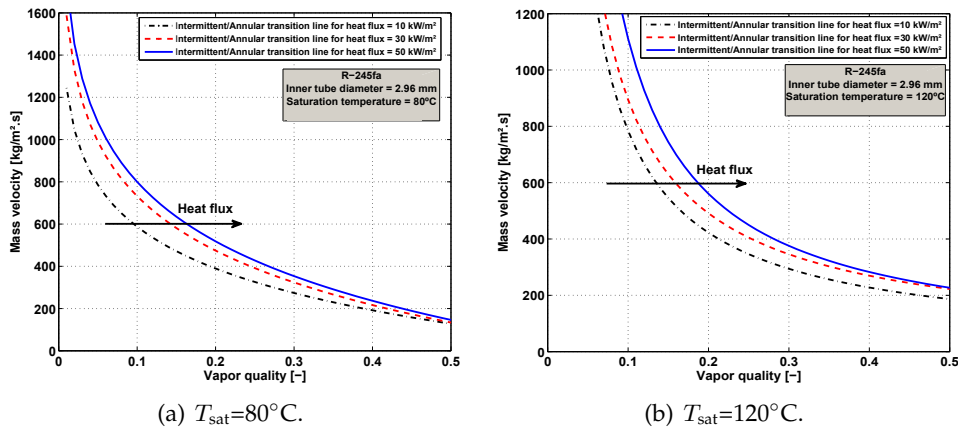


Figure 5.17: Influence of the heat flux on the intermittent-to-annular transition.

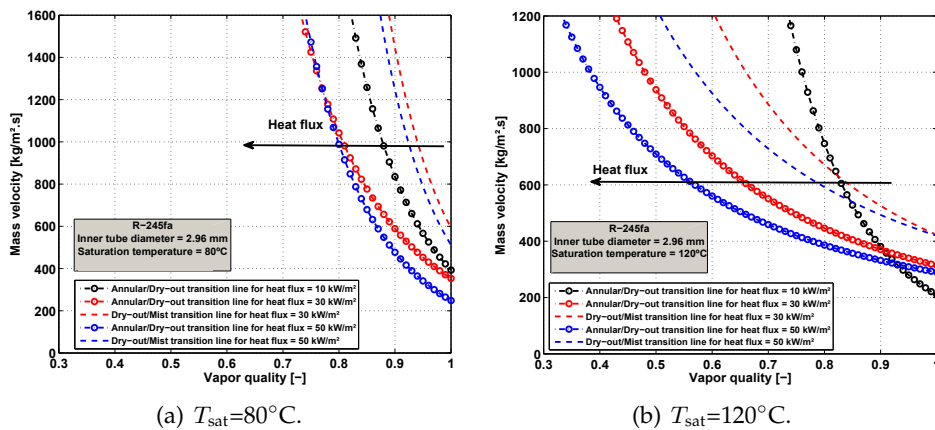


Figure 5.18: Influence of the heat flux on the annular-to-dryout and dryout-to-mist flow transition.

5.3.1 Comparison with predictive models

5.3.1.1 Intermittent-to-annular transition line

The experimental intermittent-to-annular transition lines have been compared to the predictive methods of [Kattan et al. (1998a)], [Barbieri et al. (2008)], [Revellin et al. (2006)], [Ong and Thome(2011a)], and [Costa-Patry and Thome(2013)]. The intermittent-to-annular transition predicted by [Kattan et al. (1998a)] corresponds to a constant vapor quality whereas the others depend on the mass flux as describe here below.

The transition from intermittent to annular flow regime given by [Barbieri et al. (2008)] is defined by:

$$G_{I/A}^2 = 3.75 \cdot g \cdot d_h \cdot \frac{(1-x)^{0.16}}{x^{2.16}} \cdot \frac{\rho_V^{1.2}}{\rho_L^{-0.8}} \cdot \left(\frac{\mu_L}{\mu_V} \right)^{0.24} \quad (5.3)$$

where $G_{I/A}$ is the mass velocity corresponding to the intermittent-annular transition.

The transition from intermittent to annular flow regime given by [Revellin et al. (2006)] is defined by:

$$x_{I/A} = 0.00014 \cdot \frac{\text{Re}_{LO}^{1.47}}{\text{We}_{LO}^{1.23}} \quad (5.4)$$

where $x_{I/A}$ is the vapor quality corresponding to the intermittent-annular transition, Re_{LO} is the liquid only Reynolds number and We_{LO} is the liquid only Weber number.

The transition from intermittent to annular flow regime given by [Ong and Thome(2011a)] is defined by:

$$x_{I/A} = 0.047 \cdot \text{Co}^{0.05} \cdot \left(\frac{\mu_V}{\mu_L} \right)^{0.7} \cdot \left(\frac{\rho_V}{\rho_L} \right)^{0.6} \cdot \frac{\text{Re}_{VO}^{0.8}}{\text{We}_{LO}^{0.91}} \quad (5.5)$$

where Co is the Confinement number and Re_{VO} is the vapor only Reynolds number.

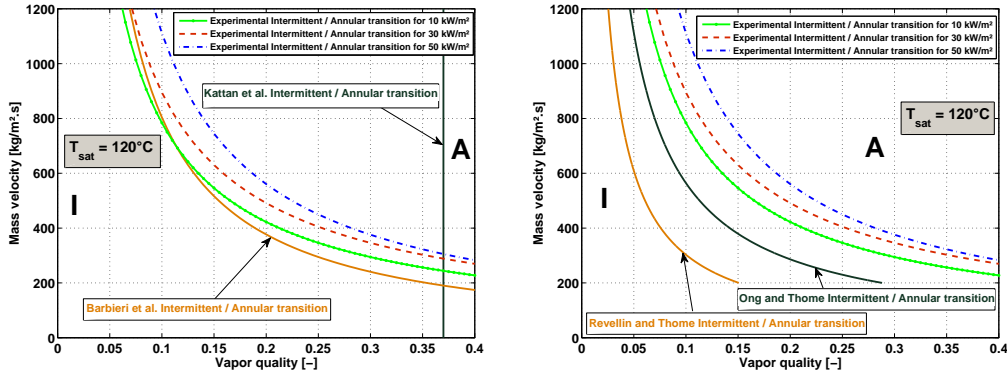
The transition from intermittent to annular flow regime given by [Costa-Patry and Thome(2013)] is defined by:

$$x_{I/A} = 425 \cdot \left(\frac{\rho_V}{\rho_L} \right)^{0.1} \cdot \frac{\text{Bo}^{1.1}}{\text{Co}^{0.5}} \quad (5.6)$$

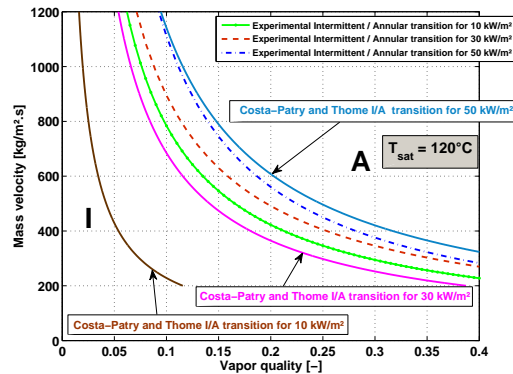
where Bo is the boiling number.

Figure 5.19(a) presents a comparison of the experimental transition lines with those given by [Kattan et al. (1998a)] and [Barbieri et al. (2008)] for the intermittent-to-annular transitions. Even though the transition line proposed by [Barbieri et al. (2008)] is not function of the heat flux, the trend is satisfactory which is not surprising since this transition is based on macrochannels results. On the contrary, the [Kattan et al. (1998a)] transition line developed also for macroscale flow does not match at all the experimental transitions. [Revellin et al. (2006)] and [Ong and Thome(2011a)] intermittent-to-annular transition lines originally developed for microchannels exhibit a trend similar to that of the experimental results (Fig. 5.19(b)).

However, these methods do not take into account the heat flux dependence unlike the [Costa-Patry and Thome(2013)] method. The latter, based on microscale results, displays a trend similar to that of the experimental lines and shows a heat flux dependence (Fig. 5.19(c)) but the experimental values are not well predicted.



(a) Comparison with [Kattan et al. (1998a)] and (b) Comparison with [Ong and Thome(2011a)] [Barbieri et al. (2008)] intermittent-to-annular and [Revellin et al. (2006)] intermittent-to-annular transition line.



(c) Comparison with [Costa-Patry and Thome(2013)] intermittent-to-annular transition line.

Figure 5.19: Comparison between present intermittent-to-annular transition lines observed for R-245fa at $T_{\text{sat}}=120^\circ\text{C}$ and predicted intermittent-to-annular transition lines.

5.3.1.2 Annular-to-dryout transition line

The experimental annular-to-dryout transition lines observed at 120°C for three different heat fluxes (10, 30 and 50 kW/m^2) have been compared to the correlations developed by [Sun and Groll (2002)] and by [Wojtan et al. (2005a)].

[Sun and Groll (2002)] developed three correlations to predict the inception of the dryout according to the saturation pressure. In the present investigation, the appropriate correlation is the one valid for $4.9 \leq P_{\text{sat}} \leq 29.4 \text{ bar}$ and expressed as:

$$x_{\text{di}} = 10.795 \cdot \left(\frac{\dot{q}_{\text{evap}}}{1000} \right)^{-0.125} \cdot G^{-0.333} \cdot (1000 \cdot d_h)^{-0.07} \cdot e^{(0.01775 \cdot 10^{-5} \cdot P_{\text{sat}})} \quad (5.7)$$

[Wojtan et al. (2005a)] proposed a correlation to predict the dryout inception from data points obtained for R-22 and R-410A:

$$x_{\text{di}} = 0.58 \cdot e^{\left[0.52 - 0.235 \cdot \text{We}_V^{0.17} \cdot \text{Fr}_V^{0.37} \cdot \left(\frac{\rho_V}{\rho_L} \right)^{0.25} \cdot \left(\frac{\dot{q}}{\dot{q}_{\text{crit}}} \right)^{0.70} \right]} \quad (5.8)$$

where \dot{q}_{crit} is the critical heat flux calculated with the following expression:

$$\dot{q}_{\text{crit}} = 0.131 \cdot \rho_V^{0.5} \cdot h_{\text{LV}} \cdot (g \cdot (\rho_L - \rho_V) \cdot \sigma)^{0.25} \quad (5.9)$$

and We_V and Fr_V are calculated as:

$$\text{We}_V = \frac{G^2 \cdot d_h}{\rho_V \cdot \sigma} \quad (5.10)$$

$$\text{Fr}_V = \frac{G^2}{\rho_V \cdot (\rho_L - \rho_V) \cdot g \cdot d_h} \quad (5.11)$$

Figure 5.20 shows that the trend is satisfactory with [Wojtan et al. (2005a)] annular-to-dryout transition lines whereas [Sun and Groll (2002)] transition lines exhibit higher values of vapor quality for dryout inception. [Kim and Mudawar (2013a)] compared their database of 997 data points to the correlation of [Sun and Groll (2002)]. They found that this correlation highly overpredicted their database which is also the case in the present investigation. They explained that this correlation was developed for CO₂ but based on equations developed by [Kon'kov (1965)] for steam-water mixture flows oriented upward vertical tubes, which can explain the discrepancy. The present experimental transition lines highlight the influence of heat flux which also appears in these both correlations.

5.3.1.3 Dryout-to-mist transition line

Two of the most quoted correlations to predict dryout completion (inception of the mist flow regime) are that by [Mori et al. (2000)] and its version modified by [Wojtan et al. (2005a)] defined by the two following expressions, respectively:

$$x_{\text{de}} = 0.61 \cdot e^{\left[0.57 - 0.0000265 \cdot \text{We}_V^{0.94} \cdot \text{Fr}_V^{-0.02} \cdot \left(\frac{\rho_V}{\rho_L} \right)^{-0.08} \right]} \quad (5.12)$$

$$x_{\text{de}} = 0.61 \cdot e^{\left[0.57 - 0.0058 \cdot \text{We}_V^{0.38} \cdot \text{Fr}_V^{0.15} \cdot \left(\frac{\rho_V}{\rho_L} \right)^{-0.09} \cdot \left(\frac{\dot{q}}{\dot{q}_{\text{crit}}} \right)^{0.27} \right]} \quad (5.13)$$

The present experimental dryout-to-mist transition lines observed at 120°C have been compared to these two correlations for two different heat fluxes: 50 kW/m² (Fig. 5.21(a)) and 30 kW/m² (Fig. 5.21(b)). The agreement is correct with [Wojtan et al. (2005a)] dryout-to-mist transition lines. This model includes the heat flux effect whereas the correlation of [Mori et al. (2000)] does not. Therefore, the agreement with [Mori et al. (2000)] transition line is not satisfactory at high heat flux (Fig. 5.21(a)).

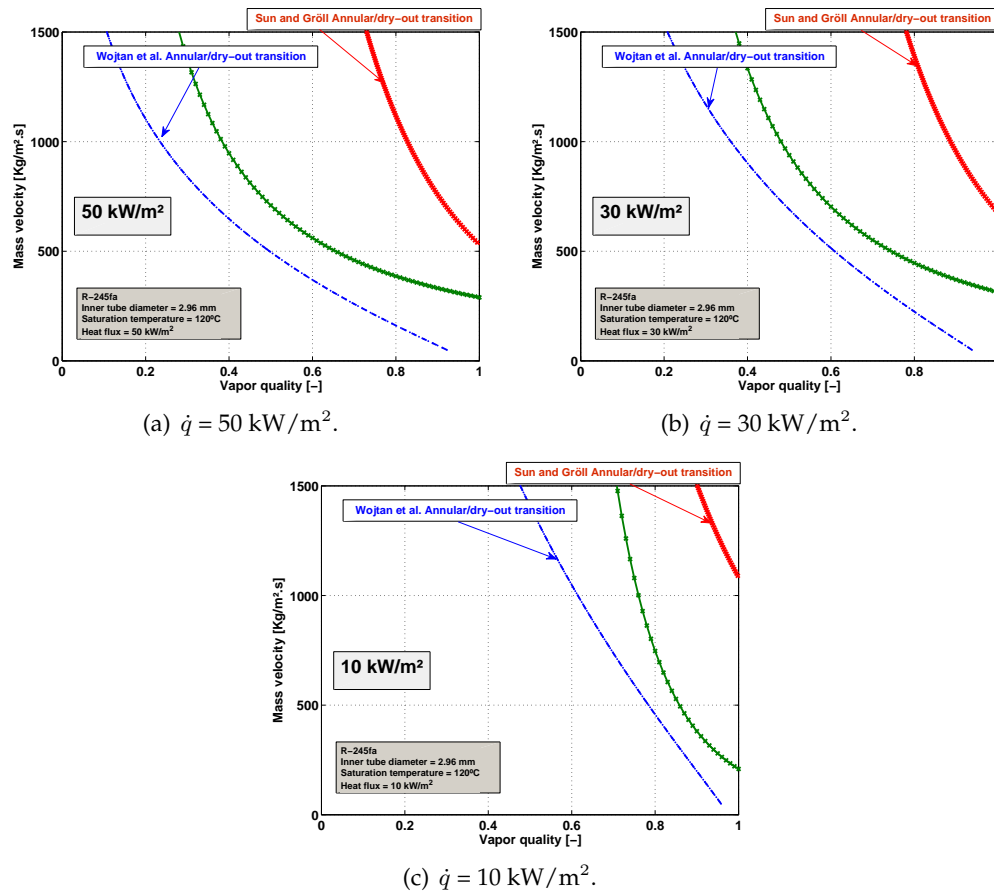


Figure 5.20: Comparison between present annular-to-dryout transition lines observed for R-245fa at $T_{\text{sat}}=120^{\circ}\text{C}$ and predicted annular-to-dryout transition lines proposed by [Sun and Groll (2002)] and [Wojtan et al. (2005a)].

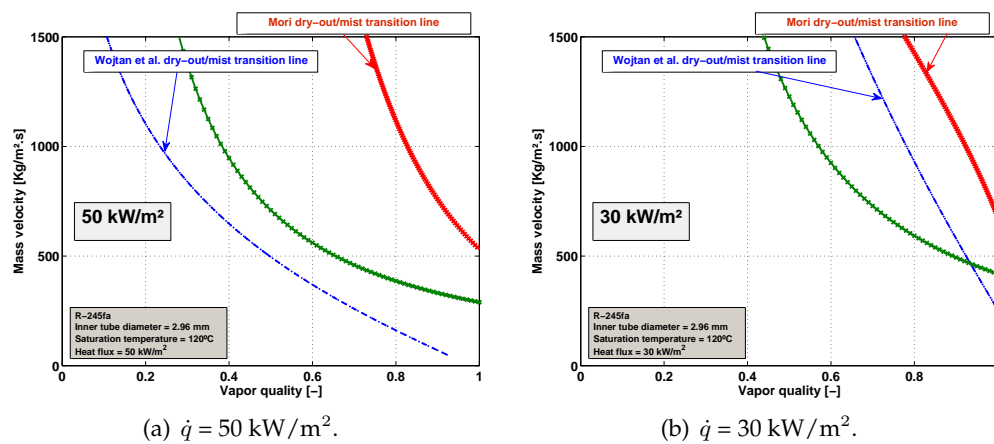


Figure 5.21: Comparison between present dryout-to-mist transition lines observed for R-245fa at $T_{\text{sat}}=120^{\circ}\text{C}$ and predicted dryout-to-mist transition lines proposed by [Mori et al. (2000)] and [Wojtan et al. (2005a)].

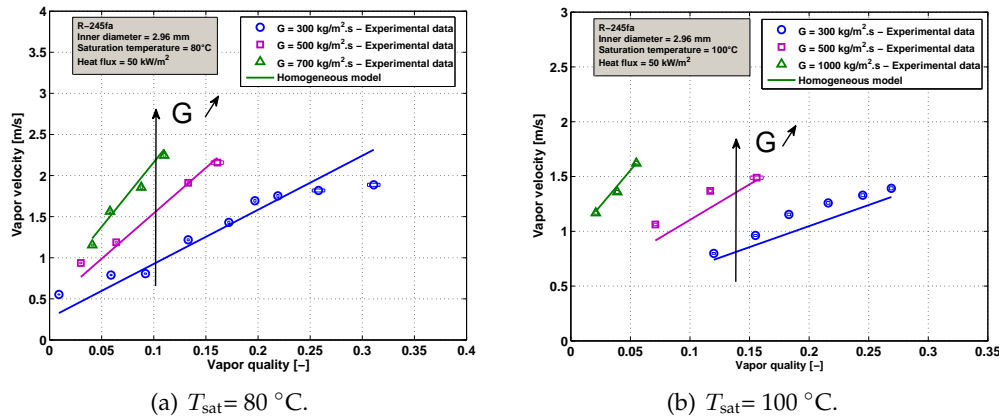


Figure 5.22: Effect of the mass velocity on the mean bubble velocity for R-245fa, $d_{\text{inner}} = 2.96 \text{ mm}$, $\dot{q} = 50 \text{ kW/m}^2$, and two different saturation temperature and comparison with the predicted void fraction calculated from the homogeneous model.

5.4 Vapor bubble velocity

The mean bubble velocity is determined using a normalized cross-correlation as explained in the description of the image processing method (see section 4.6.1.3). Figure 5.22 shows some typical results of the vapor bubble velocities as a function of the vapor quality for different mass velocities and two different saturation temperatures. These graphs exhibit the comparison with the vapor velocities calculated from the so-called homogeneous void fraction equation (U_H) as referring to the classical homogeneous model:

$$U_H = G \left[\frac{x}{\rho_V} + \frac{1-x}{\rho_L} \right] \quad (5.14)$$

The set of data ends at relatively low vapor qualities because at higher vapor quality, annular flow is reached. The increase of the vapor velocity when the mass velocity and the vapor quality increase clearly appears as pointed out by [Revellin et al. (2008)] and as recently corroborated by [Arcanjo et al. (2010)]. The comparison shows that in all the tested conditions, the experimental vapor velocity is close to that of the homogeneous model.

Figure 5.23 shows the effect of the saturation temperature on the elongated bubble velocity for $\dot{q} = 50 \text{ kW/m}^2$ and two different mass velocities: $300 \text{ kg/m}^2\cdot\text{s}$ (Fig. 5.23(a)) and $500 \text{ kg/m}^2\cdot\text{s}$ (Fig. 5.23(b)). The bubble velocity decreases when increasing the saturation temperature. These results are similar to those obtained by [Revellin et al. (2008)] and [Arcanjo et al. (2010)]. Such a behavior is explained to the fact that the vapor/liquid specific volume ratio decreases when increasing the saturation temperature, passing from 48.1 to 8.3 when the saturation temperature increases from 60 to 120°C . Therefore the fluid acceleration, inherent to the evaporation process, also decreases resulting in a decrease of the vapor bubble velocity. At 120°C , the vapor velocity is below the homogeneous model prediction which is quite unusual. This unexpected trend could be explained by two-phase flow instabilities and perhaps some back flow as suggested by [Revellin (2005)].

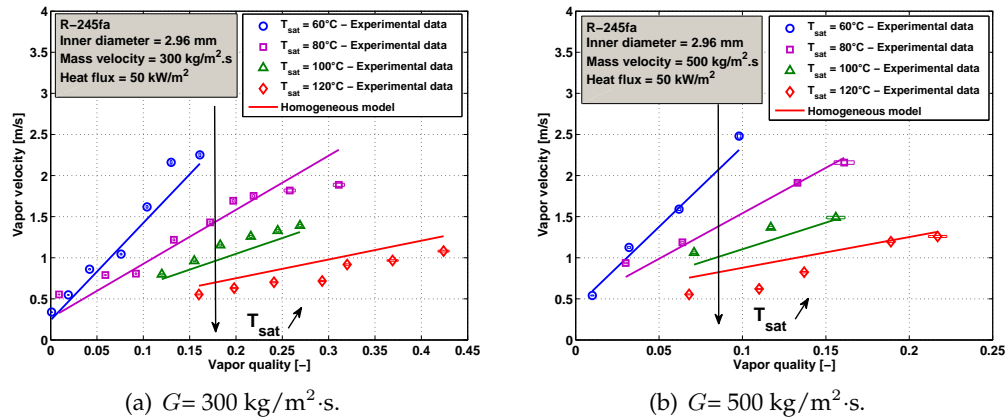


Figure 5.23: Effect of saturation temperature on the mean bubble velocity for R-245fa, $d_{\text{inner}} = 2.96$ mm, $q = 50$ kW/m², and two different mass velocities and comparison with the predicted bubble velocity calculated from the homogeneous model.

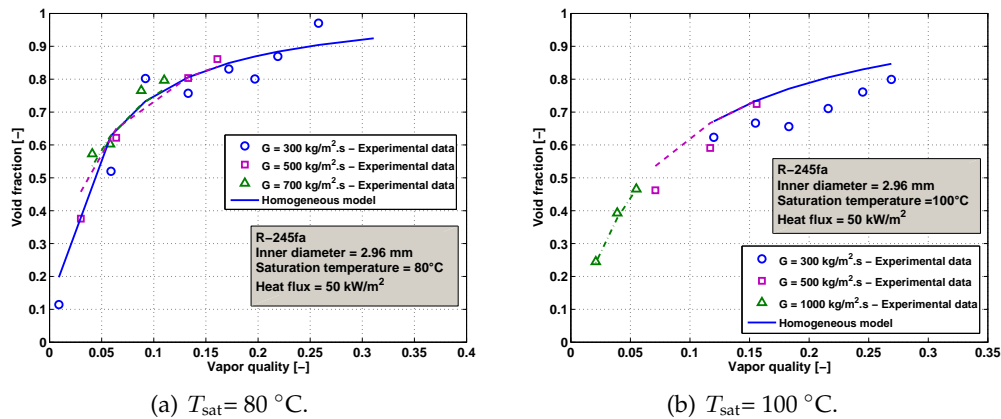


Figure 5.24: Effect of the mass velocity on the void fraction for R-245fa, $d_{\text{inner}} = 2.96$ mm, $q = 50$ kW/m², and two different saturation temperature and comparison with the predicted void fraction calculated from the homogeneous model.

Figure 5.24 shows the void fraction calculated from the vapor velocity for $q = 50$ kW/m², and two different saturation temperature: 80 °C (Fig. 5.24(a)) and 100 °C (Fig. 5.24(b)). The homogeneous void fraction represented on each graph is calculated from the following expression:

$$\epsilon_{\text{H}} = \frac{1}{1 + \left(\frac{1-x}{x}\right) \cdot \left(\frac{\rho_{\text{V}}}{\rho_{\text{L}}}\right)} \quad (5.15)$$

The void fraction data end at relatively low vapor qualities because at higher vapor quality, annular flow is reached and the method is not able to determine the void fraction. The comparisons between experimental data and prediction from homogeneous flow model exhibit a good agreement.

Figures 5.25 shows the comparison between the 239 experimental values of bubble velocity and those calculated from the void fraction (ϵ) which is determined

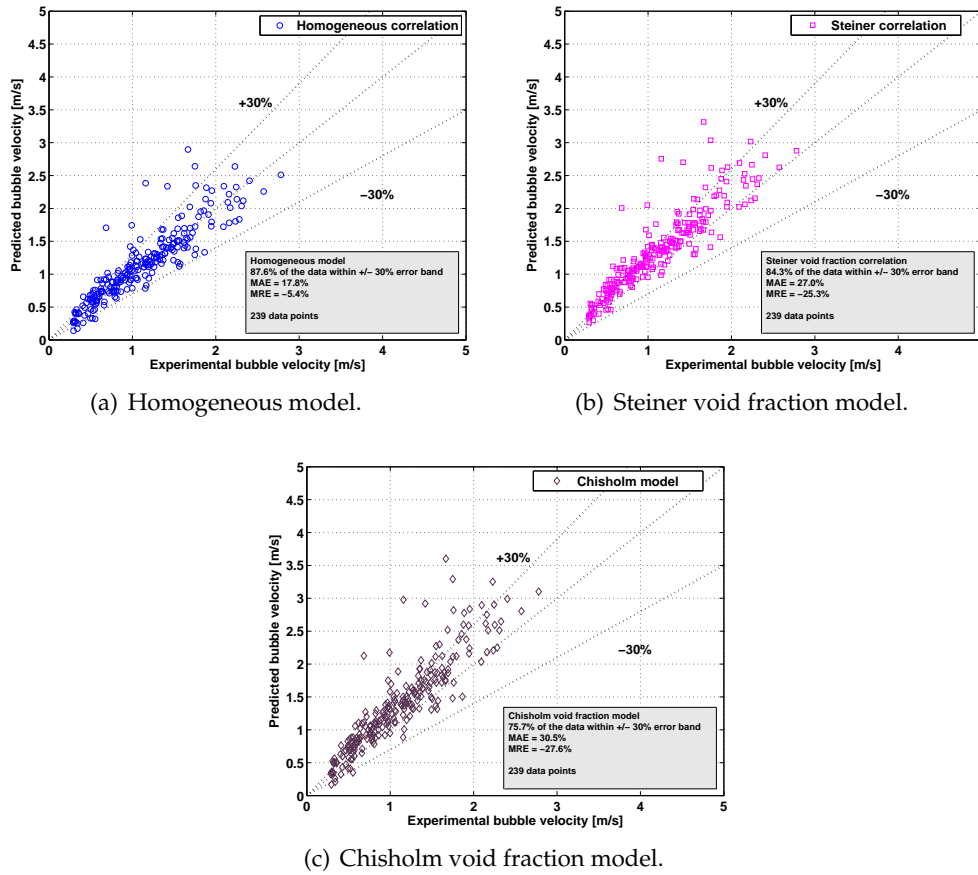


Figure 5.25: Comparison of experimental velocity with predictive models.

by the version of the [Rouhani and Axelsson (1970)] model modified by [Steiner (1993)], the homogeneous model, and the [Chisholm (1983)] model. The velocity (u_m) is expressed as:

$$u_m = \frac{G \cdot x}{\rho_V \epsilon} \quad (5.16)$$

In addition to the graphical comparison, the Mean Relative Error (MRE) and Mean Absolute Error (MAE) reported in the following tables are calculated as:

$$\text{MRE} = \frac{1}{n} \sum_{i=1}^n \left(\frac{u_{\text{pred},i} - u_{\text{exp},i}}{u_{\text{exp},i}} \right) \quad (5.17)$$

$$\text{MAE} = \frac{1}{n} \sum_{i=1}^n \left(\frac{|u_{\text{pred},i} - u_{\text{exp},i}|}{u_{\text{exp},i}} \right) \quad (5.18)$$

The percentage of data falling in a $\pm 30\%$ error band is also given in the tables in order to provide a quantitative indication of the performance of these prediction methods when extrapolated up to high saturation temperatures. Table 5.2 reports the statistical results. The homogeneous model and the one of [Steiner (1993)] work relatively well to predict the mean bubble velocity in our conditions.

Table 5.2: Comparison between the experimental results and the predicted results.

	MAE [%]	MRE [%]	% of data within $\pm 30\%$ error band
Homogeneous	17.8	-5.4	87.6
[Steiner (1993)]	27.0	-25.3	84.3
[Chisholm (1983)]	30.5	-27.6	75.7

5.5 Conclusions

Based on an image processing method and on an analysis of the inner wall temperatures and the resulting heat transfer coefficient, four main flow regimes were identified: (i) intermittent flow, (ii) annular flow, (iii) dryout and (iv) mist flow. Intermittent flow groups together bubbly flow, bubbly-slug flow and slug flow or isolated bubbles regime and coalescing bubbles regime. Flow pattern maps were presented for four different saturation temperatures. Therefore, the effect of saturation temperature and heat flux on flow patterns and their transition could be highlighted. Experimental transition lines were compared with predictive correlations. For intermittent-to-annular transition lines, the predictive methods developed by [Barbieri et al. (2008)] and [Costa-Patry and Thome(2013)] agree the best with the data. [Wojtan et al. (2005a)] transition lines present the best agreements for both annular-to-dryout and dryout-to-mist flow transitions. Whereas the flow regime would suggest an intensification of phenomena typical of the macroscale (especially stratification), the flow patterns transitions are closer to those observed at the microscale. For that reason, we believe that the term minichannel is appropriate to qualify the present type of tube in the case of flow boiling of R-245fa at high saturation temperature. More in-depth investigations are required to consolidate these results; for instance, an accurate measurement of the film thickness and an adequate way to quantify its uniformity/nonuniformity would probably allow to reach more universal conclusion.

The bubble velocity as well as the bubble frequency and the percentage of small bubbles were investigated. The influences of mass velocity and saturation temperature on the bubble characteristics were highlighted. The image processing method has been shown to be a promising tool for the detailed study of vapor bubble characteristics (i.e. bubble frequency, mean bubble length, mean bubble velocity). Even so, further experiments are required to improve the experimental database in intermittent flow. For instance, the vapor quality step should be reduced to obtain more detailed information.

Since the beginning of this work, we kept in mind the question raised by [Thome et al. (2013)] on the utility of flow pattern maps. Indeed, we believed that a flow map "is not only a sort of GPS to locate flow regime but has to provide quantitative details about the flow". In the present work, the flow regime transitions are based on these quantitative details, which are: bubble frequencies, bubble lengths and their velocities. Even though a deeper investigation is necessary to develop an optimal graphical representation, this preliminary work is a step towards developing unified mechanistic flow pattern map which would not only describe but also

explain the flow and heat transfer mechanisms.

In our objective to achieve a reliable design of an ORC evaporator, the flow pattern characterization was the first step. Knowing that heat transfer coefficients and pressure drops are related to the local two-phase flow structure of the fluid, our results will help us analyze the heat transfer and pressure drop mechanisms at high saturation temperatures. For instance, the small bubble plays a major role in the nucleate boiling contribution. Furthermore, the presented flow pattern maps will permit the comparisons of our experimental database against phenomenological heat transfer or pressure drop models (for instance 3-zone model developed by [Thome et al. (2004a)] for heat transfer coefficient, and the model of [Quibén and Thome (2007b)] for pressure drop).

The main conclusions on the influence of the saturation temperature (T_{sat}) are:

- The higher T_{sat} , the thicker the liquid film at the bottom, which increases the stratified character of the flow.
- The higher T_{sat} , the smaller and shorter the bubbles.
- The higher T_{sat} , the greater the bubble frequency.
- The higher T_{sat} , the lower the bubble velocity.
- The higher T_{sat} , the lower the value of the vapor quality for dryout inception.
- The higher T_{sat} , the narrower the range of vapor quality corresponding to annular flow whereas the larger the range of vapor quality for intermittent and mist flow regimes.

1.

Chapter 6

Heat transfer

This chapter presents experimental data concerning flow boiling heat transfer in minichannel at high saturation temperatures. The database is composed of 5964 data points covering four flow patterns: (i) intermittent flow, (ii) annular flow, (iii) dryout flow, and (iv) mist flow regimes.

A parametric analysis on the influence of the kind of flow pattern, the mass velocity and the heat flux will be presented in order to identify the dominant heat transfer mechanisms. Finally, the effect of the saturation temperature on the heat transfer coefficient will be presented.

In order to evaluate the reliability of the current flow boiling heat transfer prediction methods for conditions of high saturation temperatures, this chapter will also present comparisons between experimental results and theoretical results predicted with the commonly used correlations or models from the literature. Finally, thirty flow boiling prediction methods will be assessed against our database. The results will be presented graphically but also statistically. The effect of the saturation temperature and the kind of flow pattern on the ability of the methods to predict the flow boiling heat transfer coefficient will be investigated.

6.1 Measurements of the heat transfer coefficient

Flow boiling experiments were performed with the aim to identify the heat transfer dominant mechanisms at high temperatures. Thereby, the influence of the mass velocity and the heat flux were investigated to detect the conditions for which nucleate boiling or convective boiling predominates in their contribution to heat transfer. The effect of the saturation temperature was also investigated within a range from 60 to 120°C.

6.1.1 Influence of saturation temperature

Major modifications are expected when varying the saturation temperature from 60°C to 120°C. Indeed, some modifications in properties at high saturation temperature strongly enhance the nucleate boiling contribution to heat transfer leading to an increase of the heat transfer coefficient. Previous works performed by [Cooper (1984)] and [Gorenflo et al. (2004)] brought to the fore such an increase of the heat transfer coefficient with increasing the saturation temperature during nucleate pool boiling.

Figure 6.1 highlights the influence of the saturation temperature at a constant heat flux (50 kW/m^2) for two different mass velocities: $G = 300 \text{ kg/m}^2\cdot\text{s}$ (Fig. 6.1(a)) and $G = 700 \text{ kg/m}^2\cdot\text{s}$ (Fig. 6.1(b)). The higher the saturation temperature, the larger the heat transfer coefficient over a wide range of vapor quality until dryout inception. These graphs are hence in agreement with the typical curve previously referred to as F in the state-of-the-art review (Fig. 3.40).

For a mass velocity of $300 \text{ kg/m}^2\cdot\text{s}$, for low vapor quality, the difference between low and high saturation temperature heat transfer coefficient is more important. It is clear that small bubbles play an important role in conditions of low quality. Indeed, when the saturation temperature increases, the surface tension decreases, the vapor density increases whereas the liquid density decreases (see Table 6.1). Such variations of properties result in an intensification of the nucleate boiling heat transfer due to an increase of the number of active nucleation sites and to a decrease of the detachment bubbles radius, which increases the bubble frequency and reduces the bubbles size. These behaviors are notable in Figs. 5.10 and 5.11.

Table 6.1: R-245fa properties at 60°C and 120°C.

	P_{red} [-]	ρ_L [kg/m ³]	ρ_V [kg/m ³]	μ_L [μPa.s]	μ_V [μPa.s]	λ_L [mW/m.K]	σ [mN/m]
60°C	0.13	1237	25.7	265	12	79	9.59
120°C	0.53	998	119.7	125	15	61	2.64

For a saturation temperature of 60°C and 80°C, the heat transfer coefficient is almost constant along the vapor quality range. The typical curve B (Fig. 3.35) represents schematically the same trends. The heat transfer is mainly due to nucleate boiling. At 100°C, the curve exhibits a plateau for the vapor quality range corresponding to intermittent flow, then the heat transfer coefficient decreases gradually until reaching the dryout.

At 120°C, the heat transfer coefficient decreases over the intermittent and annular flow regimes until to reach dryout. On the one hand, the decrease of the heat transfer coefficient results from the reduction of the nucleate boiling contribution which, nonetheless, remains the dominant mechanism. For these high saturation temperatures, the contribution of nucleate boiling is very important in the low vapor quality regions. In addition, nucleate boiling is also present during annular flow with some bubbles nucleating in the thin liquid film (also observed by [Kasza et al. (1997)] and represented in Fig. 3.34). When the vapor quality increases, the annular liquid film becomes thinner and the wall superheat decreases, which leads to a decrease of the number of active nucleation sites.

On the other hand, the convective boiling contribution is not sufficient at high saturation temperature to lead to an increase of the heat transfer coefficient with increasing vapor quality. Indeed, the density of the vapor increases with saturation temperature, thereby its velocity decreases as shown in Figs. 5.23(a) and 5.23(b). Moreover, the liquid film conductivity decreases with increasing saturation temperature (see Table 6.1). Thus, the conduction and the convection through the liquid film are reduced and, by consequence, the contribution of the convective boiling is reduced too at high saturation temperature. These results are similar to those obtained by [Pettersen (2004)] for carbon dioxide. Nevertheless, no comparison is available with typical curves because these new trends have never been observed until so far at such high saturation temperatures for halogenated refrigerants.

Figure 6.1(b) represents the heat transfer coefficient as a function of vapor quality for a mass velocity of 700 kg/m²·s and for four different saturation temperatures. At 60°C and 80°C, the heat transfer coefficient exhibits a non-dependence to vapor quality (plateau) during intermittent flow, which indicates the dominance of nucleate boiling. For higher vapor quality regions, the heat transfer coefficient increases with increasing vapor quality. Convective boiling becomes predominant but that does not imply the complete suppression of nucleate boiling. When the mass velocity increases, the contribution of convective boiling becomes more important and surpasses the nucleate boiling contribution. These results are typically those observed in macrochannels as seen in section 3.4.1.1 and depicted on the typical curve A (Fig. 3.32).

At 100°C and 120°C, the heat transfer coefficient decreases sharply for the lower vapor quality region corresponding to intermittent flow regime. This abrupt decrease could correspond to the bubbles frequency reduction with increasing vapor quality. Indeed, the bubbles tend to coalesce to form bigger bubbles. The curves exhibit a minimum heat transfer coefficient value which coincides with the intermittent-annular flow pattern transition and with the suppression of bubbles (also observed by [Da Silva Lima et al. (2009)]). The vapor quality corresponding to the minimum value of heat transfer coefficient is called x_{\min} . For vapor quality higher than x_{\min} , the heat transfer coefficient depicts a plateau resulting from the decrease of the nucleate boiling and the increase of convective boiling. For higher vapor quality, the heat transfer coefficient falls sharply, which corresponds to the dryout inception at the top of the tube. The higher the saturation temperature, the lower the vapor quality for dryout inception. This is due to the decrease of surface tension which leads to a predominance of the gravity forces that gives birth to stratification. Therefore, with increasing the saturation temperature, the liquid film becomes thinner at the top of the tube and the dryout occurs for lower vapor quality. These results are similar to those presented in section 3.4.

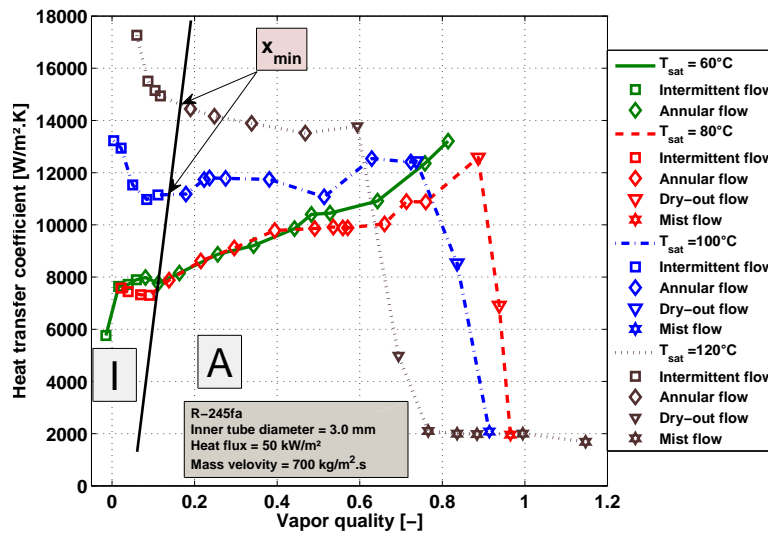
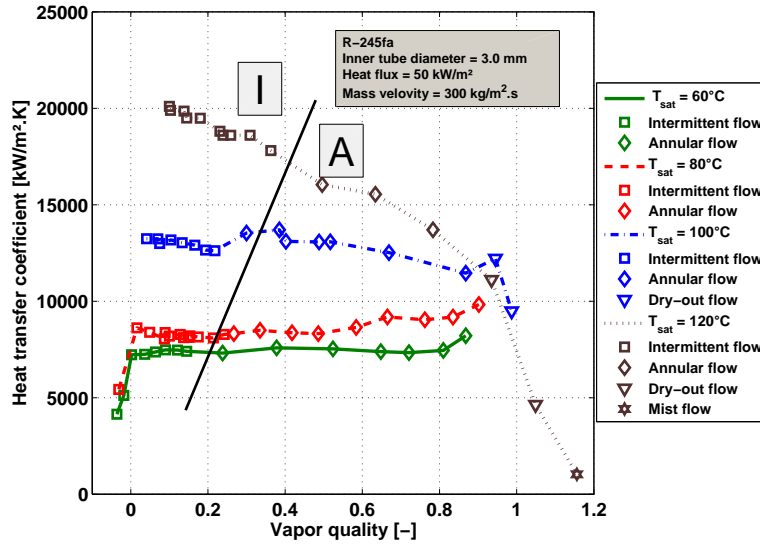


Figure 6.1: Influence of the saturation temperature on the heat transfer coefficient for R-245fa at $300 \text{ kg/m}^2 \cdot \text{s}$ and $700 \text{ kg/m}^2 \cdot \text{s}$ with a heat flux of 50 kW/m^2 (I: intermittent flow and A: annular flow).

6.1.2 Influence of mass velocity

Mass velocity is one of the physical parameters that the most strongly affects the heat transfer in convective boiling. Figure 6.2 represents the influence of the mass velocity on the heat transfer coefficient for a constant heat flux of 50 kW/m^2 and four different saturation temperatures, viz. 60°C , 80°C , 100°C and 120°C . Three different trends can be distinguished:

- on Fig. 6.2(a), at 60°C , the higher the mass velocity, the larger the heat transfer coefficient.
- on Figs. 6.2(b) and 6.2(c), at 80°C and 100°C , for lower vapor quality region, the higher the mass velocity, the smaller the heat transfer coefficient whereas for higher vapor quality region, the higher the mass velocity, the larger the heat transfer coefficient.
- on Fig. 6.2(d), at 120°C , the higher the mass velocity, the smaller the heat transfer coefficient.

These general trends clearly underline a change of heat transfer mechanisms. Indeed, convective boiling is surpassed by nucleate boiling at high saturation temperature. The third trend is similar to the one observed for carbon dioxide. For example, [Yun et al. (2003)] and [Oh et al. (2008)] observed such a trend for carbon dioxide until a vapor quality of 0.2-0.3 and concluded that nucleate boiling was dominant in this region.

At 60°C and for low vapor quality, the flow pattern is intermittent and the heat transfer coefficient is independent of the vapor quality (see Fig 6.2(a)). Moreover, the influence of the mass velocity is very limited. Hence, nucleate boiling is the dominant heat transfer mechanism during intermittent flow. For the vapor quality range corresponding to annular flow, the heat transfer coefficient exhibits an abrupt increase with increasing vapor quality except for a mass velocity of $300 \text{ kg/m}^2\cdot\text{s}$ (where the heat transfer coefficient is almost constant over the whole vapor quality range). Convective boiling is the dominant heat transfer mechanism in these conditions. When the vapor quality increases, the liquid film thickness decreases together with its thermal resistance and the vapor velocity increases. Thus, both phenomena promote the contribution of convective boiling and the heat transfer coefficient increases. This observation confirms the results found by [Cornwell and Kew (1993)] and [Ong and Thome (2009)]. These characteristics at 60°C are similar to those observed for larger diameter tubes and represented with the typical curve A (Fig. 3.32).

At 80°C and 100°C , two trends appear depending on the vapor quality range:

- For vapor quality corresponding to intermittent flow regime: the higher the mass velocity, the smaller the heat transfer coefficient. In this region, nucleate boiling predominates in the low vapor quality region, as explained in the previous section, and its contribution decreases quickly with increasing vapor quality.
- For vapor quality corresponding to annular flow regime: the higher the mass velocity, the larger the heat transfer coefficient. Convective boiling becomes the dominant heat transfer mechanism when the vapor quality increases during annular flow regime.

At 120°C, the heat transfer coefficient decreases with increasing vapor quality. The particular trend is directly related to the influence of the saturation temperature and exhibits four different zones according to the vapor quality:

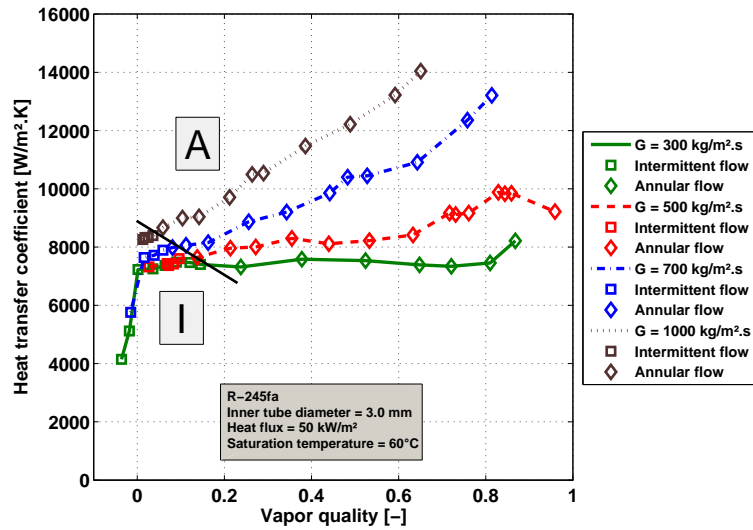
- For vapor quality corresponding to intermittent flow regime: the heat transfer coefficient decreases abruptly as observed at 100°C.
- For vapor quality corresponding to annular flow and until the dryout inception: the heat transfer coefficient diminishes with increasing vapor quality. Nucleate boiling is still the dominant heat transfer mechanism even if its contribution decreases gradually leading to the continuous decrease of the heat transfer coefficient. In annular flow, the liquid film thickness becomes thinner with increasing vapor quality, and therefore the temperature of the liquid film which covers the surface decreases to reach a relatively low value. Hence the contribution of nucleation in annular flow decreases. This phenomenon was pointed out by [Jung et al. (1989)]. Moreover, as explained before, the convective boiling is limited by the increase of vapor density and the decrease of liquid film conductivity when increasing the saturation temperature.
- The heat transfer coefficient decreases sharply due to the dryout inception at the top of the tube. The higher the mass velocity, the lower the vapor quality for dryout inception. In fact, the higher the mass velocity, the higher the shear stress and the higher the liquid entrained fraction (droplets). It is thus logical to dry out the tube for lower vapor quality.
- The heat transfer coefficient becomes nearly constant in value. This observation corresponds to the complete dryout around the tube perimeter. The flow pattern in this region is mist flow.

The trends observed at the higher saturation temperatures (100°C and 120°C) were never reported previously in the literature and therefore cannot be related to the typical curves that were identified in section 1.1.

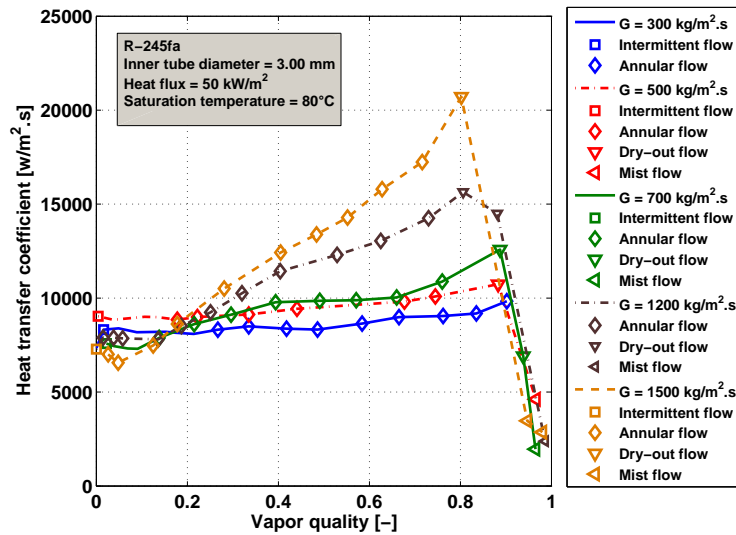
6.1.3 Influence of heat flux

The effect of the heat flux over the heat transfer coefficient is shown on Fig. 6.3 for a mass velocity of 500 kg/m²·s and for four saturation temperatures: 60°C (Fig. 6.3(a)), 80°C (Fig. 6.3(b)), 100°C (Fig. 6.3(c)) and 120°C (Fig. 6.3(d)). In general, the higher the heat flux, the larger the heat transfer coefficient.

At 60°C, the heat flux affects more the heat transfer coefficient in low vapor quality region, during intermittent flow, than during annular flow. Then, when the flow pattern becomes annular, the difference between low and high heat flux heat transfer coefficient diminishes and the curves converge, as shown on Fig. 6.3(a). This effect highlights the occurrence of nucleate boiling during intermittent flow. Furthermore, when the vapor quality increases, the nucleate boiling is gradually suppressed and the curves tend to merge into a single one. In parallel, the importance of convective boiling increases and the heat transfer mode becomes dominant. The effect is stronger at 10 kW/m² for which the heat transfer coefficient increases strongly with increasing vapor quality. These trends are typically represented by the curve A (Fig. 3.32).



(a) $T_{\text{sat}} = 60^{\circ}\text{C}$.



(b) $T_{\text{sat}} = 80^{\circ}\text{C}$.

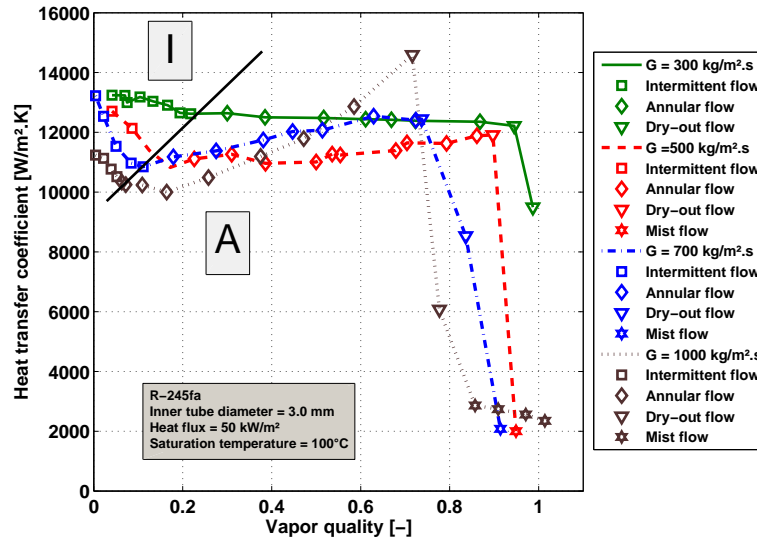
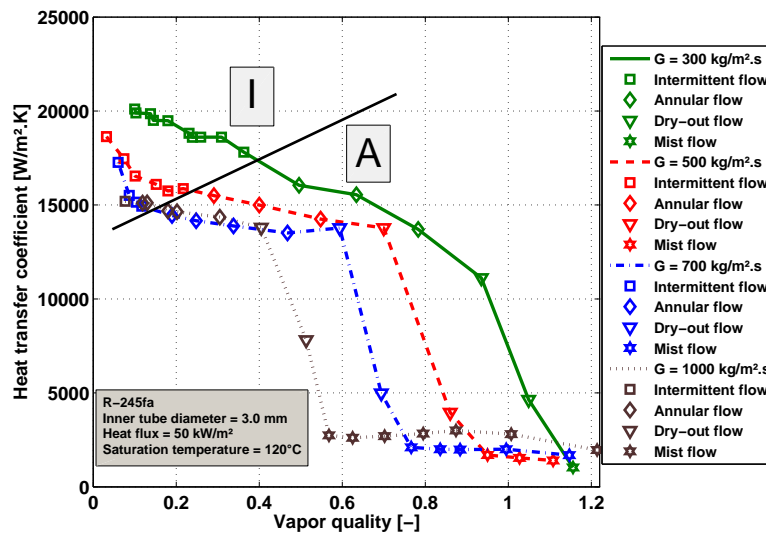
(c) $T_{\text{sat}} = 100^{\circ}\text{C}$.(d) $T_{\text{sat}} = 120^{\circ}\text{C}$.

Figure 6.2: Influence of mass velocity on heat transfer coefficient for R-245fa at 60°C , 80°C , 100°C and 120°C with a heat flux of 50 kW/m^2 (I: intermittent flow and A: annular flow).

For higher temperatures (Fig. 6.3(b) and Fig. 6.3(c)), the heat flux affects the heat transfer coefficient over the whole range of vapor qualities (until dryout inception) as represented on the typical curve B (Fig. 3.35). This trend indicates that the suppression of the nucleate boiling is delayed, i.e. it occurs at higher vapor quality. At 120°C, two different trends appear:

- At 10 kW/m²: the heat transfer increases with increasing vapor quality in annular flow. For small heat flux, the nucleate boiling does not predominate even at low vapor quality. The contribution of convective boiling to heat transfer is enhanced with increasing the vapor quality and as a consequence, the heat transfer coefficient increases.

- At 30 kW/m² and 50 kW/m²: when the heat flux increases, nucleate boiling become the dominant heat transfer mechanism, especially for low vapor quality regions. With increasing the vapor quality until the dryout inception, the nucleate boiling (which is still surpassing the convective boiling) decreases and as a consequence, the heat transfer coefficient decreases. As shown in Fig. 6.3(d), the higher the heat flux, the lower the vapor quality for dryout inception.

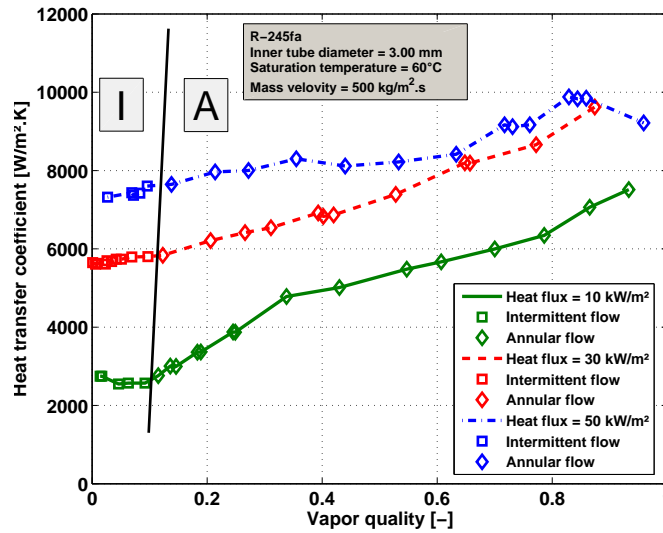
6.1.4 Synthesis

Figure 6.4 aims at summarizing the previous analysis on the influence of the main parameters (saturation temperature, vapor quality, heat flux and mass velocity) as well as on the heat transfer mechanism from a comparison of the situations at two saturation temperatures: 60°C (Fig. 6.4(a)) and 120°C (Fig. 6.4b). Both graphs show the saturation temperature which is almost constant over the range of vapor quality, the top and bottom inner wall temperatures and the mean heat transfer coefficient. A schematic of the flow regimes encountered along the evaporator is also associated to each graph to better highlight the relation between heat transfer and flow regimes.

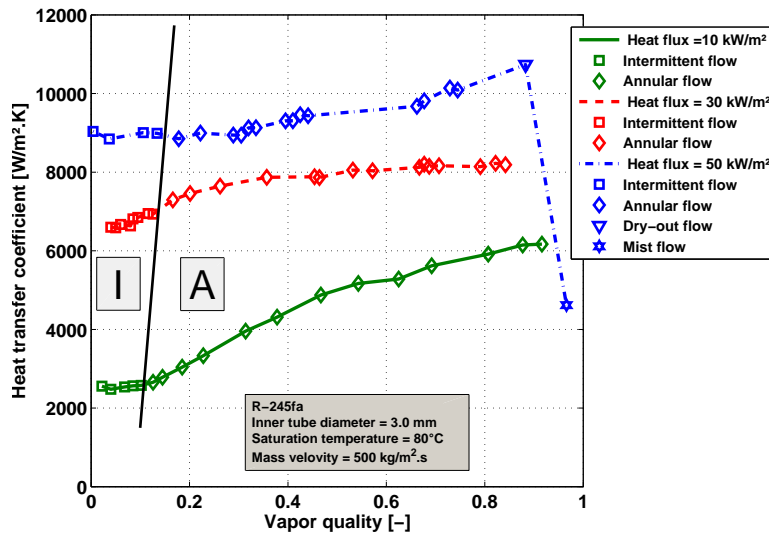
The heat transfer coefficient trend at relatively low saturation temperature ($T_{\text{sat}} = 60^\circ\text{C}$) is represented on Fig. 6.4a. This graph reveals three main zones corresponding to different heat transfer mechanisms, from the variation of the heat transfer coefficient along the evaporator:

Zone 1: liquid forced convection. Single-phase heat transfer through the liquid, which may be laminar or turbulent.

Zone 2: nucleate boiling. The heat transfer coefficient is almost independent of the vapor quality (exhibiting a plateau) and nucleate boiling is thereby predominant. This predominance is consistent with the flow pattern encountered in this region which corresponds to intermittent flow. The inner wall temperature at the bottom is higher than the one at the top of the tube. This difference is due to the nucleation which occurs more easily at the top part of the tube than at the bottom because of the stratification for these conditions.



(a) $T_{\text{sat}} = 60^\circ\text{C}$.



(b) $T_{\text{sat}} = 80^\circ\text{C}$.

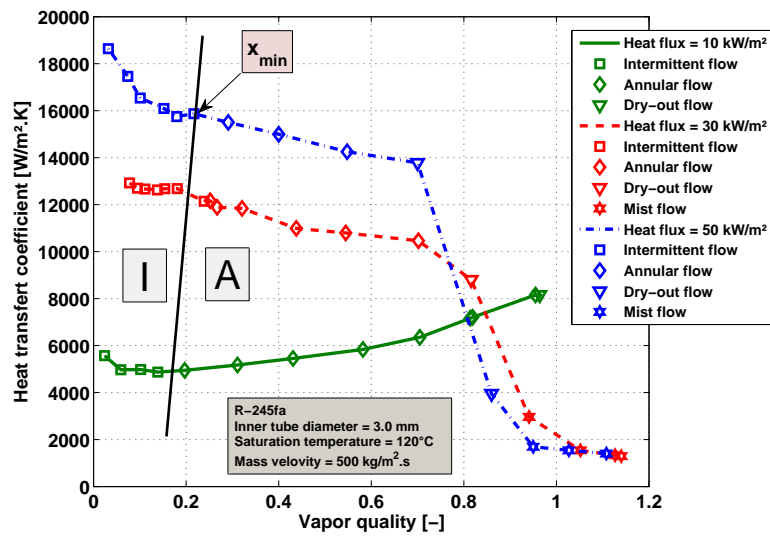
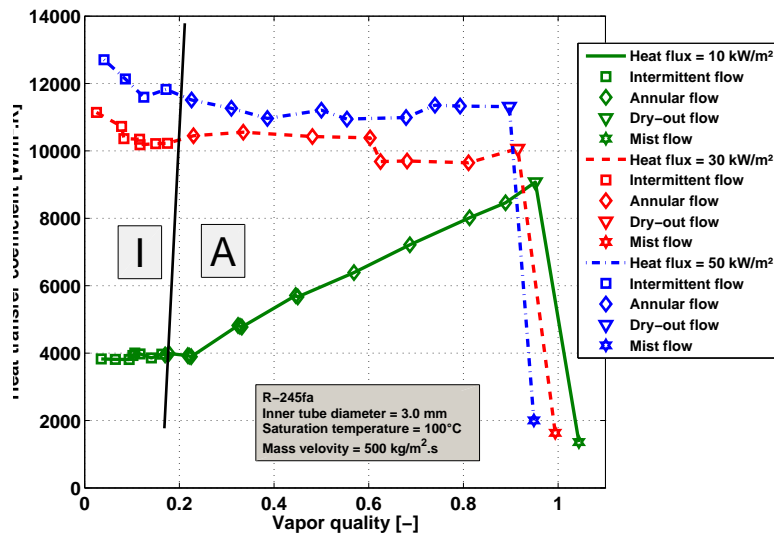


Figure 6.3: Influence of heat flux on heat transfer coefficient for R-245fa at 60°C , 80°C , 100°C and 120°C with a mass velocity of $500 \text{ kg/m}^2\cdot\text{s}$ (I: intermittent and A: annular).

Zone 3: convective boiling with some nucleate boiling. The predominance of the contribution of convective boiling to heat transfer does not imply that nucleate boiling is fully suppressed. The heat transfer coefficient increases prominently. Indeed, the density of the liquid-vapor mixture decreases, the flow accelerates and the convective transport enhances. During the vaporization, the liquid film trapped between the vapor and the tube becomes thinner and its thermal resistance decreases enhancing also heat transfer. As a result, the heat transfer coefficient rises with vapor quality

Figure 6.4b represent a type-curve of heat transfer coefficient at high saturation temperature ($T_{\text{sat}} = 120^\circ\text{C}$). Here, five main zones can be distinguished:

Zone 4: nucleate boiling. This regime is characterized by the formation of small bubbles on the heated wall of the tube. In this region, the heat transfer coefficient decreases with increasing vapor quality as the influence of nucleate boiling decreases: (i) the bubbles frequency decreases and (ii) the bubbles size increases. The heat transfer coefficient exhibits a change of slope at the transition between intermittent and annular flow.

Zone 5: nucleate boiling with a certain effect of convective boiling. The heat transfer coefficient is still predominantly influenced by nucleate boiling but convective boiling is present. Bubbles nucleate in the liquid film during annular flow. The decrease of the heat transfer coefficient is caused by the large dominance of nucleate boiling at low vapor qualities which is gradually suppressed with increasing vapor quality. Indeed, when the vapor quality increases, the annular liquid film becomes thinner and the wall superheat decreases leading to a decrease of the number of active nucleation sites for bubbles formation.

Zone 6: vapor forced convection + liquid film evaporation + droplets evaporation. The heat transfer coefficient falls over a limited quality range and then levels off. The vertical line at $x = 0.7$ indicates the inception point of dryout at the top of the horizontal tube, where locally the heat transfer begins to fall as the annular film dries out.

Zone 7: vapor forced convection + droplets evaporation. The heat transfer coefficient is constant. The vertical line at $x = 0.95$ indicates the location where dryout is complete around the tube perimeter, and thus also where the deterioration of the heat transfer ends. The dryout completion corresponds to the mist flow regime inception where the liquid film is entrained into the high velocity vapor core with or without redeposition on the channel walls.

Zone 8: vapor forced convection. Single-phase heat transfer to the vapor, all the liquid is evaporated and the heat transfer coefficient decreases.

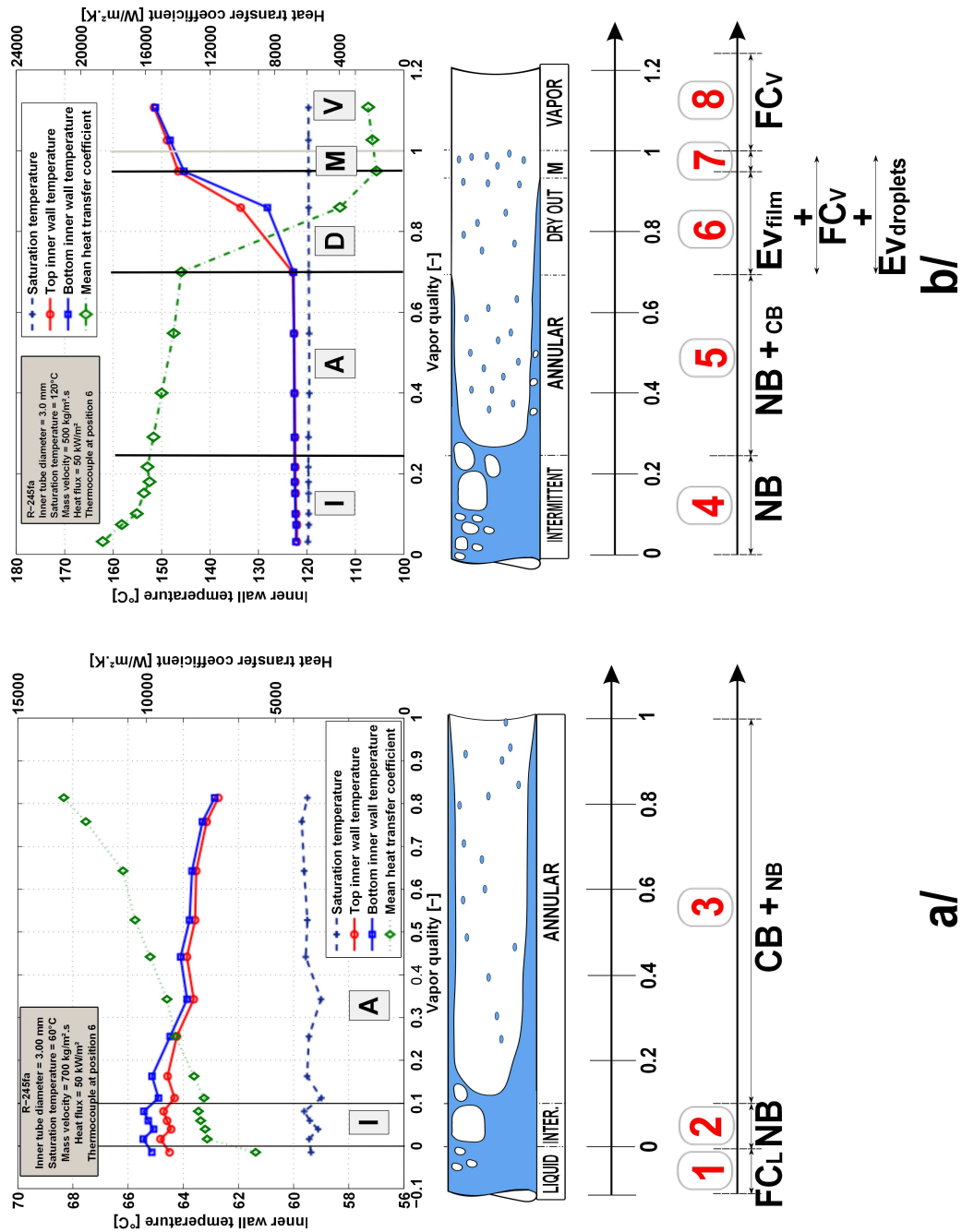


Figure 6.4: Relation between heat transfer coefficient, flow configuration and heat transfer mechanism (A: Annular, CB: Convective Boiling, D: Dryout, $Ev_{droplets}$: evaporation of the liquid droplets, Ev_{film} : evaporation of the liquid film, FC_L : liquid forced convection, FC_V : vapor forced convection, I: Intermittent, L: Liquid, M: Mist, NB: Nucleate Boiling and V: Vapor).

6.2 Comparisons of the database to prediction methods

In this section, the attention is focused on the comparison between the experimental heat transfer coefficients presented here above and theoretical results obtained with predictive methods previously quoted in section 3.4.3. The upcoming comparisons are classified according to the theoretical background of the prediction methods. To ensure the best consistency as possible, the comparisons are performed for each prediction method with the appropriate flow patterns. For instance, if a method was developed for annular flow regime, this method was tested only with data points obtained in annular flow regime. In addition to the graphical comparison, the Mean Relative Error (MRE) and Mean Absolute Error (MAE) reported in the following tables are calculated as:

$$\text{MRE} = \frac{1}{n} \sum_{i=1}^n \left(\frac{\alpha_{\text{pred},i} - \alpha_{\text{exp},i}}{\alpha_{\text{exp},i}} \right) \quad (6.1)$$

$$\text{MAE} = \frac{1}{n} \sum_{i=1}^n \left(\frac{|\alpha_{\text{pred},i} - \alpha_{\text{exp},i}|}{\alpha_{\text{exp},i}} \right) \quad (6.2)$$

The percentage of data falling in a $\pm 30\%$ error band is also given in the tables in order to provide a quantitative indication of the performance of these prediction methods when extrapolated up to high saturation temperatures. Moreover, a good prediction method should not only be statistically accurate, but also able of capturing the main trends of the experimental results. Hence, the trends in the evolution of the experimental heat transfer coefficient as a function of vapor quality as well as those predicted are compared for two situations: (i) $T_{\text{sat}} = 60^\circ\text{C}$, $\dot{q} = 50 \text{ kW/m}^2$, and $G = 700 \text{ kg/m}^2\cdot\text{s}$ and (ii) $T_{\text{sat}} = 120^\circ\text{C}$, $\dot{q} = 50 \text{ kW/m}^2$, and $G = 700 \text{ kg/m}^2\cdot\text{s}$.

6.2.1 Pre-dryout prediction heat transfer methods

6.2.1.1 Pool boiling correlations

The experimental dataset is compared to three pool boiling correlations: [Cooper (1984)], [Ribatski and Jabardo (2003)], and [Yun et al. (2005)]. Figure 6.5 displays these comparisons for two different saturation temperatures: 60°C (Figs. 6.5(a), 6.5(c), and 6.5(e)) and 120°C (Figs. 6.5(b), 6.5(d), and 6.5(f)). Table 6.2 summarizes the results of the statistical analysis of these comparisons.

In general, at 60°C , the heat transfer coefficient is largely underpredicted for both intermittent and annular flow regimes. On the one hand, for the intermittent flow regime, the correlations of [Cooper (1984)] and [Ribatski and Jabardo (2003)] predict around 60% of the data within $\pm 30\%$ error band whereas the correlation of [Yun et al. (2005)] predicts 88.9 % of the data within $\pm 30\%$ error band. These figures confirm the major role played by the nucleate boiling for the intermittent flow regimes. On the other hand, for the annular flow regime, these correlations do not take into account the increase of the heat transfer coefficient with increasing vapor quality (see Fig. 6.6(a)) and the results present a large dispersion. Indeed, as explained previously, when the vapor quality increases, the convective contribution to the overall flow boiling heat transfer is increased.

At 120°C , the results are more homogeneous than at 60°C for the comparisons with the correlations of [Cooper (1984)] and [Ribatski and Jabardo (2003)] for both intermittent and annular flow regimes. Moreover, the number of data falling within

$\pm 30\%$ error band for annular flow regime is 77.9% and 83.5% for the correlations of [Cooper (1984)] and [Ribatski and Jabardo (2003)], respectively. These figures corroborate the predominance of nucleate boiling heat transfer mechanism at high saturation temperature for both intermittent and annular flow regimes. The comparison with the correlation of [Yun et al. (2005)] fails to predict the heat transfer coefficient at 120°C. In general, this correlation overpredicts the flow boiling heat transfer coefficient. This correlation is developed for carbon dioxide which explains this discrepancy. Indeed, the heat transfer coefficient for carbon dioxide is higher than that for halogenated refrigerants for a given saturation temperature (as observed by [Grauso et al. (2013)]). These correlations fail to achieve any vapor quality effect and fail to reproduce the experimental trend (i.e. a decrease of the heat transfer coefficient with increasing vapor quality). They do not take into account the gradual suppression of the contribution of nucleate boiling to the overall heat transfer coefficient with increasing vapor quality (see Fig. 6.6(b)).

In conclusion, pool boiling correlations are not adequate to predict the whole database with accuracy and, moreover, they do not capture the experimental trends. Nevertheless, these comparisons were useful to highlight the change of dominant heat transfer mechanism when changing the vapor quality.

6.2.1.2 Asymptotic models

For a better readability of the results, the comparisons with the models developed for carbon dioxide with or without other fluids are presented separately from the others in section 6.2.1.3.

The comparisons were performed against eight heat transfer prediction models based on the asymptotic approach: [Chen (1963)], [Gungor and Winterton (1986)], [Kandlikar (1990)], [Kandlikar and Balasubramanian (2004)], [Zhang et al. (2004)], [Saitoh et al. (2007)], [Bertsch et al. (2009)], and [Liu and Winterton (1991)]. For the models of [Kandlikar (1990)] and [Kandlikar and Balasubramanian (2004)], the fluid dependent parameter (F_{fl}) is fixed at 1.43 as proposed by [Vakili-Farahani et al. (2013)]. Table 6.3 summarizes the results of the statistical analysis of these comparisons.

Figure 6.7 displays graphical results of the comparisons between experimental data and those predicted by three heat transfer coefficient prediction models: [Gungor and Winterton (1986)], [Kandlikar and Balasubramanian (2004)], and [Liu and Winterton (1991)] at two different saturation temperatures: 60°C (Figs. 6.7(a), 6.7(c), and 6.7(e)) and 120°C (Figs. 6.7(b), 6.7(d), and 6.7(f)).

At 60°C, the asymptotic models developed by [Chen (1963)], [Gungor and Winterton (1986)], [Kandlikar and Balasubramanian (2004)], and [Zhang et al. (2004)] produce homogeneous results and are relatively reliable to predict the heat transfer coefficient, especially for annular flow (see Table 6.2). The heat transfer model of [Kandlikar and Balasubramanian (2004)] developed for microchannels predicts with accuracy the data with 74.3% and 83.8% of the data falling within $\pm 30\%$ error band for intermittent and annular flow regimes, respectively.

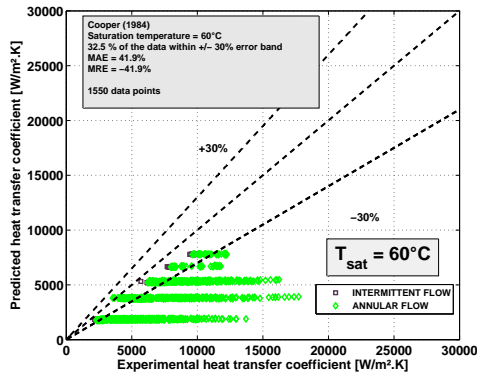
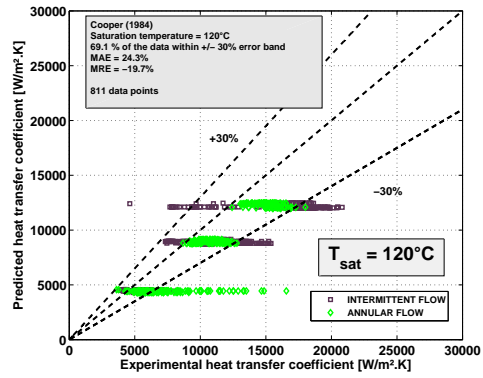
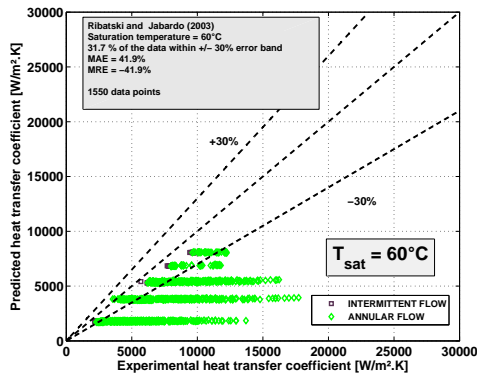
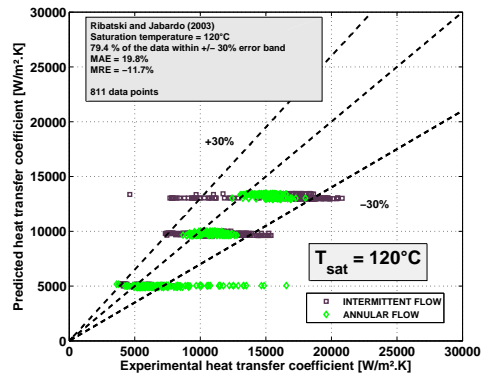
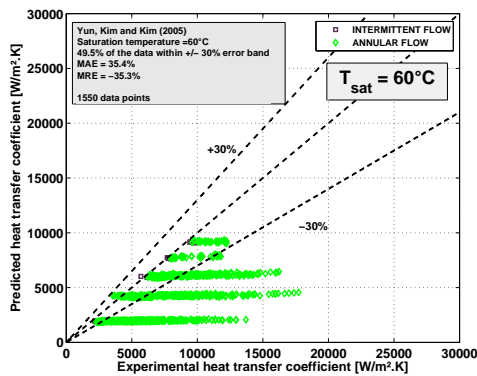
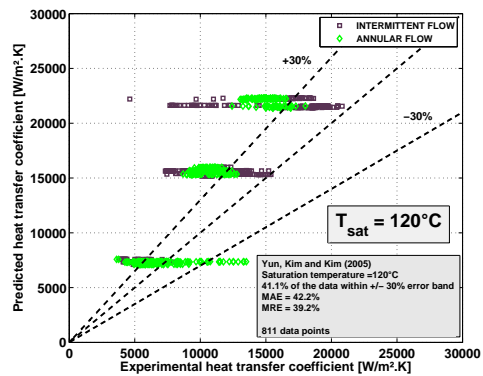
(a) [Cooper (1984)] - $T_{sat} = 60^{\circ}\text{C}$.(b) [Cooper (1984)] - $T_{sat} = 120^{\circ}\text{C}$.(c) [Ribatski and Jabardo (2003)] - $T_{sat} = 60^{\circ}\text{C}$.(d) [Ribatski and Jabardo (2003)] - $T_{sat} = 120^{\circ}\text{C}$.(e) [Yun et al. (2005)] - $T_{sat} = 60^{\circ}\text{C}$.(f) [Yun et al. (2005)] - $T_{sat} = 120^{\circ}\text{C}$.

Figure 6.5: Comparison between experimental heat transfer coefficients and those predicted by pool boiling correlations.

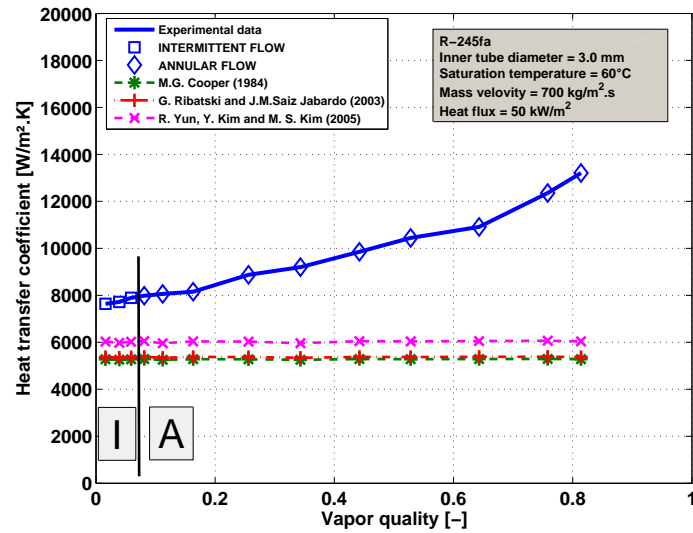
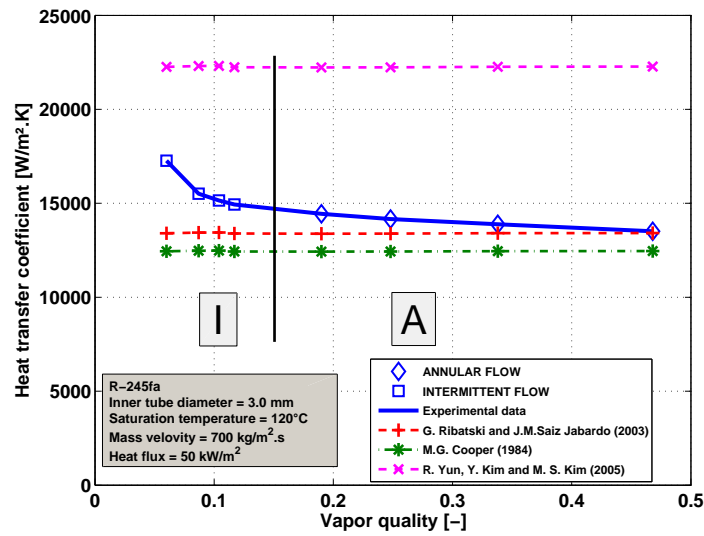
(a) $T_{\text{sat}} = 60^\circ\text{C}$.(b) $T_{\text{sat}} = 120^\circ\text{C}$.

Figure 6.6: Comparison between the experimental trends and those predicted by pool boiling correlations at 60°C and 120°C ((a) $T_{\text{sat}} = 60^\circ\text{C}$, $\dot{q} = 50 \text{ kW/m}^2$, and $G = 700 \text{ kg/m}^2\cdot\text{s}$ and (b) $T_{\text{sat}} = 120^\circ\text{C}$, $\dot{q} = 50 \text{ kW/m}^2$, and $G = 700 \text{ kg/m}^2\cdot\text{s}$).

Table 6.2: Summary of the statistical analysis of the comparisons between experimental heat transfer coefficients and those predicted by pool boiling correlations (MAE: Mean Absolute Error, MRE: Mean Relative Error and $\pm 30\%$: percentage of data predicted within 30% error bar).

	60°C						120°C						Whole database								
	Intermittent			Annular			Intermittent			Annular			Total			Intermittent			Annular		
	MAE	MRE	$\pm 30\%$	MAE	MRE	$\pm 30\%$	MAE	MRE	$\pm 30\%$	MAE	MRE	$\pm 30\%$	MAE	MRE	$\pm 30\%$	MAE	MRE	$\pm 30\%$	MAE	MRE	$\pm 30\%$
[Ribatski and Jabardo (2003)]	27.4	-27.4	56.0	46.5	-46.5	23.9	23.0	-8.7	75.9	16.4	-14.9	83.5	34.2	-32.6	51.5	22.9	-18.2	75.0	39.5	-39.3	40.7
[Cooper (1984)]	27.4	-27.4	59.7	46.7	-46.7	23.8	25.5	-16.8	60.9	23.1	-22.8	77.9	36.1	-35.1	47.4	24.7	-21.7	68.7	41.3	-41.2	37.5
[Yun et al. (2005)]	19.7	-19.6	88.9	40.5	-40.4	36.8	44.6	44.6	52.1	39.6	33.4	29.0	32.9	-5.6	53.7	27.9	16.9	74.7	35.2	-16.0	44.0

The model of [Saitoh et al. (2007)] developed for R-134a with a very limited range of saturation temperature (from 5 to 15°C), is not able to predict the heat transfer coefficient of R-245fa at 60°C with only 15.9% and 28.7% of the data falling within $\pm 30\%$ error band for intermittent and annular flow regimes, respectively. The heat transfer model of [Bertsch et al. (2009)] works well to predict the data for the intermittent flow regime (90.7% of the data falling within $\pm 30\%$ error band) whereas this model fails to estimate the flow boiling heat transfer coefficient for annular flow regime. This poor accuracy for annular flow could be due to the use of the correlation of [Hausen (1943)] for developing laminar flow to calculate the convective heat transfer in the liquid and vapor phases. It can also be due to the not well justified assumption of a linear decrease of the nucleate boiling heat transfer coefficient with increasing vapor quality. Figure 6.8(a) presents a comparison between the trends predicted by models and the experimental one at 60°C. Except those given by the models of [Bertsch et al. (2009)] and [Liu and Winterton (1991)], both experimental and predicted curves showing the heat transfer coefficient as a function of the vapor quality present a positive slope. The model of [Kandlikar and Balasubramanian (2004)] is ranked as the best to predict flow boiling heat transfer trend at 60°C.

At 120°C, the comparisons with the asymptotic models developed by [Gungor and Winterton (1986)], and [Kandlikar and Balasubramanian (2004)] (presented on Figs. 6.7(b), and 6.7(d), respectively) exhibits a broad dispersion. In general, the asymptotic models underestimate the heat transfer coefficient at high saturation temperature. In section 6.1.1, nucleate boiling was shown to remain as the dominant heat transfer mechanism at high saturation temperature over the whole range of vapor quality until the dryout inception. The poor agreement could be due to the definition of the nucleate boiling suppression factor (F) established from data taken in a limited range of saturation temperature. Nonetheless, the correlation of [Kandlikar and Balasubramanian (2004)] and [Bertsch et al. (2009)] predicts 83.3% and 81.2% of the data for annular flow within $\pm 30\%$ error band. These good agreements can be explain by the fact that these correlations were developed for microchannels. As a matter of fact, similar mechanisms govern the flow boiling heat transfer at moderate saturation temperature in microchannels and at high saturation temperature in minichannels. Indeed, nucleate boiling whose importance in the flow boiling heat transfer in microchannels was pointed out by [Kandlikar (2002)] and [Thome (2004b)] is also the dominant contribution to heat transfer at high saturation temperature. Figure 6.8(b) represents the experimental trends at 120°C and those predicted by asymptotic models. These correlations fail to capture any effect of the vapor quality when extrapolated up to high saturation temperature. Nevertheless, the models of [Gungor and Winterton (1986)] and [Bertsch et al. (2009)] reveal trends close to the experimental ones for annular flow regime, i.e. a decrease of the heat transfer coefficient. This result corroborates the choice of [Del Col (2010)] to modify the model of [Gungor and Winterton (1986)] to predict the heat transfer coefficient at high saturation temperature.

The [Kutateladze (1961)] model of [Liu and Winterton (1991)] predicts the whole database with only 42.8% of the data falling within $\pm 30\%$ error band. This approach is not adapted to predict flow boiling heat transfer coefficient of R-245fa in this range of saturation temperature.

In conclusion, these asymptotic models are relatively reliable and robust to predict the flow boiling heat transfer coefficient for R-245fa at 60°C while, at 120°C, the discrepancy increases except for the correlations developed for microchannels. A modification of the factors F and S could be an interesting way to adapt these asymptotic correlations to high saturation temperatures.

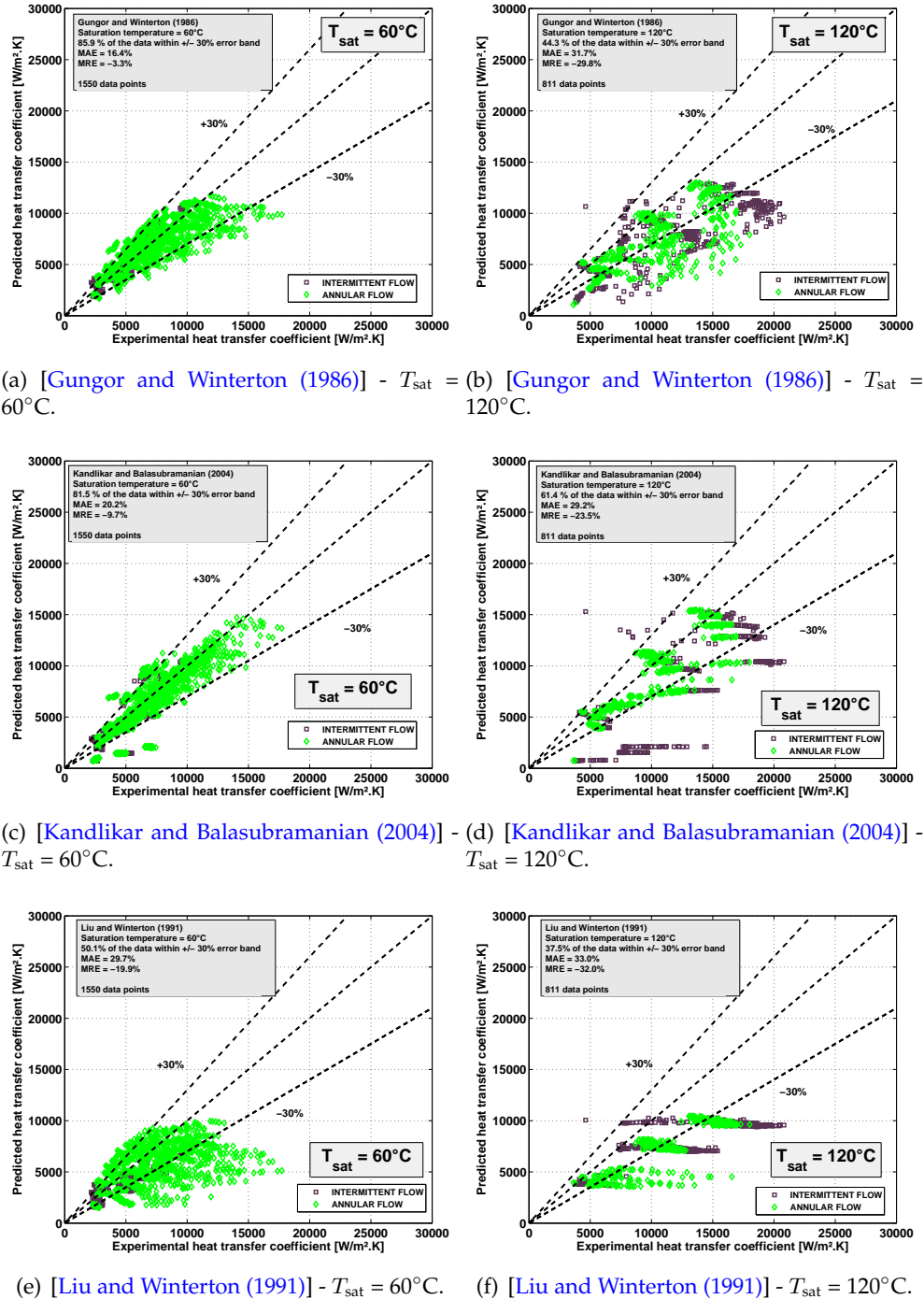


Figure 6.7: Comparison between experimental heat transfer coefficients and those predicted by asymptotic models at 60°C and 120°C.

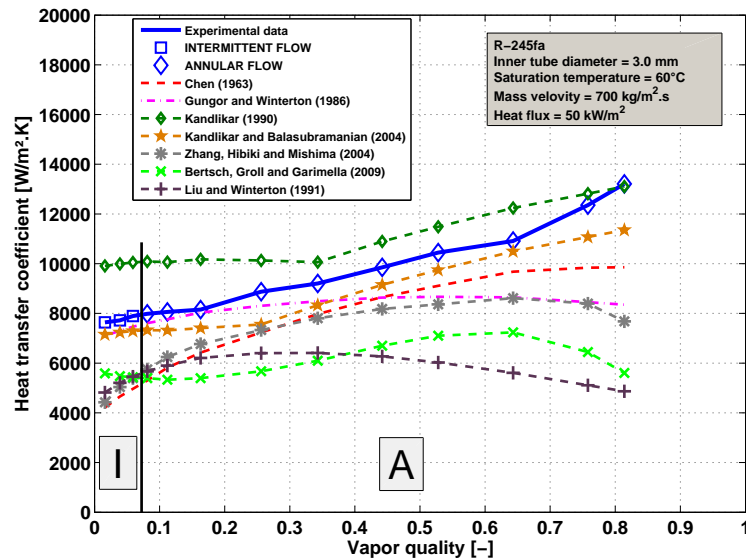
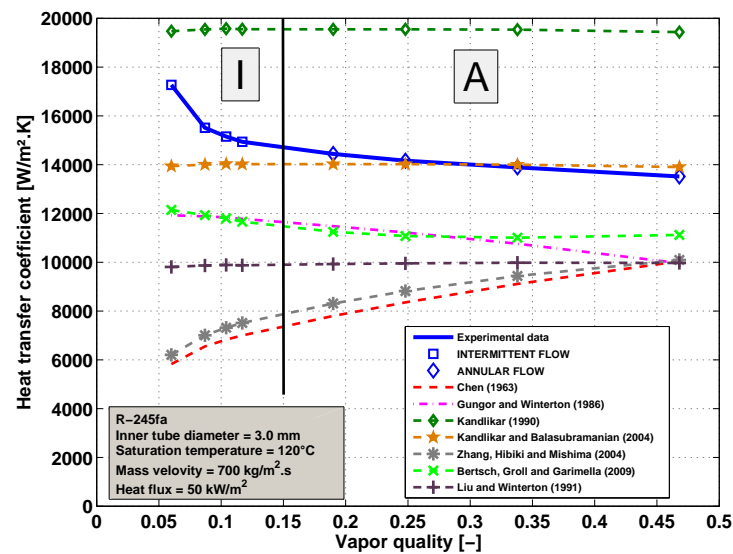
(a) $T_{\text{sat}} = 60^{\circ}\text{C}$.(b) $T_{\text{sat}} = 120^{\circ}\text{C}$.

Figure 6.8: Comparison between the experimental trends and those predicted by asymptotic models at 60°C and 120°C ((a) $T_{\text{sat}} = 60^{\circ}\text{C}$, $\dot{q} = 50 \text{ kW/m}^2$, and $G = 700 \text{ kg/m}^2\cdot\text{s}$ and (b) $T_{\text{sat}} = 120^{\circ}\text{C}$, $\dot{q} = 50 \text{ kW/m}^2$, and $G = 700 \text{ kg/m}^2\cdot\text{s}$).

Table 6.3: Summary of the statistical analysis of the comparisons between experimental heat transfer coefficients and those predicted by asymptotic models (MAE: Mean Absolute Error, MRE: Mean Relative Error and $\pm 30\%$: percentage of data predicted within 30% error bar).

	60° C						120° C						Whole database								
	Intermittent			Annular			Intermittent			Annular			Total			Intermittent			Annular		
	MAE	MRE	$\pm 30\%$	MAE	MRE	$\pm 30\%$	MAE	MRE	$\pm 30\%$	MAE	MRE	$\pm 30\%$	MAE	MRE	$\pm 30\%$	MAE	MRE	$\pm 30\%$	MAE	MRE	$\pm 30\%$
[Chen (1963)]	27.5	-16.6	51.5	15.6	-2.2	88.2	46.5	-38.0	29.6	25.7	-21.3	59.4	25.0	-13.6	66.2	38.4	-24.9	37.5	18.8	-8.4	79.3
[Gungor and Winterton (1986)]	12.4	0.6	95.7	17.7	-4.5	82.8	34.3	-31.6	35.3	28.9	-27.8	53.9	22.5	-13.6	69.5	22.5	-13.6	67.2	22.5	-13.5	70.5
[Kandlikar (1990)]	31.4	30.2	54.2	23.6	20.2	73.7	23.3	8.5	80.2	27.1	21.3	60.7	27.8	21.2	65.7	31.7	25.3	61.0	26.4	19.6	67.5
[Kandlikar and Balasubramanian (2004)]	24.7	-15.0	74.3	18.7	-8.0	83.8	40.7	-35.8	41.5	16.7	-10.1	83.3	23.2	-12.1	74.0	33.1	-22.1	59.8	18.7	-7.5	80.6
[Zhang et al. (2004)]	27.7	-13.0	50.9	20.4	-5.0	79.9	45.0	-37.5	31.8	25.6	-20.6	59.1	29.3	-14.4	60.7	38.0	-23.0	37.7	22.4	-10.5	71.4
[Saitoh et al. (2007)]	171.6	169.4	15.9	106.5	97.0	28.7	85.6	71.1	40.4	51.5	85.4	66.0	97.1	82.5	33.5	117.3	104.2	28.3	87.8	72.6	35.8
[Bertsch et al. (2009)]	20.7	-20.7	90.7	29.8	-27.0	51.8	27.2	-20.7	55.0	19.8	-15.0	81.2	25.4	-22.4	66.2	22.3	-19.0	74.8	26.8	-24.0	62.2
[Liu and Winterton (1991)]	26.5	-21.2	52.5	30.7	-19.5	49.4	33.2	-31.7	33.6	32.8	-32.6	41.6	32.4	-28.0	42.8	30.3	-27.1	41.4	33.4	-28.5	43.5

6.2.1.3 Asymptotic models developed from carbon dioxide data with or without other fluids data

The experimental heat transfer coefficients are compared to those predicted by the asymptotic models of [Choi et al. (2007b)], [Ducoulombier et al. (2011)], [Fang (2013)], and [Yoon et al. (2004)]. These models were developed from database obtained for carbon dioxide with or without other fluids. These comparisons are represented at 60°C and 120°C on Fig. 6.9. Table 6.4 summarizes the results of the statistical analysis of these comparisons. These models work relatively well to predict the whole database, especially the model of [Choi et al. (2007b)] with 88.8 % of the data falling within $\pm 30\%$ error band. For intermittent flow regime, these models overpredict the flow boiling heat transfer coefficient. Indeed, for the lower vapor quality region, the heat transfer of carbon dioxide is governed by the nucleate boiling mechanism which is very important, and by consequence the heat transfer coefficient for carbon dioxide is higher than for other refrigerants for intermittent flow. For annular flow data, the statistical results are very good at 120°C as the percentage of data falling within $\pm 30\%$ error band is ranging from 77% to 94%.

Figures 6.10(a) and 6.10(b) represent the trends of the experimental heat transfer coefficient as well as those predicted by asymptotic models for the same experimental conditions. On Fig. 6.10(a), the models of [Choi et al. (2007a)] and [Choi et al. (2007b)] provide the same trend as the experimental one. At 120°C, the trends provided by these models are more similar to the experimental trends than those provided by the asymptotic models developed for other fluids than the carbon dioxide and presented in section 4.2.1 (see Fig. 6.8(b)). The trends obtained with the asymptotic models developed by [Choi et al. (2007a)], [Ducoulombier et al. (2011)], and [Fang (2013)] depict the experimental trend, i.e. (i) a stiff decrease for intermittent flow and (ii) a gradual decrease for annular flow. The trends of asymptotic models developed for carbon dioxide with or without other fluids are good, however the discrepancies on the prediction of the heat transfer coefficient are important and require to adapt F and S to extrapolate these models to other refrigerants than carbon dioxide.

6.2.1.4 Enhancement-factor approach

Figures 6.11(a) and 6.11(b) display the comparison between the experimental heat transfer coefficients and those predicted by the correlation of [Shah (1982)] at 60°C and 120°C, respectively. The correlation for the prediction of the enhancement-factor used by [Shah (1982)] is very efficient at 60°C with 83.6% and 83.2% of the data falling within $\pm 30\%$ error band for intermittent and annular flow regimes, respectively. This correlation produces homogeneous results as its MAE is only of 16.5% and 17.9% for intermittent and annular flow regimes, respectively. At 120°C, this correlation largely underestimates the heat transfer coefficient and produces a broad dispersion of the data. Only 21.3% and 34.2% of the data fall within $\pm 30\%$ error band for intermittent and annular flow regimes, respectively.

The comparison between the experimental trends of the heat transfer coefficient as a function of the vapor quality and those predicted by the correlation of [Shah (1982)] is shown on 6.11(a) ($T_{\text{sat}} = 60^\circ\text{C}$) and 6.11(b) ($T_{\text{sat}} = 120^\circ\text{C}$). For both, the discrepancy is important but the correlation exhibits a relatively good aptitude to capture the effect of the vapor quality.

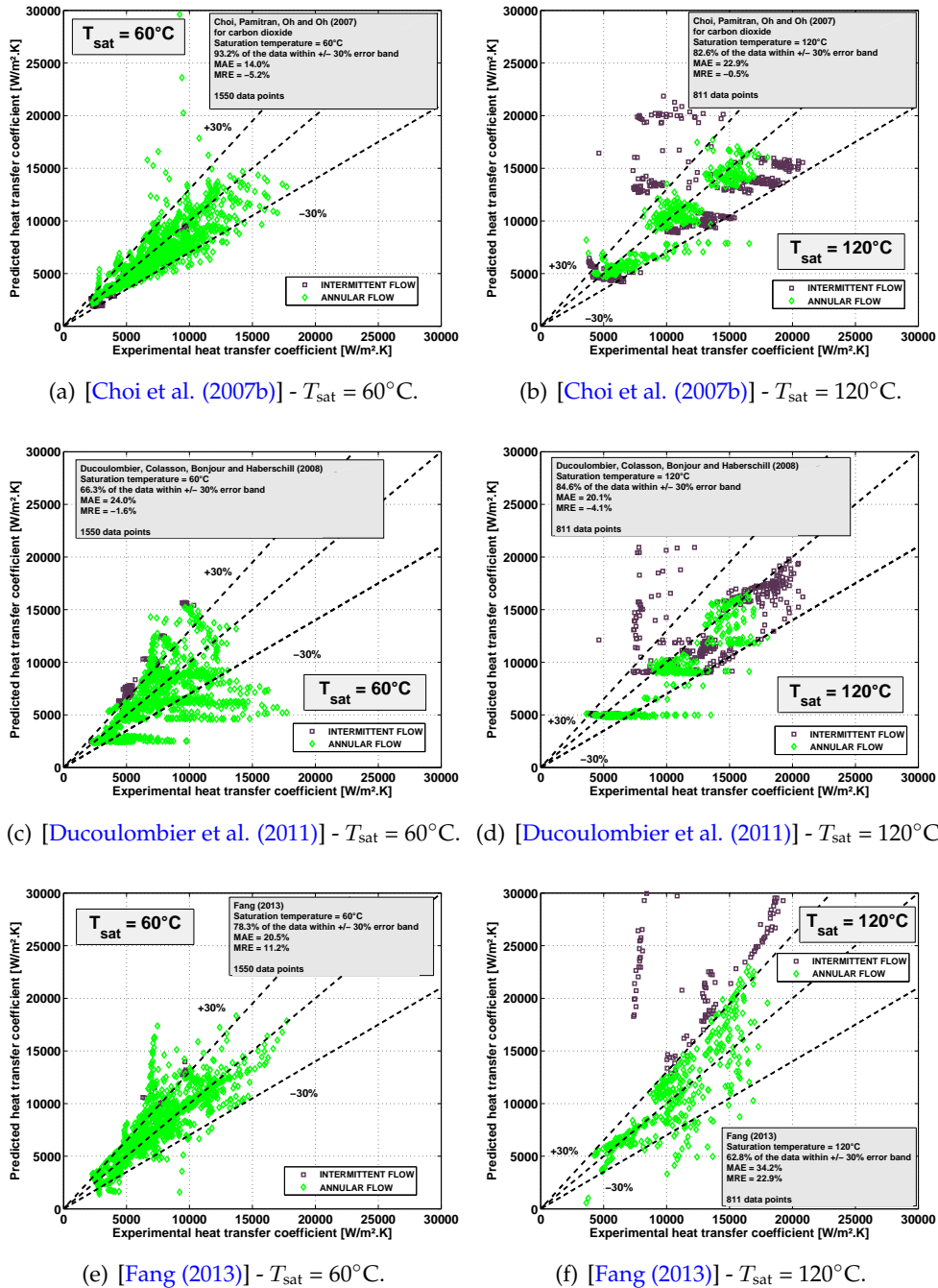


Figure 6.9: Comparison between experimental heat transfer coefficients and those predicted by asymptotic models developed for carbon dioxide with or without other fluids.

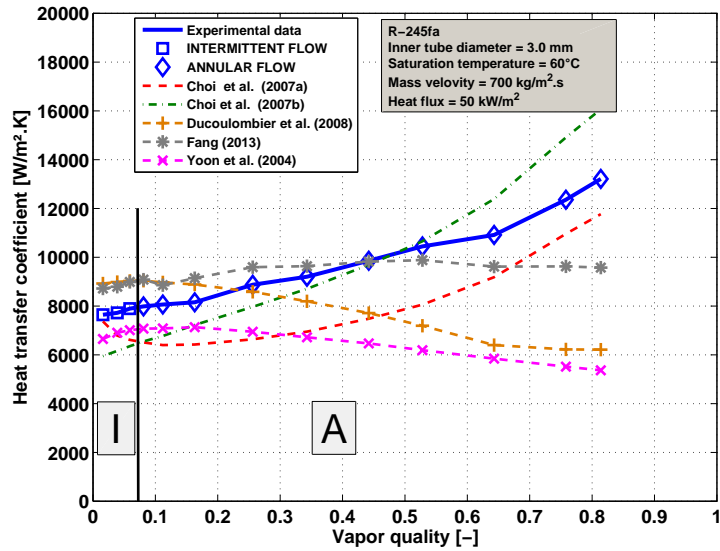
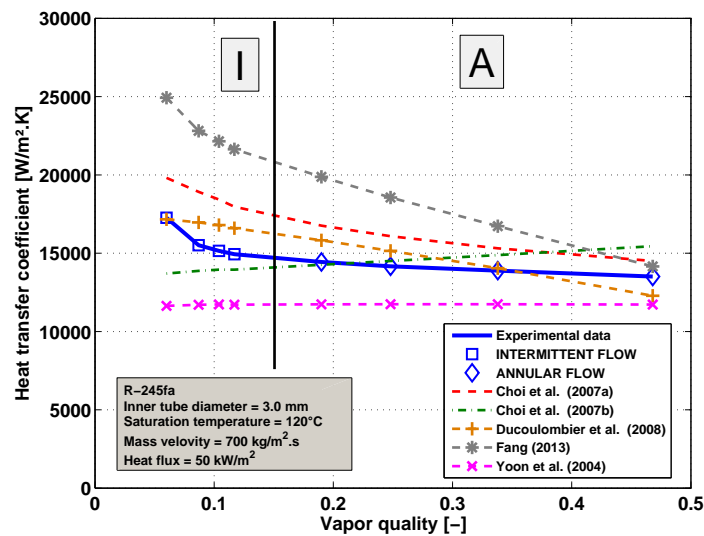
(a) $T_{\text{sat}} = 60^\circ\text{C}$.(b) $T_{\text{sat}} = 120^\circ\text{C}$.

Figure 6.10: Comparison between the experimental trends and those predicted by asymptotic models for carbon dioxide with or without other fluids at 60°C and 120°C ((a) $T_{\text{sat}} = 60^\circ\text{C}$, $\dot{q} = 50 \text{ kW/m}^2$, and $G = 700 \text{ kg/m}^2\cdot\text{s}$ and (b) $T_{\text{sat}} = 120^\circ\text{C}$, $\dot{q} = 50 \text{ kW/m}^2$, and $G = 700 \text{ kg/m}^2\cdot\text{s}$).

Table 6.4: Summary of the statistical analysis of the comparisons between experimental heat transfer coefficients and those predicted by asymptotic models developed for carbon dioxide with or without other fluids (MAE: Mean Absolute Error, MRE: Mean Relative Error and $\pm 30\%$: percentage of data predicted within 30% error bar).

	60°C						120°C						Whole database								
	Intermittent			Annular			Intermittent			Annular			Total			Intermittent			Annular		
	MAE	MRE	$\pm 30\%$	MAE	MRE	$\pm 30\%$	MAE	MRE	$\pm 30\%$	MAE	MRE	$\pm 30\%$	MAE	MRE	$\pm 30\%$	MAE	MRE	$\pm 30\%$	MAE	MRE	$\pm 30\%$
[Choi et al. (2007a)]	31.3	12.5	73.2	26.3	-9.8	70.6	82.4	69.7	65.6	18.2	-15.0	77.4	31.9	0.5	71.6	48.7	34.5	70.9	24.2	-15.3	72.0
[Choi et al. (2007b)]	11.7	10.4	98.4	14.7	-3.4	91.5	33.4	4.5	72.3	11.5	-3.8	93.9	16.7	-4.2	88.8	19.8	-3.4	89.3	15.2	-4.6	88.7
[Ducoulombier et al. (2011)]	23.9	18.8	62.1	24.0	-8.2	67.6	23.4	5.5	83.2	16.5	-14.4	86.1	23.4	-5.3	70.0	21.7	11.5	74.9	24.2	-13.0	67.7
[Fang (2013)]	34.6	34.6	47.8	16.8	7.2	85.1	83.0	83.0	12.4	16.9	1.6	85.6	25.3	14.7	72.3	49.4	46.1	43.3	17.5	5.0	84.4
[Yoon et al. (2004)]	23.9	6.6	78.8	35.9	-7.4	50.5	27.3	-18.2	49.3	20.8	-16.3	82.2	30.7	-10.8	58.9	26.1	-4.5	66.8	32.7	-13.6	53.4

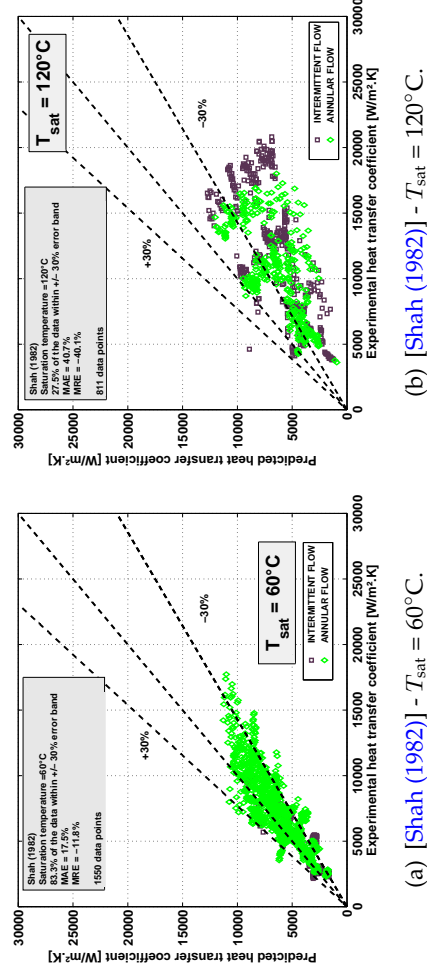


Figure 6.11: Comparison between experimental heat transfer coefficients and those predicted by the correlation of [Shah (1982)] at 60°C and 120°C .

6.2.1.5 Nusselt-type correlations

Figure 6.13 depicts the comparison between experimental results and results predicted from the Nusselt-type correlations of [Lazarek and Black (1982)], [Tran et al. (1996)] and [Kew and Cornwell (1997)] at 60°C and 120°C . Table 6.6 presents statistically the results of the comparisons between the experimental heat transfer coefficients and those predicted by the Nusselt-type correlations of [Lazarek and Black (1982)], [Tran et al. (1996)], [Warrier et al. (2002)], [Sun and Mishima (2009)], and [Kew and Cornwell (1997)]. In general, these comparisons produce generally a large dispersion for the whole database with a MAE ranging from 24.2% to 60.7%. Except with the correlation of [Tran et al. (1996)], the experimental heat transfer coefficient are underpredicted by these Nusselt-type correlations for the whole pre-dryout database as the MRE is ranging from -17.8% to -44.5%. Except, the correlation of [Sun and Mishima (2009)] developed from data obtained with carbon dioxide with other fluids which works well to predict the whole database (70.2% of the data falling within $\pm 30\%$ error band), these correlations provide poor agreement when extrapolated to this range of saturation temperatures.

Figure 6.14 displays the evolution of the heat transfer coefficients vs. vapor quality in comparison to that predicted by Nusselt-type correlations. At 60°C , the correlation of [Kew and Cornwell (1997)] is the only one to reproduce a trend similar to the experimental one. This good agreement is due to the fact that this correlation was developed from a database where convective boiling was the dominant heat transfer mechanism as in annular flow regime in the present study at 60°C . At 120°C , no correlation is able to capture the experimental trends. These correlations are assumed to be the most empirical of all, hence, it is logical to find a huge discrepancy when they are used out of their original range of experimental conditions. However, the correlation of [Sun and Mishima (2009)] developed partially with carbon dioxide data works very well to predict the flow boiling heat transfer at high saturation temperature.

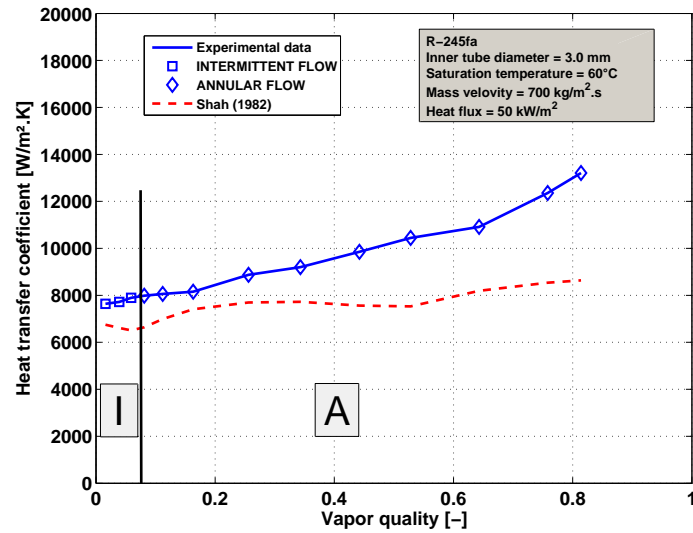
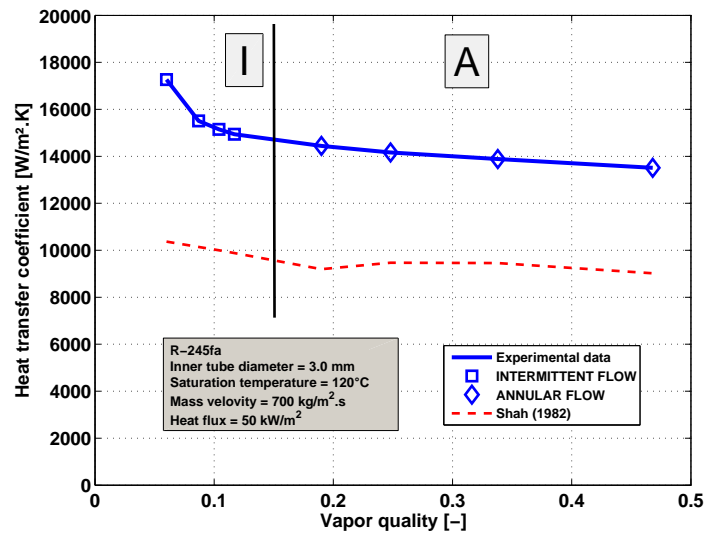
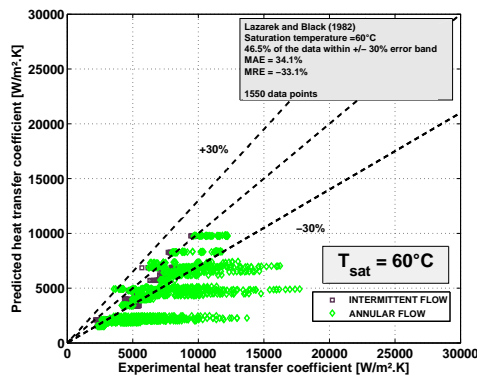
(a) $T_{\text{sat}} = 60^{\circ}\text{C}$.(b) $T_{\text{sat}} = 120^{\circ}\text{C}$.

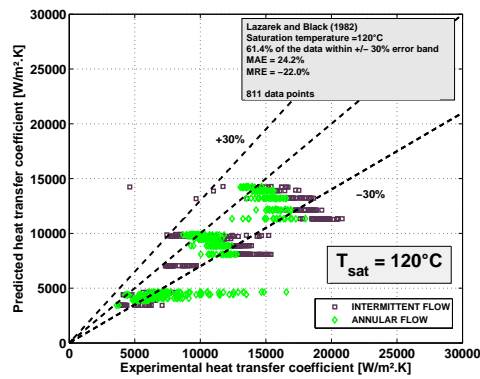
Figure 6.12: Comparison between the experimental trends and those predicted by the correlation of [Shah (1982)] ((a) $T_{\text{sat}} = 60^{\circ}\text{C}$, $\dot{q} = 50 \text{ kW/m}^2$, and $G = 700 \text{ kg/m}^2\cdot\text{s}$ and (b) $T_{\text{sat}} = 120^{\circ}\text{C}$, $\dot{q} = 50 \text{ kW/m}^2$, and $G = 700 \text{ kg/m}^2\cdot\text{s}$).

Table 6.5: Summary of the statistical analysis of the comparisons between experimental heat transfer coefficients and those predicted by the correlation of [Shah (1982)] (MAE: Mean Absolute Error, MRE: Mean Relative Error and $\pm 30\%$: percentage of data predicted within 30% error bar).

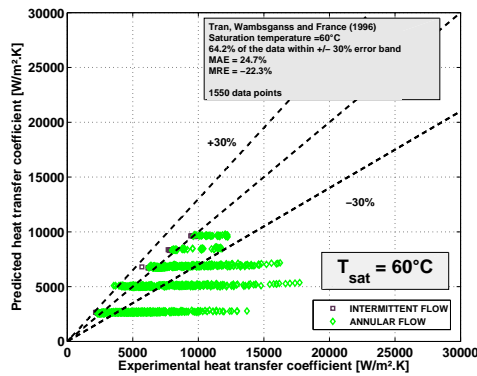
	60° C						120° C						Whole database								
	Intermittent			Annular			Intermittent			Annular			Total			Intermittent			Annular		
	MAE	MRE	$\pm 30\%$	MAE	MRE	$\pm 30\%$	MAE	MRE	$\pm 30\%$	MAE	MRE	$\pm 30\%$	MAE	MRE	$\pm 30\%$	MAE	MRE	$\pm 30\%$	MAE	MRE	$\pm 30\%$
[Shah (1982)]	16.5	-10.5	83.6	17.9	-12.2	83.2	44.1	-43.1	21.3	36.9	-36.8	34.2	26.3	-22.0	61.5	29.7	-24.2	53.6	24.8	-21.1	65.2



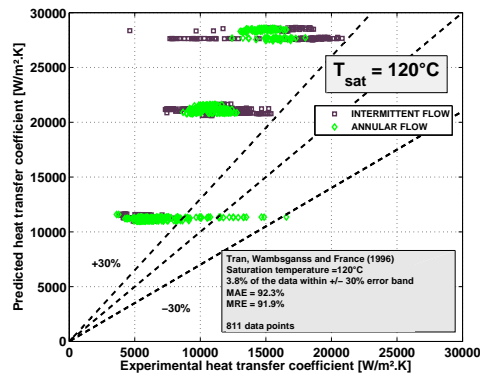
(a) [Lazarek and Black (1982)] - $T_{\text{sat}} = 60^\circ\text{C}$.



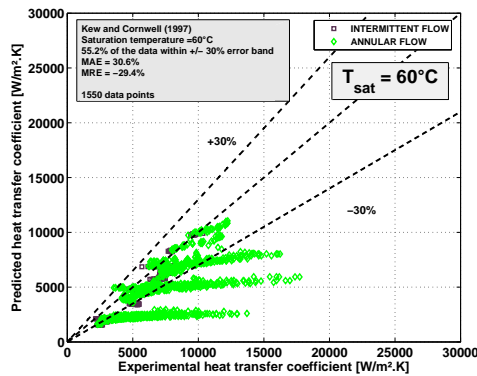
(b) [Lazarek and Black (1982)] - $T_{\text{sat}} = 120^\circ\text{C}$.



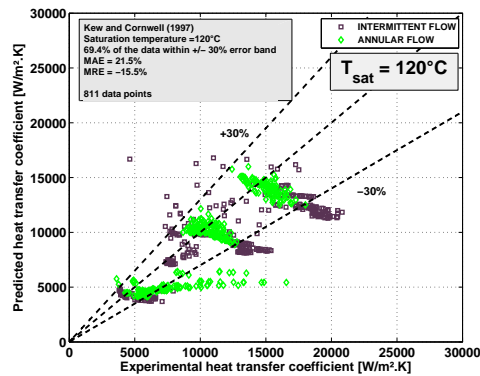
(c) [Tran et al. (1996)] - $T_{\text{sat}} = 60^\circ\text{C}$.



(d) [Tran et al. (1996)] - $T_{\text{sat}} = 120^\circ\text{C}$.



(e) [Kew and Cornwell (1997)] - $T_{\text{sat}} = 60^\circ\text{C}$.



(f) [Kew and Cornwell (1997)] - $T_{\text{sat}} = 120^\circ\text{C}$.

Figure 6.13: Comparison between the experimental heat transfer coefficients and those predicted by Nusselt-type correlations.

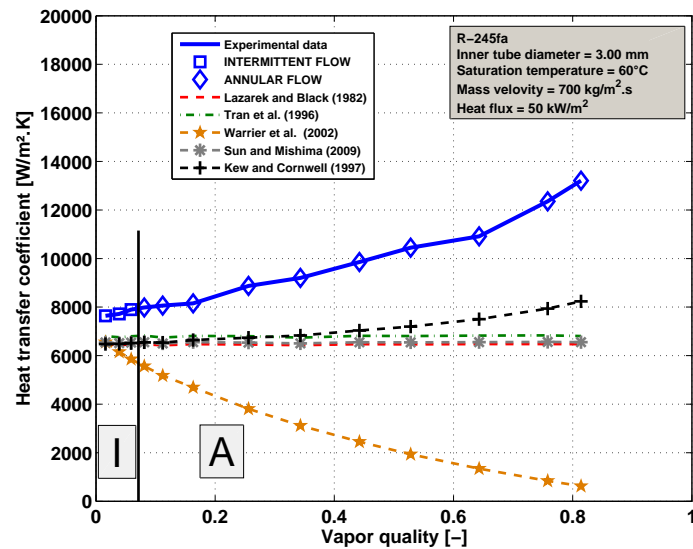
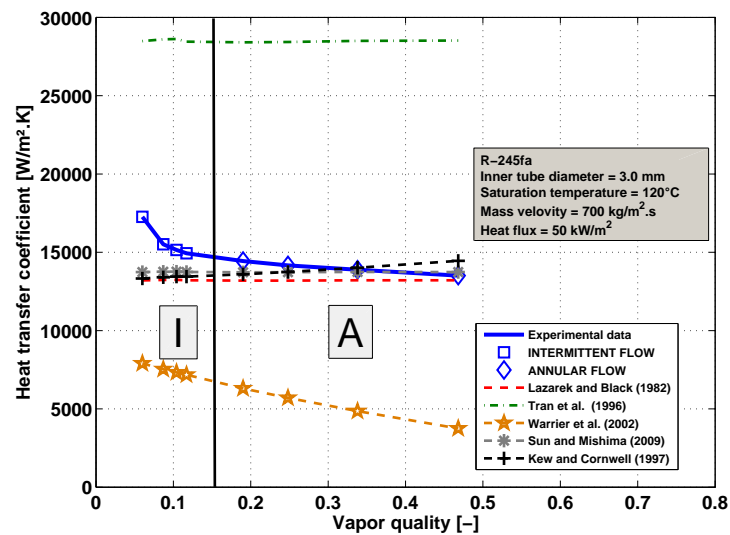
(a) $T_{\text{sat}} = 60^{\circ}\text{C}$.(b) $T_{\text{sat}} = 120^{\circ}\text{C}$.

Figure 6.14: Comparison between the experimental trends and those predicted by Nusselt-type correlations at 60°C and 120°C ((a) $T_{\text{sat}} = 60^{\circ}\text{C}$, $\dot{q} = 50 \text{ kW/m}^2$, and $G = 700 \text{ kg/m}^2\cdot\text{s}$ and (b) $T_{\text{sat}} = 120^{\circ}\text{C}$, $\dot{q} = 50 \text{ kW/m}^2$, and $G = 700 \text{ kg/m}^2\cdot\text{s}$).

Table 6.6: Summary of the statistical analysis of the comparisons between experimental heat transfer coefficients and those predicted by Nusselt-type correlations (MAE: Mean Absolute Error, MRE: Mean Relative Error and $\pm 30\%$: percentage of data predicted within 30% error bar).

	60°C						120°C						Whole database								
	Intermittent			Annular			Intermittent			Annular			Total			Intermittent			Annular		
	MAE	MRE	$\pm 30\%$	MAE	MRE	$\pm 30\%$	MAE	MRE	$\pm 30\%$	MAE	MRE	$\pm 30\%$	MAE	MRE	$\pm 30\%$	MAE	MRE	$\pm 30\%$	MAE	MRE	$\pm 30\%$
[Lazarek and Black (1982)]	20.2	-19.0	75.1	38.6	-37.7	37.3	26.0	-22.8	54.0	22.4	-21.1	69.4	31.2	-29.2	52.8	22.5	-19.3	68.2	35.3	-33.8	45.7
[Tran et al. (1996)]	7.4	-2.8	99.2	30.3	-28.6	52.9	98.0	98.0	0.0	86.1	85.3	8.0	40.4	14.3	45.2	46.4	43.5	46.6	37.6	0.8	44.5
[Warrier et al. (2002)]	42.8	-4.5	45.1	62.6	-44.8	16.5	60.4	-55.3	14.2	64.6	-63.3	13.9	60.7	-44.5	20.2	52.1	-26.7	28.2	64.6	-52.7	16.5
[Sun and Mishima (2009)]	11.8	-9.0	99.7	32.2	-30.8	52.3	19.8	-10.1	74.4	14.8	-7.4	89.2	24.2	-17.8	70.2	17.0	-5.8	88.0	27.5	-23.2	62.0
[Kew and Cornwell (1997)]	19.6	-18.3	78.2	34.1	-33.0	47.7	25.1	-17.9	57.6	17.6	-12.9	82.3	27.4	-24.2	61.8	21.8	-16.7	73.4	30.0	-27.6	56.4

6.2.1.6 Phenomenological approach

The phenomenological models of [Thome and El Hajal (2004c)], [Wojtan et al. (2005b)], [Thome et al. (2004a)], and [Cioncolini and Thome (2011)] were assessed against the heat transfer database. Table 6.7 summarizes the statistical results of these comparisons over the pre-dryout vapor quality range. The 3-zone model of [Thome et al. (2004a)] is compared only with the data obtained for intermittent flow whereas the model of [Cioncolini and Thome (2011)] is compared only with the data obtained for annular flow.

Figure 6.15 displays the comparison results for the models of [Thome and El Hajal (2004c)] and [Wojtan et al. (2005b)] at 60°C and 120°C. The model of [Thome and El Hajal (2004c)], which is a modification of the model of [Kattan et al. (1998b)] for carbon dioxide, overpredicts the experimental heat transfer coefficient at 60°C as its MRE is 70.9% and 41.5% for intermittent and annular flow regimes, respectively. This model predicts only 50.0% of the data within $\pm 30\%$ error band for the annular flow regime whereas, at 120°C, the percentage of data falling in a $\pm 30\%$ error band for the annular flow regime is 76.4%. This good agreement is due to the similarities observed between carbon dioxide and R-245fa boiling at high saturation temperature and pointed out previously. At the opposite, the model of [Wojtan et al. (2005b)] provides more accuracy to predict the heat transfer coefficient at 60°C than at 120°C. The poor agreement at 120°C is due to the range of applicability of this model.

Figure 6.16 displays a comparison between the experimental heat transfer coefficients and those predicted by the 3-zone model developed by [Thome et al. (2004a)] at four different saturation temperatures. The adjustable parameters are fixed as following: (i) $\delta_{\min} = 1.35 \mu\text{m}$, (ii) $C_{\delta_0} = 0.29$, and (iii) f was calculated from the expression proposed by [Dupont et al. (2004)]. This model provides homogeneous results and a very good accuracy at 60°C. Indeed, the percentage of data falling within $\pm 30\%$ error band is 83.0%. At 120°C, the accuracy is poor with only 29.1% of the data predicted within $\pm 30\%$ error band. This poor agreement could be explained by the fact that this model does not take into account the effect of the modification of the thermophysical parameters that increase the contribution of nucleate boiling to the overall heat transfer for intermittent flow (i.e. high vapor density, low surface tension, high vapor viscosity and low liquid viscosity).

Figure 6.17 depicts a comparison between experimental data and those predicted by the model of [Cioncolini and Thome (2011)] for four different saturation temperatures. The deviation and the dispersion increase with increasing saturation temperature. The model underpredicts the heat transfer coefficient as its MRE is equal to -17.8% for the whole database. The percentage of data falling within $\pm 30\%$ error band passes from 74.0% at 60°C to 32.6% at 120°C. This is due to the principle of the model itself that supposes that the heat transfer coefficient is governed by forced convection in the annular liquid film. This approach is correct at 60°C but inconsistent at 120°C where nucleate boiling is the dominant heat transfer mechanism for annular flow regime.

Figures 6.18(a) and 6.18(b) display the evolution of the heat transfer coefficients vs. vapor quality in comparison to the heat transfer predictive methods based on a phenomenological approach, at 60°C and 120°C, respectively. At 60°C, the model

of [Thome et al. (2004a)] does not capture the trend of the experimental results which exhibit a plateau and not a decrease for intermittent flow. The models of [Thome and El Hajal (2004c)], [Wojtan et al. (2005b)], and [Cioncolini and Thome (2011)] provide trends relatively similar to the experimental ones. At 120°C, on Fig. 6.18(b), the trend obtained with the model of [Wojtan et al. (2005b)] is plotted over the whole range of vapor quality (taking into account dryout and mist flow regimes). For intermittent and annular flow regimes, no model is able to capture the experimental trend.

In conclusion, the phenomenological models are able to predict the heat transfer coefficient with accuracy at 60°C, but when increasing the saturation temperature, the accuracy diminishes. This is mostly due to the fact that the two-phase flow configuration is modified at high saturation temperature, and this approach requires an in-depth knowledge of the flow patterns.

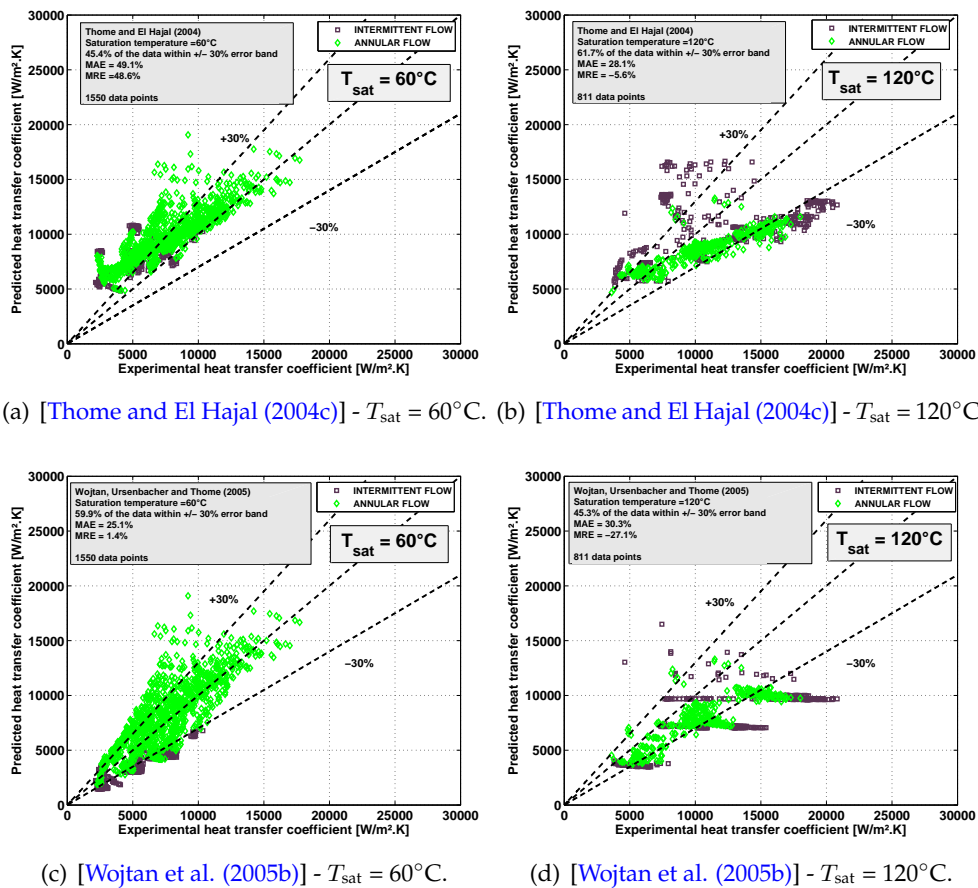


Figure 6.15: Comparison between experimental heat transfer coefficients and those predicted by the phenomenological models of [Thome and El Hajal (2004c)] and [Wojtan et al. (2005b)] at 60°C and 120°C.

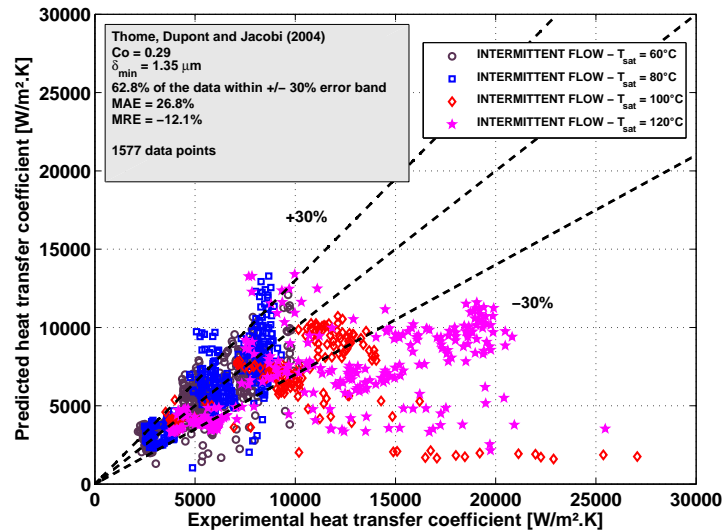


Figure 6.16: Comparison between experimental heat transfer coefficients and those predicted by the 3-zone model of [Thome et al. (2004a)].

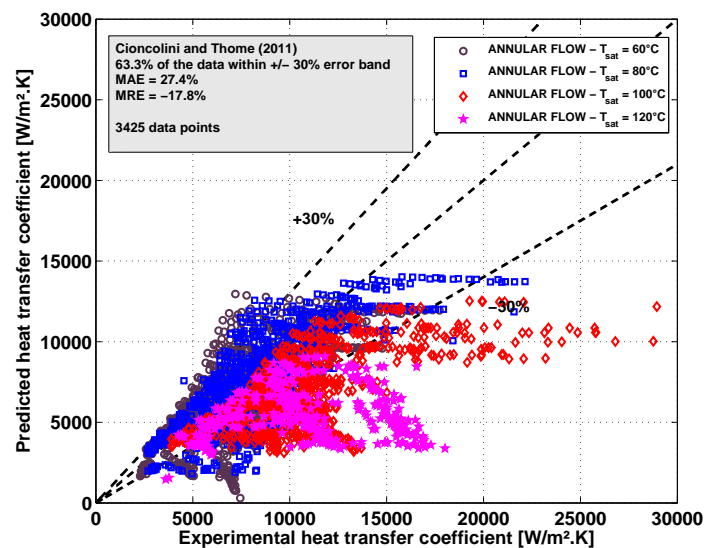


Figure 6.17: Comparison between experimental heat transfer coefficients and those predicted by the model of [Cioncolini and Thome (2011)].

Table 6.7: Summary of the statistical analysis of the comparisons between experimental heat transfer coefficients and those predicted by models based on the phenomenological approach (MAE: Mean Absolute Error, MRE: Mean Relative Error and $\pm 30\%$: percentage of data predicted within 30% error bar).

	60° C						120° C						Whole database								
	Intermittent			Annular			Intermittent			Annular			Total			Intermittent			Annular		
	MAE	MRE	$\pm 30\%$	MAE	MRE	$\pm 30\%$	MAE	MRE	$\pm 30\%$	MAE	MRE	$\pm 30\%$	MAE	MRE	$\pm 30\%$	MAE	MRE	$\pm 30\%$	MAE	MRE	$\pm 30\%$
[Thome and El Hajal (2004c)]	71.5	70.9	31.0	41.9	41.5	50.0	34.7	1.4	48.1	21.0	-13.1	76.4	37.6	26.2	58.6	50.9	36.5	45.7	21.5	31.5	64.5
[Wojtan et al. (2005b)]	32.2	-29.1	32.9	22.8	11.2	68.6	34.5	-30.5	30.6	25.7	-23.4	60.2	27.0	-9.2	58.3	34.5	-29.7	31.2	23.5	0.2	70.7
[Thome et al. (2004a)]	18.2	0.6	83.0	/	/	/	39.4	-34.7	29.1	/	/	/	26.8	-12.1	62.8	26.8	-12.1	62.8	/	/	/
[Cioncolini and Thome (2011)]	/	/	/	23.6	-7.9	74.0	/	/	/	42.5	-42.5	32.6	27.4	-17.8	63.3	/	/	/	27.4	-17.8	63.3

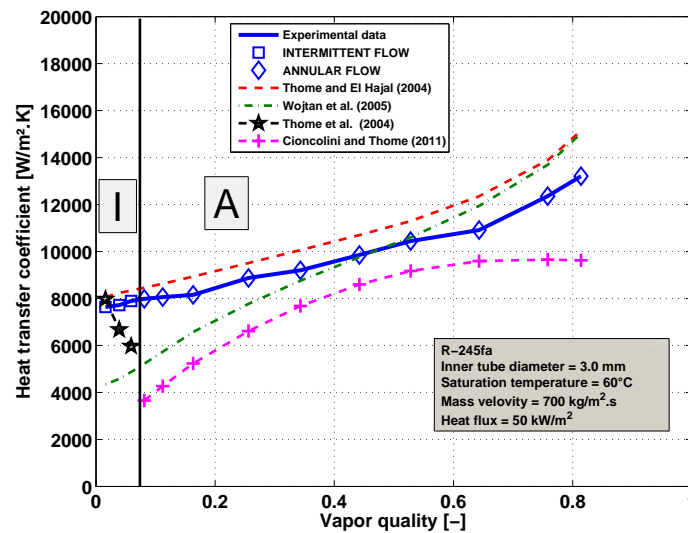
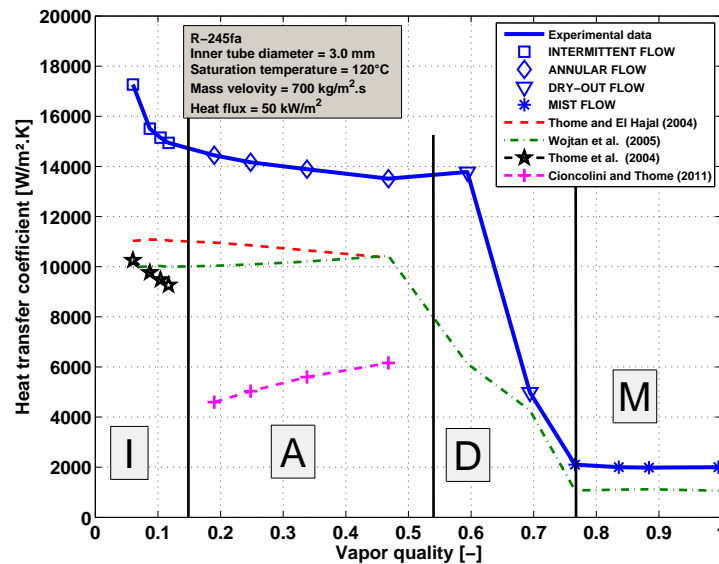
(a) $T_{\text{sat}} = 60^{\circ}\text{C}$.(b) $T_{\text{sat}} = 120^{\circ}\text{C}$.

Figure 6.18: Comparison between the experimental trends and those predicted by phenomenological methods ((a) $T_{\text{sat}} = 60^{\circ}\text{C}$, $\dot{q} = 50 \text{ kW/m}^2$, and $G = 700 \text{ kg/m}^2\cdot\text{s}$ and (b) $T_{\text{sat}} = 120^{\circ}\text{C}$, $\dot{q} = 50 \text{ kW/m}^2$, and $G = 700 \text{ kg/m}^2\cdot\text{s}$)

6.2.2 Dryout and post-dryout methods

Figure 6.19 displays the comparison between experimental results and those calculated from the following post-dryout correlations: [Dougall and Roshenow (1963)], [Ünal and Gasselt (1983)], [Saitoh et al. (2007)], and [Sindhuja et al. (2010)]. The comparisons are presented for mist flow data and for three different saturation temperatures: 80°C, 100°C and 120°C. At 80°C, the comparison is satisfactory and provides small deviation whereas at 100°C and 120°C, the deviation and the dispersion are more important. At high saturation temperature, these correlations underpredict the flow boiling heat transfer coefficient in mist flow regime. These observations are confirmed by the statistical indicators presented in Table 6.8. However,

the prediction of the all data for mist flow is relatively good with the correlations of [Dougall and Roshenow (1963)] and [Ünal and Gasselt (1983)] with 69.2% and 65.7% of the data falling within $\pm 30\%$ error band. Figure 6.20 displays a comparison between predicted trend for the heat transfer coefficient and the experimental one at 120°C . These correlations are able to capture the experimental trend. Finally, it clearly appears that the existing post-dryout heat transfer correlations do not provide accuracy to predict the flow boiling heat transfer when being extrapolated up to high saturation temperature.

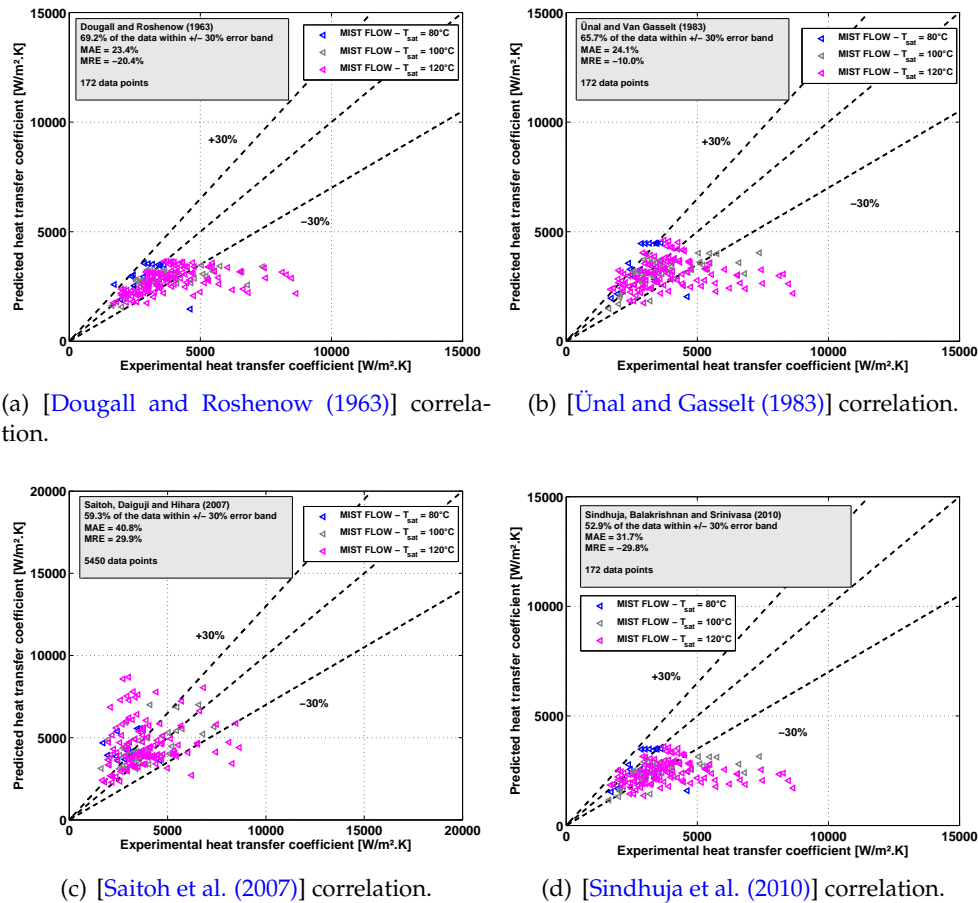


Figure 6.19: Comparison between experimental heat transfer coefficients and those predicted by post-dryout correlations.

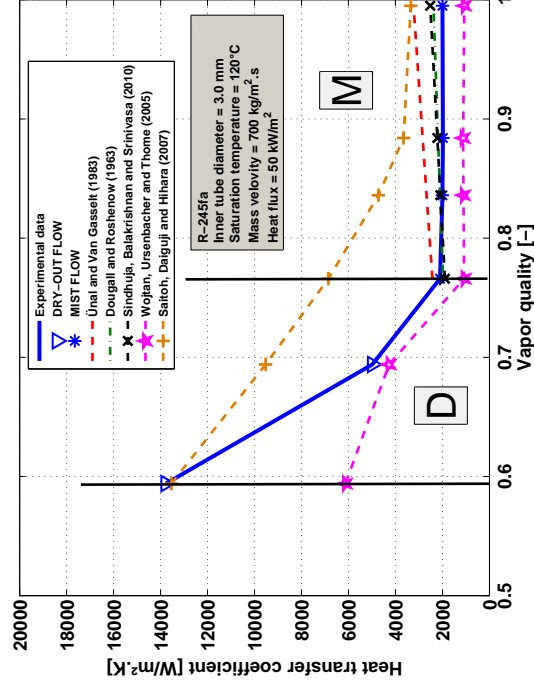


Figure 6.20: Comparison between the experimental trends and those predicted by post-dryout correlations at 120°C ($T_{\text{sat}} = 120^\circ\text{C}$, $\dot{q} = 50 \text{ kW/m}^2$, and $G = 700 \text{ kg/m}^2 \cdot \text{s}$).

6.3 Conclusion

This experimental investigation aimed at studying heat transfer characteristics of R-245fa in a 3.00 mm inner diameter tube at a saturation temperature ranging from 60 to 120°C. The evolution of the heat transfer coefficient with the vapor quality was discussed for various combinations of heat flux, mass velocity and saturation temperature while the flow regime was also fixed by these parameters. The contribution to the overall heat transfer of a variety of mechanisms was identified and discussed for medium and high saturation temperatures. At 60°C, the heat transfer coefficient is independent of vapor quality and mass flux during intermittent flow whereas it is sensitive to heat flux. In annular flow, the heat transfer coefficient increases with increasing vapor quality and/or mass velocity. As a result, at 60°C, nucleate and convective boiling are both present. At 120°C, the heat transfer coefficient exhibits completely different trends. The heat transfer coefficient decreases for both intermittent and annular flow regimes. The analysis of the results has highlighted the key role of nucleate boiling at high saturation temperature.

The experimental results were compared to the theoretical results of thirty methods selected from the literature in order to verify their ability to predict the heat transfer coefficient during flow boiling at high saturation temperature. The database was composed of 5964 data points. The following conclusions can be drawn from these comparisons:

- pool boiling correlations are not reliable to predict the heat transfer coefficient over the whole database conditions. Nevertheless, at 60°C, these correlations provide good results for intermittent flow, whereas, at 120°C, the data for annular flow are relatively well predicted. These correlations fail to catch the experimental trends of evolution of the heat transfer coefficient vs. quality.

- asymptotic models predict the data with an average of around 65% of the data within $\pm 30\%$ error band. These models are really accurate at 60°C and the predicted trends are similar to the experimental ones. At 120°C , the deviation and the dispersion are more important. In other words, these models cannot be extrapolated to conditions of high saturation temperatures. Moreover, no model is able to capture the experimental trends. Among the asymptotic models, those of [Gungor and Winterton (1986)] and [Kandlikar and Balasubramanian (2004)], developed for microchannels, provide the best agreements.

- asymptotic models developed from carbon dioxide data with or without other fluids produce good agreements for the whole database as the average percentage of data predicted within $\pm 30\%$ error band is 72.3 %. The predictions are better at 120°C for both intermittent and annular flow regimes. These models capture the experimental trends at 120°C (especially the model of [Choi et al. (2007b)]), which is not the case of the models developed without carbon dioxide. These features corroborate the similarities observed between carbon dioxide and halogenated refrigerants boiling at high saturation temperature.

- the correlation of [Shah (1982)] based on the enhancement-factor approach is able to predict the heat transfer coefficient at 60°C , whereas, at 120°C , this approach fails to estimate the heat transfer coefficient.

- Nusselt-type correlations which are the most empirical correlations produce dispersed results for the whole database and underpredict the heat transfer coefficients. However, the correlation of [Sun and Mishima (2009)] which was partially developed with carbon dioxide data predicts with accuracy the heat transfer dataset.

- the phenomenological models of [Thome et al. (2004a)] and [Cioncolini and Thome (2011)] are able to predict the flow boiling heat transfer coefficients with accuracy at 60°C for intermittent and annular flow regimes, respectively. At 120°C , these models are not reliable and require an indisputable knowledge of the flow patterns at high saturation temperature. The model of [Thome and El Hajal (2004c)] developed for carbon dioxide works well to predict the heat transfer coefficient at 120°C .

- post-dryout methods fail to predict with accuracy the flow boiling heat transfer for dryout and mist flow regimes when extrapolated up to 120°C .

With the physical reasoning in background of the present analysis, this investigation provides the basis to develop a new model or correlation or to modify an existing one to predict the heat transfer coefficient during flow boiling at high saturation temperature.

Table 6.8: Summary of the statistical analysis of the comparisons between experimental heat transfer coefficients and those predicted by post-dryout correlations (MAE: Mean Absolute Error, MRE: Mean Relative Error and $\pm 30\%$: percentage of data predicted within 30% error bar).

	120°C						Whole database								
	Dryout			Mist			Total			Dryout			Mist		
	MAE	MRE	$\pm 30\%$	MAE	MRE	$\pm 30\%$	MAE	MRE	$\pm 30\%$	MAE	MRE	$\pm 30\%$	MAE	MRE	$\pm 30\%$
[Dougall and Roshenow (1963)]	/	/	/	25.4	-24.2	65.5	23.5	-20.4	69.2	/	/	/	23.5	-20.4	69.2
[Ünal and Gasselt (1983)]	/	/	/	25.8	-13.9	62.8	24.1	-10.0	65.7	/	/	/	24.1	-10.0	65.7
[Sindhuja et al. (2010)]	/	/	/	34.5	-32.8	46.9	31.7	-29.8	52.9	/	/	/	31.7	-29.8	52.9
[Saitoh et al. (2007)]	37.3	-13.4	46.6	43.3	29.7	58.4	41.1	1.0	45.5	41.3	-17.4	36.6	40.8	29.9	59.3

Chapter 7

Pressure drops

This chapter presents experimental data concerning frictional pressure drop in a minichannel at high saturation temperatures. The database is composed of 249 data points covering four flow patterns: (i) intermittent flow, (ii) annular flow, (iii) dryout flow, and (iv) mist flow regimes.

A parametric analysis was carried out on the effect of the kind of flow pattern, the mass velocity, and the saturation temperature on the two-phase frictional pressure drop. Finally, the data set is compared against 23 well-known two-phase frictional pressure drop prediction methods. A statistical analysis for each flow regime was also carried out. The effect of the saturation temperature and the kind of flow pattern on the ability of the methods to predict the frictional pressure drop was investigated.

Two-phase pressure drop measurements were carried out under in adiabatic conditions (Fig. 4.2) and the frictional pressure drop was calculated by subtracting the momentum pressure drop from the measured pressure drop, as explained in section 3.3. The flow patterns were identified from the experimental flow pattern maps. 60% of the database (249 data points in total) refer to annular flow (150 data points), 28.5% to intermittent flow (71 data points), 6.5% to dryout flow (12 data points), and 5% to mist flow (12 data points).

7.1 Frictional pressure drop

7.1.1 Pressure drop decomposition

Figures 7.1(a) and 7.1(b) show the total, momentum and frictional pressure drops for a representative set of experimental conditions. As expected, the momentum pressure drop is higher at high mass velocity and low saturation temperature. It correspond to about 3% of the total pressure drop.

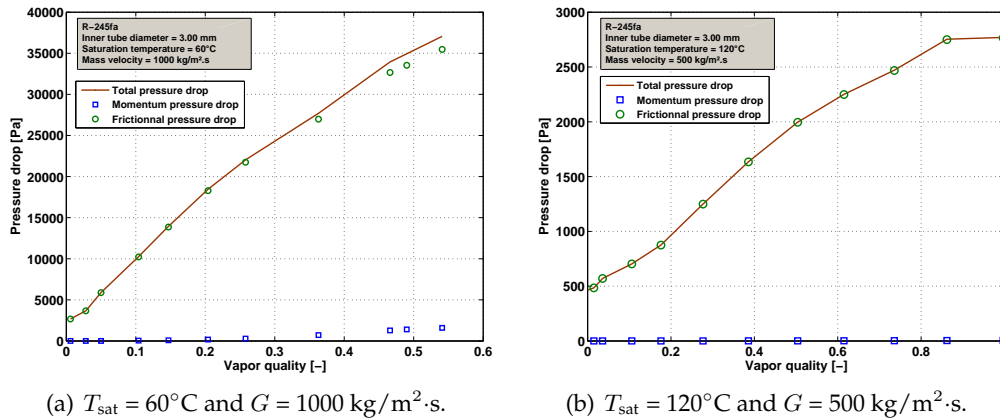


Figure 7.1: Total, frictional and momentum pressure drops versus vapor quality at different experimental conditions for R-245fa flowing in a 3.00 mm inner tube diameter.

7.1.2 Effect of mass velocity

The general trend for the two-phase frictional pressure drop as a function of the vapor quality is illustrated in Figs. 7.2, 7.3(a) and 7.3(b). The pressure drop rises with increasing vapor quality due to the higher velocity, until a maximum is reached. Then a further increase of the vapor quality leads to a decrease of the frictional pressure drop. Concerning the peak location, several scenarios are likely to occur:

- the peak location may correspond to the inception of the dryout as represented in Fig. 7.3(a) for mass velocities of 700 and 1000 $\text{kg/m}^2\cdot\text{s}$
- the maximum frictional pressure drop may occur before the dryout inception as shown in Fig. 7.3(a) for mass velocities 300 and 500 $\text{kg/m}^2\cdot\text{s}$. Such a behavior was previously pointed out by [Quibén and Thome (2007a)].
- the peak location may coincide with the inception of the mist flow regime as represented in Fig. 7.3(b) for mass velocities of 700 and 1000 $\text{kg/m}^2\cdot\text{s}$

The disappearance of the liquid film may be an explanation of the peak location at the inception of dryout or mist flow regime. In Fig. 7.2, a schematic of the flow regimes encountered along the pressure drop test section is associated to better highlight the relation between frictional pressure drop and flow regimes in this situation. Indeed, the disappearance of the liquid film results on phenoma which could explain the decrease of the pressure drop:

- the decrease of the tube surface apparent roughness seen by the vapor phase as suggested by [Ducoulombier et al. (2011)]
- the decrease of the friction factor of the phase in contact with the wall (the vapor, whose the viscosity is lower than that of the liquid, progressively replaces the liquid at the wall as represented on Fig. 7.2)

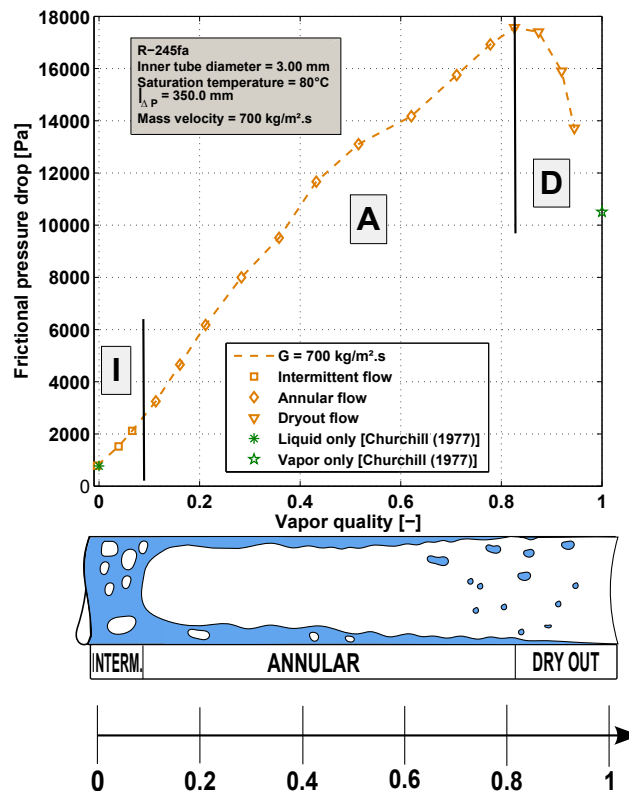


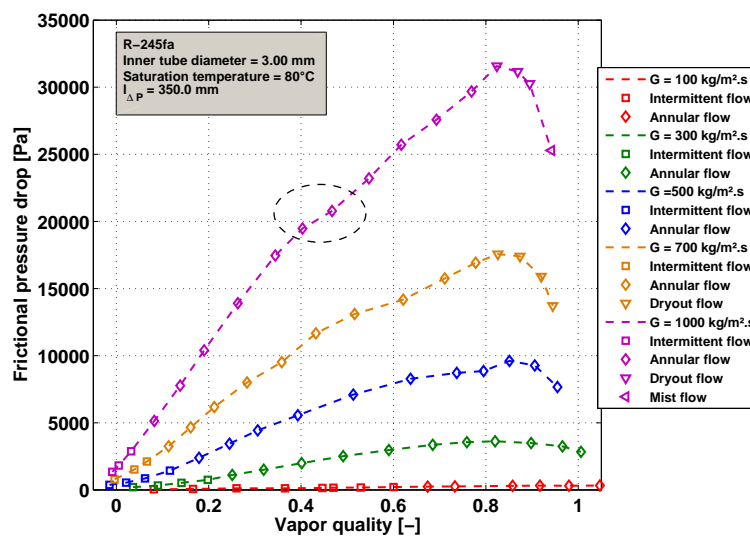
Figure 7.2: Relation between frictional pressure drop and flow configuration (A: annular, D: Dryout, and I: Intermittent)

These trends were previously observed and are similar to those observed in macroscale channels and in most of the studies concerning microscale channels. Regarding the case for which the maximum pressure drop occurs for a vapor quality lower than the vapor quality of dryout inception, [Quibén and Thome (2007a)] suggested that the appearance of this peak is associated with the damping out of interfacial waves (as the annular film thins).

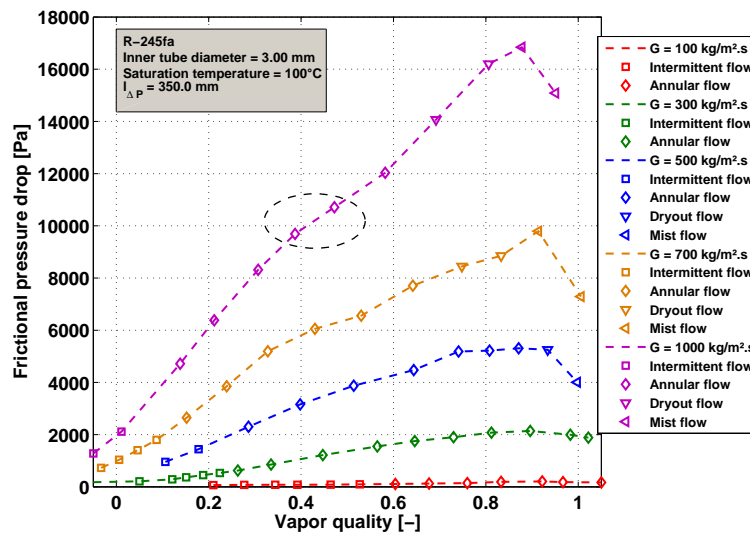
For a mass velocity of 1000 kg/m².s, a change in the trend can be observed in Figs. 7.3(a) and 7.3(b) (indicated with the dotted zone). Such a behavior was previously pointed out by [Revellin and Thome (2007b)]. In their case, this change corresponded to a change in flow pattern with the transition from wavy to smooth

annular. Such a transition could probably explain this experimental change of trend as the flow regime is annular and, in our case, it groups together wavy and smooth annular flow regimes.

Figure 7.3 presents the effect of the mass velocity on the frictional pressure drop for R-245fa at two different saturation temperatures. An increase in mass velocity results in a higher flow velocity and a higher flow inertia, which increases the frictional pressure drop. The results show the expected tendency as represented on Fig. 3.20.



(a) $T_{\text{sat}} = 80^\circ\text{C}$.



(b) $T_{\text{sat}} = 100^\circ\text{C}$.

Figure 7.3: Influence of the mass velocity on the pressure drop for R-245fa in a 3.00 mm inner tube diameter.

7.1.3 Effect of saturation temperature

Figure 7.4 depicts the effect of the saturation temperature on the frictional pressure drop. Indeed, when increasing the saturation temperature, the vapor density increases (see Table 6.1), the vapor velocity decreases and by consequence the two-phase frictional pressure drop decreases. These results show the expected tendency represented in Fig. 3.22.

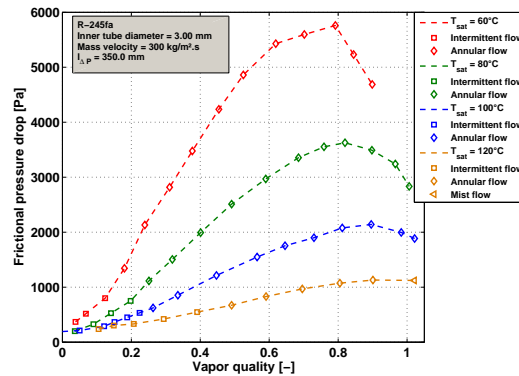
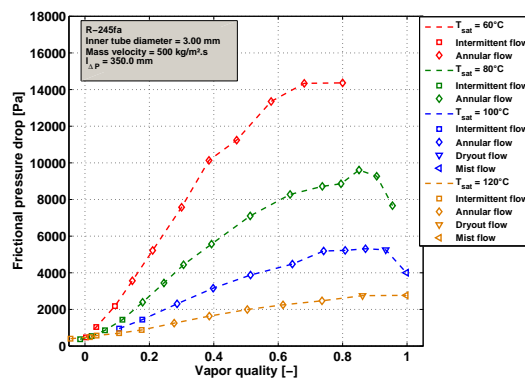
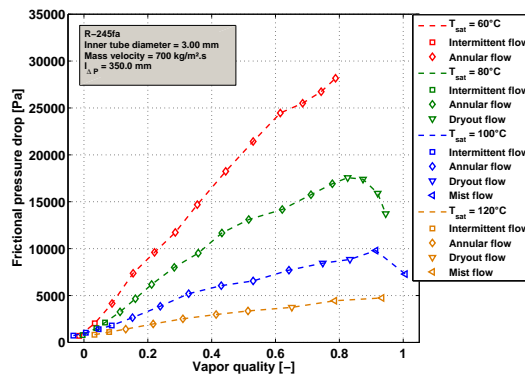
(a) $G = 300 \text{ kg/m}^2 \cdot \text{s}$.(b) $G = 500 \text{ kg/m}^2 \cdot \text{s}$.(c) $G = 700 \text{ kg/m}^2 \cdot \text{s}$.

Figure 7.4: Influence of the saturation temperature on the pressure drop for R-245fa in a 3.00 mm inner tube diameter.

7.2 Comparisons of the database to prediction methods

7.2.1 Homogeneous flow model

The experimental dataset is compared to the homogeneous model with eight definitions of two-phase viscosity. The definitions of two-phase flow viscosity assessed here were proposed by [McAdams et al. (1942)], [Cicchitti et al. (1960)], [Dukler et al. (1964)], [Beattie and Whalley (1982)], [Lin et al. (1991)], [García et al. (2003)], [Awad and Muzychka (2008)] No 1, and [Awad and Muzychka (2008)] No 2. All the definitions presented in Table 3.3 were assessed, however, only the results obtained for the eight “best” definitions of the two-phase viscosity are presented.

Figure 7.5 displays graphical results of the comparisons between experimental data and those predicted by the version of homogeneous model based on the two-phase viscosity definitions proposed by [McAdams et al. (1942)], [Cicchitti et al. (1960)] and the [Awad and Muzychka (2008)] No 1 definition. The comparisons are performed at two different saturation temperatures: 60°C (Figs. 7.5(a), 7.5(c), 7.5(e)) and 120°C (Figs. 7.5(b), 7.5(d), 7.5(f)).

At 60°C, these methods underpredict the frictional pressure drop, even if the model of [Cicchitti et al. (1960)] predicts well the experimental results with 81.5% of the data falling within $\pm 30\%$ error band. At 120°C, the deviation decreases strongly and these models are reliable to predict the two-phase frictional pressure drop. This is consistent with the idea that the homogeneous model is more adapted when the slip ratio between the two-phases decreases due to a lower density difference, i.e. when the saturation temperature increases. These results are in agreement with those of [Tibiricá and Ribatski (2011b)]. They found that the homogeneous model using the two-phase viscosity of [Cicchitti et al. (1960)] predicted 77% (within $\pm 30\%$ error band) of their data obtained with R-245fa for saturation temperatures ranging from 31 to 41°C.

Table 7.1 summarizes the results of the statistical analysis of these comparisons. These results confirm the reliability of these models to predict the frictional pressure drop at high saturation temperature. At 120°C, the percentage of data falling within $\pm 30\%$ error band ranges from 76.0% to 92%. The homogeneous model with the [Cicchitti et al. (1960)] definition and the [Awad and Muzychka (2008)] No 1 definition is robust to predict the experimental results with around 76% of the data falling within $\pm 30\%$ error band for the whole database.

Figure 7.6 presents a comparison between the trends predicted by the homogeneous model (with the eight previously identified definitions of the two-phase viscosity) and the experimental ones for a mass velocity of 500 kg/m²·s and two different saturation temperatures: 60 and 120°C. In Fig. 7.6(a), the homogeneous model with the [Cicchitti et al. (1960)] definition and the [Awad and Muzychka (2008)] No 1 definition is the only one to reproduce the experimental trends, however the discrepancies on the prediction of the frictional pressure drop are important. At 120°C, the deviations decreases and the predicted trends are relatively similar to the experimental one.

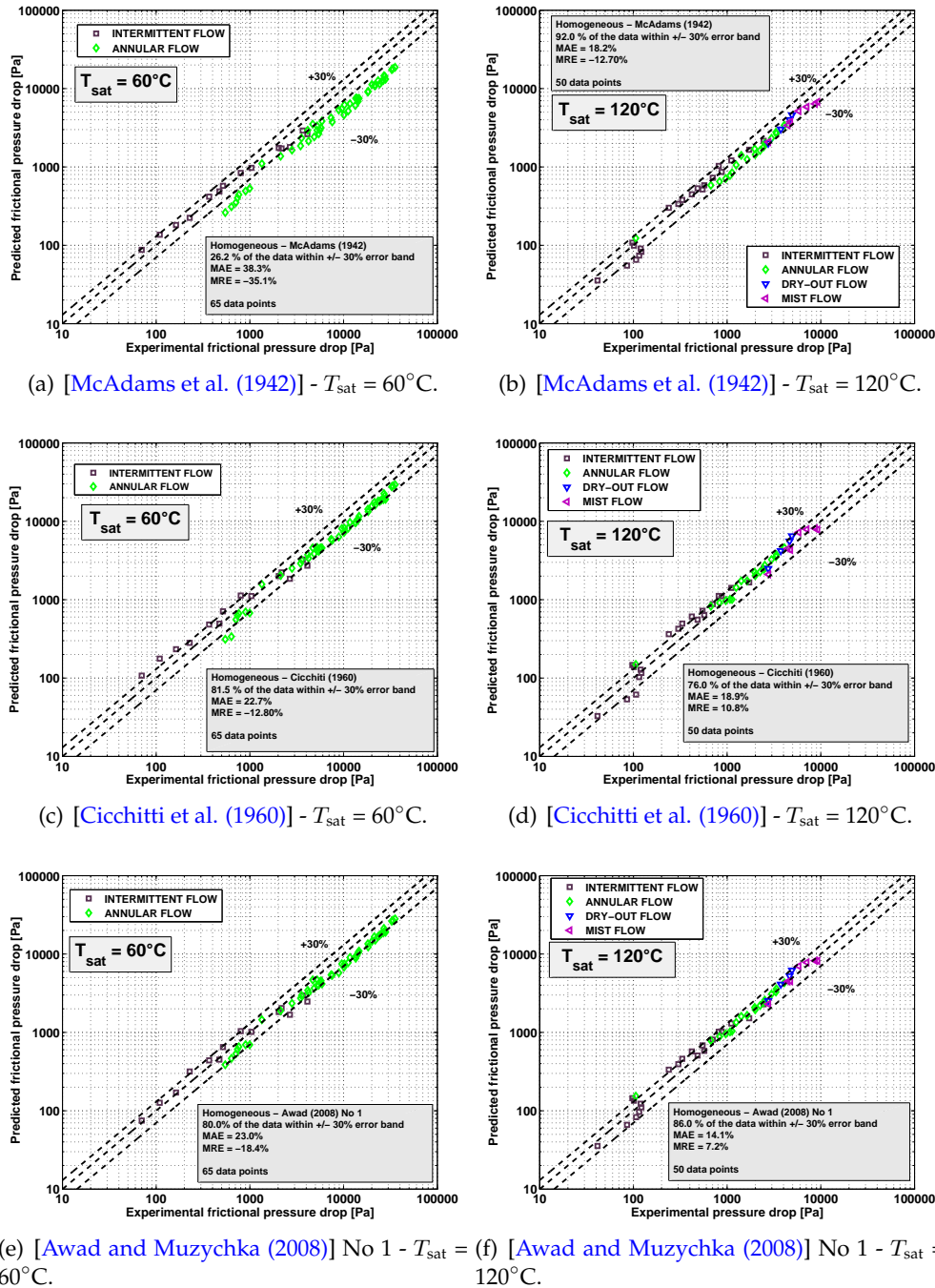


Figure 7.5: Comparison between experimental frictional pressure drop data and those predicted by several correlations based on the homogeneous flow model with different two-phase viscosity definitions.

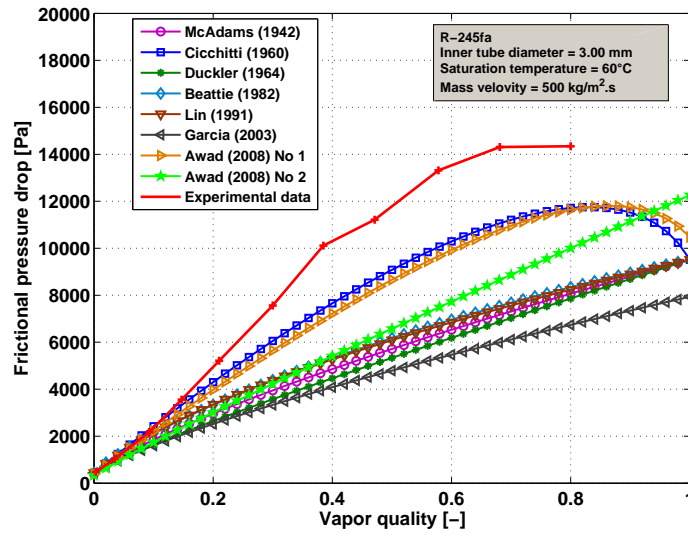
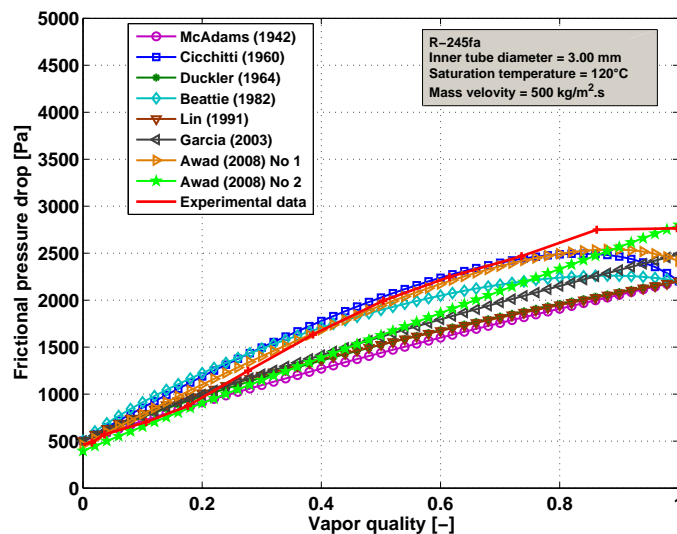
(a) $T_{\text{sat}} = 60^{\circ}\text{C}$.(b) $T_{\text{sat}} = 120^{\circ}\text{C}$.

Figure 7.6: Comparison between the experimental trends and those predicted by the correlations based on the homogeneous flow model with different two-phase viscosity definitions at 60°C and 120°C ((a) $T_{\text{sat}} = 60^{\circ}\text{C}$ and $G = 500 \text{ kg/m}^2\cdot\text{s}$ and (b) $T_{\text{sat}} = 120^{\circ}\text{C}$ and $G = 500 \text{ kg/m}^2\cdot\text{s}$).

Table 7.1: Summary of the statistical analysis of the comparisons between experimental frictional pressure drops and those predicted by the correlations based on the homogeneous flow model with different two-phase viscosity definitions (MAE: Mean Absolute Error, MRE: Mean Relative Error and $\pm 30\%$: percentage of data predicted within 30% error bar).

		60°C			120°C					Whole database				
		Intermittent	Annular	All data	Intermittent	Annular	Dryout	Mist	all data	Intermittent	Annular	Dryout	Mist	All data
[McAdams et al. (1942)]	MAE MRE $\pm 30\%$	11.9 2.9 100.0	45.5 -45.5 5.9	38.3 -35.1 26.2	15.6 -4.0 81.0	20.1 -18.3 100.0	16.6 -16.6 100.0	21.5 -21.5 100.0	18.2 -12.7 92.0	19.7 5.9 76.1	37.7 -35.8 26.0	36.1 -36.1 25.0	27.7 -27.7 66.7	32.0 -23.5 42.2
[Cicchitti et al. (1960)]	MAE MRE $\pm 30\%$	27.4 16.3 42.9	21.4 -20.8 92.2	22.7 -12.8 81.5	27.5 16.1 52.4	11.2 9.2 94.5	18.5 13.8 75.0	13.0 -2.5 100.0	18.9 10.8 76.0	37.1 30.1 46.5	21.0 -11.1 90.0	23.6 -15.5 75.0	19.0 -12.9 91.7	25.7 0.3 76.7
[Dukler et al. (1964)]	MAE MRE $\pm 30\%$	14.9 -11.0 85.7	49.3 -49.3 3.9	41.9 -41.1 21.5	18.0 -0.5 71.4	16.5 -13.9 100.0	12.2 -12.2 100.0	19.6 -19.6 100.0	17.2 -8.9 88.0	19.4 3.9 73.2	39.1 -37.2 23.3	34.7 -34.7 25.0	26.6 -26.6 66.7	32.6 -24.8 39.8
[Beattie and Whalley (1982)]	MAE MRE $\pm 30\%$	18.6 7.7 78.6	40.1 -40.1 11.8	35.5 -29.8 26.2	28.1 18.4 52.4	11.9 4.6 100.0	15.1 6.2 100.0	14.3 -10.0 100.0	19.3 8.5 80.0	31.4 25.5 52.1	31.3 -26.1 38.7	32.2 -26.9 31.3	22.5 -20.1 66.7	31.0 -11.1 43.4
[Lin et al. (1991)]	MAE MRE $\pm 30\%$	18.5 5.1 78.6	40.9 -40.9 11.8	36.1 -30.9 26.2	19.2 2.6 80.9	16.1 -13.1 100.0	12.2 -12.2 100.0	20.0 -20.0 100.0	17.6 -7.4 92.0	24.6 14.8 64.8	34.1 -31.6 31.3	33.8 -33.8 25.0	26.7 -26.7 66.7	31.0 -18.3 42.2
[García et al. (2003)]	MAE MRE $\pm 30\%$	15.8 -12.8 78.6	53.4 -53.4 2.0	45.3 -44.7 18.5	18.9 1.8 76.2	13.3 -9.0 94.4	8.8 -6.3 100.0	11.2 -11.2 100.0	15.0 -4.6 88.0	19.3 3.5 76.1	40.7 -38.9 22.0	35.5 -34.9 25.0	21.4 -21.4 66.7	33.3 -25.7 39.8
[Awad and Muzychka (2008)] No 1	MAE MRE $\pm 30\%$	18.7 1.5 78.6	24.2 -23.9 80.4	23.0 -18.4 80.0	20.9 11.0 71.4	7.6 5.1 94.4	14.4 10.5 100.0	10.0 -1.0 100.0	14.1 7.2 86.0	32.8 23.2 57.8	22.7 -14.0 83.3	21.9 -15.6 81.3	15.8 -10.6 91.7	25.2 -3.3 76.3
[Awad and Muzychka (2008)] No 2	MAE MRE $\pm 30\%$	19.8 -11.9 78.6	39.8 -39.8 7.8	35.5 -33.8 23.1	16.9 -6.9 80.9	14.1 -9.1 94.4	6.5 -3.8 100.0	4.8 -3.8 100.0	13.3 -7.0 90.0	23.2 2.1 69.0	33.4 -27.6 29.3	22.6 -21.9 75.0	11.0 -10.5 100.0	28.8 -17.9 47.0

7.2.2 Empirical models based on the separated flow model

7.2.2.1 The Φ_L^2 , Φ_V^2 based methods

The frictional pressure drop dataset is compared to four correlations based on the separated flow model: the correlations of [Lockhart and Martinelli (1949)], [Mishima and Hibiki (1996)], [Zhang et al. (2010)], and [Yamamoto et al. (2007)]. These correlations assume that the liquid and the vapor phases flow separately in the entire cross section of the tube. Table 7.2 presents the statistical results of the comparisons for each flow regime and different saturation temperatures.

Figure 7.7 displays graphical results of the comparisons between the experimental frictional pressure drops and those predicted by the correlations of [Lockhart and Martinelli (1949)], [Zhang et al. (2010)], and [Yamamoto et al. (2007)] at two different saturation temperatures (60 and 120°C). At 60°C, the macroscale correlation of [Lockhart and Martinelli (1949)] overpredicts the frictional pressure drop whereas the microscale correlations of [Zhang et al. (2010)] and [Yamamoto et al. (2007)] underpredict the experimental data. At 120°C, all the correlations overpredicts the frictional pressure drop as their MRE is ranging from 17 to 216%.

The first comparison shows that the correlation of [Lockhart and Martinelli (1949)] fails to predict the frictional pressure drop at moderate and high saturation temperature as its MAE is 61.4% and 216% at 60 and 120°C, respectively. As one can see on Fig. 7.7(b), the deviation increases when the saturation temperature increases. [Whalley (1980)] recommends to use the [Lockhart and Martinelli (1949)] correlation when the liquid to vapor viscosity ratio (μ_L/μ_V) is greater than 1000 and when the mass velocity is lower than 100 kg/m²·s. In the present investigation, the liquid to vapor viscosity ratio ranges from 22 to 8 when the saturation temperature passes from 60 to 120°C and the mass velocity ranges from 100 to 1200 kg/m²·s. Moreover, this method is not suited to describe the behavior of synthetic refrigerants. Thus, it is logical to find huge discrepancies.

As observed by [Tibiricá and Ribatski (2011b)] with R-245fa, the correlation of [Mishima and Hibiki (1996)] developed for microchannels underpredicts the frictional pressure drop for both temperatures and fails at predicting the frictional pressure drop with only 21% of the data falling within $\pm 30\%$ error band for the whole database. This correlation is a modification of the [Lockhart and Martinelli (1949)] correlation to fit air/water pressure drop and it does not seem to be reliable to predict the frictional pressure drop of R-245fa in minichannel. The correlation of [Zhang et al. (2010)] developed for minichannel works relatively well to predict the frictional pressure drop at 60°C with around 85% of the data falling within $\pm 30\%$ error band. However, at 120°C, this correlation overpredicts the frictional pressure drop as its MRE is 138.2%. For the whole database, this correlation presents a MAE of 65% and predicts 50% of the data within $\pm 30\%$ error band.

The last comparison deals with the correlation of [Yamamoto et al. (2007)] developed for carbon dioxide. As we saw previously, the heat transfer coefficient has a behavior close to that of carbon dioxide at high saturation temperature, therefore it is interesting to compare our dataset to a correlation developed for carbon dioxide. At 60°C, this correlation underpredicts the frictional pressure drop as its MRE is -40%.

Table 7.2: Summary of the statistical analysis of the comparisons between experimental frictional pressure drops and those predicted by the Φ_L^2 , Φ_V^2 correlations based on the separated flow model (MAE: Mean Absolute Error, MRE: Mean Relative Error and $\pm 30\%$: percentage of data predicted within 30% error bar).

		60°C			120°C					Whole database				
		Intermittent	Annular	All data	Intermittent	Annular	Dryout	Mist	all data	Intermittent	Annular	Dryout	Mist	All data
[Lockhart and Martinelli (1949)]	MAE	106.7	49.0	61.4	228.4	237.0	256.0	108.0	216.9	202.7	95.8	89.3	71.5	124.7
	MRE	103.9	34.4	49.4	228.4	237.0	256.0	101.5	215.9	202.2	87.5	66.5	50.7	117.1
	$\pm 30\%$	28.6	41.2	38.5	9.5	5.6	25.0	42.9	14.0	11.3	32.0	62.5	58.3	29.3
[Mishima and Hibiki (1996)]	MAE	56.9	68.5	66.0	35.1	45.7	38.5	21.2	37.2	41.6	58.0	37.9	22.2	50.3
	MRE	-56.9	-68.5	-66.0	-34.5	-42.4	-38.5	-17.1	-35.2	-41.4	-55.6	-37.9	-17.7	-48.6
	$\pm 30\%$	7.2	2.0	3.1	38.1	11.1	25.0	85.7	34.0	31.0	11.3	25.0	75.0	20.9
[Zhang et al. (2010)]	MAE	35.8	19.9	23.3	153.1	142.8	148.0	75.9	138.2	116.0	42.9	48.5	47.9	64.3
	MRE	28.4	-18.8	-8.7	153.1	142.8	148.0	75.9	138.2	114.5	26.7	36.0	45.2	53.2
	$\pm 30\%$	50.0	94.1	84.6	4.8	0.0	0.0	14.3	4.0	16.9	64.0	68.8	50.0	50.2
[Yamamoto et al. (2007)]	MAE	17.3	50.0	42.9	46.7	20.1	15.2	27.5	31.9	43.3	39.8	39.6	32.4	40.4
	MRE	-0.9	-50.0	-39.4	46.5	7.5	-15.2	-27.5	17.2	38.9	-31.5	-39.6	-32.4	-12.0
	$\pm 30\%$	85.7	3.9	21.6	38.1	72.3	75.0	57.2	56.0	45.1	26.0	18.8	41.7	31.7

These results can be explained by the untypical properties of the carbon dioxide due to its high reduced pressure resulting in a lower frictional pressure drop. Namely, the carbon dioxide exhibits a low liquid to vapor density ratio which differs from that of conventional fluids. At 120°C, the deviation decreases and the correlation of [Yamamoto et al. (2007)] predicts 56 % of the data within $\pm 30\%$ error band. This observation can be explained by the fact that when the saturation temperature increases, the reduced pressure increases and the behavior of the fluid is closer to that of carbon dioxide.

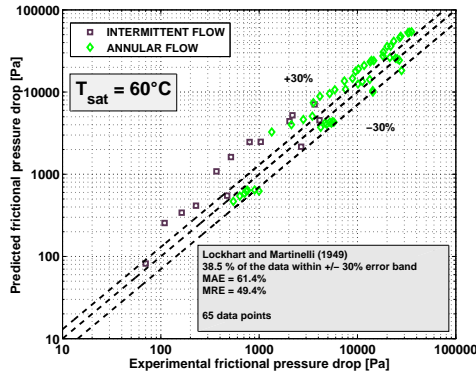
Figures 7.8(a) and 7.8(b) present the trends of the experimental frictional pressure drop as well as those predicted by the models of [Lockhart and Martinelli (1949)], [Mishima and Hibiki (1996)], [Zhang et al. (2010)], and [Yamamoto et al. (2007)]. None of these correlations are able to reproduce the experimental trends of R-245fa at 60 and 120°C.

7.2.2.2 The Φ_{LO}^2 , Φ_{VO}^2 based method

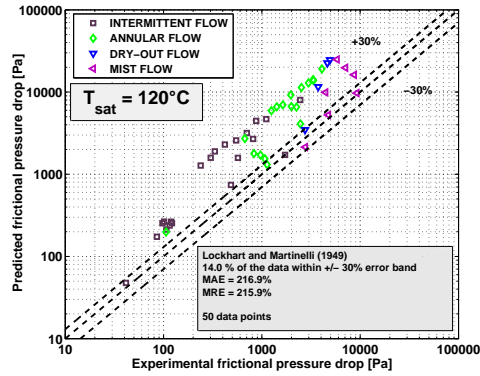
The experimental frictional pressure drops are compared to those predicted by the correlations based on the separated flow model. The following correlations consider the liquid and the vapor phases flowing alone in the channel with the total mass flow rate. The comparisons are performed against the correlations of [Martinelli and Nelson (1948)], [Jung et al. (1989)], [Friedel (1979)], [Zhang and Webb (2001)], [Grønnerud (1979)], [Müller-Steinhagen and Heck (1986)], [Chisholm (1973)], and [Tran et al. (2000)]. Table 7.3 summarizes the results of the statistical analysis of these comparisons.

Figure 7.9 displays the comparisons between the experimental data points and those predicted by the correlations of [Friedel (1979)], [Müller-Steinhagen and Heck (1986)], and [Zhang and Webb (2001)] at 60 and 120°C. At 60°C, these correlations are able to predict the experimental results with accuracy. They predict 80%, 75%, and 71% of the data within $\pm 30\%$ error band, respectively. These results are in agreement with the recommendations made by [Whalley (1980)]. Indeed, he suggested that the correlation of [Friedel (1979)] was the best one at predicting the frictional pressure drop for liquid to vapor viscosity ratios lower than 1000 and mass velocities less than 2000 kg/m²·s.

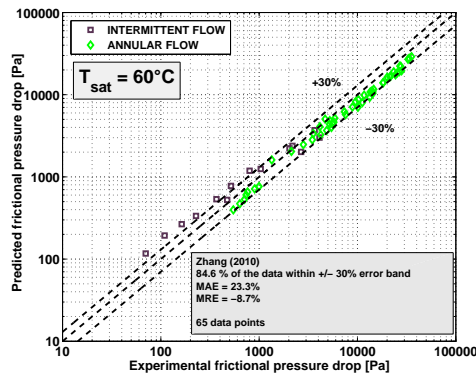
At 120°C, the correlations of [Müller-Steinhagen and Heck (1986)] and [Zhang and Webb (2001)] are still able to predict the frictional pressure at high saturation temperature with accuracy. Indeed, these correlations predict 80% and 82% of the data within $\pm 30\%$ error band. The correlation of [Zhang and Webb (2001)] is a modification of the [Friedel (1979)] correlation for minichannel taking into account the reduced pressure. In these conditions, the modification is very efficient in that sense that the [Friedel (1979)] correlation predicts only 16% of the data within $\pm 30\%$ error band whereas the [Zhang and Webb (2001)] correlation predicts 82% of the data within $\pm 30\%$. In conclusion, the correlation of [Zhang and Webb (2001)] takes into account the effect of the reduced pressure on the frictional pressure drop successfully.



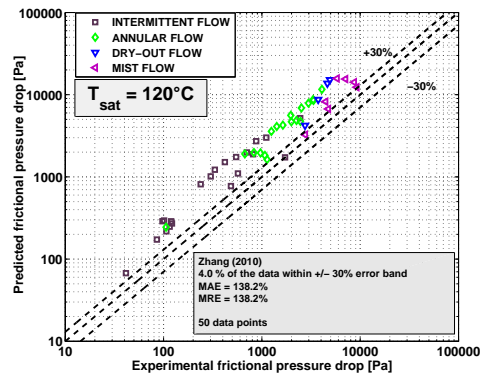
(a) [Lockhart and Martinelli (1949)] - $T_{sat} = 60^{\circ}\text{C}$.



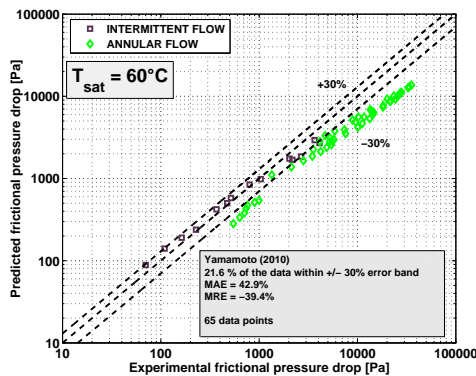
(b) [Lockhart and Martinelli (1949)] - $T_{sat} = 120^{\circ}\text{C}$.



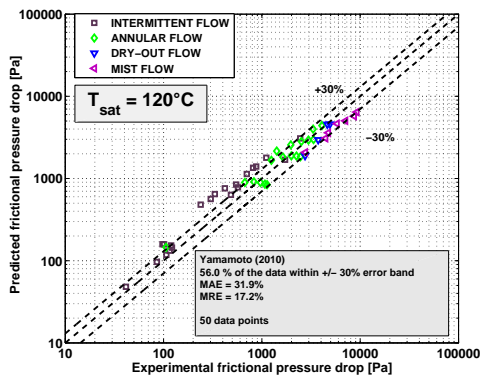
(c) [Zhang et al. (2010)] - $T_{sat} = 60^{\circ}\text{C}$.



(d) [Zhang et al. (2010)] - $T_{sat} = 120^{\circ}\text{C}$.



(e) [Yamamoto et al. (2007)] - $T_{sat} = 60^{\circ}\text{C}$.



(f) [Yamamoto et al. (2007)] - $T_{sat} = 120^{\circ}\text{C}$.

Figure 7.7: Comparison between experimental frictional pressure drop data and those predicted by correlations based on the separated flow model and the Φ_L^2 , Φ_V^2 method.

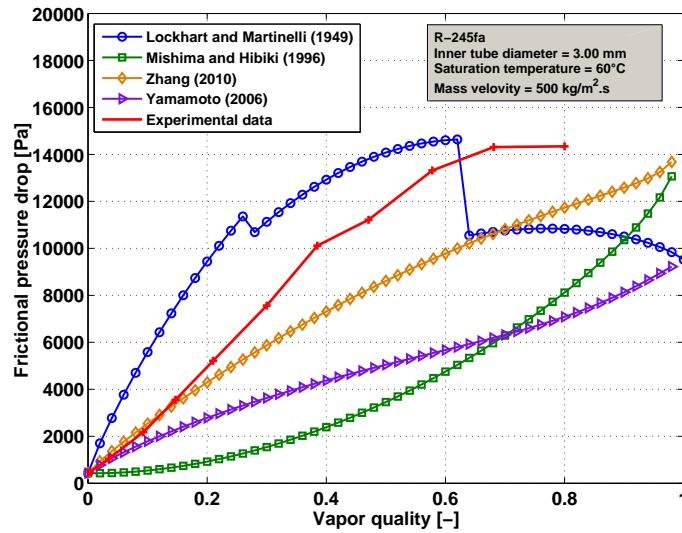
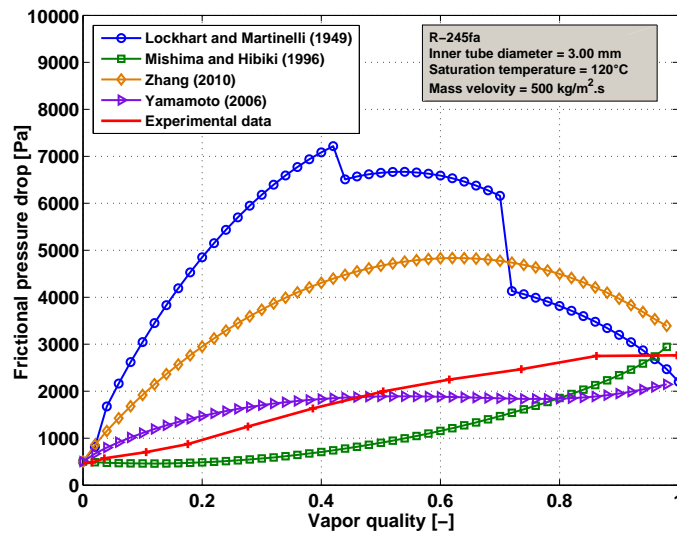
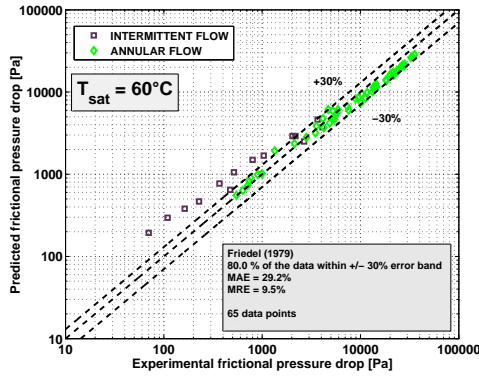
(a) $T_{\text{sat}} = 60^\circ\text{C}$.(b) $T_{\text{sat}} = 120^\circ\text{C}$.

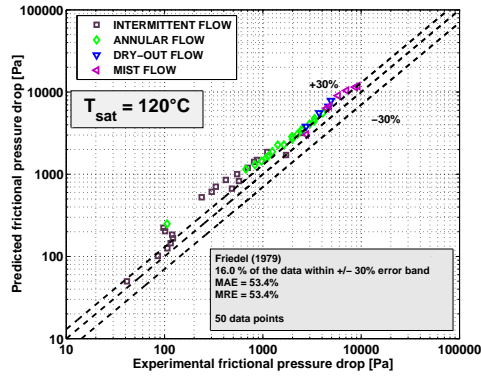
Figure 7.8: Comparison between the experimental trends and those predicted by the Φ_L^2 , Φ_V^2 correlations based on the separated flow model at 60°C and 120°C ((a) $T_{\text{sat}} = 60^\circ\text{C}$ and $G = 500 \text{ kg/m}^2\cdot\text{s}$ and (b) $T_{\text{sat}} = 120^\circ\text{C}$ and $G = 500 \text{ kg/m}^2\cdot\text{s}$).

According to Table 7.3, the correlation of [Müller-Steinhagen and Heck (1986)] is ranked as the first to predict the whole database. The correlation of [Müller-Steinhagen and Heck (1986)] was found to be the best in many published studies as shown in section 3.3.1. [Ducoulombier et al. (2011)] found that this correlation was the best one to predict the frictional pressure drop of carbon dioxide. This result is consistent with our conclusion knowing that when the saturation temperature increases, the behavior of the fluid get closer to that of carbon dioxide when used as refrigerant in temperature range typical of refrigeration. Generally speaking, the correlations assessed in this section (excepted the correlations of [Müller-Steinhagen and Heck (1986)] and [Zhang and Webb (2001)]) provide more deviations to predict the frictional pressure drop when the saturation temperature increases from 60 to 120°C (see Table 7.3).

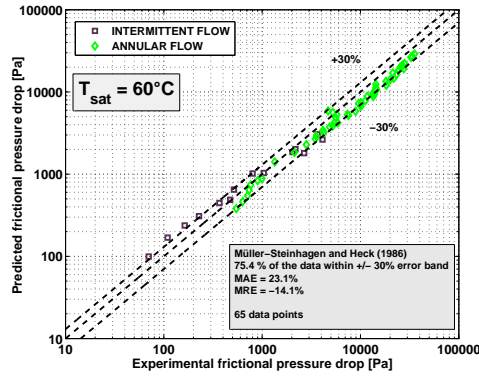
Figures 7.10(a) and 7.10(b) depict comparisons between the experimental trends and those predicted by the previous correlations for two different saturation temperatures: 60°C and 120°C. At 60°C, for a vapor quality lower than 0.4, the experimental trend is close to those predicted by [Grønnerud (1979)], [Tran et al. (2000)], and [Zhang and Webb (2001)]. For a vapor quality ranging from 0.4 to 0.6, the correlation of [Zhang and Webb (2001)] is able to reproduce the experimental trend, however, for higher vapor quality than 0.6, the experimental frictional pressure drop levels off and none of the correlations follows this tendency. At 120°C, the correlations of [Müller-Steinhagen and Heck (1986)], [Friedel (1979)], and [Zhang and Webb (2001)] reveal trends close to the experimental one. Nevertheless, for high vapor quality, the experimental trend differs from those predicted by these correlations.



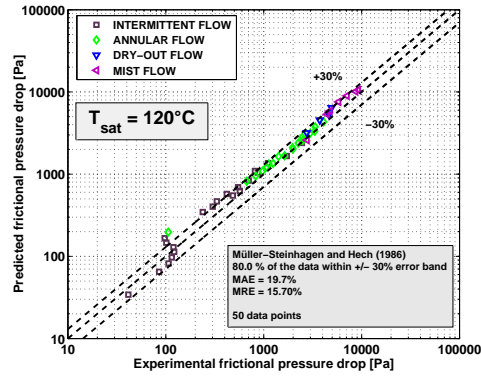
(a) [Friedel (1979)] - $T_{sat} = 60^{\circ}\text{C}$.



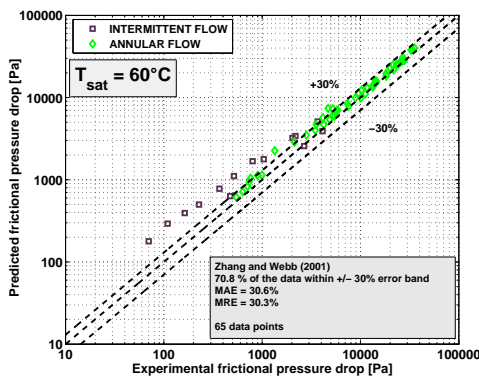
(b) [Friedel (1979)] - $T_{sat} = 120^{\circ}\text{C}$.



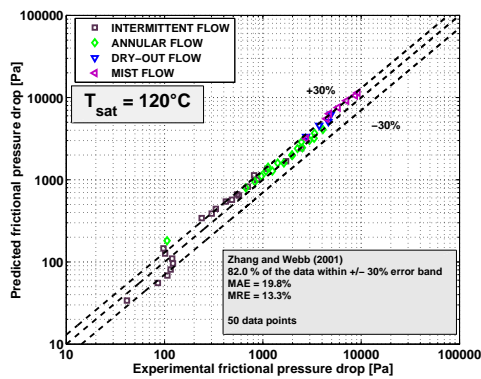
(c) [Müller-Steinhagen and Heck (1986)] - $T_{sat} = 60^{\circ}\text{C}$.



(d) [Müller-Steinhagen and Heck (1986)] - $T_{sat} = 120^{\circ}\text{C}$.



(e) [Zhang and Webb (2001)] - $T_{sat} = 60^{\circ}\text{C}$.



(f) [Zhang and Webb (2001)] - $T_{sat} = 120^{\circ}\text{C}$.

Figure 7.9: Comparison between experimental frictional pressure drop data and those predicted by the Φ_{LO}^2 , Φ_{VO}^2 correlations based on the separated flow model correlations based on the separated flow model.

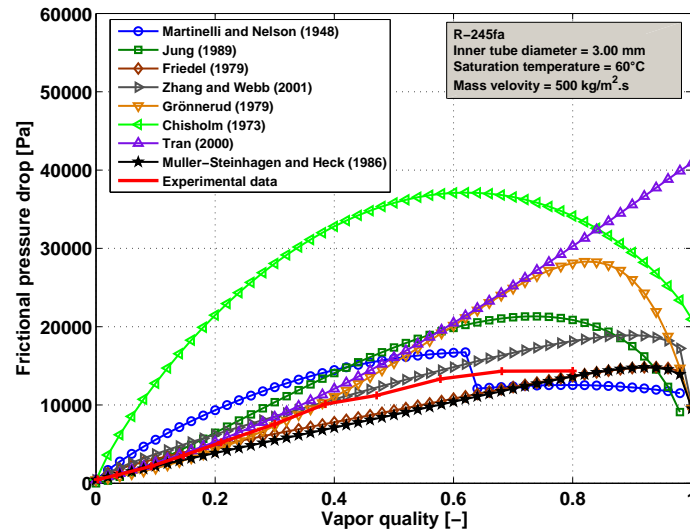
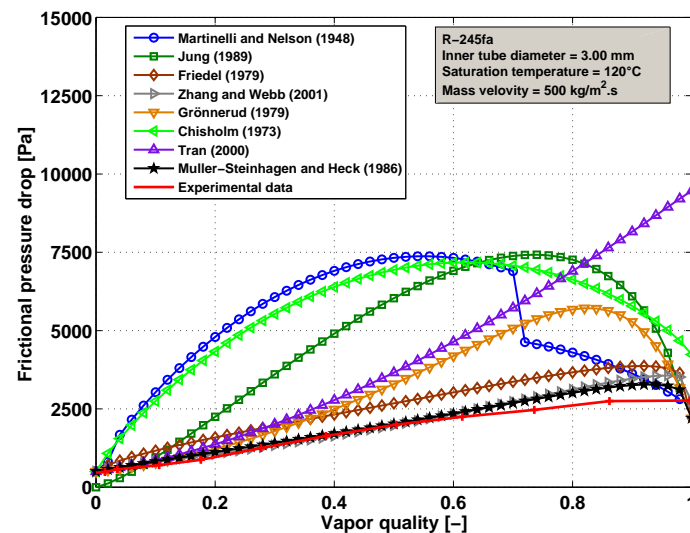
(a) $T_{\text{sat}} = 60^{\circ}\text{C}$.(b) $T_{\text{sat}} = 120^{\circ}\text{C}$.

Figure 7.10: Comparison between the experimental trends and those predicted by the Φ_{LO}^2 , Φ_{VO}^2 correlations based on the separated flow model at 60°C and 120°C ((a) $T_{\text{sat}} = 60^{\circ}\text{C}$ and $G = 500 \text{ kg/m}^2\cdot\text{s}$ and (b) $T_{\text{sat}} = 120^{\circ}\text{C}$ and $G = 500 \text{ kg/m}^2\cdot\text{s}$).

Table 7.3: Summary of the statistical analysis of the comparisons between experimental frictional pressure drops and those predicted the Φ_{LO}^2 , Φ_{VO}^2 correlations based on the separated flow model (MAE: Mean Absolute Error, MRE: Mean Relative Error and $\pm 30\%$: percentage of data predicted within 30% error bar).

		60°C			120°C					Whole database				
		Intermittent	Annular	All data	Intermittent	Annular	Dryout	Mist	all data	Intermittent	Annular	Dryout	Mist	All data
[Martinelli and Nelson (1948)]	MAE	114.3	47.3	61.7	230.3	244.3	262.2	120.2	222.5	204.9	96.9	88.9	66.7	126.1
	MRE	111.6	41.4	56.5	230.0	244.3	262.2	116.8	221.9	204.2	93.5	76.3	74.7	122.6
	$\pm 30\%$	28.6	41.2	38.5	9.5	0.0	0.0	42.9	10.0	11.3	29.3	56.3	64.4	27.7
[Jung et al. (1989)]	MAE	74.2	40.2	47.5	120.4	179.7	226.9	162.3	156.1	124.6	83.9	101.3	113.7	98.1
	MRE	14.6	35.6	31.1	85.2	179.7	226.9	146.8	139.2	89.5	81.9	101.3	93.4	85.9
	$\pm 30\%$	21.4	27.5	26.2	9.5	0.0	0.0	0.0	4.0	14.1	15.4	12.5	8.4	14.5
[Friedel (1979)]	MAE	78.9	15.6	29.2	62.8	49.9	48.1	36.8	53.4	88.6	25.6	18.9	23.9	43.0
	MRE	76.7	-8.9	9.5	62.8	49.9	48.1	36.8	53.4	88.2	14.5	11.7	22.9	34.5
	$\pm 30\%$	21.4	96.1	80.0	28.6	0.0	0.0	28.6	16.0	18.3	76.7	75.0	58.4	59.0
[Zhang and Webb (2001)]	MAE	84.8	15.8	30.6	24.1	12.4	20.4	25.5	19.8	51.9	16.3	8.2	16.5	25.9
	MRE	83.6	15.6	30.3	9.6	11.3	20.4	25.5	13.3	46.8	7.8	3.9	14.7	19.0
	$\pm 30\%$	14.3	86.3	70.8	71.4	94.5	100.0	71.4	82.0	39.5	88.0	100.0	83.4	74.7
[Grønnerud (1979)]	MAE	19.1	35.2	31.7	34.2	68.1	100.2	97.1	60.5	36.2	47.5	79.5	76.0	47.7
	MRE	-9.0	16.5	11.0	21.6	68.1	100.2	91.7	54.4	22.8	38.6	79.5	68.9	38.2
	$\pm 30\%$	78.6	52.9	58.5	57.2	22.2	0.0	14.3	34.0	56.3	42.0	0.0	16.7	42.2
[Müller-Steinhagen and Heck (1986)]	MAE	25.4	22.5	23.1	24.6	13.8	20.7	19.7	19.7	36.7	21.9	9.8	14.1	24.9
	MRE	10.9	-21.0	-14.1	15.7	13.8	20.7	18.0	15.7	28.2	-6.1	1.4	9.0	5.2
	$\pm 30\%$	57.2	80.4	75.4	66.7	94.4	75.0	85.7	80.0	50.7	84.7	93.8	91.7	75.9
[Chisholm (1973)]	MAE	160.7	31.0	58.9	95.2	59.8	33.3	16.0	66.4	159.5	40.2	24.1	20.7	72.3
	MRE	155.2	22.1	50.8	94.9	59.8	33.3	1.0	64.2	158.3	33.5	-7.5	-10.8	64.3
	$\pm 30\%$	21.4	62.7	53.8	9.5	16.7	25.0	85.7	24.0	12.7	56.7	62.5	83.4	45.8
[Tran et al. (2000)]	MAE	42.9	43.5	43.4	57.0	106.2	136.1	186.1	99.5	75.2	77.9	126.1	177.8	85.0
	MRE	33.1	38.4	37.2	54.1	106.2	136.1	186.1	98.3	71.0	75.8	126.1	177.8	82.6
	$\pm 30\%$	42.9	51.0	49.3	47.6	11.2	0.0	0.0	24.0	39.4	34.0	0.0	0.0	31.8

7.2.3 Phenomenological model

The last comparison deals with the phenomenological models developed by [Quibén and Thome (2007b)] and [Cioncolini et al. (2009)]. Table 7.4 depicts the statistical comparisons of these models to the present database. The comparison with the model of [Cioncolini et al. (2009)] deals only with the annular flow data.

The model of [Quibén and Thome (2007b)] is based on data obtained with R-22, R-134a, and R-410A in macrochannels at a saturation temperature of 5°C. Figures 7.11(a) and 7.11(b) display the comparisons between the present experimental frictional pressure drops and those predicted by this model at 60°C and 120°C. At 60°C, 34% of the data fall within $\pm 30\%$ error band whereas at 120°C, only 2% of the data are predicted within $\pm 30\%$ error band. This model overpredicts the frictional pressure drop. This model was developed from data obtained at a low saturation temperature and for a reduced pressure ranging from 0.12 to 0.19. As shown previously, the flow patterns are strongly dependent on the saturation temperature (see section 5.5). As a consequence, these modifications of configuration seem to have an influence on the reliability of this model when it is extended up to high saturation temperatures, since the model is based on considerations of geometrical distribution of the phases.

Figures 7.12(a) and 7.12(b) display comparisons between the experimental annular flow data and those predicted by the micro- and macroscale models of [Cioncolini et al. (2009)]. At 60°C, the method initially developed for microscale tubes is found to be the best of the 23 predicting methods with 86% of the predicted values falling within $\pm 30\%$ error band (see Table 7.4). Such a result was previously obtained by [Tibiricá and Ribatski (2010)] and [Tibiricá et al. (2011a)]. The method for macroscale tubes predicts only 40% of the data within $\pm 30\%$ error band and presents a larger dispersion than the microscale method. This result is quite surprising when the experimental conditions suggest a macroscale type of flow. At 120°C, the deviation and the percentage of data falling within $\pm 30\%$ error band decreases sharply for the microscale model. Whereas, for the macroscale model, the percentage of data falling within $\pm 30\%$ error band is almost not affected (it passes from 40% to 44% when increasing the saturation temperature from 60°C to 120°C). These results are consistent with the fact that when the saturation temperature increases, the phenomena typical of macroscale flow increasingly become stronger.

Figure 7.13 shows the evolution of the frictional pressure drop data with vapor quality according to the experimental results and predictive models. This figure shows that at 60°C, the microscale model of [Cioncolini et al. (2009)] properly capture the trend in the frictional pressure drop data. At 120°C, the microscale model of [Cioncolini et al. (2009)] is not statistically accurate but it captures the experimental trend. For both temperatures, the model of [Quibén and Thome (2007b)] is not able to reproduce the experimental trend.

In conclusion, the microscale model of [Cioncolini et al. (2009)] is very accurate to predict the frictional pressure drop at 60°C whereas at 120°C it is not able to predict the experimental data. This kind of model requires an indisputable knowledge of the flow patterns at high saturation temperature and they cannot be extrapolated up to 120°C.

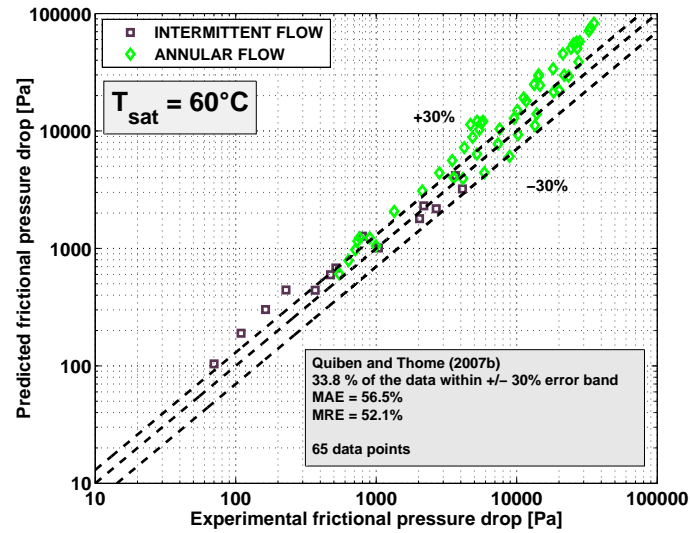
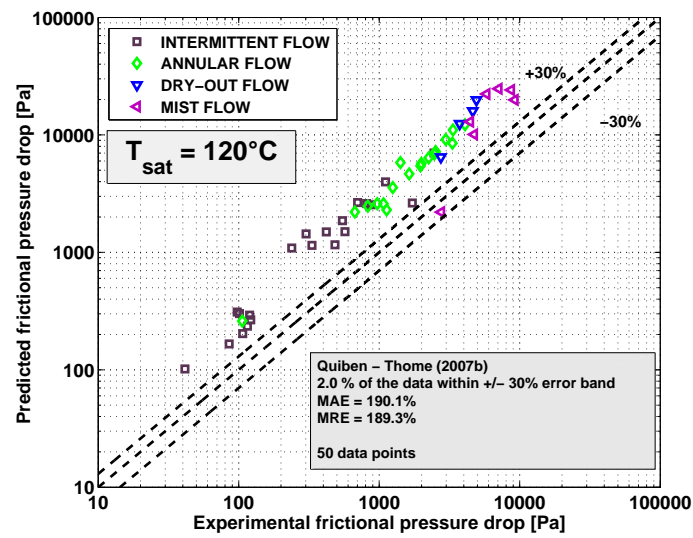
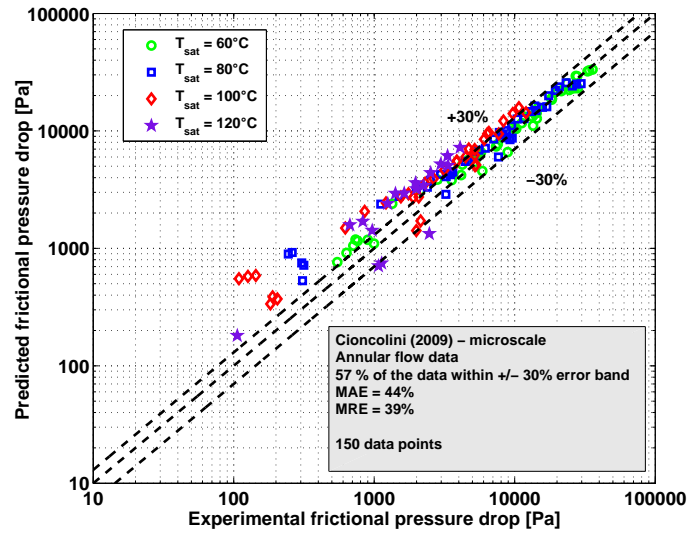
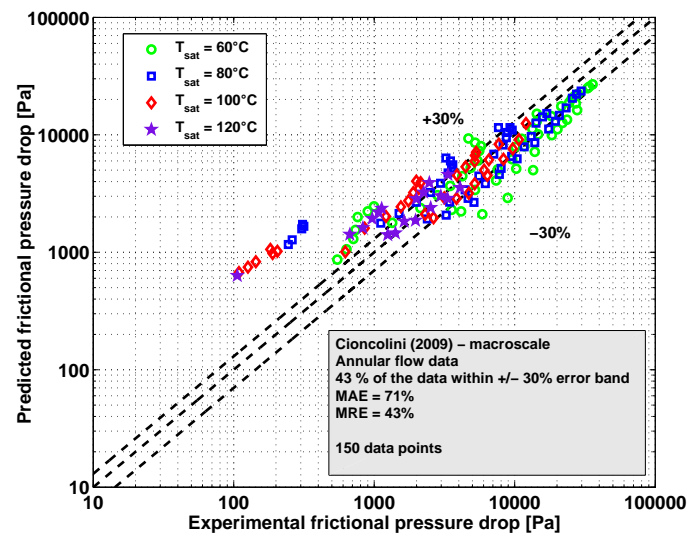
(a) [Quibén and Thome (2007b)] - $T_{\text{sat}} = 60^{\circ}\text{C}$.(b) [Quibén and Thome (2007b)] - $T_{\text{sat}} = 120^{\circ}\text{C}$.

Figure 7.11: Comparison between experimental frictional pressure drop data and those predicted by the phenomenological model of [Quibén and Thome (2007b)].



(a) microscale model.



(b) macroscale model.

Figure 7.12: Comparison between experimental frictional pressure drop and those predicted by (a) the microscale model and (b) the macroscale model of [Cioncolini et al. (2009)].

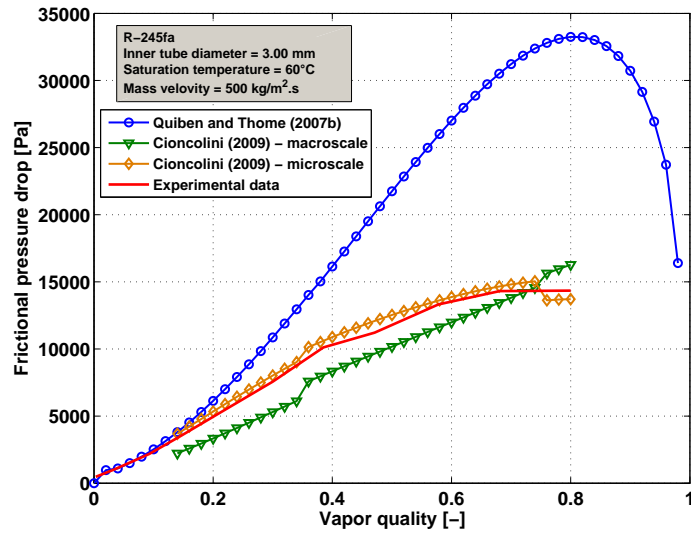
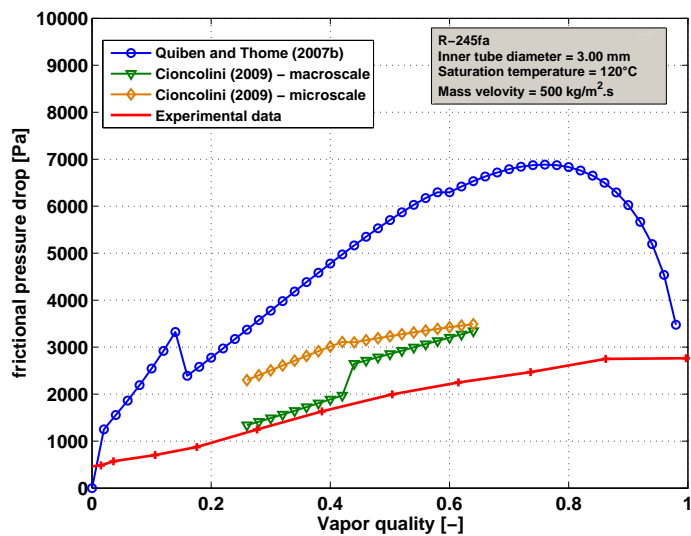
(a) $T_{\text{sat}} = 60^\circ\text{C}$.(b) $T_{\text{sat}} = 120^\circ\text{C}$.

Figure 7.13: Comparison between the experimental trends and those predicted by the phenomenological models of [Quibén and Thome (2007b)] and [Cioncolini et al. (2009)] for two situations: (a) $T_{\text{sat}} = 60^\circ\text{C}$ and $G = 500\text{ kg/m}^2\cdot\text{s}$ and (b) $T_{\text{sat}} = 120^\circ\text{C}$ and $G = 500\text{ kg/m}^2\cdot\text{s}$.

Table 7.4: Summary of the statistical analysis of the comparisons between experimental frictional pressure drops and those predicted by the phenomenological models (MAE: Mean Absolute Error, MRE: Mean Relative Error and $\pm 30\%$: percentage of data predicted within 30% error bar).

		60°C			120°C					Whole database				
		Intermittent	Annular	All data	Intermittent	Annular	Dryout	Mist	all data	Intermittent	Annular	Dryout	Mist	All data
[Quibén and Thome (2007b)]	MAE	36.6	62.0	56.5	193.9	187.0	229.0	164.5	190.1	148.7	11.3	149.0	130.3	120.6
	MRE	28.7	58.5	52.1	193.9	187.0	229.0	158.6	189.3	147.2	103.5	149.0	122.7	119.1
	$\pm 30\%$	57.2	27.5	33.8	0.0	0.0	0.0	14.3	2.0	14.1	102.2	0.0	16.7	11.7
[Cioncolini et al. (2009)] - microscale	MAE	/	16.7	16.7	/	72.7	/	/	72.7	/	44.5	/	/	44.5
	MRE	/	11.2	11.2	/	60.1	/	/	60.1	/	39.1	/	/	39.1
	$\pm 30\%$	/	85.4	85.4	/	0.0	/	/	0.0	/	56.7	/	/	56.7
[Cioncolini et al. (2009)] - macroscale	MAE	/	42.9	42.9	/	70.3	/	/	70.3	/	71.0	/	/	71.0
	MRE	/	0.0	0.0	/	66.2	/	/	66.2	/	43.2	/	/	43.2
	$\pm 30\%$	/	39.2	39.2	/	44.0	/	/	44.0	/	43.4	/	/	43.4

7.3 Conclusions

Adiabatic frictional pressure drops have been experimentally determined during flow boiling of R-245fa in a 3.00 mm inner tube diameter, for saturation temperatures ranging from 60 to 120°C and mass velocities ranging from 100 to 1200 kg/m²·s. The flow patterns were determined from the flow pattern map developed during the present investigation. The influence of the mass velocity and the saturation temperature on the frictional pressure drop was investigated. The results agreed with the expectations, i.e. the higher the saturation temperature, the lower the frictional pressure drop and the higher the mass velocity, the higher the frictional pressure drop. The 249 experimental data were compared against several correlations found in the literature. The conclusions can be summarized as follows:

- ***the homogeneous model:*** the homogeneous model with the definitions of [Cicchitti et al. (1960)] and [Awad and Muzychka (2008)] No 1 for the two-phase viscosity provide the best accuracy with 76.7% and 76.3%, respectively, of the data falling within $\pm 30\%$ error band for the whole database. Generally speaking, the homogeneous model is more robust for the prediction of the frictional pressure drop when the saturation temperature increases.
- ***methods based on the separated flow model:*** the best correlations to predict the whole database are those of [Müller-Steinhagen and Heck (1986)], [Zhang and Webb (2001)], and [Friedel (1979)], respectively. Except for these correlations, the deviation increases when the saturation temperature increases.
- ***phenomenological model:*** None of the phenomenological model assessed in this PhD work is reliable to predict the frictional pressure drop at high saturation temperature. This kind of model requires an indisputable knowledge of the flow patterns at high saturation temperature. At moderate saturation temperature, the microscale model of [Cioncolini et al. (2009)] is found to be the best predicting method for annular flow data.

With a view to obtain a better fit to the whole database and capture the influence of the saturation temperature, several ways could be investigated including:

- a new two-phase flow viscosity definition to be employed in the homogeneous model
- a new C parameter in a correlation based on the [Lockhart and Martinelli (1949)] correlation
- a new two-phase multiplier Φ_{LO} to adapt the correlation of [Friedel (1979)] at high saturation temperature
- a new phenomenological approach based on our conclusions on the influence of the high saturation temperature on the flow patterns.

Chapter 8

Conclusions and Perspectives

This chapter concludes the present PhD thesis by giving a brief synthesis of the main results obtained in this experimental investigation on flow boiling of R-245fa in a minichannel at high saturation temperature. Aspects deserving further investigation, as well as recommendations concerning the experimental system will be detailed.

8.1 Synthesis

A state-of-the-art review related to the existing studies on flow visualization, flow pattern map, pressure drop, and heat transfer during flow boiling of refrigerants has been carried out. It was shown that the effect of the high saturation temperature had, so to say, never been studied so far for T_{sat} higher than 100°C. However, some works investigated the influence of saturation temperature on flow boiling. With their limited range of saturation temperature, the authors concluded by noting that the two-phase flow patterns and their transitions, the two-phase flow pressure drop, and the two-phase flow boiling heat transfer coefficients were strongly influenced by the saturation temperature.

In order to fill the gap observed in the literature and reach the main objectives of this PhD work, a new multipurpose minichannel test facility was built at the Centre Thermique de Lyon (CETHIL UMR5008) to investigate flow boiling of refrigerants at high saturation temperatures. A test section was developed to perform flow visualizations, flow boiling heat transfer coefficient measurements, and two-phase flow pressure drop measurements. In addition, a new image processing method was developed to quantitatively identify flow patterns, determine bubble frequencies and lengths and measure bubble velocities. This method was coupled with a method of analysis of heat transfer coefficient to characterize dryout inception and completion.

The present study deals with flow boiling of R-245fa in a wide range of conditions for a horizontal minichannel. These experimental conditions were chosen to obtain experimental values over a wide range of test parameters so that the effect of each parameter could be easily identified. The range of experimental conditions covered was: seven mass velocities, five heat fluxes, and four saturation temperatures over a large range of vapor quality. The campaign led to acquire:

- 994 data points for flow pattern

- 239 data points for bubble velocity, bubble frequency, and mean bubble length
- 5964 data points for flow boiling heat transfer coefficient
- 249 data points for two-phase pressure drop

The first part of this thesis dealt with flow patterns and bubble dynamics. Based on an image processing method (including the determination of flow parameters such as bubble velocity, bubble frequency or bubble size distribution) and on an analysis of the inner wall temperatures and the resulting heat transfer coefficient, four main flow regimes were identified: (i) intermittent flow, (ii) annular flow, (iii) dryout and (iv) mist flow. Experimental transition lines were compared with a variety of prediction tools. For intermittent-to-annular transition lines, the predictive methods developed by [Barbieri et al. (2008)] and [Costa-Patry and Thome(2013)] were the most accurate at predicting the data. [Wojtan et al. (2005a)] transition lines were in the best agreements with experiments for both annular-to-dryout and dryout-to-mist flow transitions. Whereas the flow regime would suggest a macroscale type of flow, the flow patterns transitions are closer to those observed at the microscale. For that reason, we retained the term minichannel to describe the present experimental conditions.

The main conclusions on the influence of the saturation temperature on the flow patterns are:

- The higher T_{sat} , the thicker the liquid film thickness at the bottom, which increases the stratified character of the flow.
- The higher T_{sat} , the smaller and shorter the bubbles.
- The higher T_{sat} , the greater the bubble frequency.
- The higher T_{sat} , the lower the bubble velocity.
- The higher T_{sat} , the lower the value of the vapor quality for dryout inception.
- The higher T_{sat} , the narrower the range of vapor quality corresponding to annular flow whereas the larger the range of vapor quality for intermittent and mist flow regimes.

In the second part of the present manuscript, results were presented concerning the flow boiling heat transfer coefficient. The evolution of the heat transfer coefficient with the vapor quality was discussed for various combinations of heat flux, mass velocity and saturation temperature while the flow regime was also fixed by these parameters. The contribution to the overall heat transfer of a variety of mechanisms was identified and discussed for medium and high saturation temperatures.

At 60°C, the heat transfer coefficient is independent of vapor quality and mass flux during intermittent flow whereas it is sensitive to heat flux. In annular flow, the heat transfer coefficient increases with increasing vapor quality and/or mass velocity. As a result, at 60°C, nucleate and convective boiling are both present. At 120°C, the heat transfer coefficient exhibits completely different trends. The heat transfer coefficient decreases for both intermittent and annular flow regimes. The analysis of the results has highlighted the key role of nucleate boiling at high

saturation temperature. Thus, similar mechanisms were found to govern the flow boiling heat transfer at moderate saturation temperature in microchannels and at high saturation temperature in minichannels.

The main conclusions on the influence of the saturation temperature on the heat transfer are:

- The higher T_{sat} , the greater the flow boiling heat transfer coefficient.
- The higher T_{sat} , the greater the contribution of nucleate boiling to the overall heat transfer coefficient.
- The higher T_{sat} , the lower the contribution of convective boiling to the overall heat transfer coefficient.
- The higher T_{sat} , the closer the behavior of R-245fa to the one of carbon dioxide.

The experimental database of 5964 data points was compared to the theoretical results of thirty one methods selected from the literature in order to verify their ability to predict the heat transfer coefficient during flow boiling at high saturation temperature. The best correlations or models to predict the whole database are those of [Choi et al. (2007b)], [Kandlikar and Balasubramanian (2004)], and [Fang (2013)]. Most of the well-known methods are relatively accurate to predict the flow boiling heat transfer coefficient at moderate saturation temperature, whereas when extrapolating up to high saturation temperature, these methods are not robust and provide large deviations. The phenomenological models are the perfect examples of this tendency.

According to the results, the best solution to predict the flow boiling heat transfer coefficient is to divide the prediction by flow regime using the present flow pattern maps. To date, the best combination of correlations or models to predict the heat transfer in the conditions of ORC is the following:

- intermittent flow: the asymptotic model of [Ducoulombier et al. (2011)]
- annular flow: the asymptotic model of [Choi et al. (2007b)]
- dryout flow: the correlation of [Saitoh et al. (2007)]
- mist flow: the correlation of [Dougall and Roshenow (1963)]

In the last part of this PhD thesis, experimental results on two-phase frictional pressure drop were presented. The influence of the mass velocity and the saturation temperature on the frictional pressure drop was investigated. The results agreed with the expectations, i.e. the higher the saturation temperature, the lower the frictional pressure drop and the higher the mass velocity, the higher the frictional pressure drop. The 249 experimental data have been compared against twenty three correlations found in the literature. The best correlations to predict the whole frictional pressure drop database are those of [Müller-Steinhagen and Heck (1986)], [Zhang and Webb (2001)], and [Friedel (1979)], as well as the homogeneous models with the two-phase viscosity definitions of [Cicchitti et al. (1960)] and [Awad and Muzychka (2008)] No 1. From the statistical results, several conclusions can be drawn:

- The higher T_{sat} , the more accurate the homogeneous models.
- The higher T_{sat} , the less accurate the most of the correlations based on the separated flow model.
- The higher T_{sat} , the less accurate the phenomenological models.

To date, the best solution to predict the two-phase frictional pressure drop in the conditions of ORC is to use the correlation of [Zhang and Webb (2001)] for the whole database.

In summary, important new databases were created for two-phase flow boiling at high saturation temperature. Numerous prediction methods were assessed from these databases.

8.2 Perspectives

As some of the aspects of this work are particularly complex and as for some of them, no definite conclusions could be done, further research definitely needs to be carried out. Specific areas that should be given priority for future works are suggested below:

- Extend the database to another fluid, in particular for a fluid with a lower Global Warming Potential.
- Extend the present database to smaller diameters in order to investigate in-depth the macro-to-microscale transition zone. To reach this objective, the image processing method must be adapted to perform film thickness measurement. In addition the image processing method should be extended to include possibilities to investigate the symmetric/asymmetric character of the flow: this would help characterize the occurrence of stratification and thus better discuss the concept of micro and macroscale tubes in the context of flow boiling.
- Complete the present database with more data points for intermittent flow regime in order to investigate the bubble characteristics, especially the bubble velocity. The investigation of the bubble velocity will allow to investigate the void fraction.
- Develop a new flow boiling heat transfer coefficient prediction method based on a modification of the suppression factor S and the enhancement factor F to better capture the influence of the saturation temperature on the heat transfer mechanisms.
- Develop a new two-phase pressure drop prediction method based either on a new two-phase flow viscosity definition, or a new C parameter in a correlation based on the [Lockhart and Martinelli (1949)] correlation, or a new two-phase multiplier Φ_{LO} to adapt the correlation of [Friedel (1979)].
- Adapt the phenomenological model taking into account the modification of the two-phase flow structure at the high saturation temperature.

Bibliography

- [[Agostini et al. \(2008\)](#)] Agostini, B., Thome, J.R., Fabbri, M., Michel, B., Calmi, D., Kloter, U., 2008. High heat flux flow boiling in silicon multi-microchannels - Part II: Heat transfer characteristics of refrigerant R-245fa. *International Journal of Heat and Mass Transfer* 51 (21-22), 5415 – 5425.
- [[Akbar et al. \(2003\)](#)] Akbar, M., Plummer, D., Ghiaasiaan, S., 2003. On gas-liquid two-phase flow regimes in microchannels. *International Journal of Multiphase Flow* 29 (5), 855 – 865.
- [[Ali et al. \(2011\)](#)] Ali, R., Palm, B., Maqbool, M., 2011. Flow boiling heat transfer characteristics of a minichannel up to dryout condition. *Journal of Heat Transfer* 133 (8), 1–10.
- [[Arcanjo et al. \(2010\)](#)] Arcanjo, A.A., Tibiriça, C.B., Ribatski, G., 2010. Evaluation of flow patterns and elongated bubble characteristics during the flow boiling of halocarbon refrigerants in a micro-scale channel. *Experimental Thermal and Fluid Science* 34 (6), 766 – 775.
- [[Awad and Muzychka \(2008\)](#)] Awad, M.M., Muzychka, Y.S., 2008. Effective property models for homogeneous two-phase flows. *Experimental Thermal and Fluid Science* 33 (1), 106 – 113.
- [[Baker \(1954\)](#)] Baker, O., 1954. Simultaneous flow of oil and gas. *Oil and Gas Journal* 53, 185–190.
- [[Baldassari and Marengo \(2013\)](#)] Baldassari, C., Marengo, M., 2013. Flow boiling in microchannels and microgravity. *Progress in Energy and Combustion Science* 39, 1–36.
- [[Bandel \(1973\)](#)] Bandel, J., 1973. Druckverlust und Wärmeübergang bei der Verdampfung siedender Kältemittel im durchströmten waagerechten Rohr. Ph.D. Thesis, University of Karlsruhe.
- [[Bankoff \(1960\)](#)] Bankoff, S., 1960. A variable density single-fluid model for two-phase flow with particular reference to steam-water flow. *Journal of Heat Transfer* 82, 265–272.
- [[Bao et al. \(2000\)](#)] Bao, Z., Fletcher, D., Haynes, B., 2000. Flow boiling heat transfer of Freon R-11 and HCFC-123 in narrow passages. *International Journal of Heat and Mass Transfer* 43, 3347 – 3358.
- [[Barbieri et al. \(2008\)](#)] Barbieri, P.E.L., Jabardo, J.M.S., Bandarra Filho, E.B., 2008. Flow patterns in convective boiling of refrigerant R-134a in smooth tubes of several diameters. *Proceedings of the 5th European Thermal-Sciences Conference, Eindhoven, The Netherlands.*

- [Barnea et al. (1980)] Barnea, D., Shoham, O., Taitel, Y., 1980. Flow pattern characterization in two-phase flow by electrical conductance probe. *International Journal of Multiphase Flow* 6 (5), 387 – 397.
- [Baroczy (1965)] Baroczy, C., 1965. A systematic correlation for two-phase pressure drop. *Chemical Engineering Progress Symposium* 62 (44), 232–249.
- [Basu et al. (2011)] Basu, S., Ndao, S., Michna, G., Peles, Y., Jensen, M., 2011. Flow boiling of R-134a in circular microtubes - Part I: study of heat transfer characteristics. *Journal of Heat Transfer* 133 (5), 1–9.
- [Beattie and Whalley (1982)] Beattie, D., Whalley, P., 1982. A simple two-phase frictional pressure drop calculation method. *International Journal of Multiphase Flow* 8, 83–87.
- [Bertsch et al. (2008)] Bertsch, S.S., Groll, E.A., Garimella, S.V., 2008. Review and comparative analysis of studies on saturated flow boiling in small channels. *Nanoscale and Microscale Thermophysical Engineering* 12, 187–227.
- [Bertsch et al. (2009)] Bertsch, S. S., Groll, E. A., Garimella, S. V., 2009. A composite heat transfer correlation for saturated flow boiling in small channels. *International Journal of Heat and Mass Transfer* 52 (7), 2110 – 2118.
- [Bortolin et al. (2011)] Bortolin, S., Del Col, D., Rossetto, L., 2011. Flow boiling of R245fa in a single circular microchannel. *Heat Transfer Engineering* 32 (13), 1160–1172.
- [Canière et al. (2010)] Canière, H., Bauwens, B., T'Joel, C., Paepe, M. D., 2010. Mapping of horizontal refrigerant two-phase flow patterns based on clustering of capacitive sensor signals. *International Journal of Heat and Mass Transfer* 53 (23), 5298 – 5307.
- [Cavallini et al. (2005)] Cavallini, A., Del Col, D., Doretti, L., Matkovic, M., Rossetto, L., Zilio, C., 2005. Two-phase frictional pressure gradient of R-236ea, R-134a and R-410A inside multi-port mini-channels. *Experimental Thermal and Fluid Science* 29 (7), 861 – 870.
- [Celata et al. (2012)] Celata, G., Cumo, M., Dossevi, D., Jilisen, R., Saha, S., Zummo, G., 2012. Flow pattern analysis of flow boiling inside a 0.48 mm microtube. *International Journal of Thermal Sciences* 58, 1 – 8.
- [Chang et al. (2000)] Chang, Y., Chiang, S., Chung, T., Wang, C., 2000. Two-phase frictional characteristics of R-410A and air-water in a 5 mm smooth tube. *ASHRAE Transactions* 104 (2), 792–797.
- [Charnay et al. (2011)] Charnay, R., Revellin, R., Bonjour, J., 2011. Review on two-phase pressure drop and heat transfer coefficient during flow boiling of natural and synthetic refrigerants: a parametric analysis (keynote lecture). The 23rd IIR International Congress of Refrigeration. Prague, Czech Republic.
- [Charnay et al. (2013)] Charnay, R., Revellin, R., Bonjour, J., 2013. Flow pattern characterization for R-245fa in minichannels: optical measurement technique and experimental results. *International Journal of Multiphase Flow* 57, 169 - 181.

- [Chawla (1968)] Chawla, J. M., 1968. Wärmeübergang und Druckverlust bei der Kältemittelverdampfung im waagerechten Strömungsrohr. *Chemie Ingenieur Technik* 40 (5), 229–234.
- [Chen (1963)] Chen, J., 1963. A correlation for boiling heat transfer to saturated fluids in convective flow. MA (Ed.), ASME Paper 63-HT-34, 6th International Heat Transfer Conference. Boston, USA.
- [Chen (1966)] Chen, J. C., 1966. Correlation for boiling heat transfer to saturated fluids in convective flow. *Industrial Engineering Chemistry Process Design and Development* 5 (3), 322–329.
- [Cheng et al. (2006a)] Cheng, L., Ribatski, G., Wojtan, L., Thome, J., 2006. New flow boiling heat transfer model and flow pattern map for carbon dioxide evaporating inside horizontal tubes. *International Journal of Heat and Mass Transfer* 49 (21), 4082 – 4094.
- [Cheng and Wu (2006b)] Cheng, L., Wu, H.Y., 2006. Mesoscale and microscale phase change heat transfer. *Advances in Heat Transfer* 39, 461–563.
- [Cheng et al. (2008)] Cheng, L., Ribatski, G., Thome, J., 2008. New prediction methods for CO₂ evaporation inside tubes: Part II - an updated general flow boiling heat transfer model based on flow patterns. *International Journal of Heat and Mass Transfer* 51 (1), 125 – 135.
- [Chisholm (1967)] Chisholm, D., 1967. A theoretical basis for the Lockhart-Martinelli correlation for two-phase flow. *International Journal of Heat and Mass Transfer* 10 (12), 1767 – 1778.
- [Chisholm (1973)] Chisholm, D., 1973. Pressure gradients due to friction during the flow of evaporating two-phase mixtures in smooth tubes and channels. *International Journal of Heat and Mass Transfer* 16 (2), 347 – 358.
- [Chisholm (1983)] Chisholm, D., 1983. Two-phase flow in pipelines and heat exchangers. George Godwin in association with the Institution of Chemical Engineers, London.
- [Choi et al. (1999)] Choi, J., Kedzierski, A., Domanski, P., 1999. A generalized pressure drop correlation for boiling and condensation of alternative refrigerants in smooth tube and micro-fin tube. NISTIR 6333, I7–15.
- [Choi et al. (2007a)] Choi, K., Pamitran, A., Oh, C., Oh, J., 2007. Boiling heat transfer of R-22, R-134a, and CO₂ in horizontal smooth minichannels. *International Journal of Refrigeration* 30 (8), 1336 – 1346.
- [Choi et al. (2007b)] Choi, K., Pamitran, A., Oh, J., 2007. Two-phase flow heat transfer of CO₂ vaporization in smooth horizontal minichannels. *International Journal of Refrigeration* 30 (5), 767 – 777.
- [Chung and Kawaji (2004)] Chung, P., Kawaji, M., 2004. The effect of channel diameter on adiabatic two-phase flow characteristics in microchannels. *International Journal of Multiphase Flow* 30 (7-8), 735 – 761.
- [Churchill and Usagi (1972)] Churchill, S.W., Usagi, R., 1972. A general expression for the correlation of rates of transfer and other phenomena. *AIChE Journal* 18 (6), 1121–1128.

- [Churchill (1977)] Churchill, S.W., 1977. Friction factor equation spans all fluid flow regimes. *Chemical Engineering* 7, 91–92.
- [Cicchitti et al. (1960)] Cicchitti, A., Lombardi, C., Silvestri, M., Soldaini, G., Zavattarelli, R., 1960. Two-phase cooling experiments: Pressure drop, heat transfer and burnout measurements. *Energia Nucleare* 7, 407–425.
- [Cioncolini et al. (2009)] Cioncolini, A., Thome, J.R., Lombardi, C., 2009. Unified macro-to-microscale method to predict two-phase frictional pressure drops of annular flows. *International Journal of Multiphase Flow* 35 (12), 1138 – 1148.
- [Cioncolini and Thome (2010a)] Cioncolini, A., Thome, J.R., 2010. Prediction of the entrained liquid fraction in vertical annular gas-liquid two-phase flow. *International Journal of Multiphase Flow* 36 (4), 293 – 302.
- [Cioncolini et al. (2010b)] Cioncolini, A., Thome, J. R., Consolini, L., Ong, C.L., 2010. Microscale adiabatic gas-liquid annular two-phase flow: analytical model description, void fraction, and pressure gradient predictions. *Heat Transfer Engineering* 31 (4), 310–320.
- [Cioncolini and Thome (2011)] Cioncolini, A., Thome, J., 2011. Algebraic turbulence modeling in adiabatic and evaporating annular two-phase flow. *International Journal of Heat and Fluid Flow* 32 (4), 805 – 817.
- [Cioncolini and Thome (2012a)] Cioncolini, A., Thome, J. R., 2012. Entrained liquid fraction prediction in adiabatic and evaporating annular two-phase flow. *Nuclear Engineering and Design* 243, 200 – 213.
- [Cioncolini and Thome (2012b)] Cioncolini, A., Thome, J.R., 2012. Void fraction prediction in annular two-phase flow. *International Journal of Multiphase Flow* 43, 72 – 84.
- [Coleman and Garimella (1999)] Coleman, J., Garimella, S., 1999. Characterization of two-phase flow patterns in small diameter round and rectangular tubes. *International Journal of Heat and Mass Transfer* 42 (15), 2869 – 2881.
- [Coleman and Garimella (2000)] Coleman, J., Garimella, S., 2000. Two-phase flow regime transitions in microchannel tubes: the effect of hydraulic diameter. *Proceedings of ASME Heat Transfer Division-2000. ASME IMECE 2000*, 71 – 83.
- [Collier and Thome (1994)] Collier, J.G., Thome, J.R., 1994. *Convective boiling and condensation*, third edition. Oxford University Press, Oxford.
- [Cooper (1984)] Cooper, M., 1984. Heat flow rates in saturated nucleate pool boiling a wide-ranging examination using reduced properties. *Advances in Heat Transfer* 16, 157–239.
- [Cornwell and Kew (1993)] Cornwell, K., Kew, A., 1993. Boiling in small parallel channels. *Proceedings of CEC Conference on Energy Efficiency in Process Technology*, Elsevier Applied Science (Ed.), Athens. 624–638.
- [Cornwell and Kew (1995)] Cornwell, K., Kew, A., 1995. Evaporation in microchannel heat exchangers, 289 – 293.

- [Costa-Patry and Thome (2012)] Costa-Patry, E., Thome, J.R., 2012. Flow pattern based flow boiling heat transfer model for microchannels. ECI 8th International Conference on Boiling and Condensation Heat Transfer. Lausanne, Switzerland.
- [Costa-Patry and Thome(2013)] Costa-Patry, E., Thome, J., 2013. Flow pattern-based flow boiling heat transfer model for microchannels. *International Journal of Refrigeration* 36 (2), 414 – 420.
- [Da Silva Lima et al. (2009)] Da Silva Lima, R.J., Quibén, J.M., Thome, J.R., 2009. Flow boiling in horizontal smooth tubes: New heat transfer results for R-134a at three saturation temperatures. *Applied Thermal Engineering* 29 (7), 1289 – 1298.
- [Damianidis and Westwater (1987)] Damianidis, C., Westwater, J., September 1987. Two-phase flow patterns in a compact heat exchanger and in small tubes. *Proceedings of Second UK National Conference on Heat Transfer*. Glasgow, UK. 1257 – 1268.
- [Davidson et al. (1943)] Davidson, W.F., Hardie, P.H., Humphreys, C.G.R., Markson, A.A., Mumford, A.R., Ravese T., 1943. Studies of heat transmission through boiler tubing at pressures from 500 - 3300 Lbs. *Journal of Heat Transfer*, 65 (6), 553 - 591.
- [De Rossi et al. (2009)] De Rossi, F., Mauro, A., Rosato, A., 2009. Local heat transfer coefficients and pressure gradients for R-134a during flow boiling at temperatures between -9°C and +20°C. *Energy Conversion and Management* 50 (7), 1714 – 1721.
- [Del Col (2010)] Del Col, D. D., 2010. Flow boiling of halogenated refrigerants at high saturation temperature in a horizontal smooth tube. *Experimental Thermal and Fluid Science* 34 (2), 234 – 245.
- [Delhaye (1990)] Delhaye, J.M., 1990. Two-phase flows and heat transfer in the process industries. Hemisphere, New-York, 1990.
- [Dittus and Boetler (1930)] Dittus, F., Boetler, L., 1930. Heat transfer in automobile radiators of the tubular type. *Publications in Engineering Chemistry* 2, 443–461.
- [Dougall and Roshenow (1963)] Dougall, R., Roshenow, W., 1963. Film boiling on the inside of vertical tubes with upward flow of the fluid at low vapor qualities. In: MIT Report no. 9079-86.
- [Ducoulombier et al. (2011)] Ducoulombier, M., Colasson, S., Bonjour, J., Haberschill, P., 2011. Carbon dioxide flow boiling in a single microchannel - Part II: Heat transfer. *Experimental Thermal and Fluid Science* 35 (4), 597 – 611.
- [Dupont et al. (2004)] Dupont, V., Thome, J.R., Jacobi, A., 2004. Heat transfer model for evaporation in microchannels. Part II: comparison with the database. *International Journal of Heat and Mass Transfer* 47 (14-16), 3387 – 3401.
- [Dukler et al. (1964)] Dukler, A.E., Wicks, M., Cleveland, R.G., 1964. Pressure drop and hold-up in two-phase flow Part A - a comparison of existing correlations and Part B - an approach through similarity analysis. *AIChE Journal* 10 (1), 38–43.

- [Ebisu and Torikoshi (1998)] Ebisu, T., Torikoshi, K., 1998. Heat transfer characteristics and correlations for R-410A flowing inside a horizontal smooth tube. *ASHRAE Transactions* 104, 556–561.
- [El Hajal et al. (2003)] El Hajal, J., Thome, J., Cavallini, A., 2003. Condensation in horizontal tubes, part 1: two-phase flow pattern map. *International Journal of Heat and Mass Transfer* 46 (18), 3349 – 3363.
- [Fang (2013)] Fang, X., 2013. A new correlation of flow boiling heat transfer coefficients for carbon dioxide. *International Journal of Heat and Mass Transfer* 64, 802 – 807.
- [Filho et al. (2004)] Filho, E. P., Jabardo, J. M., Barbieri, P. E., 2004. Convective boiling pressure drop of refrigerant R-134a in horizontal smooth and microfin tubes. *International Journal of Refrigeration* 27 (8), 895 – 903.
- [Forster and Zuber (1955)] Forster, H. K., Zuber, N., 1955. Dynamics of vapor bubbles and boiling heat transfer. *AIChE Journal* 1, 531–535.
- [Fourar and Bories (1995)] Fourar, M., Bories, S., 1995. Experimental study of air-water two-phase flow through a fracture (narrow channel). *International Journal of Multiphase Flow* 21 (4), 621 – 637.
- [Friedel (1979)] Friedel, L., 1979. Improved friction pressure drop correlations for horizontal and vertical two phase pipe flow. Paper E2, European Two Phase Flow Group Meeting. Ispra, Italia.
- [Fritz (1935)] Fritz, W., 1935. Berechnung des Maximalvolumen von Dampfblasen. *Phys. Zeitung* 36, 379.
- [Galvis and Culham (2012)] Galvis, E., Culham, R., 2012. Measurements and flow pattern visualizations of two-phase flow boiling in single channel microevaporators. *International Journal of Multiphase Flow* 42, 52 – 61.
- [García et al. (2003)] García, F., García, R., Padrino, J.C., Mata, C., Trallero, J.L., Joseph D.D., 2003. Power law and composite power law friction factor correlations for laminar and turbulent gas-liquid flow in horizontal pipelines. *International Journal of Multiphase Flow* 29 (10), 1605 – 1624.
- [Gnielinski (1976)] Gnielinski, V., 1976. New equations for heat and mass transfer in turbulent pipe and channel flow. *International Chemical Engineering* 16 (2), 359–368.
- [Gorenflo(1993)] Gorenflo, D., 1993. Pool boiling. *VDI Heat Atlas*, VDI-Verlag, Düsseldorf (English version).
- [Gorenflo et al. (2004)] Gorenflo, D., Chandra, U., Kotthoff, S., Luke, A., 2004. Influence of thermophysical properties on pool boiling heat transfer of refrigerants. *International Journal of Refrigeration* 27 (5), 492 – 502.
- [Grauso et al. (2013)] Grauso, S., Mastrullo, R., Mauro, A., Vanoli, G., 2013. Flow boiling of R410A and CO₂ from low to medium reduced pressures in macro channels: Experiments and assessment of prediction methods. *International Journal of Heat and Mass Transfer* 56 (1-2), 107 – 118.

- [Greco and Vanoli (2005)] Greco, A., Vanoli, G., 2005. Flow boiling heat transfer with HFC mixtures in a smooth horizontal tube. Part II: Assessment of predictive methods. *Experimental Thermal and Fluid Science* 29 (2), 199 – 208.
- [Greco and Vanoli (2006)] Greco, A., Vanoli, G., 2006. Experimental two-phase pressure gradients during evaporation of pure and mixed refrigerants in a smooth horizontal tube. *Heat and Mass Transfer* 42, 709-725.
- [Groeneveld (1973)] Groeneveld, D., 1973. Post dry-out heat transfer at reactor operating conditions. ANS Topical Meeting on Water Reactor Safety. Salt Lake City, USA.
- [Grønnerud (1979)] Grønnerud, R., 1979. Investigation of liquid hold-up, flow-resistance and heat transfer in circulation type of evaporators, part IV: two-phase flow resistance in boiling refrigerants. In: Annexe1972-1, Bulletin De l'Institut du Froid.
- [Gungor and Winterton (1986)] Gungor, K., Winterton, R., 1986. A general correlation for flow boiling in tubes and annuli. *International Journal of Heat and Mass Transfer* 29, 351–358.
- [Haberschill et al.(2003)] Haberschill, P., Branescu, C., Lallemand, M., 2003. Pressure drop of microfinned tubes during boiling of R-22 and R-407C. Eurotherm seminar no 72 (Ed.), Heat and Mass Transfer of Refrigeration Machines and Heat Pumps. Valencia, Spain. 75–79.
- [Hanafizadeh et al. (2011)] Hanafizadeh, P., Saidi, M., Gheimasi, A. N., Ghanbarzadeh, S., 2011. Experimental investigation of air-water, two-phase flow regimes in vertical mini pipe. *Scientia Iranica* 18 (4), 923 – 929.
- [Hambraeus (1991)] Hambraeus, K., 1991. Heat transfer coefficient during two-phase flow boiling of HFC-134a. *International Journal of Refrigeration* 14 (6), 357 – 362.
- [Harirchian and Garimella (2010)] Harirchian, T., Garimella, S., 2010. A comprehensive flow regime map for microchannel flow boiling with quantitative transition criteria. *International Journal of Heat and Mass Transfer* 53, 2694 – 2702.
- [Harirchian and Garimella (2012)] Harirchian, T., Garimella, S., 2012. Flow regime-based modeling of heat transfer and pressure drop in microchannel flow boiling. *International Journal of Heat and Mass Transfer* 55 (4), 1246 – 1260.
- [Hashin and Shtrikman (1962)] Hashin, Z., Shtrikman, S., 1962. A variational approach to the theory of the effective magnetic permeability of multiphase materials. *Journal of Applied Physics* 33, 3125 – 3131.
- [Hausen (1943)] Hausen, H., 1943. Darstellung des Wärmeüberganges in Röhren durch verallgemeinerte Potenzbeziehungen. *Z. VDI Beiheft Verfahrenstechnik* 4.
- [Hewitt and Roberts (1969)] Hewitt, G., Roberts, D., 1969. Studies of two-phase flow patterns by simultaneous X-ray and flash photography.
- [Ishii (1975)] Ishii, M., 1975. Thermo-fluid dynamic theory of two-phase flow. NASA STI/Recon Technical Report A 75.

- [Jabardo and Bandarra Filho (2000)] Jabardo, J.S., Bandarra Filho, E., 2000. Convective boiling of halocarbon refrigerants flowing in a horizontal copper tube - an experimental study. *Experimental Thermal and Fluid Science* 23 (3-4), 93 – 104.
- [Jacobi and Thome (2002)] Jacobi, A. M., Thome, J., 2002. Heat transfer model for evaporation of elongated bubble flows in microchannels. *Journal of Heat Transfer* 124 (6), 1131–1136.
- [Jensen and Memmel (1986)] Jensen, M. K., Memmel, G. J., 1986. Evaluation of bubble departure diameter correlations. 8th International Heat Transfer Conference. San Francisco, USA. 1907–1912.
- [Jones and Zuber (1975)] Jones, O.C., Zuber, N., 1975. The interrelation between void fraction fluctuations and flow patterns in two-phase flow. *International Journal of Multiphase Flow* 2 (3), 273 – 306.
- [Jung et al. (1989)] Jung, D., McLinden, M., Radermacher, R., Didion, D., 1989. A study of flow boiling heat transfer with refrigerant mixtures. *International Journal of Heat and Mass Transfer* 32 (9), 1751 – 1764.
- [Jung et al. (2003)] Jung, D., Kim, Y., Ko, Y., Song, K., 2003. Nucleate boiling heat transfer coefficients of pure halogenated refrigerants. *International Journal of Refrigeration* 26 (2), 240 – 248.
- [Kaew-On and Wongwises (2009)] Kaew-On, J., Wongwises, S., 2009. Experimental investigation of evaporation heat transfer coefficient and pressure drop of R-410A in a multiport mini-channel. *International Journal of Refrigeration* 32 (1), 124 – 137.
- [Kandlikar (1990)] Kandlikar, S. G., 1990. A general correlation for saturated two-phase flow boiling heat transfer inside horizontal and vertical tubes. *Journal of Heat Transfer* 112, 219–228.
- [Kandlikar (2002)] Kandlikar, S., 2002. Fundamental issues related to flow boiling in minichannels and microchannels. *Experimental Thermal and Fluid Science* 26 (2), 389–407.
- [Kandlikar and Grande (2003)] Kandlikar, S.G., Grande, W.J., 2003. Evolution of microchannel flow passages—thermohydraulic performance and fabrication technology. *Heat Transfer Engineering* 24 (1), 3–17.
- [Kandlikar and Balasubramanian (2004)] Kandlikar, S.G., Balasubramanian, P., 2004. An extension of the flow boiling correlation to transition, laminar, and deep laminar flows in minichannels and microchannels. *Heat Transfer Engineering* 25 (3), 86–93.
- [Kasza et al. (1997)] Kasza, K., Didascalou, T., Wambsganss, M., 1997. Microscale flow visualization of nucleate boiling in small channels: mechanisms influencing heat transfer. *Proceedings of International Conference on Compact Heat Exchangers for Process Industries*. Begell House, New York, USA. 343–352.
- [Kattan et al. (1998a)] Kattan, N., Thome, J., Favrat, D., 1998. Flow boiling in horizontal tubes: Part 1 - development of a diabatic two-phase flow pattern map. *Journal of Heat Transfer* 120 (1), 140 – 147.

- [Kattan et al. (1998b)] Kattan, N., Thome, J., Favrat, D., 1998. Flow boiling in horizontal tubes: Part 2 - new heat transfer data for five refrigerants. *Journal of Heat Transfer* 120, 148–155.
- [Katto (1984)] Katto, Y., 1984. Prediction of critical heat flux for annular flow in tubes taking into account the critical liquid film thickness concept. *International Journal of Heat and Mass Transfer* 27 (6), 883 – 891.
- [Kew and Cornwell (1997)] Kew, P., Cornwell, K., 1997. Correlations for the prediction of boiling heat transfer in small-diameter channels. *Applied Thermal Engineering* 17 (8-10), 705 – 715.
- [Kim and Mudawar (2013a)] Kim, S.-M., Mudawar, I., 2013. Universal approach to predicting saturated flow boiling heat transfer in mini/micro-channels - Part I. Dryout incipience quality. *International Journal of Heat and Mass Transfer* 64, 1226–1238.
- [Kim and Mudawar (2013b)] Kim, S.-M., Mudawar, I., 2013. Universal approach to predicting saturated flow boiling heat transfer in mini/micro-channels - Part II: two-phase heat transfer coefficient. *International Journal of Heat and Mass Transfer* 64, 1239–1256.
- [Klimenko and Fyodorov (1990)] Klimenko, V., Fyodorov, M., 1990. Prediction of heat transfer for two-phase forced flow in channels of different orientation. 9th International Heat Transfer Conference, Jerusalem, Israel. 65 – 70.
- [Kon'kov (1965)] Kon'kov, A.S., 1965. Experimental study of the conditions under which heat exchanger deteriorates when a steam-water mixture flows in heated tube. *Teplotenergetika* 13.
- [Kuo and Wang (1996)] Kuo, C., Wang, C., 1996. Horizontal flow boiling of R-22 and R-407c in a 9.52 mm micro-fin tube. *Applied Thermal Engineering* 16 (8-9), 719 – 731.
- [Kutateladze (1961)] Kutateladze, S., 1961. Boiling heat transfer. *International Journal of Heat and Mass Transfer* 4, 31–45.
- [Kuwahara et al. (2000)] Kuwahara, K., Koyama, S., Yu, J., Watanabe, C., Osa, N., 2000. Flow pattern of pure refrigerant HFC134a evaporating in a horizontal capillary tube. *Proceedings of Symposium on Energy Engineering in the 21st Century*. Hong Kong. 445 – 450.
- [Lazarek and Black (1982)] Lazarek, G., Black, S., 1982. Evaporative heat transfer, pressure drop and critical heat flux in a small vertical tube with R-113. *International Journal of Heat and Mass Transfer* 25 (7), 945 – 960.
- [Lee and Lee (2001)] Lee, H., Lee, S., 2001. Heat transfer correlation for boiling flows in small rectangular horizontal channels with low aspect ratios. *International Journal of Multiphase Flow* 27 (12), 2043 – 2062.
- [Lee and Mudawar (2005)] Lee, J., Mudawar, I., 2005. Two-phase flow in high-heat-flux micro-channel heat sink for refrigeration cooling applications: Part I-pressure drop characteristics. *International Journal of Heat and Mass Transfer* 48 (5), 928 – 940.

- [Li and Wang (2003)] Li, J., Wang, B., 2003. Size effect on two-phase regime for condensation in micro/mini tubes. *Heat Transfer-Asian Research* 32 (1), 65–71.
- [Lin et al. (1991)] Lin, S., Kwok, C., Li, R.-Y., Chen, Z.-H., Chen, Z.-Y., 1991. Local frictional pressure drop during vaporization of R-12 through capillary tubes. *International Journal of Multiphase Flow* 17 (1), 95 – 102.
- [Lin et al. (2001)] Lin, S., Kew, P., Cornwell, K., 2001. Two-phase heat transfer to a refrigerant in a 1 mm diameter tube. *International Journal of Refrigeration* 24 (1), 51 – 56.
- [Liu and Winterton (1991)] Liu, Z., Winterton, R., 1991. A general correlation for saturated and subcooled flow boiling in tubes and annuli, based on a nucleate pool boiling equation. *International Journal of Heat and Mass Transfer* 34 (11), 2759 – 2766.
- [Lockhart and Martinelli (1949)] Lockhart, R. W., Martinelli, R. C., 1949. Proposed correlation of data for isothermal two-phase, two-component flow in pipes. *Chemical Engineering Progress* 45 (1), 39–48.
- [Mandhane et al. (1974)] Mandhane, J., Gregory, G., Aziz, K., 1974. A flow pattern map for gas-liquid flow in horizontal pipes. *International Journal of Multiphase Flow* 1 (4), 537 – 553.
- [Martinelli and Nelson (1948)] Martinelli, R., Nelson, D., 1948. Prediction of pressure drop during forced-circulation boiling of water. *Journal of Heat Transfer* 70, 695–702.
- [Mastrullo et al. (2012)] Mastrullo, R., Mauro, A., Thome, J.R., Toto, D., Vanoli, G., 2012. Flow pattern maps for convective boiling of CO₂ and R-410A in a horizontal smooth tube: Experiments and new correlations analyzing the effect of the reduced pressure. *International Journal of Heat and Mass Transfer* 55 (5), 1519 – 1528.
- [Matsui (1984)] Matsui, G., 1984. Identification of flow regimes in vertical gas-liquid two-phase flow using differential pressure fluctuations. *International Journal of Multiphase Flow* 10 (6), 711 – 719.
- [Matsui (1986)] Matsui, G., 1986. Automatic identification of flow regimes in vertical two-phase flow using differential pressure fluctuations. *Nuclear Engineering and Design* 95, 221 – 231.
- [Mauro et al. (2007)] Mauro, A.W., Quibén, J.M., Mastrullo, R., Thome, J.R., 2007. Comparison of experimental pressure drop data for two phase flows to prediction methods using a general model. *International Journal of Refrigeration* 30 (8), 1358 – 1367.
- [McAdams et al. (1942)] McAdams, W., Woods, W., Bryan, R., 1942. Vaporization inside horizontal tubes-ii-benzene-oil mixtures. *Journal of Heat Transfer* 64, 193-200.
- [Mehendale et al. (2000)] Mehendale, S.S., Jacobi, A.M., Shah, R.K., 2000. Fluid flow and heat transfer at micro and meso-Scales with application to heat exchanger design. *Applied Mechanics Reviews* 53 (7), 175–193.

- [Mertz et al. (1996)] Mertz, R., Wein, A., Groll, M., 1996. Experimental investigation of flow boiling heat transfer in narrow channels. Second European Thermal Sciences and 14th UIT National Heat Transfer Conference. Rome, Italia. 204 – 208.
- [Mishima and Hibiki (1996)] Mishima, K., Hibiki, T., 1996. Some characteristics of air-water two-phase flow in small diameter vertical tubes. *International Journal of Multiphase Flow* 22 (4), 703 – 712.
- [Mori et al. (2000)] Mori, H., Yoshida, S., Ohishi, K., Kokimoto, Y., 2000. Dryout quality and post dryout heat transfer coefficient in horizontal evaporator tubes. Proceedings of 3rd European Thermal Sciences Conference. Heidelberg, Germany. 839 – 844.
- [Müller-Steinhagen and Heck (1986)] Müller-Steinhagen, H., Heck, K., 1986. A simple friction pressure drop correlation for two-phase flow in pipes. *Chemical Engineering and Processing: Process Intensification* 20 (6), 297 – 308.
- [Olivier et al. (2007)] Olivier, J.A., Liebenberg, L., Thome, J.R., Meyer, J.P., 2007. Heat transfer, pressure drop, and flow pattern recognition during condensation inside smooth, helical micro-fin, and herringbone tubes. *International Journal of Refrigeration* 30 (4), 609 – 623.
- [Oh et al. (2008)] Oh, H., Ku, H., Roh, G., Son, C., Park, S., 2008. Flow boiling heat transfer characteristics of carbon dioxide in a horizontal tube. *Applied Thermal Engineering* 28 (8-9), 1022 – 1030.
- [Oh and Son (2011)] Oh, H.-K., Son, C.-H., 2011. Flow boiling heat transfer and pressure drop characteristics of CO₂ in horizontal tube of 4.57-mm inner diameter. *Applied Thermal Engineering* 31 (2-3), 163 – 172.
- [Ong and Thome (2009)] Ong, C., Thome, J., 2009. Flow boiling heat transfer of R134a, R236fa and R245fa in a horizontal 1.030 mm circular channel. *Experimental Thermal and Fluid Science* 33 (4), 651 – 663.
- [Ong and Thome(2011a)] Ong, C., Thome, J., 2011. Macro-to-microchannel transition in two-phase flow : Part 1 two-phase flow patterns and film thickness measurements. *Experimental Thermal and Fluid Science* 35 (1), 37 – 47.
- [Ong and Thome (2011b)] Ong, C., Thome, J., 2011. Macro-to-microchannel transition in two-phase flow: Part II - Flow boiling heat transfer and critical heat flux. *Experimental Thermal and Fluid Science* 35 (6), 873 – 886.
- [Ould Didi et al. (2002)] Ould Didi, M., Kattan, N., Thome, J., 2002. Prediction of two-phase pressure gradients of refrigerants in horizontal tubes. *International Journal of Refrigeration* 25 (7), 935 – 947.
- [Padilla et al. (2011)] Padilla, M., Revellin, R., Haberschill, P., Bensafi, A., Bonjour, J., 2011. Flow regimes and two-phase pressure gradient in horizontal straight tubes: Experimental results for HFO-1234yf, R-134a and R-410A. *Experimental Thermal and Fluid Science* 35 (6), 1113 – 1126.
- [Pamitran et al. (2007)] Pamitran, A., Choi, K.-I., Oh, J.-T., Oh, H.-K., 2007. Forced convective boiling heat transfer of R-410A in horizontal minichannels. *International Journal of Refrigeration* 30 (1), 155 – 165.

- [Pamitran et al. (2010)] Pamitran, A., Choi, K., Oh, J., Hrnjak, P., 2010. Characteristics of two-phase flow pattern transitions and pressure drop of five refrigerants in horizontal circular small tubes. *International Journal of Refrigeration* 33 (3), 578 – 588.
- [Park and Hrnjak (2007)] Park, C., Hrnjak, P., 2007. CO₂ and R410A flow boiling heat transfer, pressure drop, and flow pattern at low temperatures in a horizontal smooth tube. *International Journal of Refrigeration* 30 (1), 166 – 178.
- [Pettersen (2004)] Pettersen, J., 2004. Flow vaporization of CO₂ in microchannel tubes. *Experimental Thermal and Fluid Science* 28 (2-3), 111 – 121.
- [Qu and Mudawar (2003)] Qu, W., Mudawar, I., 2003. Flow boiling heat transfer in two-phase micro-channel heat sinks-I. Experimental investigation and assessment of correlation methods. *International Journal of Heat and Mass Transfer* 46 (15), 2755 – 2771.
- [Quibén and Thome (2007a)] Quibén, J.M., Thome, J.R., 2007. Flow pattern based two-phase frictional pressure drop model for horizontal tubes. Part I: Diabatic and adiabatic experimental study. *International Journal of Heat and Fluid Flow* 28 (5), 1049 – 1059.
- [Quibén and Thome (2007b)] Quibén, J.M., Thome, J.R., 2007. Flow pattern based two-phase frictional pressure drop model for horizontal tubes, Part II: New phenomenological model. *International Journal of Heat and Fluid Flow* 28 (5), 1060 – 1072.
- [Revellin (2005)] Revellin, R., 2005. Experimental two-phase fluid flow in microchannels. PhD thesis, Ecole Polytechnique Fédérale de Lausanne.
- [Revellin et al. (2006)] Revellin, R., Dupont, V., Ursenbacher, T., Thome, J. R., Zun, I., 2006. Characterization of diabatic two-phase flows in microchannels: Flow parameter results for R-134a in a 0.5 mm channel. *International Journal of Multiphase Flow* 32 (7), 755 – 774.
- [Revellin and Thome (2007a)] Revellin, R., Thome, J.R., 2007. Experimental investigation of R-134a and R-245fa two-phase flow in microchannels for different flow conditions. *International Journal of Heat and Fluid Flow* 28 (1), 63 – 71.
- [Revellin and Thome (2007b)] Revellin, R., Thome, J.R., 2007. Adiabatic two-phase frictional pressure drops in microchannels. *Experimental Thermal and Fluid Science* 31 (7), 673 – 685.
- [Revellin and Thome (2007c)] Revellin, R., Thome, J.R., 2007. A new type of diabatic flow pattern map for boiling heat transfer in microchannels. *Journal of Micromechanics and Microengineering* 17, 788-796.
- [Revellin et al. (2008)] Revellin, R., Agostini, B., Ursenbacher, T., Thome, J. R., 2008. Experimental investigation of velocity and length of elongated bubbles for flow of R-134a in a 0.5 mm microchannel. *Experimental Thermal and Fluid Science* 32 (3), 870 – 881.
- [Revellin and Haberschill (2009)] Revellin, R., Haberschill, P., 2009. Prediction of frictional pressure drop during flow boiling of refrigerants in horizontal tubes: Comparison to an experimental database. *International Journal of Refrigeration* 32 (3), 487 – 497.

- [Revellin et al. (2012)] Revellin, R., Lips, S., Neveu, P., Bonjour, J., 2012. A comprehensive non-equilibrium thermodynamic analysis applied to a vapor-liquid two-phase flow of a pure fluid. *International Journal of Multiphase Flow* 42, 184–193.
- [Ribatski and Jabardo (2003)] Ribatski, G., Jabardo, J.M., 2003. Experimental study of nucleate boiling of halocarbon refrigerants on cylindrical surfaces. *International Journal of Heat and Mass Transfer* 46 (23), 4439 – 4451.
- [Rouhani and Axelsson (1970)] Rouhani, S.Z., Axelsson, E., 1970. Calculation of void volume fraction in the subcooled and quality boiling regions. *International Journal of Heat Transfer* 13, 383–393.
- [Rouhani and Sohal (1983)] Rouhani, S., Sohal, M., 1983. Two-phase flow patterns: A review of research results. *Progress in Nuclear Energy* 11 (3), 219 – 259.
- [Saisorn and Wongwises(2010a)] Saisorn, S., Wongwises, S., 2010. The effects of channel diameter on flow pattern, void fraction and pressure drop of two-phase air-water flow in circular micro-channels. *Experimental Thermal and Fluid Science* 34 (4), 454 – 462.
- [Saisorn et al. (2010b)] Saisorn, S., Kaew-On, J., Wongwises, S., 2010. Flow pattern and heat transfer characteristics of R-134a refrigerant during flow boiling in a horizontal circular mini-channel. *International Journal of Heat and Mass Transfer* 53, 4023 – 4038.
- [Saisorn et al. (2011)] Saisorn, S., Kaew-On, J., Wongwises, S., 2011. Two-phase flow of R-134a refrigerant during flow boiling through a horizontal circular mini-channel. *Experimental Thermal and Fluid Science* 35 (6), 887 – 895.
- [Saitoh et al.(2005)] Saitoh, S., Daiguji, H., Hihara, E., 2005. Effect of tube diameter on boiling heat transfer of R-134a in horizontal small-diameter tubes. *International Journal of Heat and Mass Transfer* 48 (23), 4973 – 4984.
- [Saitoh et al. (2007)] Saitoh, S., Daiguji, H., Hihara, E., 2007. Correlation for boiling heat transfer of R-134a in horizontal tubes including effect of tube diameter. *International Journal of Heat and Mass Transfer* 50 (25), 5215 – 5225.
- [Sato et al. (1972)] Sato, T., Minamiyama, T., Yanai, M., Tokura, T., 1972. Study of heat transfer in boiling two-phase channel flow - Part 1: Flow patterns in a boiling channel. *Heat Transfer Japanese Research* 1 (1), 1 –14.
- [Sato et al. (1971)] Sato, T., Minamiyama, T., Yanai, M., Tokura, T., Ito, Y., 1971. Study of heat transfer in boiling two-phase channel flow - Part 2: heat transfer in the nucleate boiling region. *Heat Transfer Japanese Research* 1 (1), 15-30.
- [Schrock and Grossman (1962)] Schrock, V., Grossman, L., 1962. Forced convection boiling in tubes. *Nuclear Science Engineering* 12, 474–481.
- [Sempértegui-Tapia et al. (2013)] Sempértegui-Tapia, D., De Oliveira Alves, J., Ribatski, G., 2013. Two-phase flow characteristics during convective boiling of halocarbon refrigerants inside horizontal small-diameter tubes. *Heat Transfer Engineering* 34 (13), 1073-1087.
- [Serizawa et al. (1975)] Serizawa, A., Kataoka, I., Michiyoshi, I., 1975. Turbulence structure of air-water bubbly flow I. measuring techniques. *International Journal of Multiphase Flow* 2 (3), 221 – 233.

- [Serizawa et al. (2002)] Serizawa, A., Feng, Z., Kawara, Z., 2002. Two-phase flow in microchannels. *Experimental Thermal and Fluid Science* 26 (67), 703 – 714.
- [Shah and London (1978)] Shah, R., London, A., 1978. Laminar flow forced convection in ducts. Supplement to *Advances in Heat Transfer*, New York.
- [Shah (1982)] Shah, M., 1982. Chart correlation for saturated boiling heat transfer. *Industrial Engineering Chemistry Process Design and Development: Equations and Further Study* 88 (1), 165–196.
- [Shah (1986)] Shah, R., 1986. Classification of heat exchangers. In: Kabac, S. Bergles, A.E. Mayinger, F. (Eds). *Heat Exchangers: Thermal Hydraulic Fundamentals and Design*. Hemisphere Publishing Corp.
- [Sheng and Palm (2000)] Sheng, C., Palm, B., 2000. The visualisation of boiling in small diameter tubes. *Proceedings of Heat Transfer and Transport Phenomena in Microscale*, 204–208.
- [Sindhuja et al. (2010)] Sindhuja, R., Balakrishnan, A., Murthy, S. S., 2010. Post-CHF heat transfer during two-phase upflow boiling of R-407C in a vertical pipe. *Applied Thermal Engineering* 30 (2-3), 167 – 173.
- [Srinivasan et al. (2010)] Srinivasan, K., Mago, P., Krishnan, S., 2010. Analysis of exhaust waste heat recovery from a dual fuel low temperature combustion engine using an organic rankine cycle. *Energy* 35 (6), 2387 – 2399.
- [Stephan and Abdelsalam (1980)] Stephan, K., Abdelsalam, M., 1980. Heat-transfer correlations for natural convection boiling. *International Journal of Heat and Mass Transfer* 23 (1), 73 – 87.
- [Steiner and Taborek (1992)] Steiner, D., Taborek, J., 1992. Flow boiling heat transfer in vertical tubes correlated by an asymptotic model. *Heat Transfer Engineering* 13, 43–69.
- [Steiner (1993)] Steiner, D., 1993. VDI-Wärmeatlas (VDI Heat Atlas) chapter Hbb. Verein Deutscher Ingenieure. Wiley-Interscience.
- [Sun and Groll (2002)] Sun, Z., Groll, E., 2002. CO₂ flow boiling heat transfer in horizontal tubes. Part 1: flow regime and prediction of dry-out. *Proceedings of 5th IIR-Gustav Lorentzen Conference on Natural Working Fluids*. 131 – 140.
- [Sun and Mishima (2009)] Sun, L., Mishima, K., 2009. An evaluation of prediction methods for saturated flow boiling heat transfer in mini-channels. *International Journal of Heat and Mass Transfer* 52 (23-24), 5323 – 5329.
- [Suo and Griffith (1963)] Suo, M., Griffith, P., 1963. Two phase flow in capillary tubes. Technical report Massachusetts Institute of Technology. Heat Transfer Laboratory. Massachusetts Institute of Technology, Department of Mechanical Engineering.
- [Taitel and Dukler (1976)] Taitel, Y., Dukler, A., 1976. A model for predicting flow regime transitions in horizontal and near horizontal gas-liquid flow. *AIChE Journal* 22, 47–55.
- [Taylor (2000)] Taylor, J., 2000. *Incertitudes et analyses des erreurs dans les mesures physiques*. Dunod.

- [Thome et al. (2004a)] Thome, J., Dupont, V., Jacobi, A., 2004. Heat transfer model for evaporation in microchannels. Part I: presentation of the model. *International Journal of Heat and Mass Transfer* 47 (14), 3375 – 3385.
- [Thome (2004b)] Thome, J.R., 2004. Boiling in microchannels: a review of experiment and theory. *International Journal of Heat and Fluid Flow* 25 (2), 128 – 139.
- [Thome and El Hajal (2004c)] Thome, J.R., El Hajal, J.E., 2004. Flow boiling heat transfer to carbon dioxide: general prediction method. *International Journal of Refrigeration* 27 (3), 294 – 301.
- [Thome et al. (2013)] Thome, J., Bar-Cohen, A., Revellin, R., Zun, I., 2013. Unified mechanistic multiscale mapping of two-phase flow patterns in microchannels. *Experimental Thermal and Fluid Science* 44, 1–22.
- [Tibiricá and Ribatski (2010)] Tibiricá, C.T., Ribatski, G., 2010. Flow boiling heat transfer of R-134a and R245fa in a 2.30 mm tube. *International Journal of Heat and Mass Transfer* 53 (11-12), 2459 – 2468.
- [Tibiricá et al. (2011a)] Tibiricá, C.B., da Silva, J.D., Ribatski, G., 2011. Experimental investigation of flow boiling pressure drop of R-134a in a microscale horizontal smooth tube. *Journal of Thermal Science and Engineering Applications* 3 (1), 1–8.
- [Tibiricá and Ribatski (2011b)] Tibiricá, C.B., Ribatski, G., 2011. Two-phase frictional pressure drop and flow boiling heat transfer for R-245fa in a 2.32-mm tube. *Heat Transfer Engineering* 32 (13-14), 1139–1149.
- [Tran et al. (1996)] Tran, T., Wambsganss, M., France, D., 1996. Small circular and rectangular channel boiling with two refrigerants. *International Journal of Multiphase Flow* 22 (3), 485 – 498.
- [Tran et al. (1997)] Tran, T., Wambsganss, M., Chyu, M., France, D., 1997. A correlation for nucleate flow boiling in small channels. *Compact Heat Exchangers for the Process Industries Conference*. Boston.
- [Tran et al. (2000)] Tran, T., Chyu, M.-C., Wambsganss, M., France, D., 2000. Two-phase pressure drop of refrigerants during flow boiling in small channels: an experimental investigation and correlation development. *International Journal of Multiphase Flow* 26 (11), 1739 – 1754.
- [Triplett et al. (1999)] Triplett, K., Ghiaasiaan, S., Abdel-Khalik, S., Sadowski, D., 1999. Gas-liquid two-phase flow in microchannels Part I: two-phase flow patterns. *International Journal of Multiphase Flow* 25 (3), 377 – 394.
- [Ullmann and Brauner (2007)] Ullmann, A., Brauner, N., 2007. The prediction of flow pattern maps in minichannels. *Multiphase Science and Technology* 19 (1), 49 – 73.
- [Ünal and Gasselt (1983)] Ünal, H., Gasselt, M. V., 1983. Post-dryout heat transfer in steam generator tubes at high pressures. *International Journal of Heat and Mass Transfer* 26 (3), 459 – 464.

- [Ursenbacher et al. (2004)] Ursenbacher, T., Wojtan, L., Thome, J.R., 2004. Interfacial measurements in stratified types of flow. Part I: New optical measurement technique and dry angle measurements. *International Journal of Multiphase Flow* 30, 107-124.
- [Vakili-Farahani et al. (2013)] Vakili-Farahani, F., Agostini, B., Thome, J., 2013. Experimental study on flow boiling heat transfer of multiport tubes with R245fa and R1234ze(E). *International Journal of Refrigeration* 36 (2), 335 – 352.
- [Wambsganss et al. (1991)] Wambsganss, M., Jendrzejczyk, J., France, D., 1991. Two-phase flow patterns and transitions in a small, horizontal, rectangular channel. *International Journal of Multiphase Flow* 17 (3), 327 – 342.
- [Wambsganss et al. (1993)] Wambsganss, M., France, D., Jendrzejczyk, J., Tran, T., 1993. Boiling heat transfer in a horizontal small-diameter tube. *Journal of Heat Transfer* 115 (4), 963–972.
- [Wang et al. (1998)] Wang, C., Yu, J., Lin, S., Lu, C., 1998. An experimental study of convective boiling of refrigerants R-22 and R-410A. *Proceedings of ASHRAE Transactions*. Toronto, Canada. 1144–1150.
- [Wang et al. (2001)] Wang, C., Chiang, S. K., Chang, Y. J., Chung, T. W., 2001. Two-phase flow resistance of refrigerants R-22, R-410A and R-407C in small diameter tubes. *Transactions IChemE* 79, 1879–1891.
- [Wang et al. (2011)] Wang, E.H., Zhang, H.G., Fan, B.Y., Ouyang, M.G., Zhao, Y., Mu, Q.H., 2011. Study of working fluid selection of organic Rankine cycle (ORC) for engine waste heat recovery. *Energy* 36, 3406–3418.
- [Warrier et al. (2002)] Warrier, G., Dhir, V., Momoda, L., 2002. Heat transfer and pressure drop in narrow rectangular channels. *Experimental Thermal and Fluid Science* 26 (1), 53 – 64.
- [Wattelet et al. (1994)] Wattelet, J.P., Chato, J.C., Christoffersen, B.R., Gaibel, J.A., Ponchner, M., Kenny, P.J., Shimon, R.L., Villaneuva, T.C., Rhines, N.L., Sweeney, K.A., Allen, D.G., Heshberger, T.T., 1994. Heat transfer flow regimes of refrigerants in a horizontal tube evaporator. ACRC TR-55, University of Illinois at Urbana-Champaign.
- [Whalley (1980)] Whalley, P.B., 1980. Multiphase flow and pressure drop. *Heat Exchanger Design Handbook*, Hemisphere, Washington D.C., Vol.2, 181–188.
- [Wojtan et al. (2005a)] Wojtan, L., Ursenbacher, T., Thome, J.R., 2005. Investigation of flow boiling in horizontal tubes: Part I - a new diabatic two-phase flow pattern map. *International Journal of Heat and Mass Transfer* 48 (14), 2955 – 2969.
- [Wojtan et al. (2005b)] Wojtan, L., Ursenbacher, T., Thome, J.R., 2005. Investigation of flow boiling in horizontal tubes: Part II - development of a new heat transfer model for stratified-wavy, dryout and mist flow regimes. *International Journal of Heat and Mass Transfer* 48 (14), 2970 – 2985.
- [Wongsa-ngam et al. (2004)] Wongsa-ngam, J., Nualboonrueng, T., Wongwises, S., 2004. Performance of smooth and micro-fin tubes in high mass flux region of R-134a during evaporation. *Heat and Mass Transfer* 40 (6-7), 425–435.

- [Xu and Xu (1998)] Xu, L., Xu, L., 1998. Gas/liquid two-phase flow regime identification by ultrasonic tomography. *Flow Measurement and Instrumentation* 8 (34), 145 – 155.
- [Yamamoto et al. (2007)] Yamamoto, T., Ueda, Y., Ishihara, I., Ozawa, M., Umekawa, H., Matsumoto, R., 2007. Flow boiling heat transfer of carbon dioxide at high pressure in horizontal mini-channels. 6th International Conference on Multiphase Flow, Leipzig, Germany.
- [Yang and Shieh (2001)] Yang, C., Shieh, C., 2001. Flow pattern of air-water and two-phase R-134a in small circular tubes. *International Journal of Multiphase Flow* 27 (7), 1163 – 1177.
- [Yoon et al. (2004)] Yoon, S.H., Cho, E.S., Hwang, Y.W., Kim, M.S., Min, K., Kim, Y., 2004. Characteristics of evaporative heat transfer and pressure drop of carbon dioxide and correlation development. *International Journal of Refrigeration* 27 (2), 111 – 119.
- [Yu et al. (2002)] Yu, W., France, D., Wambsganss, M., Hull, J., 2002. Two-phase pressure drop, boiling heat transfer, and critical heat flux to water in a small-diameter horizontal tube. *International Journal of Heat and Mass Transfer* 28, 927 – 941.
- [Yu and Chau (2010)] Yu, C., Chau, K.T., 2010. Thermoelectric automotive waste heat energy recovery using maximum power point tracking. *Energy Conversion and Management* 50, 1506-1512.
- [Yun et al. (2003)] Yun, R., Kim, Y., Kim, M., Choi, Y., 2003. Boiling heat transfer and dryout phenomenon of CO₂ in a horizontal smooth tube. *International Journal of Heat and Mass Transfer* 46 (13), 2353 – 2361.
- [Yun and Kim (2004)] Yun, R., Kim, Y., 2004. Two-phase pressure drop of CO₂ in minitubes and microchannels. *Microscale Thermophysical Engineering* 8, 259–270.
- [Yun et al. (2005)] Yun, R., Kim, Y., Kim, M.S., 2005. Flow boiling heat transfer of carbon dioxide in horizontal mini tubes. *International Journal of Heat and Fluid Flow* 26 (5), 801 – 809.
- [Yun et al. (2006)] Yun, R., Heo, J. H., Kim, Y., 2006. Evaporative heat transfer and pressure drop of R-410A in microchannels. *International Journal of Refrigeration* 29 (1), 92 – 100.
- [Zeguai et al. (2013)] Zeguai, S., Chikh, S., Tadrist, L., 2013. Experimental study of two-phase flow pattern evolution in a horizontal circular tube of small diameter in laminar flow conditions. *International Journal of Multiphase Flow* 55 (1), 99-110.
- [Zhang and Webb (2001)] Zhang, M., Webb, R. L., 2001. Correlation of two-phase friction for refrigerants in small-diameter tubes. *Experimental Thermal and Fluid Science* 25 (3-4), 131 – 139.
- [Zhang et al. (2004)] Zhang, W., Hibiki, T., Mishima, K., 2004. Correlation for flow boiling heat transfer in mini-channels. *International Journal of Heat and Mass Transfer* 47 (26), 5749 – 5763.

- [Zhang et al. (2010)] Zhang, W., Shih, F. Y., Jin, N., Liu, Y., 2010. Recognition of gas-liquid two-phase flow patterns based on improved local binary pattern operator. *International Journal of Multiphase Flow* 36 (10), 793 – 797.
- [Zhang et al. (2011)] Zhang, S., Wang, H., Guo, T., 2011. Performance comparison and parametric optimization of subcritical Organic Rankine Cycle (ORC) and transcritical power cycle system for low-temperature geothermal power generation. *Applied Energy* 88, 2740–2754.
- [Zivi (1964)] Zivi, S.M., 1964. Estimation of steady-state steam void-fraction by means of the principle of minimum entropy production. *Journal of Heat Transfer* 86 (2), 247–251.
- [Zurcher et al. (2002)] Zurcher, O., Favrat, D., Thome, J.R., 2002. Development of a diabatic two-phase flow pattern map for horizontal flow boiling. *International Journal of Heat and Mass Transfer* 45(2), 291 – 301.
- [Zyhowski et al. (2002)] Zyhowski, G.J., Spatz, M.M., Motta, S.Y., 2002. An overview of the properties and applications of HFC-245fa. *International Refrigeration and Air Conditioning Conference*. Purdue, USA.

List of Publications

Articles in peer reviewed journals

P. Bermejo, R. Revellin, R. Charnay, O. Garbrecht, J. Hugon and J. Bonjour, 2013. Modeling of a microchannel evaporator for space electronics cooling: entropy generation minimization approach, *Heat Transfer Engineering* 34, 1-10.

Charnay, R., Revellin, R., Bonjour, J., 2013. Flow pattern characterization for R-245fa in minichannels: optical measurement technique and experimental results. *International Journal of Multiphase Flow* 57, 169 - 181.

Charnay, R., Revellin, R., Bonjour, J., 2013. Experimental investigation of R-245fa flow boiling in minichannels at high saturation temperatures: flow patterns and flow pattern maps. *International Journal of Heat and Fluid Flow* (IN PRESS).

Charnay, R., Revellin, R., Bonjour, J., 2013. Flow boiling characteristics of R-245fa in a minichannel at medium saturation temperatures. *Experimental Thermal and Fluid Science* (Submitted).

Charnay, R., Revellin, R., Bonjour, J., 2013. Flow boiling heat transfer in minichannels at high saturation temperatures: Part I- Experimental investigation and analysis of the heat transfer mechanisms. *International Journal of Heat and Mass Transfer* (Submitted).

Charnay, R., Revellin, R., Bonjour, J., 2013. Flow boiling heat transfer in minichannels at high saturation temperatures: Part II- Assessment of predictive methods and impact of flow regimes. *International Journal of Heat and Mass Transfer* (Submitted).

Communications

Charnay, R., Revellin, R., Bonjour, J., 2013. Experimental study of R-245fa during flow boiling in minichannels at high saturation temperatures. In: 8th World Conference on Experimental Heat Transfer, Fluid Dynamics and Thermodynamics, Lisbon, Portugal.

Charnay, R., Revellin, R., Bonjour, J., 2012. Experimental study of R-245fa during flow boiling in minichannels. In: IIR 3rd Workshop on Refrigerant Charge Reduction, Valencia, Spain.

Charnay, R., Revellin, R., Bonjour, J., 2012. Flow boiling of R-245fa at high saturation temperature. In: 8th ECI conference Boiling and Condensation, Lausanne, Switzerland.

Charnay, R., Revellin, R., Bonjour, J. Review on two-phase pressure drop and heat transfer coefficient during flow boiling of natural and synthetic refrigerants: a parametric analysis. In: The 23rd IIR International Congress of Refrigeration, Prague, Czech Republic (Keynote lecture).

Charnay, R., Revellin, R., Bonjour, J. Experimental investigation of R-245fa flow boiling in minichannels for different flow conditions. In: 51st European Two-Phase Group Meeting, Lyon, France.

Revellin, R., Charnay, R., Bonjour, J., 2012. Flow boiling of R-245fa at high saturation temperature. In: 50th European Two-Phase Group Meeting, Udine, Italy.

